

THESIS ON NATURAL AND EXACT SCIENCES B221

Revealing Aspects of Cardiac Function from Fluorescence and Electrophysiological Recordings

MARTIN LAASMAA

TUT
PRESS

TALLINN UNIVERSITY OF TECHNOLOGY

Institute of Cybernetics
Laboratory of Systems Biology

This dissertation was accepted for the defense of the degree of Doctor of Philosophy (Engineering Physics) on 31 October, 2016.

Supervisor: Marko Vendelin, PhD
Laboratory of Systems Biology, Institute of Cybernetics,
Tallinn University of Technology, Tallinn, Estonia

Co-supervisors: Pearu Peterson, PhD
Laboratory of Systems Biology, Institute of Cybernetics,
Tallinn University of Technology, Tallinn, Estonia

Rikke Birkedal Nielsen, PhD
Laboratory of Systems Biology, Institute of Cybernetics,
Tallinn University of Technology, Tallinn, Estonia

Opponents: William Edward Louch, PhD, Prof.
Institute for Experimental Medical Research,
Oslo University Hospital and University of Oslo, Oslo, Norway

Pasi Tavi, PhD, Prof.
Department of Biotechnology and Molecular Medicine,
A.I. Virtanen Institute, University of Eastern Finland, Kuopio, Finland

Defense of the thesis: 14 December, 2016

Declaration:

I hereby declare that this doctoral thesis, submitted for the doctoral degree at Tallinn University of Technology, is my original investigation and achievement and has not been submitted for the defense of any academic degree elsewhere.

Martin Laasmaa

Copyright: Martin Laasmaa, 2016, Creative Commons Attribution-NonCommercial-NoDerivs 3.0 Unported License

Colophon: This thesis was typeset with L^AT_EX 2_ε using André Miede's *classicthesis* style with modifications by David Schryer and Ardo Illaste to conform with Tallinn University of Technology style guidelines. The main font is Times. Biolinum is used for sans-serif text.

ISSN 1406-4723

ISBN 978-9949-83-040-4 (publication)

ISBN 978-9949-83-041-1 (PDF)

LOODUS- JA TÄPPISTEADUSED B221

Südametalituse uuringud fluorestsentsi ja elektrofüsioloogiliste mõõtmiste abil

MARTIN LAASMAA

CONTENTS

SUMMARY	vii
KOKKUVÕTE	ix
LIST OF PUBLICATIONS	xi
LIST OF CONFERENCE PRESENTATIONS	xiii
ACKNOWLEDGMENTS	xvi
ACRONYMS	xvii
THESIS	19
1 INTRODUCTION	21
2 DECONVOLVING MICROSCOPE IMAGES	25
2.1 What is Deconvolution?	25
2.2 The Richardson-Lucy Algorithm	26
2.3 Estimating the Total Variation Regularization Parameter	27
2.4 Stopping Criterion for the Algorithm	29
2.5 Example Results of Deconvolution	29
2.6 Conclusions	30
3 DIFFUSION IN CARDIOMYOCYTES	33
3.1 The Nature of Diffusion Restrictions	33
3.2 Cytoplasmic Diffusion Barriers	34
3.3 Diffusion Across the Mitochondrial Outer Membrane	36
3.4 Conclusions	37
4 DETERMINING CALCIUM FLUXES IN CARDIOMYOCYTES	39
4.1 The Approach	40
4.2 Calcium Fluxes in Trout Cardiomyocytes	41
4.3 Physiological Implications	43
4.4 Novelty, Limitations, Outlook	44
4.5 Conclusions	44
5 CONCLUSIONS	45
Image enhancement	45
Diffusion barriers	45
Calcium pathways	46

CONTENTS

REFERENCES	47
CURRICULUM VITAE	57
APPENDIX	67
PUBLICATION I	69
PUBLICATION II	89
PUBLICATION III	113
PUBLICATION IV	129

SUMMARY

THIS DISSERTATION deals with three topics in the field of cardiovascular research. First, the dissertation deals with confocal microscope image enhancement. Second, diffusion restrictions in a single cardiomyocyte is studied. And third, different calcium fluxes in a single cardiomyocyte are determined with electrophysiological techniques. All three topics include experimental measurements, mathematical analysis and modeling. Fluorescence imaging has a central role in the dissertation.

With the help of image enhancement one can gain more information than is visible from raw data at first sight. One of the aims of this study was to improve the Richardson-Lucy deconvolution algorithm with total variation regularization for image enhancement. There are two major issues with the original algorithm: 1) it depends on a certain free parameter that determines the quality of enhancement but the choice of its value lacks definite criterion; 2) it lacks a reliable stopping criterion that has a great importance in balancing between noise reduction and detail enhancement. In this study a solution to these issues are provided. For that, a formula was derived to compute the parameter value during the iteration process. As demonstrated on the analysis of synthetic images, the algorithm yields equally good results as with optimal parameter value. Moreover, the analysis showed that the evolution of the parameter value can be effectively used as stopping criterion.

Deconvolution of confocal images is used to visualize the intracellular structures that may form diffusion barriers. These barriers govern intracellular energy transfer, which is crucial for proper cardiac function. There are two types of diffusion obstacles that interfere with energy transfer from mitochondria to ATPases: cytoplasmic diffusion barriers grouping ATP-producers and -consumers, and mitochondrial outer membrane (MOM) with voltage-dependent anion channel (VDAC) permeable to small hydrophilic molecules. Such profound diffusion restrictions are expected to play a major role in energy transfer, signaling, distribution of apoptotic factors and reactive oxygen species. Another aim of this work was to establish the partitioning of intracellular diffusion obstacles in cardiomyocytes. To determine the diffusion coefficient, partitioning of intracellular diffusion obstacles, and MOM permeability, two supplemental approaches based on fluorescence imaging and mathematical modeling were used. In the first method, raster image correlation spectroscopy was applied to determine diffusion coefficients of two fluorescently labeled molecules that differ in size. The analysis of the obtained experimental

data revealed that in rat cardiomyocytes diffusion of smaller molecules is relatively more restricted than that of larger molecules compared with the surrounding solution. This counterintuitive result can be explained with diffusion restrictions in the cell consisting of semi-permeable barriers that form a regular lattice-like structure. The second method is based on the analysis of permeabilized cardiomyocyte mitochondrial response to different concentrations of extracellular ADP through the measurement of NADH autofluorescence. The results suggest that in permeabilized rat cardiomyocytes a small number of opened VDACs contribute only to half of the observed diffusion restriction between mitochondrial inner membrane and the surrounding solution. The other half of the overall diffusion restriction is clearly positioned in the cytosol on the way between the solution and the MOM.

The diffusion barriers near MOM and in the cytosol are essential for an adequate regulation of mitochondrial ATP-production. This, as well as mitochondrial metabolic capacity, seems in turn to be connected to excitation-contraction coupling (ECC). In cardiac function, Ca^{2+} has a central role in ECC, where changes in intracellular Ca^{2+} concentration regulate contraction. The changes in intracellular Ca^{2+} concentration are caused by a precise balance between different cellular Ca^{2+} fluxes. In case of heart failure, this balance is altered, which results, for example, in a diminished cardiac output. The aim of the last topic of the thesis was to develop a robust method to quantify Ca^{2+} fluxes in cardiac ECC. To determine the kinetics and contribution of different Ca^{2+} fluxes a mathematical model of Ca^{2+} -dynamics that combines the electrophysiological measurements of transsarcolemmal Ca^{2+} currents during action potential clamp and their impact on the Ca^{2+} mediated fluorescence transients was applied. With the aid of the novel method the contributions of different Ca^{2+} fluxes in trout ECC were determined. Also, a significant role of sarcoplasmic reticulum in trout ECC was discovered, which is in sharp contrast with previous estimates. Moreover, the method is not trout specific and is applicable to other species as well.

In summary, the results of the dissertation represent broad range of research on different aspects of cardiac functioning, wherein substantial contributions have been made in the advancement of existing methods as well as in the development of novel methods.

KOKKUVÕTE

S ELLES DOKTORITÖÖS KÄSITLETAKSE kolme teemat südame-veresoonkonna uuringute vallas. Täpsemalt puudutab see töö konfokaal-mikroskoobi piltide matemaatilist parendamist, difusioonitakistusi ja kaltsiumi ringlust ühes südame-lihasrakus. Kõik uuringud hõlmavad endas nii eksperimentaalseid mõõtmisi, kui ka andmete matemaatilist analüüsi ja modelleerimist. Eksperimentaalse osa poolelt on tööd läbivaks elemendiks fluorestsentsi nähtuse kasutamine seatud eesmärkide saavutamiseks, mida rakendatakse siin struktuuride, difusioonikoefitsientide ja ioonide kontsentratsiooni määramiseks rakus.

Nagu eelpool mainitud, siis on üheks töö osaks konfokaal-mikroskoobi piltide matemaatiline parendamine. Konfokaal-mikroskoopias kasutatakse rakustruktuuride nähtavaks muutmiseks nende värvimist fluorestseeruvate molekulidega. Fluorestseeruvatest molekulidest kiirgunud valgus juhitakse läbi optika detektorisse ning arvuti kaasabil koostatakse rakust digitaalne kujutis. Kujutise digitaliseerimise käigus tekib pildidel paratamatult ka müra, mis on tingitud elektroonikast ja footonite loendamisest. Samuti on pildid moonduvad optikast tingitud aberatsioonide tõttu. Pildi matemaatilist parendust kasutades on võimalik vähendada neid efekte pildil ning saada rohkem informatsiooni, kui esmapilgul paistab. Sellest tulenevalt on üheks töö eesmärgiks täieliku variatsiooni regulariseerimisega kombineeritud Richardson-Lucy iteratiivse dekonvolutsiooni algoritmi edasiarendus. Selle algoritmiga kaasnevad kaks järgnevat murekohta: 1) algoritm sõltub kasutajale regularisatsiooni parameetri tundmatust väärtusest; 2) algoritmil puudub usaldusväärne kriteerium iteratsiooni protsessi peatamiseks. Vastavas töö osas tuletati valem antud parameetri väärtuse leidmiseks. Tehislikke konfokaal-mikroskoopia pilte kasutades näidati, et selle valemi abil leitud parameetri väärtusega on võimalik saada sama häid dekonvolutsiooni tulemusi, kui parameeter oleks eelnevalt teada. Lisaks sellele näidati, et leitud valemi abil arvutatud parameetri väärtuse muutumise kulgu iteratsiooni protsessi käigus saab edukalt kasutada ka selle peatamiseks.

Rakusisene energia ülekanne on südame talituses üliolulisel kohal. On teada, et südame-lihasrakus on kaht tüüpi difusioonitakistusi, mis tõkestavad energia ülekannet ATP-d tootvate mitokondrite ja seda tarbivate ATP-aaside vahel. Sellisteks takistuseks võivad olla tsütoplasmaatilised difusioonibarjäärid ja mitokondri välismembraan. Arvatavalt mängivad need difusioonitakistused suurt rolli energia ülekandes, signaliseerimises, apoptootiliste faktorite ja reaktiivsete hapniku radikaal-

lide jaotuses. Teiseks töö eesmärgiks on selliste difusioonitakistuste tuvastamine ja jaotuse määramine südamelihaskus. Selleks kasutati kaht teineteist täiendavat uurimisviisi, mis põhinevad fluorestsents-pilditehnikal ja matemaatilisel modelleerimisel. Üheks meetodiks on rasterpildi korrelatsiooni spektroskoopia, mille abil määrati kahe suuruselt erineva fluorestsentsmolekuli difusioonikoefitsiendid roti südamelihaskus. Antud katseandmete analüüs paljastas, et väiksemate molekulide difusioon rakus võrreldes seda ümbritseva lahusega on suhteliselt rohkem tõkestatud, kui suuremate molekulide difusioon. Ühe võimalusena saab sellist näiliselt ebaloomulikku tulemust selgitada matemaatilise modelleerimise abil osaliselt läbilaskvate barjääridega, mis moodustavad rakus regulaarse võreolise struktuuri. Teine meetod põhineb mitokondrite hingamise analüüsil. Selleks stimuleeriti roti permeabiliseeritud südamelihasku mitokondriaalset hingamist raku ümbritseva lahuse ADP kontsentratsiooni muutmise teel ning mõõdeti samaaegselt NADH autofluorestsentsi, mis on sõltuvuses hingamismääraga. Katseandmete matemaatilise modelleerimise tulemusena leiti, et roti permeabiliseeritud südamelihaskudes moodustab mitokondrite välismembraan poole üleüldisest difusioonitakistusest ning teine pool üleüldisest difusioonitakistusest asetseb mitokondrite välismembraani ja raku välise lahuse vahel.

Südamelihaskus mängib kesksel rollil samuti kaltsium, mille kontsentratsiooni muutus elektromehaanilise sidestuse ajal reguleerib raku kokkutõmbumist ja lõõgastumist. Muutused rakusiseses kaltsiumi kontsentratsioonis on tingitud erinevatest kaltsiumvoogudest, mis on omavahel ülimalt täpselt tasakaalustatud. Kuid südamehaiguse korral on see tasakaal muutunud, mis põhjustab näiteks südame väiksemat tootlikust. Töö viimaseks eesmärgiks on välja töötada meetod, mille abil on võimalik määrata erinevate kaltsiumvoogude dünaamikat ja panust kaltsiumi kontsentratsiooni muutusse südame elektromehaanilise sidestuse jooksul. Selle tarvis loodi kaltsiumi tasakaalu matemaatiline mudel, mis kombineerib rakumembraani läbivate kaltsiumvoogude elektrofüsioloogilisi mõõtmisi aktsioonipotentsiaali vältel ja nende mõju kaltsiumi poolt vahendatud fluorestsentsi signaalile. Selle uude meetodi abil määrati erinevate kaltsiumvoogude kineetika ja panus vikerforelli südamelihaskus elektromehaanilise sidestuse ajal. Samuti näidati, et vikerforelli südamelihaskus on suur roll sarkoplasmaatilisel retiikulil, mida eelnevalt on peetud tühiuks. Lisaks sellele ei ole arendatud meetod forelli-spetsiifiline ning on kasutatav teistegi liikide korral.

Kokkuvõtteks esindavad antud väitekirja tulemused erinevaid aspekte südamelihaskude talituses ning selle käigus on antud oluline panus nii olemasolevate uurimisviiside edasiarendamisele, kui ka uute meetodite väljatöötamisele.

LIST OF PUBLICATIONS

- I **Laasmaa M**, Vendelin M and Peterson P; **Application of regularized Richardson-Lucy algorithm for deconvolution of confocal microscopy images**, *Journal of Microscopy*, 243(2), 124–140, 2011
- II Illaste A, **Laasmaa M**, Peterson P, and Vendelin M; **Analysis of molecular movement reveals latticelike obstructions to diffusion in heart muscle cells**, *Biophysical Journal*, 102(4), 739–748, 2012
- III Simson P, Jepihhina N, **Laasmaa M**, Peterson P, Birkedal R, and Vendelin M; **Restricted ADP movement in cardiomyocytes: Cytosolic diffusion obstacles are complemented with a small number of open mitochondrial voltage-dependent anion channels**, *Journal of Molecular and Cellular Cardiology*, 97, 197–203, 2016
- IV **Laasmaa M**, Birkedal R, and Vendelin M; **Revealing calcium fluxes by analyzing inhibition dynamics in action potential clamp**, *Journal of Molecular and Cellular Cardiology*, 100, 93–108, 2016

Summary of the author's contributions

- I In Publication I, I was the main author, I carried out all the experiments, participated in building confocal microscope and wrote the deconvolution software package, performed all the necessary analysis and simulations, prepared all the presented figures and wrote the manuscript.
- II For Publication II, I participated in the building of the equipment, measured the point spread function for the analysis, took part in the discussions.
- III In the study summarized with Publication III, I was involved throughout the project. I participated in the designing of the study, co-supervised experiments and analysis, measured the point spread function for the analysis, wrote a part of analyzing software. In addition, I participated in discussions and revising the manuscript.

CONTENTS

IV As the main author of Publication IV, I designed and carried out all the experiments, I made all the necessary theoretical analysis on synthetic data as well as analyzed the experimental data. I wrote the manuscript and prepared all figures and tables presented in the article.

LIST OF CONFERENCE PRESENTATIONS

- I **Laasmaa* M**, Peterson P, Birkedal R, Vendelin M; **3D confocal microscope image enhancement by Richardson-Lucy deconvolution algorithm with total variation regularization**; *Biophysical Society 53rd Annual Meeting*, Boston, Massachusetts, February 28 – March 4, 2009
- II Birkedal* R, Sokolova N, **Laasmaa M**, Vendelin M; **Using rainbow trout cardiomyocytes to identify the diffusion restrictions found specifically in oxidative muscles**; *Annual Meeting of the Society of Experimental Biology*, Glasgow, UK, June 28 – July 1, 2009
- III **Laasmaa* M**, Vendelin M, Peterson P; **3D confocal microscope image enhancement by Richardson-Lucy deconvolution algorithm with total variation regularization: parameters estimation**; *Biophysical Society 54th Annual Meeting*, San Francisco, California, USA, February 20 – 24, 2010
- IV Illaste* A, **Laasmaa M**, Schryer D, Birkedal R, Peterson P, Vendelin M; **Determination of Regional Diffusion Coefficients of Fluorescent ATP in Rat Cardiomyocytes**; *Biophysical Society 54th Annual Meeting*, San Francisco, California, USA, February 20 – 24, 2010
- V **Laasmaa* M**, Vendelin M, Peterson P; **Application of regularized Richardson-Lucy algorithm for deconvolution of confocal microscopy images**; *Biophysical Society 55th Annual Meeting*, Baltimore, Maryland, USA, March 5 – 9, 2011
- VI Illaste* A, **Laasmaa M**, Birkedal R, Peterson P, Vendelin M; **Mapping Diffusion Coefficients of Fluorescent Dyes in Cardiomyocytes**; *Biophysical Society 55th Annual Meeting*, Baltimore, Maryland, USA, March 5 – 9, 2011
- VII Illaste* A, **Laasmaa M**, Peterson P, Vendelin M; **Analysis of Molecular Movement Reveals Latticelike Obstructions to Diffusion in Heart Muscle Cells**; *Biophysical Society 56th Annual Meeting*, San Diego, California, USA, February 25 – 29, 2012

*The presenting author

- VIII **Laasmaa* M**, Birkedal R, Vendelin M; **An integrated method to quantify calcium fluxes in cardiac excitation-contraction coupling**; *Biophysical Society 57th Annual Meeting*, Philadelphia, Pennsylvania, USA, February 2 – 6, 2013
- IX **Laasmaa* M**, Birkedal R, Vendelin M; **An integrated method to quantify calcium fluxes in cardiac excitation-contraction coupling**; *37th International Congress of Physiological Sciences (IUPS2013)*, Birmingham, UK, July 21 – 26, 2013
- X Sokolova* N, Sepp M, Kotlyarova S, **Laasmaa M**, Vendelin M, Birkedal R; **Metabolic compartmentation and regulation in rainbow trout cardiomyocytes**; *37th International Congress of Physiological Sciences (IUPS2013)*, Birmingham, UK, July 21 – 26, 2013
- XI Jepihhina* N, Simson P, **Laasmaa M**, Peterson P, Birkedal R, Vendelin M; **The characterization of diffusion obstacles in rat cardiomyocytes**; *Biophysical Society 59th Annual Meeting*, Baltimore, Maryland USA, February 7 – 11, 2015
- XII **Laasmaa* M**, Peterson P, Vendelin M, Birkedal R; **Action potential clamp data analysis reveals large contribution of sarcoplasmic reticulum in excitation-contraction coupling of trout cardiomyocytes**; *The Joint Meeting of the Federation of European Physiological Societies and the Baltic Physiological Societies (FEPS2015)*, Kaunas, Lithuania, August 26 – 29, 2015
- XIII Jepihhina* N, Simson P, **Laasmaa M**, Birkedal R, Vendelin M; **The characterization of diffusion obstacles in rat cardiomyocytes**; *The Joint Meeting of the Federation of European Physiological Societies and the Baltic Physiological Societies (FEPS2015)*, Kaunas, Lithuania, August 26 – 29, 2015
- XIV Simson P, Jepihhina N, **Laasmaa M**, Birkedal R, Vendelin* M; **The characterization of diffusion obstacles in rat cardiomyocytes**; *44th European Muscle Conference 2015*, Warsaw, Poland, September 21 – 26, 2015
- XV **Laasmaa* M**, Peterson P, Vendelin M, Birkedal R; **Calcium fluxes in cardiac excitation-contraction coupling in rainbow trout**; *44th European Muscle Conference 2015*, Warsaw, Poland, September 21 – 26, 2015
- XVI **Laasmaa* M**, Vendelin M, Birkedal R; **Using action potential clamp data to determine the calcium fluxes and contributions in excitation-contraction coupling *in vivo* in cardiomyocytes**; *Biophysical Society 60th Annual Meeting*, Los Angeles, California, USA, February 27 – March 2, 2016

XVII Simson P, Jepihhina N, **Laasmaa M**, Branovets J, Peterson P, Birkedal R, Vendelin* M; **Number of open mitochondrial VDACs and intracellular diffusion coefficient in heart muscle**; *Biophysical Society 60th Annual Meeting*, Los Angeles, California, USA, February 27 – March 2, 2016

ACKNOWLEDGMENTS

This study was carried out at the Laboratory of Systems Biology, the Institute of Cybernetics at the Tallinn University of Technology. First of all, I would like to thank my supervisors Dr. Marko Vendelin, Dr. Pearu Peterson and Dr. Rikke Birkedal for their guidance, advice, and active support. They all possess different sets of skills that complement each other and during my doctoral studies I have learned a lot from them. Therefore, I am really grateful that I have had a chance to have them as my supervisors.

I would also like to thank all my wonderful former and present colleagues for the help, support and valuable discussions. It has been a great pleasure working with all of you.

My gratitude belongs also to my dear friends, who have been with me throughout the process helping me to take some time off and charge my batteries.

And finally, I like to express my deepest gratitude to my parents who have been supporting me in every possible way from beginning to end of my studies all these years.

Financial support from the Wellcome Trust (081755), the Estonian Science Foundation (ETF8041), the European Union through the European Regional Development Fund (CENS Estonian Center of Excellence in Research), as well as Archimedes Foundation is appreciated.

ACRONYMS

ADP	adenosine diphosphate
AP	action potential
APC	action potential clamp
ATP	adenosine triphosphate
ATPase	adenosine triphosphatase
CICR	Ca ²⁺ -induced Ca ²⁺ -release
DC	diffusion coefficient
ECC	excitation-contraction coupling
K _m (ADP)	apparent Michaelis constant of mitochondrial respiration to ADP
LTCC	L-type calcium channel
MSE	mean squared error
MIM	mitochondrial inner membrane
MOM	mitochondrial outer membrane
NADH	reduced nicotinamide adenine dinucleotide
NCX	Na ⁺ /Ca ²⁺ exchange
NIF	nifedipine
PSF	point spread function
RICS	raster image correlation spectroscopy
RL	Richardson-Lucy
SERCA	sarcoplasmic reticulum Ca ²⁺ ATPase
SNR	peak signal-to-noise ratio
SR	sarcoplasmic reticulum
TV	total variation
VDAC	voltage-dependent anion channel

THESIS

INTRODUCTION

DURING MY DOCTORAL STUDIES I have been involved in many projects in the field of cardiac research wherein the overall subject has been investigating aspects of cardiac functioning in single cardiomyocytes. Within the thesis, I moved from structural studies and image enhancement to investigate molecular movement within cells and with their surroundings. The main goals of the dissertation can be divided into three following topics: 1) finding a practical method to determine image enhancement algorithm input parameters; 2) investigating molecular movements in cardiomyocytes; 3) describing calcium cycling in cardiomyocytes.

This chapter gives a general overview of the three goals. More specific aims of the constituted research topics with background and motivation are brought to the reader in the three following chapters. Finally, the last chapter of the thesis outlines all the main conclusions of the work done during my doctoral studies.

Cardiomyocytes, cardiac muscle cells, are the building blocks of the heart muscle with complex structure and high energy demand. Cardiomyocytes convert chemical energy to mechanical work to shorten and lengthen, therefore, giving the heart the ability to pump blood throughout the body. As heart muscle is made up from a great number of cardiomyocytes, they have to synchronously contract and relax. The synchronous behavior is regulated by a periodical electrical signal. Hence, structural properties, electrical signals, mechanical work, and energy management in cardiomyocytes are tightly coupled. This all makes cardiomyocyte a very complex biological system where a single process cannot take place without influencing other processes. Therefore, experimental data in whatever form obtained from this kind of system is linked to by many processes. In my doctoral studies I have focused on signal processing of fluorescence and electrical measurements.

The most straightforward way to get information about an object or phenomenon is through a visual observation. If the object that is under investigation is as small as a cardiomyocyte, roughly on the scale of a tenth of a millimeter, then it remains invisible to the naked eye. Therefore, microscopes are required. One choice among many types of microscopes, is the optical one. When using the simplest type of optical microscope, where visible light passes through the specimen and a set of

lenses is used for magnification, we can detect objects that are non-transparent and large enough. For example, in mammalian cardiomyocytes, nuclei and arrays of sarcomeres will be visible. Unfortunately, the majority of cellular structures are transparent and/or too small to be optically resolved. One option to make cellular structures visible is to take advantage of the fluorescence phenomenon. For instance, using a chemical compound that is known to interact with a specific organelle and has certain fluorescent properties, we can detect these organelles in a cell.

In practice, all measurements, to some extent, suffer from random and systematic errors, determined by measuring devices or physical properties. That is also true for confocal microscopes as used in this study. The main error sources in confocal microscopy are noise from electronics and aberrations from the optical components [1]. By using mathematical analyzing tools it is possible to reduce noise, eliminate optical aberrations, and even improve resolution, in other words enhance the quality of recorded images [2].

In this work, we employ a deconvolution algorithm for image restoration. Such algorithms can be iterative, which in practice means that user has to know when to stop an iteration process. Furthermore, algorithms may depend on parameters, whose values the user has to guess [3]. Therefore, in Publication I, we improved a popular deconvolution algorithm and proposed a method to automatically determine the missing parameter values as well as determined a stopping criterion for the iteration process. We demonstrated that this method performs as well as with the optimal parameter value. Moreover, the developed deconvolution algorithm have been applied frequently in the Laboratory of Systems Biology everyday work and the results are used in publications [4, 5]. An overview of the work done in the field of image enhancement is presented in Chapter 2.

Fluorescence is useful not only for imaging cellular structures but also for measuring concentrations [6] and diffusion properties of fluorescent molecules [7]. The ability of a molecule to diffuse depends on the environment. For example, a molecule can diffuse more freely in solution than in a cardiomyocyte [8]. Moreover, when speaking of cardiomyocytes, it has been shown that diffusion depends on the state of the cell. Namely, according to several respiration kinetics analyses [9–11], diffusion is restricted more in healthy cells than in failing cells.

To study diffusion in cardiomyocytes, we used two different methods. Both of these approaches take advantage of fluorescence and mathematical modeling. In the first approach, we use two different fluorescently labeled molecules. Their diffusional properties in rat cardiomyocytes were determined by using raster image correlation spectroscopy (RICS). The RICS method is based on recorded fluorescence fluctuation in space and time of a single molecule. From the data analysis, we determined diffusivity for both molecules. Moreover, from the combina-

tion of RICS analysis and stochastic mathematical modeling, we predicted that in cardiomyocytes, diffusion restrictions may form a lattice-like structure with semi-permeable barriers. In the second approach, we took advantage of reduced nicotinamide adenine dinucleotide (NADH) autofluorescence properties. In the mitochondrial matrix, NADH is a product of the tricarboxylic acid cycle and is used to build up the proton gradient across mitochondrial inner membrane (MIM) that is utilized by the adenosine triphosphate (ATP) synthase protein in the MIM to convert adenosine diphosphate (ADP) to ATP. Thus, the intracellular ADP concentration is closely related to NADH in mitochondria [12]. We used this knowledge and performed experiments where respiration of permeabilized cardiomyocytes was stimulated at different exogenous ADP concentration levels. For the analysis, we composed a cell specific diffusion-reaction model. With this model we determined the permeability of cytoplasmic barriers and MOM. The study of diffusion in cardiomyocyte is summarized in Chapter 3 giving an overview of the research done in Publication II and Publication III.

The last topic of my doctoral studies was to determine Ca^{2+} fluxes in cardiomyocytes during ECC. The importance of intracellular Ca^{2+} cannot be emphasized enough as it is the main regulator of cardiac contractility [13]. During a cardiomyocyte contraction intracellular free Ca^{2+} concentration varies roughly ten fold. This dynamic process is induced by Ca^{2+} fluxes from multiple sources that have either extra- or intracellular origin [13]. The interplay between and the magnitude of these fluxes vary significantly between species and stage of life [14–16]. Moreover, it has been shown by many researchers that the balance of different Ca^{2+} fluxes is altered in the case of heart disease [17–21]. Thus, to gain better understanding of how and why these changes in Ca^{2+} fluxes take place in health and disease, we need to have a reliable method that enables to estimate the dynamics of Ca^{2+} fluxes during ECC. The method, that is proposed here, combines fluorescence, electrophysiological measurements, and mathematical modeling. In short, we use a Ca^{2+} sensitive fluorescent dye to monitor changes in free Ca^{2+} concentration in cytosol. At the same time, we use electrophysiology to measure Ca^{2+} transmembrane currents. As mentioned above, changes in cellular Ca^{2+} concentration originate from Ca^{2+} fluxes from different sources. These fluxes are blended together in measurements. To separate individual Ca^{2+} fluxes from raw data we use a simple Ca^{2+} balance model. The detailed description and validation of the method as well as results gained from the analysis of data from trout cardiomyocytes are described in Publication IV and summarized in Chapter 4.

DECONVOLVING MICROSCOPE IMAGES

IN LIFE SCIENCES, imaging biological samples has a major role. There are many imaging techniques like electron, scanning probe, and optical microscopy. Optical microscopy can be divided into different techniques from which widefield fluorescence microscopy and confocal microscopy are one of the most commonly used in research of biological systems. Along with measurements of physical quantities, there is always undesired noise and some degradation of data. Taking into account physical processes, we can mathematically restore measured microscopy objects that are transformed during the imaging process by using a deconvolution algorithm.

There are many deconvolution algorithms developed so far. The most popular one is the iterative Richardson-Lucy (RL) maximum-likelihood algorithm. However, this algorithm involves parameters which have to be specified by the user. Therefore, *one of the aims of my doctoral studies was to find practical means of determining the values of these parameters.*

2.1 WHAT IS DECONVOLUTION?

In confocal as well as in widefield fluorescence microscopes, the image of the sample is degraded by the optics. The process of optical distortions by the measurement system to the sample can be described by a mathematical operation known as convolution. This means the studied object emitting detectable photons is convolved with a point spread function (PSF) when the object image is transformed through the optical pathway. The PSF itself can be defined as an image of single point viewed through the measurement optics. In addition to the optical distortions comes the noise that is introduced by the electronic recording devices that convert detected photons to a digital signal — for example, by charge-coupled device cameras, photomultiplier tubes, etc. An illustrative image formation scheme is shown in Fig. 1.



Figure 1 – A scheme of image formation in microscope. A is true object that is observed. In B, optical pathway convolves the object with PSF resulting C. After image C digitization (D) noise is introduced resulting a noisy and optically degraded image E.

One of the simplest image formation models in a microscope can be mathematically formulated as follows:

$$i = \mathcal{P}(o \otimes h). \quad (2.1)$$

This image formation model is generally used in confocal microscopy. Here, the observed image i is the result of convolution of the true object o with the PSF h and degraded with Poisson noise \mathcal{P} . Knowing the microscopes' image formation model, it is possible to reverse the effects of degradation of the observed image to some extent. This kind of image restoration is referred to as deconvolution.

There are many deconvolution algorithms developed so far. For example, Jansson-van Cittert algorithm [22, 23], Carrington algorithm [24], constrained Tikhonov-Miller algorithm [25], Fourier-wavelet regularized algorithm [26], expectation maximization algorithm [27, 28], RL algorithm [29, 30], and blind deconvolution algorithms [31–33]. The choice of deconvolution algorithm depends largely on the user's requirements (e.g., whether the deconvolved image has to be pleasant to the viewer's eye or it should be quantitatively as correct as possible), computational resources, and other limitations [2, 34].

2.2 THE RICHARDSON-LUCY ALGORITHM

In Publication I, we focused on improving the RL algorithm. This algorithm is widely used for deconvolution of microscope images and it leads to a quantitatively correct solution in the case of noise free data [35]. But it has some undesired properties. Namely, in the presence of noise, the deconvolution process will converge to a solution dominated by the noise in an infinite number of iterations [3]. Therefore, we used the algorithm together with the total variation (TV) regularization that blurs the noise artifacts to some extent.

An iterative scheme of a multiplicative gradient type RL algorithm with the TV regularization is [3]:

$$o^{(s+1)} = \left(\frac{i}{o^{(s)} \otimes h} \otimes \tilde{h} \right) \cdot \frac{o^{(s)}}{1 - \lambda \operatorname{div} \left(\frac{\nabla o^{(s)}}{|\nabla o^{(s)}|} \right)}, \quad (2.2)$$

where h is PSF, $\tilde{h}(v) = h(-v)$, λ is a TV regularization parameter, and differentiation operations are defined with respect to voxel coordinates v . For the first estimate $o^{(0)}$ we used the measured image i .

Here, we deal with two questions of very practical nature that every user has to face when using this deconvolution algorithm. Firstly, the TV regularization part of the Eq. 2.2 depends on the parameter λ . Thus, what is the best value for the regularization parameter λ ? Secondly, all iterative deconvolution algorithms, as well as this one, require a stopping criterion. Namely, how many iterations give the best or satisfying result? My contribution was to provide the answers to these questions as outlined in the following sections. In our approach (in Publication I), the regularization parameter estimation and the proposed stopping criterion are closely connected.

2.3 ESTIMATING THE TOTAL VARIATION REGULARIZATION PARAMETER

It has been shown that the RL algorithm with TV regularization gives good results if the regularization parameter λ is chosen appropriately. Since determining a good parameter value is challenging, we derived a formula for estimating this value, λ_{lsq} , from microscope images. The formula is based on the least squares method and is given in Publication I with Eq. 5. With this formula, the λ_{lsq} is computed for each iteration step, and hence, is constantly updated during iteration process. We demonstrated in Publication I that by using our derived formula for estimating λ_{lsq} on synthetic images, we can obtain results that are as good as results achieved by using an optimal regularization parameter value (λ_{opt}) of a particular case.

The use of synthetic images is one way to quantify an algorithms' performance. This is because we know the end result that should be achieved, which is not true in most cases while imaging real objects. By deconvolving the synthetic image that is transformed according to the image formation as it is in microscope (Fig. 1), we can then directly validate the deconvolution result. This can be done by comparing the result with the true object. Generally, for the comparison, some norm between the images has to be defined. In this work, we used the mean squared error (MSE) as the norm.

Usually, synthetic images contain simple geometrical objects that have either very sharp intensity transitions or large regions with constant intensity or both. If an algorithm is fine-tuned to perform well in such conditions, it may fail in restoring real experimental data by producing artifacts that the user is unaware of, leading to the misinterpretation of certain features. In this study we used synthetic images that were created on the basis of real confocal images (detailed description is given in Publication I). Such images are more suitable for testing algorithms because they contain real cellular structures and features that we eventually want to recover.

In this work we determined the λ_{opt} value for a wide range of peak signal-to-noise ratio (SNR) levels. The value of λ_{opt} was found from degraded synthetic images by deconvolving them with different fixed λ values and comparing the deconvolution results obtained with the initial synthetic images using the MSE. Note that, the exact value of λ_{opt} can be determined only when using synthetic images. A summarizing example of the deconvolution algorithm performance at different SNR levels (ranging from 2 to 100) using λ_{opt} , λ_{lsq} and $\lambda = 0$ (i.e., no TV regularization is applied) is shown in Fig. 2A.

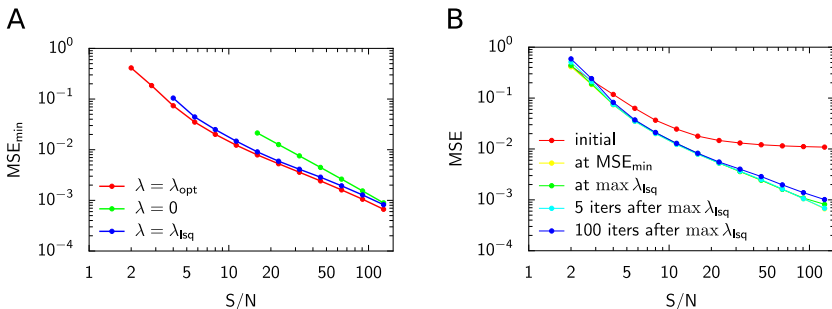


Figure 2 – The analysis of deconvolution at different SNR. In A the relationship between SNR and minimal MSE is shown in case of λ_{opt} , λ_{lsq} , and $\lambda = 0$. In B, MSE as a function of SNR and stopping iteration step is shown.

It is evident from the Fig. 2A that use of λ_{opt} or λ_{lsq} gives similar deconvolution results with respect to MSE. Furthermore, this shows the necessity of using regularization of the RL. Namely, when no regularization is used (see Fig. 2A, $\lambda = 0$), the RL algorithm can handle only images that have high SNR. In the case where the synthetic images have low SNR, the deconvolution process became unstable and failed.

From the analysis, we also found that λ_{opt} is in inverse relation with SNR. This means that with the increase of SNR less TV regularization of the algorithm is required. We found that the optimal λ depends on the SNR: $\lambda_{opt} \approx 50/\text{SNR}$. This relation is illustrated in Fig. 5B in Publication I. This relation can be used as a

robust estimate for determining optimal λ when knowing SNR approximately. In practice, we recommend to use λ_{lsq} estimation when deconvolving experimental images since this does not require estimation of SNR.

2.4 STOPPING CRITERION FOR THE ALGORITHM

The used iterative deconvolution algorithm can basically “work forever”. The problem with the algorithm is that it converges to a solution dominated by noise ($\lambda = 0$) and produces artifacts if the iteration process is not stopped in time. So, an adequate stopping criterion is needed to interrupt the process.

As mentioned before, our proposed stopping criterion for the deconvolution algorithm is related to the estimation of the regularization parameter. From the analysis using synthetic images, we noticed that the maximum value of λ_{lsq} is in good correlation with the minimum point of MSE. As a result, we suggest to interrupt the iteration process five steps after the λ_{lsq} has reached its maximum value. A comparison of MSE of the deconvolution results stopped at different iteration points is presented in Fig. 2B. Here, the red line shows the MSE between an initial degraded synthetic image and the original image at different SNR. The yellow line in Fig. 2B represents the best achievable deconvolution results under the given conditions with respect to MSE. This means that MSE is minimal between the original image and the result. If we compare the results obtained when the iteration process is stopped at the maximum λ_{lsq} (green) or 5 iterations after the maximum λ_{lsq} (cyan) then the achieved result is as good as the best results (yellow). If the process is stopped after 100 iterations of the maximum value of λ_{lsq} (blue), then the result can deviate from the best results. For example, in this particular case Fig. 2B where SNR is larger than 30, this leads to larger MSE compared to results obtained were iteration process were stopped earlier (at or 5 iterations after the λ_{lsq} maximum). Therefore, it is critical to stop the process at the right time otherwise one may produce artifacts in the deconvolved results.

2.5 EXAMPLE RESULTS OF DECONVOLUTION

An example of deconvolved confocal microscope 3D images are presented in Publication I. Here, we used images of mitochondria and sarcolemma of rat cardiomyocytes. Mitochondria were visualized by using MitoTracker Green FM and the sarcolemma was labeled using the potential sensitive dye di-8-ANEPPS. The respective recorded and deconvolved images can be viewed in Publication I in Fig. 6 and Fig. 7. In both cases the contrast of the images is improved and noise is smoothed

out. Mitochondria and t-tubules are more visible and clear. Also, there is a significant contrast enhancement in the cross-sections of 3D images (yz plane).

Another example is presented in Fig. 3, where the deconvolved confocal microscopy images show the morphology of trout cardiomyocytes. Here, actin filaments labeled with Atto633-phalloidin (yellow) and the immunolabeling of tubulin (cyan) are shown. In C, sarcolemma and mitochondria were labeled with di-8-ANEPPS (green) and MitoTracker Red CMXRos (red), respectively. Again, the deconvolution has brought out fine details and reduced the noise.

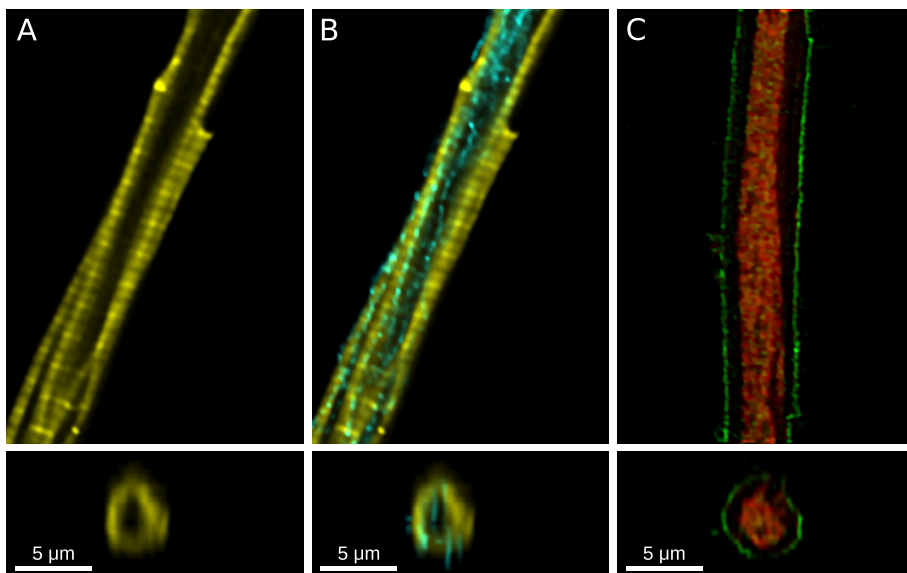


Figure 3 – Deconvolved confocal microscopy images of trout cardiomyocytes. Actin filaments are shown in yellow, tubulin in cyan, sarcolemma in green, mitochondria in red. Figure from [5].

2.6 CONCLUSIONS

In summary, we derived a formula to estimate the total variation regularization parameter for regularized Richardson-Lucy deconvolution algorithm and showed that over a certain range of noise levels the estimated regularization parameter gives as good results as with the optimal regularization parameter. This proposed method estimates the regularization parameter depending on the measured confocal microscope images during the iteration process, and therefore, no educated guess is needed to find the TV regularization parameter. Furthermore, the inverse relation between the optimal TV regularization parameter and image signal-to-noise ratio is given and taken into account in the regularization estimation. In addition, new

stopping criterion for the deconvolution process has been proposed. Moreover, we have developed an open source software package *IOCBio Microscope* wherein the RL with the TV regularization is implemented that can be used for deconvolving images in practice. The developed software package can be also used as a platform for testing new deconvolution algorithms.

DIFFUSION IN CARDIOMYOCYTES

FOR EVERY WORKING MACHINE there is a need for energy. If leaving out the symbolic meanings and biological buildup of a heart, then this muscular organ can be considered as a pump — a machine that pumps blood throughout the body by regularly contracting and relaxing. The energy for the contraction comes from ATP that is utilized by contractile elements of heart muscle cells, cardiomyocytes. Other intracellular processes depend on ATP as well, such as the production of proteins, the transportation of substances into and out of a heart cell, maintaining ion-balance, Ca^{2+} cycling, etc.

In adult mammalian cardiomyocytes, ATP production mainly takes place in mitochondria by oxidative phosphorylation of ADP. From there, ATP either participates in the creatine kinase system or passively diffuses to ATP consumers, ATPases. However, the diffusion of ADP and ATP has been found to be restricted in cardiomyocytes. This has been shown in a wide range of research such as the respiration experiments done on permeabilized fibers or cells [36, 37], autofluorescence measurements of single cells [12], and with mathematical modeling of experimental data [38]. Although the exact role of diffusion restriction in cardiomyocytes is not clear yet, there is a connection between the state of heart and diffusion restrictions. In the case of chronic heart failure or after acute ischemia the overall diffusion restriction are reduced severely based on several respiration kinetics analysis [9–11]. This effect, however, can be reduced by ischemic preconditioning [39]. Hence, understanding the nature of diffusion restrictions in cardiomyocytes could be used to develop new therapies for heart failure. Therefore, *a part of my doctoral studies was dedicated to the investigation of diffusion restrictions in cardiomyocytes.*

3.1 THE NATURE OF DIFFUSION RESTRICTIONS

In principle, the overall diffusion restriction can be divided into two different groups. The first group is related to mitochondria. Namely, the synthesis of ATP from ADP in mammalian cardiomyocytes takes place in the mitochondrial matrix and is exported by adenine nucleotide translocator to intermembrane space where

ATP participates in the creatine kinase reaction or passively diffuses to ATPases, as mentioned before. For that, ATP has to pass through a physical barrier, mitochondrial outer membrane (MOM), which restricts the free diffusion of ATP and, thus, makes it a diffusion obstacle. The second group of diffusion obstacles is situated in the cytoplasm. Particularly, it has been suggested that ATP producing mitochondria are grouped together with ATP consuming systems such as myosin ATPases and sarcoplasmic reticulum Ca^{2+} ATPase (SERCA) by proteins associated with the cytoskeleton, thus, forming discrete functional units [40]. It is estimated that between these units, the diffusion of ADP/ATP is more restricted compared the diffusion within the units [36, 41]. In Publication II, we studied the diffusion of two different molecules in cytoplasm using an extended RICS technique and estimated the distribution and permeability of diffusion barriers by a stochastic mathematical model. Further knowledge of the diffusion of ADP in cytoplasm and permeability of MOM was gained in Publication III, where a novel approach was developed that combines NADH autofluorescence imaging at different respiration levels stimulated by exogenous ADP and cell-specific mathematical modeling.

3.2 CYTOPLASMIC DIFFUSION BARRIERS

To gain information about the cytoplasmic diffusion restrictions we turned to the RICS technique and mathematical modeling as previously stated. The RICS technique is essentially a merge of confocal imaging and fluorescence correlation spectroscopy that allows to measure molecular dynamics and concentrations from fluorescence confocal images [7].

For our study, RICS required specialized hardware and software. There were two main shortcomings with the equipment at our disposal at the time: 1) a photomultiplier tube used for photon detection, and 2) limited data acquisition automation. More specifically, first, the commercial confocal microscope was equipped with an analog photomultiplier tube that is optimized for imaging. When used with RICS, analog photomultiplier tube requires the use of long pixel acquisition times to avoid interference between pixels [7, 8]. The long acquisition times are not suitable for the fast diffusing molecules used in the study. Thus, we had to use photon counting detector, as commonly used in fluorescence correlation spectroscopy. Second, as intensity fluctuations of fast diffusing single molecules are measured, there is need for a great number of experiments to get a significant amount of data for analysis. To be able to do that, full automation of the experiment is required. My task in this project was to build a custom confocal microscope to overcome problems listed above.

In Publication II, we employed RICS to determine the diffusion coefficients (DCs) of two fluorescent molecules that differed in size. A larger molecule Alexa647-dextran 10K and a smaller fluorescently labeled ATP, ATTO633-ATP, having molecular weights of 10000 and 1127 Da, respectively. The DCs in cardiomyocytes were determined in the transverse and longitudinal direction as illustrated in Fig. 4. The respective DCs for Alexa647-dextran 10K are 16 ± 2 and $19 \pm 3 \mu\text{m}^2/\text{s}$, and for ATTO633-ATP 24 ± 6 and $35 \pm 8 \mu\text{m}^2/\text{s}$ (mean \pm standard deviation). When we compared DCs found in cardiomyocytes with DCs in the surrounding solution, we discovered to our surprise that the diffusion of the smaller molecules was relatively more hindered than the movement of the larger molecules (Fig. 4C). In general, in a crowded environment one would expect an opposite result [42].

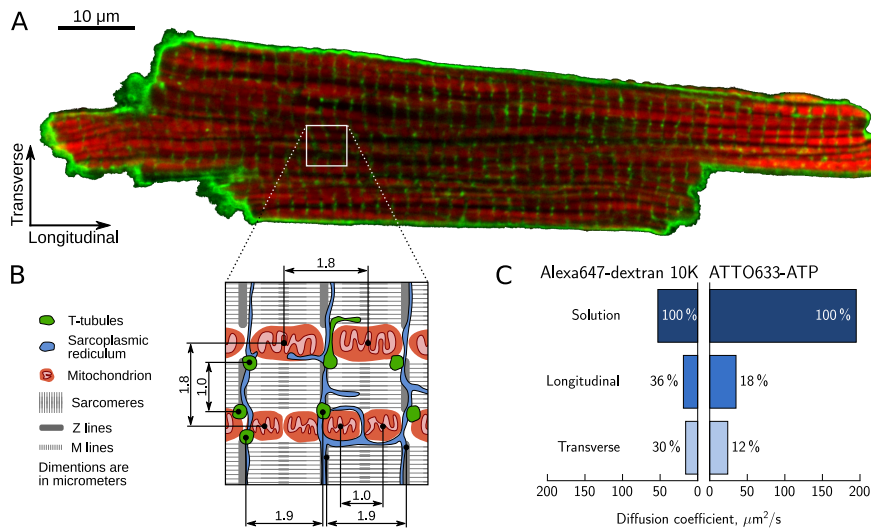


Figure 4 – Structure and diffusion obstacles in a cardiomyocyte. A confocal image of a cardiomyocyte is shown in A, where mitochondria are marked in red, and sarcolemma together with t-tubules are in green. Note the lattice-like structure in longitudinal and transverse directions. B: a scheme of regularly arranged intracellular structures and organelles are shown. C: DCs of Alexa647-dextran 10K and ATTO633-ATP in solution and cardiomyocyte are given. Percentages represent the relative fractions of DCs compared to solution.

To explain this counter-intuitive result, we composed a stochastic mathematical model that mimics the diffusion pathway in the heart muscle. The detailed model description can be found in Publication II Supporting Material. In short, our aim was to determine the barrier parameters with which DC values obtained from the model coincide with those from the experiments. Namely, we simulated diffusion of Alexa647-dextran 10K and ATTO633-ATP in a three-dimensional periodical lattice of permeable barriers in all directions. At the same time, we generated simulated confocal microscope images analogous to the images obtained from our

experiments. This was done using different distances between barriers and different barrier permeabilities. From these simulated images, we then calculated the apparent DCs for each dimension as was done with the experimental data. Assuming that the diffusion obstacles are arranged as permeable physical barriers in a three-dimensional lattice, we found from our numerical simulations that, the diffusion barriers are situated $\leq 1 \mu\text{m}$ apart and have rather few small openings — around 0.3 % of barrier surface is covered with pores. ($\sim 1 \dots 30$ openings per μm^2 of radius 7 ... 30 nm).

It is not clear from which intracellular structures these kind of diffusion obstacles originate. However, the distances between the barriers found in Publication II are in agreement with the morphology of rat cardiomyocytes (see Fig. 4A and B). For example, the transverse distances between t-tubules previously reported in several works [43–46] are close to what we estimated in Publication II. Moreover, Birkedal et al. (2006) showed that in rat ventricular myocytes the distance between the centers of mitochondria in transverse direction is $\sim 1.8 \mu\text{m}$ [47], which indicates that there could be two barriers at this distance. Whereas, in longitudinal direction, they found two possible distances $\sim 1.0 \mu\text{m}$ and $\sim 1.8 \mu\text{m}$, suggesting either there is one or two mitochondria per sarcomere, respectively [47]. In addition, sarcoplasmic reticulum (SR) can play also significant role in restricting diffusion in cardiomyocytes. It can form planular cisternae [46] and invaginate the the space between sarcomeres [48].

3.3 DIFFUSION ACROSS THE MITOCHONDRIAL OUTER MEMBRANE

It is known that MOM restricts the movement of ADP and ATP [49]. These nucleotides can pass through the MOM only via a large mitochondrial channel VDAC. Thus, the permeability of MOM is regulated by VDAC's conductivity and in turn it can possibly act as a regulator of respiration rate [49, 50].

In Publication III we developed a new method to simultaneously quantify ADP movement through cytoplasm and MOM in a single cardiomyocyte. In short, the method is based on a mathematical analysis of experimentally measured NADH autofluorescence images of a permeabilized cardiomyocyte, in which respiration rate was stimulated by different concentrations of exogenous ADP. This was done under conditions where NADH autofluorescence is linearly related to respiration rate as shown previously in [12]. For the analysis, we composed a cell-specific diffusion-reaction mathematical model to describe the diffusion of ADP/ATP in the cell's cytoplasm and the reactions of ATP production and consumption by mitochondria and ATPases, respectively. With this model, we generated synthetic NADH autofluorescence images at different combinations of cytosolic DC and apparent

Michaelis constant of mitochondrial respiration to ADP ($K_m(\text{ADP})$). This was done for each exogenous ADP concentration used in the experiments. These calculated images were then compared with experimental images recorded at the same exogenous ADP concentration. From the best fit between calculated and measured images, the values for DC and $K_m(\text{ADP})$ were determined.

We found that on average the cytosolic DC for ADP/ATP is $\sim 30 \mu\text{m}^2/\text{s}$. That is close to the DC of fluorescently labeled ATP determined by using RICS in research published in Publication II. Together with the DC, we estimated an average apparent mitochondrial affinity to ADP of permeabilized rat cardiomyocytes, $K_m(\text{ADP}) = 0.16 \text{ mM}$. In respiration experiments, the overall apparent K_m for ADP of permeabilized rat cardiomyocytes is 0.3 mM . From here it is clear that MOM permeability is responsible for restricting the overall ADP diffusion about a half, and thus, the second half is attributed to the cytoplasmic diffusion barriers. Knowing the $K_m(\text{ADP})$ value, we related the permeability of a single VDAC to ADP respiration rate of a single mitochondrion. This was done under assumption that in the steady state the flow of ADP through the MOM is balanced out by the ATP synthase in the mitochondrial matrix. Taking into account the permeability of a single VDAC to ADP and total number of VDACs, derived in Publication III Supporting Material, we estimated that only around 2% of VDACs are open for ADP. On average, this is approximately 300 open VDACs per mitochondrion out of ~ 14000 .

3.4 CONCLUSIONS

Diffusion of different metabolites and macromolecules, including ADP/ATP, are considerably restricted in cardiomyocytes. With the research published in Publication II we propose that in rat cardiomyocytes these diffusion obstacles form a lattice-like structure of physical barriers situated around $1 \mu\text{m}$ apart. Most strikingly, we discovered that the diffusion of larger molecules are relatively less restricted than the movement of smaller ones. Moreover, latter research published in Publication III suggests that approximately a half of overall diffusion restriction to ADP is caused by cytoplasmic diffusion barriers and the other half is due to the large fraction of closed VDACs in MOM.

DETERMINING CALCIUM FLUXES IN CARDIOMYOCYTES

CALCIUM HAS MANY ROLES in different cellular processes. For instance, in cardiomyocytes calcium takes a part in ECC as the main regulator of cardiac contractility. When a cardiomyocyte undergoes an action potential (AP), a transient change of membrane potential, various ionic currents like sodium, potassium and calcium flow through the cell's plasmamembrane. During an AP, the Ca^{2+} entry into the cell cytosol causes a transient elevation in the intracellular Ca^{2+} concentration. Such elevation of cytosolic Ca^{2+} leads to activation of contraction through complex reactions including binding of Ca^{2+} to troponin C [13]. In the later phase of the AP, Ca^{2+} dissociates from troponin C as it is extruded from cytosol causing the cell to relax. Therefore, in healthy cardiomyocytes, a well balanced interplay between influx and efflux of Ca^{2+} ensures flawless contractions that is the basis for a heart to fulfill its main purpose — to maintain a blood supply throughout an organism.

In cardiomyocytes, there are three main Ca^{2+} influx pathways that contribute to the overall Ca^{2+} transient. Namely, transsarcolemmal Ca^{2+} flux via L-type calcium channel (LTCC) and $\text{Na}^+/\text{Ca}^{2+}$ exchange (NCX) running in reverse, which in turn trigger Ca^{2+} -induced Ca^{2+} -release (CICR) from the SR. The roles of these pathways during a cardiac beat vary between species, stage of life, and in health and disease. For example, contribution of NCX in reverse is considered negligible in rabbit cardiomyocytes [51], whereas in mouse cardiomyocytes it participates in the regulation of Ca^{2+} release and contractility [52–54]. Moreover, in mammalian ECC, CICR from SR plays a large role. In rat heart, it was estimated to contribute 80 % to the overall Ca^{2+} transient [55]. In contrast, in some fish species, LTCC and NCX contribute more or less equally to the Ca^{2+} transient, and CICR does not take place [56]. Failing cardiomyocytes of adult mammals return to an “immature ECC” with diminished CICR and increased Ca^{2+} influx via NCX [57]. Thus, the ability to quantitatively determine Ca^{2+} fluxes in cardiomyocytes at different states is highly beneficial. Hence, *one of the aims of my doctoral studies was to develop an approach to estimate calcium fluxes in a single cardiomyocyte.*

4.1 THE APPROACH

To my best knowledge, there is no direct way to quantitatively measure Ca^{2+} fluxes in cardiomyocytes in physiological conditions. This is mainly because different Ca^{2+} fluxes are deeply interconnected. For example, CICR is proportional to the size of the trigger [58] and will decrease if Ca^{2+} influx via LTCC or NCX is inhibited. Inhibition of LTCC and/or CICR affects the Ca^{2+} balance across the sarcolemma and the shape of the AP, which in turn, affects NCX current. Therefore, to accomplish the challenging aim that was set, we used a combination of action potential clamp (APC) together with fluorescence imaging of a Ca^{2+} -sensitive dye, and mathematical modeling. The overall scheme of the method is presented with Fig.5.

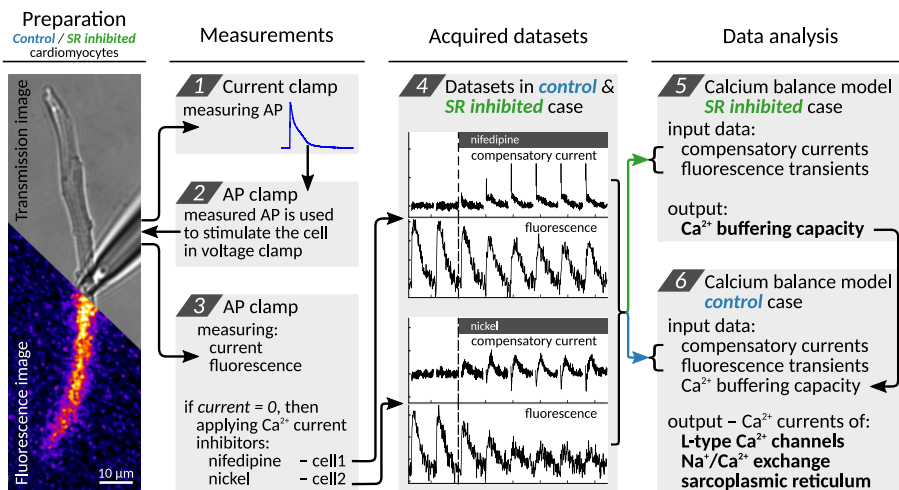


Figure 5 – The overall scheme of APC technique: from preparation to data analysis.

The APC is an electrophysiological method during which the cell is voltage clamped with its own AP that is recorded before in current-clamp mode. As a result, if the intrinsic AP is used as the stimulus, then measured current is zero [59]. If the cell is exposed to an ionic current inhibitor, a non-zero current is measured by the patch-clamp amplifier (see current traces in Fig.5 panel 4). This current is a compensatory current injected by the amplifier to compensate for the loss of the transmembrane current and is proportional to the extent of inhibition.

In this study we used blockers that inhibit transsarcolemmal Ca^{2+} currents. Since Ca^{2+} influx triggers intracellular Ca^{2+} release from SR which will not be reflected in electrophysiological measurements, we need more information to describe all Ca^{2+} fluxes during ECC. This additional information can be gained by following intensity transients of cells loaded with a Ca^{2+} sensitive dye, simultaneously with APC measurements. These Ca^{2+} transients reflect the sum of all cellular Ca^{2+} fluxes that

is modulated by intracellular Ca^{2+} buffering. To determine this intracellular Ca^{2+} buffering capacity, we used data from cardiomyocytes where SR Ca^{2+} release and uptake were inhibited prior to the APC experiment. In this case only transsarcolemmal Ca^{2+} fluxes induce the overall Ca^{2+} transient, and the intracellular Ca^{2+} buffer can be determined. As it is mentioned before, Ca^{2+} fluxes are deeply interconnected. Therefore, we composed a simple mathematical model of Ca^{2+} dynamics to separate different Ca^{2+} fluxes from each other. Using the combination of measured compensatory currents and respective Ca^{2+} transient induced as the model input, we determined the kinetics and contributions of LTCC, NCX and CICR. To evaluate our mathematical approach, we generated synthetic data similar to experimental. A detailed overview of the generation of synthetic data, the mathematical formalism, the model evaluation, and the least squares optimization procedures are given in Publication IV and in Publication IV Supporting Material.

4.2 CALCIUM FLUXES IN TROUT CARDIOMYOCYTES

The first task, in the quantification process of different Ca^{2+} fluxes, was to determine total intracellular buffering capacity in trout cardiomyocytes. For that, we used in our analysis cells where the Ca^{2+} release and uptake from SR was inhibited as explained in previous Section. Combining the experiments where Ni^{2+} and nifedipine (NIF) were used as inhibitors, we separated the Ca^{2+} fluxes through LTCC and NCX. Knowing these fluxes, we fitted calculated Ca^{2+} transients at different total buffer concentrations with measured transients. From the best fits, the average total intracellular Ca^{2+} buffering capacity was found to be equal to $51.2 \pm 15.6 \mu\text{M}$.

After we estimated the intracellular Ca^{2+} buffering capacity, we were able to proceed with determination of the Ca^{2+} fluxes via different Ca^{2+} pathways. Fig. 6 shows sample dynamics of the three Ca^{2+} fluxes (A), the gradual changes of Ca^{2+} influxes during inhibition with Ni^{2+} (B), and the relation to the overall Ca^{2+} transient (C). Note that in C, the numbers above the loops correspond to the same pulse numbers as in B. It is clear from Fig. 6A and B that, in this particular case, the SR is the largest contributor in trout ventricular cardiomyocytes within a beat. We found that under baseline conditions, on average, SR contributes $53 \pm 10 \%$, NCX $30 \pm 6 \%$, and LTCC $18 \pm 7 \%$ to overall Ca^{2+} influx. In SR inhibited case the main contributor is NCX with $60 \pm 7 \%$ and rest $40 \pm 7 \%$ comes from LTCC. While comparing the results obtained from cells where SR Ca^{2+} release and uptake were inhibited with cells where SR was active we found several significant differences, which are summarized in Table 1. For example, on average transsarcolemmal fluxes via LTCC and NCX increased in SR inhibited case by $\sim 40 \%$ and 20% , respectively. Fur-

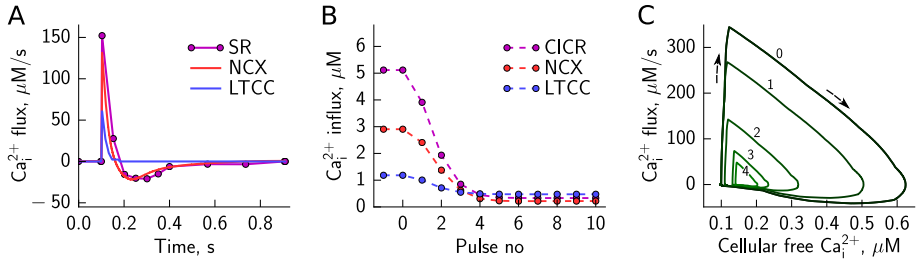


Figure 6 – An example of Ca^{2+} fluxes and their gradual change during inhibition. In A, the dynamics of different Ca^{2+} fluxes during ECC in a single cardiomyocyte is shown. B and C show, in the same cell, the changes in Ca^{2+} influxes via different pathways and the total Ca^{2+} flux relation to overall Ca^{2+} transient, respectively, during inhibition by Ni^{2+} . The numbers above the loops in C correspond to the pulse numbers in B.

thermore, SR inhibition clearly reduced overall Ca^{2+} transient. Also, SR inhibition slowed significantly down overall Ca^{2+} dynamics that is characterized by smaller value in Ca^{2+} transient raise time and by prolonged time to peak and relaxation time values. Therefore, it is necessary to always take caution if using results from one state (non-physiological condition) and extrapolating these results to estimate some other state (physiological condition).

	Control		SR inhibited		p-value
	mean \pm SEM	n	mean \pm SEM	n	
Ca^{2+} influx via LTCC, μM	2.1 \pm 0.7	4	2.9 \pm 0.8	5	<0.03
Ca^{2+} influx via NCX, μM	3.5 \pm 0.8	6	4.3 \pm 1.3	5	0.081
Ca^{2+} transient peak before inhibition, nM	880 \pm 139	10	480 \pm 114	9	<10 ⁻⁵
LTCC inactivation time, ms	21.3 \pm 2.6	4	31.0 \pm 9.5	5	0.083
Rate of rise of Ca^{2+} transient, $\mu\text{M/s}$	19.9 \pm 5.5	10	7.5 \pm 2.4	9	<10 ⁻⁴
Time to peak of Ca^{2+} transient, ms	71.0 \pm 20.0	10	111.2 \pm 32.1	9	<0.01
Relaxation time of Ca^{2+} transient, ms	200.4 \pm 52.8	10	254.8 \pm 55.5	9	<0.05

Table 1 – Comparison of results from SR inhibited and control case.

The importance of the SR in trout ventricular myocytes has been studied for years. It has been suggested that SR is more important at high temperatures and low pacing frequencies [60, 61], and mainly is recruited in ECC at temperatures above 20 °C [60–62] or acts as a safety mechanism in trout under adrenergic stimulation [63]. Our study gives a quantitative measure to the fluxes. We kept the conditions close to physiological and found that under baseline conditions transmembrane fluxes triggered a significant CICR from the SR that is roughly a half of the overall Ca^{2+} transient. It has been shown before that transmembrane Ca^{2+} influxes via both LTCC and NCX can trigger CICR [64]. Furthermore, a large Ca^{2+} influx through NCX was expected on basis of the high intracellular Na^{+} concentra-

tion found in trout cardiomyocytes [65]. The relatively small contribution of LTCC to the transsarcolemmal Ca^{2+} fluxes fits well with the results of Cros et al. [63]. They used Na^+ -free solution to block NCX and found that LTCC alone only triggers CICR during adrenergic stimulation, but not under baseline conditions. Our results show that the larger, combined Ca^{2+} influx through NCX and LTCC under physiological conditions triggers a significant CICR.

It is questionable whether different studies from different laboratories are directly comparable. Farmed rainbow trout are highly inbred, and different populations may have different cardiovascular defects [66]. Therefore, tissue, temperature, and frequency effects on the role of the SR should preferably be studied all together on the same population.

4.3 PHYSIOLOGICAL IMPLICATIONS

Under baseline conditions NCX is the main transsarcolemmal Ca^{2+} influx pathway in trout ventricular cardiomyocytes providing roughly a third of overall Ca^{2+} influx. Therefore, NCX is an important regulator of contractility and may provide an explanation for the negative force-frequency relationship [67]. The duration of the AP depends on the heart rate i.e., the AP duration increases as the heart rate decreases. Thus, increase in the AP duration will result in a larger Ca^{2+} influx via NCX that in turn will provide a larger trigger of CICR from the SR.

The large SR contribution in trout ventricular cardiomyocytes could explain the relatively high SR Ca^{2+} load found in these myocytes [68]. Neither the SR Ca^{2+} load nor the ryanodine receptor expression or localization change with temperature acclimation [68, 69]. However, SERCA expression increases with cold-acclimation in atrium as well as in ventricle [70]. Although there are temperature dependent adaptations, it seems that the SR is always ready to be recruited. This also could explain why trout manage relatively large acute temperature shifts. Moreover, trout cardiomyocytes resemble neonatal mammalian cardiomyocytes in many ways. For example, morphologically, both are long and slender, and lacking t-tubules [71, 72]. Energetically they are more hypoxia-tolerant having a higher glycolytic capacity [73], and lack functional coupling of mitochondrial creatine kinase to respiration [72, 74], but are coupled to hexokinase as we show in [5]. On the basis of the present study, we can extend the resemblance on ECC level as well. Namely, it has been shown that in neonatal rabbit cardiomyocytes a relatively large Ca^{2+} influx through NCX triggers CICR [75], and ryanodine receptors are co-localized with NCX rather than LTCC [71, 76]. Although, such co-localization studies are missing on trout, we have now shown that, in functional terms, trout ECC is similar to neonatal mammalian cardiomyocytes.

4.4 NOVELTY, LIMITATIONS, OUTLOOK

When compared to the approaches that rely on determining Ca^{2+} current properties to estimate Ca^{2+} fluxes, our method has the advantage of disturbing the cell as little as possible. For the experiments we use solutions that resemble the intra- and extracellular ionic composition. Moreover, the data for analysis is taken shortly before and after the inhibition occurs. This avoids problems that arise when analyzing data taken from the steady state at the end of inhibition. Namely, in the beginning of the inhibition, the intracellular ionic composition is close to the physiological composition and effects that emerge from this can be considered secondary. Therefore, the changes in transmembrane currents are primarily caused by the inhibition.

Like with any method there are some limitations with the proposed method. The proposed method is experimentally time consuming. Since the interactions between Ca^{2+} currents have to be accounted for, we cannot use inhibitor after inhibitor to sequentially determine currents in the same cell, as it has been done for Na^+ and K^+ [77].

We envision that this approach can be combined with state-of-the-art mathematical models, which allows to study details of Ca^{2+} dynamics *in vivo*. Recently, a combination of traditional APC and dynamic clamp techniques was used to refine guinea-pig rapid delayed rectifier K^+ current model [78]. We expect that the combination of analysis of inhibition dynamics used in this work with dynamic clamp would allow to reveal properties of Ca^{2+} fluxes that have eluded researchers so far.

4.5 CONCLUSIONS

In Publication IV, we developed a novel approach to quantify Ca^{2+} fluxes in cardiomyocytes during ECC under physiological conditions as close as possible. Furthermore, the method was successfully applied on rainbow trout ventricular cardiomyocytes. As a result, we were able to quantify the kinetics of LTCC, NCX and CICR and the contributions of these Ca^{2+} fluxes to overall Ca^{2+} transient. With this, we demonstrated a significant Ca^{2+} release from the SR and hence, resolved the long standing issue on the role of SR under physiological conditions in trout ventricular myocytes. In addition, we think that this approach can be further developed by combining it with dynamic clamp and full electrophysiological models to study different currents during ECC *in vivo*.

CONCLUSIONS

THIS DISSERTATION FOCUSES on the research of cardiomyocytes to gain a deeper understanding of their structure, energy transfer systems and calcium handling which all are crucial for proper functioning of a cardiomyocyte. The main results are listed below.

IMAGE ENHANCEMENT

- a) The derived formula to estimate the TV regularization parameter for regularized RL deconvolution algorithm gives good deconvolution results over a wide range of noise levels.
- b) The formula estimates the regularization parameter value from the measured confocal microscope images during iteration process, and therefore, no educated guess is needed to find the parameter value.
- c) The dynamics of estimated TV regularization parameter can be effectively used as a stopping criterion for iterative RL deconvolution process: stop after λ_{lsq} has achieved maximum value.
- d) A relation between the optimal TV regularization parameter and image signal-to-noise ratio was found.
- e) During the study an open source software package for deconvolution purposes was developed.

DIFFUSION BARRIERS

- f) Two different methods were developed to determine and quantify diffusion obstacles in cardiomyocyte.
- g) The diffusion of larger molecules is relatively less restricted than the movement of smaller ones.

CONCLUSIONS

- h) In rat cardiomyocytes, two significant intracellular diffusion restrictions were found: cytoplasmic and mitochondrial nature.
- i) In cardiomyocytes, cytoplasmic diffusion obstacles may possibly form a lattice-like structure of physical barriers situated around 1 μm apart.
- j) Approximately a half of overall diffusion restriction to ADP is caused by cytosolic diffusion obstacles and the other half is due to the large fraction of closed VDACs in MOM.

CALCIUM PATHWAYS

- k) A novel approach was developed for quantifying different Ca^{2+} fluxes in cardiomyocytes during ECC under physiological conditions.
- l) The method was successfully applied on rainbow trout ventricular cardiomyocytes to quantify the kinetics of LTCC, NCX and CICR as well as contributions of these Ca^{2+} fluxes to overall Ca^{2+} transient.
- m) The method was used to demonstrate significant Ca^{2+} release from the SR and hence, resolving the long standing issue on the role of SR under physiological conditions in trout ventricular myocytes.

REFERENCES

REFERENCES

- [1] Peter J. Shaw. Comparison of widefield/deconvolution and confocal microscopy for three-dimensional imaging. In James B. Pawley, editor, *Handbook of Biological Confocal Microscopy*, chapter 23, pages 453–467. Springer, New York, 3 edition, 2006.
- [2] Mark B. Cannell, Angus McMorland, and Christian Soeller. Image enhancement by deconvolution. In James B. Pawley, editor, *Handbook of Biological Confocal Microscopy*, chapter 25, pages 488–497. Springer, New York, 3 edition, 2006.
- [3] Nicolas Dey, Laure Blanc-Feraud, Christophe Zimmer, Pascal Roux, Zvi Kam, Jean-Christophe Olivo-Marin, and Josiane Zerubia. 3D microscopy deconvolution using Richardson-Lucy algorithm with total variation regularization. Technical Report 5272, INRIA, April 2004.
- [4] R. Birkedal, M. Laasmaa, and M. Vendelin. The location of energetic compartments affects energetic communication in cardiomyocytes. *Front. Physiol.*, 5:376, 2014.
- [5] N. Karro, M. Sepp, S. Jugai, M. Laasmaa, M. Vendelin, and R. Birkedal. Metabolic compartmentation in rainbow trout cardiomyocytes: coupling of hexokinase but not creatine kinase to mitochondrial respiration. *J. Comp. Physiol. B, Biochem. Syst. Environ. Physiol.*, NA, 2016.
- [6] J. R. Berlin and M. Konishi. Ca²⁺ transients in cardiac myocytes measured with high and low affinity ca²⁺ indicators. *Biophys. J.*, 65(4):1632–1647, 1993.
- [7] C. M. Brown, R. B. Dalal, B. Hebert, M. A. Digman, A. R. Horwitz, and E. Gratton. Raster image correlation spectroscopy (rics) for measuring fast protein dynamics and concentrations with a commercial laser scanning confocal microscope. *J. Microsc.*, 229(1):78–91, 2008.
- [8] M. Vendelin and R. Birkedal. Anisotropic diffusion of fluorescently labeled atp in rat cardiomyocytes determined by raster image correlation spectroscopy. *Am. J. Physiol. Cell. Physiol.*, 295(5):C1302–1315, 2008.

References

- [9] L. Kay, V. A. Saks, and A. Rossi. Early alteration of the control of mitochondrial function in myocardial ischemia. *J. Mol. Cell. Cardiol.*, 29(12):3399–3411, 1997.
- [10] L. Kay, Z. Daneshrad, V. A. Saks, and A. Rossi. Alteration in the control of mitochondrial respiration by outer mitochondrial membrane and creatine during heart preservation. *Cardiovasc. Res.*, 34(3):547–556, 1997.
- [11] S. Boudina, M. Laclau, L. Tariosse, D. Daret, G. Gouverneur, S. Bonoron-Adele, V. Saks, and P. Santos. Alteration of mitochondrial function in a model of chronic ischemia in vivo in rat heart. *Am. J. Physiol. Heart Circ. Physiol.*, 282(3):H821–H831, 2002.
- [12] N. Jepihhina, N. Beraud, M. Sepp, R. Birkedal, and M. Vendelin. Permeabilized rat cardiomyocyte response demonstrates intracellular origin of diffusion obstacles. *Biophys. J.*, 101(9):2112–2121, 2011.
- [13] D. Bers. Calcium fluxes involved in control of cardiac myocyte contraction. *Circ. Res.*, 87(4):275–281, 2000.
- [14] H. Shiels and G. J. Galli. The sarcoplasmic reticulum and the evolution of the vertebrate heart. *Physiology*, 29(6):456–469, 2014.
- [15] C. Terracciano and K. Macleod. Measurements of ca^{2+} entry and sarcoplasmic reticulum ca^{2+} content during the cardiac cycle in guinea pig and rat ventricular myocytes. *Biophys. J.*, 72(3):1319–1326, 1997.
- [16] J. Huang, L. Hove-Madsen, and G. Tibbits. Na^{+}/ca^{2+} exchange activity in neonatal rabbit ventricular myocytes. *AJP: Cell Physiology*, 288(1):C195–C203, 2005.
- [17] D. J. Beuckelmann, M. Näbauer, and E. Erdmann. Intracellular calcium handling in isolated ventricular myocytes from patients with terminal heart failure. *Circulation*, 85(3):1046–1055, 1992.
- [18] A. M. Gómez, H. H. Valdivia, H. Cheng, M. Lederer, L. F. Santana, M. B. Cannell, S. A. Mccune, R. A. Altschuld, and W. J. Lederer. Defective excitation-contraction coupling in experimental cardiac hypertrophy and heart failure. *Science (80-)*, 276(5313):800–806, 1997.
- [19] S. Pogwizd, M. Qi, W. Yuan, A. Samarel, and D. Bers. Upregulation of na^{+}/ca^{2+} exchanger expression and function in an arrhythmogenic rabbit model of heart failure. *Circ. Res.*, 85(11):1009–1019, 1999.

- [20] R. Dash, K. Frank, A. Carr, C. Moravec, and E. Kranias. Gender influences on sarcoplasmic reticulum Ca^{2+} -handling in failing human myocardium. *J. Mol. Cell. Cardiol.*, 33(7):1345–1353, 2001.
- [21] J. Weisser-Thomas, V. Piacentino, J. P. Gaughan, K. Margulies, and S. R. Houser. Calcium entry via Na/Ca exchange during the action potential directly contributes to contraction of failing human ventricular myocytes. *Cardiovasc. Res.*, 57(4):974–985, 2003.
- [22] D. A. Agard. Optical sectioning microscopy: cellular architecture in three dimensions. *Annu. Rev. Biophys. Bio.*, 13:191–219, 1984.
- [23] B. Abdelhak and M.R. Sedki. Filtering capabilities and convergence of the van-Cittert deconvolution technique. *IEEE T. Instrum. Meas.*, 41(2):246–250, April 1992.
- [24] W.A. Carrington, R.M. Lynch, E.M. Moore, G. Isenberg, K.E. Fogarty, and F.S. Fay. Superresolution three-dimensional images of fluorescence in cells with minimal light exposure. *Science*, 268:1483–1487, 1995.
- [25] G.M.P. van Kempen, L.J. van Vliet, P.J. Verveer, and H.T.M. van der Voort. A quantitative comparison of image restoration methods for confocal microscopy. *J. Microsc.*, 185(3):354–365, March 1997.
- [26] R. Neelamani, Hyeokho Choi, and R. Baraniuk. ForWaRD: Fourier-wavelet regularized deconvolution for ill-conditioned systems. *IEEE T. Signal Process.*, 52(2):418–433, Feb. 2004.
- [27] J.-A. Conchello. Superresolution and convergence properties of the expectation-maximization algorithm for maximum-likelihood deconvolution of incoherent images. *J. Opt. Soc. Am. A*, 15(10):2609–2619, 1998.
- [28] C. Preza and J.-A. Conchello. Depth-variant maximum-likelihood restoration for three-dimensional fluorescence microscopy. *J. Opt. Soc. Am. A*, 21(9):1593–1601, 2004.
- [29] W.H. Richardson. Bayesian-based iterative method of image restoration. *J. Opt. Soc. Am.*, 62(1):55–59, January 1972.
- [30] L.B. Lucy. An iterative technique for the rectification of observed distributions. *Astron. J.*, 79(6):745–754, June 1974.
- [31] J. Holmes, M. Hünlich, and G. Hasenfuss. Energetics of the frank-starling effect in rabbit myocardium: economy and efficiency depend on muscle length. *Am. J. Physiol. Heart Circ. Physiol.*, 283(1):H324–H330, 2002.

References

- [32] G.B. Avinash. Data-driven, simultaneous blur and image restoration in 3-D fluorescence microscopy. *J. Microsc.*, 183:145–167, 1996.
- [33] J. Markham and J. Conchello. Parametric blind deconvolution of microscopic images: a robust method for the simultaneous estimation of image and blur. *J. Opt. Soc. Am. A*, 16(10):2377–2391, 1999.
- [34] Y. Sun, P. Davis, E. A. Kosmacek, F. Ianzini, and M. A. Mackey. An open-source deconvolution software package for 3-D quantitative fluorescence microscopy imaging. *J. Microsc.*, 236(3):180–193, 2009.
- [35] M. Laasmaa, M. Vendelin, and P. Peterson. Application of regularized richardson–lucy algorithm for deconvolution of confocal microscopy images. *J. Microsc.*, 243(2):124–140, 2011.
- [36] L. Kümmel. Ca, mg-atpase activity of permeabilised rat heart cells and its functional coupling to oxidative phosphorylation of the cells. *Cardiovasc. Res.*, 22(5):359–367, 1988.
- [37] M. Sepp, M. Vendelin, H. Vija, and R. Birkedal. ADP compartmentation analysis reveals coupling between pyruvate kinase and ATPases in heart muscle. *Biophys. J.*, 98(12):2785–2793, 2010.
- [38] M. Vendelin, M. Eimre, E. Seppet, N. Peet, T. Andrienko, M. Lemba, J. Engelbrecht, E. Seppet, and V. Saks. Intracellular diffusion of adenosine phosphates is locally restricted in cardiac muscle. *Mol. Cell. Biochem.*, 256-257(1):229–241, 2004.
- [39] M. N. Laclau, S. Boudina, J. B. Thambo, L. Tariosse, G. Gouverneur, S. Bonoron-Adele, V. A. Saks, K. D. Garlid, and S. Dos. Cardioprotection by ischemic preconditioning preserves mitochondrial function and functional coupling between adenine nucleotide translocase and creatine kinase. *J. Mol. Cell. Cardiol.*, 33(5):947–956, 2001.
- [40] V. A. Saks, T. Kaambre, P. Sikk, M. Eimre, E. Orlova, K. Paju, A. Piirsoo, F. Appaix, L. Kay, V. Regitz-Zagrosek, E. Fleck, and E. Seppet. Intracellular energetic units in red muscle cells. *Biochem. J.*, 356(Pt 2):643–657, 2001.
- [41] E. K. Seppet, T. Kaambre, P. Sikk, T. Tiivel, H. Vija, M. Tonkonogi, K. Sahlin, L. Kay, F. Appaix, U. Braun, M. Eimre, and V. A. Saks. Functional complexes of mitochondria with ca,mgatpases of myofibrils and sarcoplasmic reticulum in muscle cells. *BBA*, 1504(2-3):379–395, 2001.

- [42] N. Muramatsu and A. P. Minton. Tracer diffusion of globular proteins in concentrated protein solutions. *PNAS*, 85(9):2984–2988, 1988.
- [43] Y. Chen-Izu, S. L. McCulle, C. W. Ward, C. Soeller, B. M. Allen, C. Rabang, M. B. Cannell, C. W. Balke, and L. T. Izu. Three-dimensional distribution of ryanodine receptor clusters in cardiac myocytes. *Biophys. J.*, 91(1):1–13, 2006.
- [44] V. Salnikov, Y. Lukyanenko, W. Lederer, and V. Lukyanenko. Distribution of ryanodine receptors in rat ventricular myocytes. *J. Muscle Res. Cell. Motil.*, 30(3):161–170, 2009.
- [45] C. Soeller and M. Cannell. Examination of the transverse tubular system in living cardiac rat myocytes by 2-photon microscopy and digital image-processing techniques. *Circ. Res.*, 84(3):266, 1999.
- [46] T. Hayashi, M. E. Martone, Z. Yu, A. Thor, M. Doi, M. J. Holst, M. H. Ellisman, and M. Hoshijima. Three-dimensional electron microscopy reveals new details of membrane systems for ca^{2+} signaling in the heart. *J. Cell. Sci.*, 122(7):1005, 2009.
- [47] R. Birkedal, H. Shiels, and M. Vendelin. Three-dimensional mitochondrial arrangement in ventricular myocytes: From chaos to order. *AJP: Cell Physiology*, 291(6):C1148–C1158, 2006.
- [48] A. R. Muir. The effects of divalent cations on the ultrastructure of the perfused rat heart. *J. Anat.*, 101(2):239–261, 1967.
- [49] T. Rostovtseva and S. Bezrukov. Vdac regulation: role of cytosolic proteins and mitochondrial lipids. *J. Bioenerg. Biomembr.*, 40(3):163–170, 2008.
- [50] T. Rostovtseva, K. Sheldon, E. Hassanzadeh, C. Monge, V. Saks, S. Bezrukov, and D. Sackett. Tubulin binding blocks mitochondrial voltage-dependent anion channel and regulates respiration. *PNAS*, 105(48):18746–18751, 2008.
- [51] D. M. Bers. *Excitation-Contraction Coupling and Cardiac Contractile Force*. Kluwer Academic Publishers, 2001.
- [52] A. Yao, Z. Su, A. Nonaka, I. Zubair, L. Lu, K. Philipson, J. B. Bridge, and W. Barry. Effects of overexpression of the na^{+} - ca^{2+} exchanger on $[ca^{2+}]_i$ transients in murine ventricular myocytes. *Circ. Res.*, 82(6):657–665, 1998.
- [53] C. Terracciano, A. De Souza, K. Philipson, and K. Macleod. Na^{+} - ca^{2+} exchange and sarcoplasmic reticular ca^{2+} regulation in ventricular myocytes

References

- from transgenic mice overexpressing the $\text{na}^+ - \text{ca}^{2+}$ exchanger. *J. Physiol. (Lond.)*, 512(Pt 3):651–667, 1998.
- [54] R. Larbig, N. Torres, J. Bridge, J. Goldhaber, and K. Philipson. Activation of reverse $\text{na}^+ - \text{ca}^{2+}$ exchange by the na^+ current augments the cardiac ca^{2+} transient: evidence from *ncx* knockout mice. *J. Physiol. (Lond.)*, 588(Pt 17):3267–3276, 2010.
- [55] M. Vornanen. Excitation-contraction coupling of the developing rat heart. *Mol. Cell. Biochem.*, 163-164:5–11, 1996.
- [56] M. Vornanen. $\text{Na}^+/\text{ca}^{2+}$ exchange current in ventricular myocytes of fish heart: contribution to sarcolemmal ca^{2+} influx. *J. Exp. Biol.*, 202 (Pt 13):1763–1775, 1999.
- [57] D. M. Bers and S. Despa. Cardiac myocytes ca^{2+} and na^+ regulation in normal and failing hearts. *J. Pharmacol. Sci.*, 100(5):315–322, 2006.
- [58] J. W. Bassani, W. Yuan, and D. M. Bers. Fractional sr ca release is regulated by trigger ca and sr ca content in cardiac myocytes. *Am. J. Physiol.*, 268(5 Pt 1):C1313–C1319, 1995.
- [59] T. Doerr, R. Denger, and W. Trautwein. Calcium currents in single sa nodal cells of the rabbit heart studied with action potential clamp. *Pflugers Arch.*, 413(6):599–603, 1989.
- [60] L. Hove-Madsen. The influence of temperature on ryanodine sensitivity and the force-frequency relationship in the myocardium of rainbow trout. *J. Exp. Biol.*, 167:47–60, 1992.
- [61] H. A. Shiels, E. D. Stevens, and A. P. Farrell. Effects of temperature, adrenaline and ryanodine on power production in rainbow trout *oncorhynchus mykiss* ventricular trabeculae. *J. Exp. Biol.*, 201 (Pt 19):2701–2710, 1998.
- [62] E. Aho and M. Vornanen. Contractile properties of atrial and ventricular myocardium of the heart of rainbow trout *oncorhynchus mykiss*: effects of thermal acclimation. *J. Exp. Biol.*, 202 (Pt 19):2663–2677, 1999.
- [63] C. Cros, L. Salle, D. E. Warren, H. A. Shiels, and F. Brette. The calcium stored in the sarcoplasmic reticulum acts as a safety mechanism in rainbow trout heart. *AJP: Regul. Integr. Comp. Physiology*, 307(12):R1493–R1501, 2014.

- [64] L. Hove-Madsen, A. Llach, G. F. Tibbits, and L. Tort. Triggering of sarcoplasmic reticulum Ca^{2+} release and contraction by reverse mode Na^{+}/Ca^{2+} exchange in trout atrial myocytes. *Am. J. Physiol. Regul. Integr. Comp. Physiol.*, 284(5):R1330–R1339, 2003.
- [65] R. Birkedal and H. A. Shiels. High $[Na^{+}]_i$ in cardiomyocytes from rainbow trout. *Am. J. Physiol. Regul. Integr. Comp. Physiol.*, 293(2):R861–R866, 2007.
- [66] T. Poppe, R. Johansen, G. Gunnes, and B. Tørud. Heart morphology in wild and farmed atlantic salmon *salmo salar* and rainbow trout *oncorhynchus mykiss*. *Dis. Aquat. Org.*, 57(1-2):103–108, 2003.
- [67] W. R. Driedzic and H. Gesser. Ca^{2+} protection from the negative inotropic effect of contraction frequency on teleost hearts. *J. Comp. Physiol. [B]*, 156:135–142, 1985.
- [68] J. Haverinen and M. Vornanen. Comparison of sarcoplasmic reticulum calcium content in atrial and ventricular myocytes of three fish species. *AJP: Regul. Integr. Comp. Physiology*, 297(4):R1180–R1187, 2009.
- [69] R. Birkedal, J. Christopher, A. Thistlethwaite, and H. Shiels. Temperature acclimation has no effect on ryanodine receptor expression or subcellular localization in rainbow trout heart. *J. Comp. Physiol. B, Biochem. Syst. Environ. Physiol.*, 179(8):961–969, 2009.
- [70] H. Korajoki and M. Vornanen. Expression of serca and phospholamban in rainbow trout (*oncorhynchus mykiss*) heart: comparison of atrial and ventricular tissue and effects of thermal acclimation. *J. Exp. Biol.*, 215(7):1162–1169, 2012.
- [71] F. Sedarat, L. Xu, E. D. Moore, and G. F. Tibbits. Colocalization of dihydropyridine and ryanodine receptors in neonate rabbit heart using confocal microscopy. *Am. J. Physiol. Heart Circ. Physiol.*, 279(1):H202–H209, 2000.
- [72] N. Sokolova, M. Vendelin, and R. Birkedal. Intracellular diffusion restrictions in isolated cardiomyocytes from rainbow trout. *BMC Cell Biol.*, 10(1):90, 2009.
- [73] B. Ostadal, I. Ostadalova, and N. Dhalla. Development of cardiac sensitivity to oxygen deficiency: Comparative and ontogenetic aspects. *Physiol. Rev.*, 79(3):635–659, 1999.

References

- [74] J. A. Hoerter, R. Ventura-Clapier, and A. Kuznetsov. Compartmentation of creatine kinases during perinatal development of mammalian heart. *Mol. Cell. Biochem.*, 133-134:277–286, 1994.
- [75] J. Huang, L. Hove-Madsen, and G. F. Tibbits. Ontogeny of ca^{2+} -induced ca^{2+} release in rabbit ventricular myocytes. *Am. J. Physiol. Cell. Physiol.*, 294(2):C516–C525, 2008.
- [76] P. Dan, E. Lin, J. Huang, P. Biln, and G. F. Tibbits. Three-dimensional distribution of cardiac na^{+} - ca^{2+} exchanger and ryanodine receptor during development. *Biophys. J.*, 93(7):2504–2518, 2007.
- [77] T. Banyasz, B. Horvath, Z. Jian, L. Izu, and Y. Chen-Izu. Sequential dissection of multiple ionic currents in single cardiac myocytes under action potential-clamp. *J. Mol. Cell. Cardiol.*, 50(3):578–581, 2011.
- [78] C. Bartolucci, C. Altomare, M. Bennati, S. Furini, A. Zaza, and S. Severi. Combined action potential- and dynamic-clamp for accurate computational modelling of the cardiac ikr current. *J. Mol. Cell. Cardiol.*, 79:187–194, 2015.

CURRICULUM VITAE

Curriculum Vitae

MARTIN LAASMAA

PERSONAL INFORMATION

Date of birth January 15, 1984
Contact Siili 25 – 28, Tallinn, Estonia, 13422
E-mail martin@sysbio.ioc.ee

EDUCATION

2009 – 2016 Tallinn University of Technology (TUT)

Subject **PhD, Engineering Physics**

Thesis Revealing Aspects of Cardiac Function from Fluorescence and Electrophysiological Recordings

Supervisors Dr. Marko Vendelin, *markov@sysbio.ioc.ee*

Head of Laboratory of Systems Biology, Institute of Cybernetics at TUT (IoC)

Dr. Pearu Peterson, *pearu@cens.ioc.ee*

Senior Researcher of Laboratory of Systems Biology (till 2016), Laboratory of Photoelasticity (from 2016) at IoC

Dr. Rikke Birkedal Nielsen, *rikke@sysbio.ioc.ee*

Senior Researcher of Laboratory of Systems Biology at IoC

2007 – 2009 Tallinn University of Technology

Subject **MSc, Engineering Physics, cum laude**

Thesis The Analysis of Richardson-Lucy Deconvolution Algorithm with Application to Microscope Images

Supervisors Dr. Marko Vendelin, *markov@sysbio.ioc.ee*

Head of Laboratory of Systems Biology at IoC

Dr. Pearu Peterson, *pearu@cens.ioc.ee*

Senior Researcher of Systems Biology at IoC

2004 – 2007 Tallinn University of Technology

Subject **BSc, Engineering Physics**

Thesis Electrical properties of spray pyrolysed ZnO thin films

Supervisor Dr. Arvo Mere, *arvo.mere@ttu.ee*

Associate Professor of Department of Physics, Faculty of Science, TUT

1991 – 2003 Tallinn Technical Gymnasium, Secondary education

Curriculum Vitae

RESEARCH EXPERIENCE

- 2007 – present** **Institute of Cybernetics at TUT**
Laboratory of Systems Biology
Main duties Fluorescence imaging and electrophysiological measurements of cardiomyocytes, programming data analysis tools, writing scientific articles, animal care, building research equipment
- 2006 – 2007** **Department of Materials Science at TUT**
Laboratory of Thin Film Chemical Technologies
Main duties Measurements of electrical properties of spray pyrolysed ZnO thin films, building research equipment

WORK EXPERIENCE

- 2009 – present** **Institute of Cybernetics at TUT**
Laboratory of Systems Biology
Position Engineer & PhD student
- 2008 – 2009** **Institute of Cybernetics at TUT**
Laboratory of Systems Biology
Position Technician
- 2006 – 2007** **Department of Materials Science at TUT**
Laboratory of Thin Film Chemical Technologies
Position Technician
- 2003 – 2004** **Estonian Armed Forces (compulsory military service)**
Artillery Battalion
Position junior non-commissioned officer (sergeant)

COMPUTER SKILLS

- ▷ Operating Systems: Linux, Windows
- ▷ Day-to-day usage of Python programming language
- ▷ Familiar with: C++, FORTRAN, VBA programming languages
- ▷ Routine use of LaTeX document preparation, MS Office, OpenOffice
- ▷ Experience in computer algebra system Mathematica
- ▷ Competent with raster and vector image creation programs
- ▷ Familiar with CAD software AutoCAD and SolidWorks

EXPERIMENTAL EXPERIENCE

- ▷ Electrophysiology of cardiomyocytes
- ▷ Fluorescence and confocal microscopy
- ▷ Isolation of trout cardiomyocytes

SPECIAL COURSES

- 2012** Federation of Laboratory Animal Science Associations (FELASA): C-category competence certificate

Curriculum Vitae

SCHOLARSHIPS AND AWARDS

Archimedes/DoRa travel grants for presenting at international conferences 2009, 2010, 2013

PUBLICATIONS

1. **Laasmaa M**, Birkedal R, and Vendelin M; **Revealing calcium fluxes by analyzing inhibition dynamics in action potential clamp**, *Journal of Molecular and Cellular Cardiology*, 100, 93–108, 2016
2. Simson P, Jepihina N, **Laasmaa M**, Peterson P, Birkedal R, and Vendelin M; **Restricted ADP movement in cardiomyocytes: Cytosolic diffusion obstacles are complemented with a small number of open mitochondrial voltage-dependent anion channels**, *Journal of Molecular and Cellular Cardiology*, 97, 197–203, 2016
3. Karro N, Sepp M, Jugai S, **Laasmaa M**, Vendelin M, and Birkedal R; **Metabolic compartmentation in rainbow trout cardiomyocytes: Coupling of hexokinase but not creatine kinase to mitochondrial respiration**, *Journal of Comparative Physiology - B*, 2016
4. Birkedal R, **Laasmaa M** and Vendelin M; **The location of energetic compartments affects energetic communication in cardiomyocytes**, *Frontiers in Physiology*, 5, 376, 2014
5. Illaste A, **Laasmaa M**, Peterson P, and Vendelin M; **Analysis of Molecular Movement Reveals Latticelike Obstructions to Diffusion in Heart Muscle Cells** *Biophysical Journal*, 102(4), 739–748, 2012
6. **Laasmaa M**, Vendelin M, and Peterson P; **Application of regularized Richardson-Lucy algorithm for deconvolution of confocal microscopy images** *Journal of Microscopy*, 243(2):124–140, 2011

Curriculum Vitae

SELECTED CONFERENCE PRESENTATIONS

- 2016** **Biophysical Society 60th Annual Meeting**, Los Angeles, California, USA
Poster Laasmaa M, Vendelin M, Birkedal R
Using action potential clamp data to determine the calcium fluxes and contributions in excitation-contraction coupling in vivo in cardiomyocytes
- 2015** **44th European Muscle Conference 2015**, Warsaw, Poland
Oral Laasmaa M, Peterson P, Vendelin M, Birkedal R
Calcium fluxes in cardiac excitation-contraction coupling in rainbow trout
- 2015** **The Joint Meeting of the Federation of European Physiological Societies and the Baltic Physiological Societies (FEPS2015)**, Kaunas, Lithuania
Oral Laasmaa M, Peterson P, Vendelin M, Birkedal R
Action potential clamp data analysis reveals large contribution of sarcoplasmic reticulum in excitation-contraction coupling of trout cardiomyocytes
- 2013** **37th International Congress of Physiological Sciences (IUPS2013)**, Birmingham, UK
Poster Laasmaa M, Birkedal R, Vendelin M
An integrated method to quantify calcium fluxes in cardiac excitation-contraction coupling
- 2013** **Biophysical Society 57th Annual Meeting**, Philadelphia, Pennsylvania, USA
Poster Laasmaa M, Birkedal R, Vendelin M
An integrated method to quantify calcium fluxes in cardiac excitation-contraction coupling
- 2011** **Biophysical Society 55th Annual Meeting**, Baltimore, Maryland, USA
Poster Laasmaa M, Vendelin M, Peterson P
Application of regularized Richardson-Lucy algorithm for deconvolution of confocal microscopy images
- 2010** **Biophysical Society 54th Annual Meeting**, San Francisco, California, USA
Poster Laasmaa M, Vendelin M, Peterson P
3D confocal microscope image enhancement by Richardson-Lucy deconvolution algorithm with total variation regularization: parameters estimation
- 2009** **Biophysical Society 53rd Annual Meeting**, Boston, Massachusetts, USA
Poster Laasmaa M, Peterson P, Birkedal R, Vendelin M
3D confocal microscope image enhancement by Richardson-Lucy deconvolution algorithm with total variation regularization

EXTRAS

Languages Estonian (mother tongue), English (fluent), Finnish, Russian (all basic)

Elulookirjeldus
MARTIN LAASMAA

ÜLDINFO

Sünniaeg 15. jaanuar, 1984
Kontakt Siili 25 – 28, Tallinn, Estonia, 13422
E-mail martin@sysbio.ioc.ee

HARIDUS

2009 – 2016 Tallinna Tehnikaülikool (TTÜ)

Eriala **PhD, tehniline füüsika**

Teema Südamealalise uuringud fluorestsentsi ja elektrofüsioloogiliste mõõtmiste abil

Juhendajad Dr. Marko Vendelin, *markov@sysbio.ioc.ee*

Süsteemibioloogia laboratooriumi juhataja, Süsteemibioloogia laboratoorium, TTÜ
Küberneetika Instituut (KüBI)

Dr. Pearu Peterson, *pearu@cens.ioc.ee*

KüBI Süsteemibioloogia laboratooriumi (kuni 2016) vanemteadur, KüBI Fotoelastsuse laboratooriumi (alates 2016) vanemteadur

Dr. Rikke Birkedal Nielsen, *rikke@sysbio.ioc.ee*

KüBI Süsteemibioloogia laboratooriumi vanemteadur

2007 – 2009 Tallinna Tehnikaülikool

Eriala **MSc, tehniline füüsika, cum laude**

Teema Richardson-Lucy dekonvolutsiooni algoritmi analüüs ja rakendus mikroskoopias

Juhendajad Dr. Marko Vendelin, *markov@sysbio.ioc.ee*

Süsteemibioloogia laboratooriumi juhataja, Süsteemibioloogia laboratoorium, KüBI

Dr. Pearu Peterson, *pearu@cens.ioc.ee*

KüBI Süsteemibioloogia laboratooriumi vanemteadur

2004 – 2007 Tallinna Tehnikaülikool

Eriala **BSc, tehniline füüsika**

Teema Pihustussadestatud ZnO kilede elektriliste omaduste uurimine

Juhendaja Dr. Arvo Mere, *arvo.mere@ttu.ee*

TTÜ Füüsikainstituudi Rakendusfüüsika õppetooli dotsent

1991 – 2003 Tallinna Tehnikagümnaasium, keskharidus

Elulookirjeldus

TEADUSTÖÖ KOGEMUS

- 2007 – present** **TTÜ Küberneetika Instituut**
Süsteemibioloogia laboratoorium
- Põhiülesanded* Fluorestsentspilditehnika rakendamine ja elektrofüsioloogiliste mõõtmise teostamine südamelihaskudedel, andmeanalüüsi tarkvara programmeerimine, teaduspublikatsioonide kirjutamine, teadustöök vajalike seadmete valmistamine, katseloomade eest hoolitsemine
- 2006 – 2007** **TTÜ Materjaliteaduse Instituut**
Keemiliste kiletehnoloogiate teaduslaboratoorium
- Põhiülesanded* Pihustussadestatud ZnO kilede elektriliste omaduste uurimine, teadustöök vajalike seadmete valmistamine

TÖÖKOGEMUS

- 2009 – ...** **TTÜ Küberneetika Instituut**
Süsteemibioloogia laboratoorium
- Ametikoht* Insener
- 2008 – 2009** **TTÜ Küberneetika Instituut**
Süsteemibioloogia laboratoorium
- Ametikoht* Tehnik
- 2006 – 2007** **TTÜ Materjaliteaduse Instituut**
Keemiliste kiletehnoloogiate teaduslaboratoorium
- Ametikoht* Tehnik
- 2003 – 2004** **Eesti kaitseväge (ajateenistus)**
Suurtükiväepataljon
- Ametikoht* nooremallohvitser (seersant)

ARVUTIOSKUS

- ▷ Operatsioonisüsteemid: Linux, Windows
- ▷ Igapäevane programmeerimiskeele Python kasutaja
- ▷ Algajatasel programmeerimiskeeltes: C++, FORTRAN, VBA
- ▷ LaTeX dokumentide ettevalmistussüsteemi, MS Office ja OpenOffice igapäevane kasutaja
- ▷ Erinevate vektor- ja rastergraafika tarkvara igapäevane kasutaja
- ▷ Tuttav arvutialgebra tarkvaraga Mathematica
- ▷ Tuttav raalprojekteerimise tarkvara AutoCAD ja SolidWorks

PRAKTILINE KOGEMUS TEADUSTÖÖ VALLAS

- ▷ Südamelihaskude elektrofüsioloogia
- ▷ Fluorestsents- ja konfokaalmikroskoopia
- ▷ Südamelihaskude isoleerimine

TÄIENDÖPE

- 2012** Katseloomateaduse kursus (Federation of Laboratory Animal Science Associations): C-katekoria kompetents

Archimedes/DoRa stipendiumid rahvusvahelistel konverentsidel osalemiseks 2009, 2010, 2013

1. **Laasmaa M**, Birkedal R, and Vendelin M; **Revealing calcium fluxes by analyzing inhibition dynamics in action potential clamp**, *Journal of Molecular and Cellular Cardiology*, 100, 93–108, 2016
2. Simson P, Jepihhina N, **Laasmaa M**, Peterson P, Birkedal R, and Vendelin M; **Restricted ADP movement in cardiomyocytes: Cytosolic diffusion obstacles are complemented with a small number of open mitochondrial voltage-dependent anion channels**, *Journal of Molecular and Cellular Cardiology*, 97, 197–203, 2016
3. Karro N, Sepp M, Jugai S, **Laasmaa M**, Vendelin M, and Birkedal R; **Metabolic compartmentation in rainbow trout cardiomyocytes: Coupling of hexokinase but not creatine kinase to mitochondrial respiration**, *Journal of Comparative Physiology - B*, 2016
4. Birkedal R, **Laasmaa M** and Vendelin M; **The location of energetic compartments affects energetic communication in cardiomyocytes**, *Frontiers in Physiology*, 5, 376, 2014
5. Illaste A, **Laasmaa M**, Peterson P, and Vendelin M; **Analysis of Molecular Movement Reveals Latticelike Obstructions to Diffusion in Heart Muscle Cells** *Biophysical Journal*, 102(4), 739–748, 2012
6. **Laasmaa M**, Vendelin M, and Peterson P; **Application of regularized Richardson-Lucy algorithm for deconvolution of confocal microscopy images** *Journal of Microscopy*, 243(2):124–140, 2011

Elulookirjeldus

VALITUD ETTEKANDED RAHVUSVAHELISTELT KONVERENTSIDELT

- 2016 Biophysical Society 60th Annual Meeting**, Los Angeles, California, USA
Poster Laasmaa M, Vendelin M, Birkedal R
Using action potential clamp data to determine the calcium fluxes and contributions in excitation-contraction coupling in vivo in cardiomyocytes
- 2015 44th European Muscle Conference 2015**, Warsaw, Poland
Suuline Laasmaa M, Peterson P, Vendelin M, Birkedal R
Calcium fluxes in cardiac excitation-contraction coupling in rainbow trout
- 2015 The Joint Meeting of the Federation of European Physiological Societies and the Baltic Physiological Societies (FEPS2015)**, Kaunas, Lithuania
Suuline Laasmaa M, Peterson P, Vendelin M, Birkedal R
Action potential clamp data analysis reveals large contribution of sarcoplasmic reticulum in excitation-contraction coupling of trout cardiomyocytes
- 2013 37th International Congress of Physiological Sciences (IUPS2013)**, Birmingham, UK
Poster Laasmaa M, Birkedal R, Vendelin M
An integrated method to quantify calcium fluxes in cardiac excitation-contraction coupling
- 2013 Biophysical Society 57th Annual Meeting**, Philadelphia, Pennsylvania, USA
Poster Laasmaa M, Birkedal R, Vendelin M
An integrated method to quantify calcium fluxes in cardiac excitation-contraction coupling
- 2011 Biophysical Society 55th Annual Meeting**, Baltimore, Maryland, USA
Poster Laasmaa M, Vendelin M, Peterson P
Application of regularized Richardson-Lucy algorithm for deconvolution of confocal microscopy images
- 2010 Biophysical Society 54th Annual Meeting**, San Francisco, California, USA
Poster Laasmaa M, Vendelin M, Peterson P
3D confocal microscope image enhancement by Richardson-Lucy deconvolution algorithm with total variation regularization: parameters estimation
- 2009 Biophysical Society 53rd Annual Meeting**, Boston, Massachusetts, USA
Poster Laasmaa M, Peterson P, Birkedal R, Vendelin M
3D confocal microscope image enhancement by Richardson-Lucy deconvolution algorithm with total variation regularization

LISAD

Keeled Eesti (emakeel), inglise (vilunud keelekasutaja), soome ja vene (algfase)

APPENDIX

PUBLICATION I

Laasmaa M, Vendelin M, and Peterson P

Application of regularized Richardson-Lucy algorithm for deconvolution of confocal microscopy images

Journal of Microscopy, 243(2), 124–140, 2011

Application of regularized Richardson–Lucy algorithm for deconvolution of confocal microscopy images

M. LAASMAA, M. VENDELIN & P. PETERSON

Laboratory of Systems Biology, Institute of Cybernetics, Tallinn University of Technology, Tallinn, Estonia

Key words. Deconvolution, estimating regularization parameters, fluorescence microscopy, 3D quantitative fluorescence microscopy imaging.

Summary

Although confocal microscopes have considerably smaller contribution of out-of-focus light than widefield microscopes, the confocal images can still be enhanced mathematically if the optical and data acquisition effects are accounted for. For that, several deconvolution algorithms have been proposed. As a practical solution, maximum-likelihood algorithms with regularization have been used. However, the choice of regularization parameters is often unknown although it has considerable effect on the result of deconvolution process. The aims of this work were: to find good estimates of deconvolution parameters; and to develop an open source software package that would allow testing different deconvolution algorithms and that would be easy to use in practice. Here, Richardson–Lucy algorithm has been implemented together with the total variation regularization in an open source software package IOCBio Microscope. The influence of total variation regularization on deconvolution process is determined by one parameter. We derived a formula to estimate this regularization parameter automatically from the images as the algorithm progresses. To assess the effectiveness of this algorithm, synthetic images were composed on the basis of confocal images of rat cardiomyocytes. From the analysis of deconvolved results, we have determined under which conditions our estimation of total variation regularization parameter gives good results. The estimated total variation regularization parameter can be monitored during deconvolution process and used as a stopping criterion. An inverse relation between the optimal regularization parameter and the peak signal-to-noise ratio of an image is shown. Finally, we demonstrate the use of the developed

software by deconvolving images of rat cardiomyocytes with stained mitochondria and sarcolemma obtained by confocal and widefield microscopes.

Introduction

In biosciences, fluorescence microscopy is an extremely useful and important method for studying living organisms. As one of the implementations of fluorescence microscopy, confocal fluorescence microscopy can be used to study live cells and analyse the response of the cells to external stimuli. Confocal microscopy has several advantages over traditional widefield microscopy. The main advantage is the ability to produce in-focus images of thick specimens via elimination or reduction of background information outside of the focal plane and ability to control the depth of field (within the accuracy of an Airy disk size) (Inoué, 2006). Despite the advantages over widefield microscopy, confocal images contain imperfections, for example, aberrations due to nonideal optical pathway, residual out-of-focus light, noise from detector electronics, etc. (Shaw, 2006).

In this paper we focus on image enhancement of microscope images by deconvolution (Cannell *et al.*, 2006). Each microscope alters the appearance of specimens in a specific way. Image formation can be described by the mathematical operation of convolution, where the ‘true’ image is convolved with distortion effects from the microscope. Deconvolution is a method to reverse the aberrations caused by convolution, that is remove the distortions of the optical train, contributions from out-of-focus objects, and with regularization enabled, reduce the noise originated from detector electronics. Deconvolution takes into account microscope optics and the nature of noise. Therefore, it is a method that can efficiently enhance both widefield microscopy and confocal microscopy images. It can considerably improve image contrast and reduce noise in microscope images.

Correspondence to: Pearu Peterson, Laboratory of Systems Biology, Institute of Cybernetics, Tallinn University of Technology, Akadeemia Road 21, 12618 Tallinn, Estonia. Tel: +372 6204162; fax: +372 6204151; e-mail: pearu@sysbio.ioc.ee

Re-use of this article is permitted in accordance with the Terms and Conditions set out at http://wileyonlinelibrary.com/onlineopen/OnlineOpen_Terms

Several deconvolution algorithms have been proposed for three-dimensional (3D) microscopy. For example, noniterative algorithms such as regularized inverse-filtering algorithm (Preza *et al.*, 1992), nearest-neighbour algorithm, Wiener filtering algorithm (Shaw & Rawlins, 1991a), etc.; iterative algorithms such as Richardson–Lucy (RL) algorithm (Richardson, 1972; Lucy, 1974), Jansson-van Cittert algorithm (Agard, 1984; Abdelhak & Sedki, 1992), Carrington algorithm (Carrington *et al.*, 1995), constrained Tikhonov–Miller algorithm (van Kempen *et al.*, 1997), Fourier-wavelet regularized algorithm (Neelamani *et al.*, 2004), expectation maximization algorithm (Conchello, 1998; Preza & Conchello, 2004), etc; blind deconvolution algorithms (Holmes, 1992; Avinash, 1996; Markham & Conchello, 1999). Usually, noniterative methods are fastest but these do not provide optimal image quality, especially in the presence of noise (Cannell *et al.*, 2006). The particular choice of deconvolution algorithm depends on users requirements (should the deconvolved image be pleasant to the viewers eye or be quantitatively as correct as possible), computational resources and limitations (Cannell *et al.*, 2006; Sun *et al.*, 2009).

In this paper, we analyse the RL iterative algorithm that is derived for Poisson noise (Richardson, 1972; Lucy, 1974). The assumption of Poisson noise is adequate for confocal microscopes because these use photodetection devices such as avalanche photodiodes to count the number of photons that are emitted from specimens. Because of the quantum nature of light, the number of detected photons is a Poisson process whose variance is equal to the mean of counted photons.

The RL algorithm is commonly used for telescope and microscope image enhancement (Dey *et al.*, 2006). An undesired property of the RL algorithm is that, in the presence of noise, the deconvolution process converges to a solution which is dominated by the noise (Dey *et al.*, 2004). An option to circumvent this, is to prefilter images (Cannell *et al.*, 2006). Another option is to introduce regularization terms such as Tikhonov–Miller (van Kempen & van Vliet, 2000) or maximum entropy to the RL algorithm (de Monvel *et al.*, 2001, 2003). Algorithms which are based on Tikhonov–Miller regularization, are often used for deconvolving 3D images. Such algorithms avoid noise amplification but operate poorly near the object edges. Alternatively, to increase the sharpness of object borders and obtain smooth homogeneous areas, total variation (TV) regularization is often applied in the RL algorithm (Dey *et al.*, 2004). However, regularization terms contain unknown parameters that must be carefully chosen to achieve optimal deconvolution results that would be as close as possible to the ‘true’ image. Some regularized algorithms provide means to determine how much regularization to use in each restoration step (Sun *et al.*, 2009; Liao *et al.*, 2009). In this paper, we introduce a method to estimate the

regularization parameter for the regularized RL deconvolution algorithm.

All iterative deconvolution algorithms have to deal with the problem of stopping the iteration process. Provided that the iteration converges, seemingly the most natural, in fact, also the most popular stopping criteria are based on measuring the stationary state of the iteration process. For example, this can be measured by computing the relative changes of subsequent estimates and specifying a stopping threshold (Dey *et al.*, 2004, 2006; Sun *et al.*, 2009). Surprisingly, as we show in this work, such stopping criteria turn out to be suboptimal: the converged estimate may be less accurate (when comparing with the ‘true’ image) than some of the intermediate estimates. So, a better stopping criteria is needed for improving quantitative results of iterative deconvolution algorithms.

For image restoration by deconvolution, both commercial and open source computer programs are available. Commercial image restoration software solutions give good results in image enhancement and are easy to use, but, as a drawback, they are expensive and do not support testing alternative deconvolution algorithms due to their closed source development policy. Several open source software libraries exist that implement various deconvolution algorithms (Peterson, 2010b). For example, Clarity Deconvolution Library (Quammen, 2007) (GPL license) is a C/C++ library that currently implements Wiener filtering (Shaw & Rawlins, 1991b), Jansson-van Cittert iterative (Agard, 1984), maximum likelihood iterative (Richardson, 1972; Lucy, 1974) with symmetric point spread function (PSF) algorithms; COSMOS (Valdimarsson & Preza, 2007) is a C++ library (GPL, the successor of XCOSM software) that currently implements depth variant expectation maximization (Preza & Conchello, 2004), a linear least square (Preza *et al.*, 1992), a linear maximum *a posteriori* (Preza *et al.*, 1993), the Jansen-van Cittert (Agard, 1984) and the expectation maximization (Conchello, 1998) algorithms; Deconv is a C++ library (GPL) that currently implements maximum likelihood–Landweber, -conjugate gradient and -expectation maximization iterative deconvolution (Sun *et al.*, 2009) algorithms. For a scientist who prefers to focus on solving scientific problems, this variety of software and algorithms makes it difficult to decide which of the algorithms is most suitable for particular image data and available computational resources. Therefore, a software platform is needed that would support testing and comparing different deconvolution algorithms and their implementations in an unified manner for variety of microscopy image file formats. For this, we use Python programming language that is becoming an increasingly popular choice for scientific computing because of its many features that are attractive for scientists: Python has very clean and easy-to-learn syntax, it supports very high-level object-oriented programming paradigm, and is easy to extend. High-quality scientific

computational packages in Python have emerged within the last 10 years (Oliphant, 2007; Jones *et al.*, 2001) and well-developed tools exist for interfacing existing C/C++ and Fortran libraries to Python (Beazley, 2003; Peterson, 2009).

The aims of this work are: (1) to work out a practical method for using deconvolution algorithms, in particular, to find good estimates to regularization parameters as well as to establish a robust criterion for stopping iteration process that would give closest result to the 'true' image rather than just detecting deconvolution process stationarity; (2) to develop an open source software package that would allow testing different deconvolution algorithms and at the same time would be easy to use in practice.

Material and methods

Description of the deconvolution process

To deconvolve microscope images we use the RL algorithm (Richardson, 1972; Lucy, 1974). The algorithm is based on the following mathematical image formation model:

$$i = \mathcal{P}(o \otimes h), \quad (1)$$

where i represents the recorded image stack represented as 3D array, where each item value corresponds to the intensity of a measured voxel, o is the object, h is the PSF defined by the optical train of a specific microscope, \otimes denotes convolution operation, \mathcal{P} represents Poisson noise originating from counting photons. With maximum likelihood approach and TV regularization, the model provides the following equation (Dey *et al.*, 2004):

$$1 - \frac{i}{o \otimes h} \otimes \tilde{h} - \lambda \operatorname{div} \left(\frac{\nabla o}{|\nabla o|} \right) = 0, \quad (2)$$

where $\tilde{h}(v) = h(-v)$, λ is regularization parameter and differentiation operations are defined with respect to voxel coordinates v . From Eq. (2), a multiplicative gradient-type RL algorithm for one iteration can be derived (Dey *et al.*, 2004):

$$o^{(s+1)} = \left(\frac{i}{o^{(s)} \otimes h} \otimes \tilde{h} \right) \cdot \frac{o^{(s)}}{1 - \lambda \operatorname{div} \left(\frac{\nabla o^{(s)}}{|\nabla o^{(s)}} \right)}, \quad (3)$$

whereby in this paper we use $o^{(0)} = i$. In general, the initial estimate $o^{(0)}$ can be denoised, for example, by convolving i with h , or applying Gaussian filter to i , etc. Note also that Eq. (3) may introduce negative values to deconvolution estimate. This happens when the denominator of Eq. (3) becomes negative for some voxel value. The negativity usually indicates unstable deconvolution process due to an inappropriate choice of λ value. In such cases, the iteration process should be stopped immediately.

We denote the result of deconvolution with the above scheme as $o^{(S)} = i \otimes_{\lambda, S}^{-1} h$, where S denotes the number of iteration steps.

Estimation of the TV regularization parameter value

Let us define a functional

$$F(o; \lambda) = \sum_v \left(1 - \left(\frac{i}{o \otimes h} \otimes \tilde{h} \right)_v - \lambda \operatorname{div} \left(\frac{\nabla o}{|\nabla o|} \right)_v \right)^2, \quad (4)$$

which ought to have zero value when Eq. (2) is fulfilled; $v = (i, j, k)$ defines the location of a voxel in 3D image. At the s th deconvolution iteration, the regularization parameter λ can be chosen such that $F(o^{(s)}; \lambda)$ is minimal. It is easy to show that the minimal value of the functional Eq. (4) is $F(o^{(s)}; \lambda_{\text{lsq}}^{(s)})$ where

$$\lambda_{\text{lsq}}^{(s)} = C \frac{\sum_v \left(1 - \frac{i}{o^{(s)} \otimes h} \otimes \tilde{h} \right)_v \cdot \operatorname{div} \left(\frac{\nabla o^{(s)}}{|\nabla o^{(s)}} \right)_v}{\sum_v \operatorname{div} \left(\frac{\nabla o^{(s)}}{|\nabla o^{(s)}} \right)_v^2} \quad (5)$$

and formally $C = 1$. The coefficient C is chosen such that at the first iteration the λ value is close to the optimal λ value (see Results), that is, $\lambda_{\text{lsq}}^{(0)} \equiv 50/\text{SNR}$ where SNR denotes peak signal-to-noise ratio (SNR) of the recorded image i [Eq. (6)].

Note that λ_{lsq} in Eq. (5) is closely related to Lagrange multiplier method used in (Gilboa *et al.*, 2003) when taking $\sum_v \operatorname{div} \left(\frac{\nabla o^{(s)}}{|\nabla o^{(s)}} \right)_v$ as a constant that describes texture variations in the estimate $o^{(s)}$.

Estimation of the peak SNR

To quantify the noise level in recorded images, we use the peak SNR. The peak SNR is defined as the ratio of mean to standard deviation of the brightest part of the recorded images. Because all of our image data is recorded with a photon counting module then the peak SNR can be directly estimated from Poisson statistics: it is the square of mean photon count in the brightest part of an image. The mean photon count is estimated as a maximum value of an averaged image. The averaging of the image is carried out with $3 \times 3 \times 3$ uniform kernel.

In summary, the SNR of a recorded image i that values are counts of detected photons per voxel time, is

$$\text{SNR} = \max_v \sqrt{\frac{1}{27} \sum_{d \in \{-1, 0, 1\}^3} i_{v+d}}. \quad (6)$$

Numerical methods

The deconvolution algorithm is implemented in Python programming language (van Rossum, 1991) and released as open source software IOCBio Microscope (Peterson, 2010a). For array operations, the NumPy package is used. For correcting PSF to correct voxel size, the SciPy (Jones *et al.*, 2001) Ndimimage package is used. Convolution operation is

carried out via FFT using FFTW library (Frigo & Johnson, 2005) and the numerical scheme for computing $\text{div}(\frac{\nabla o}{|\nabla o|})$ is implemented in C programming language for better performance. The original scheme for computing $\text{div}(\frac{\nabla o}{|\nabla o|})$ as given in (Dey *et al.*, 2004) has a typo and below follows the corrected scheme:

$$\begin{aligned} \text{div} \left(\frac{\nabla o}{|\nabla o|} \right)_{ijk} &= \Delta^x \frac{\Delta_+^x o_{ijk}}{\sqrt{(\Delta_+^x o_{ijk})^2 + m(\Delta_+^y o_{ijk}, \Delta_-^y o_{ijk})^2 + m(\Delta_+^z o_{ijk}, \Delta_-^z o_{ijk})^2}} \\ &+ \Delta^y \frac{\Delta_+^y o_{ijk}}{\sqrt{(\Delta_+^y o_{ijk})^2 + m(\Delta_+^x o_{ijk}, \Delta_-^x o_{ijk})^2 + m(\Delta_+^z o_{ijk}, \Delta_-^z o_{ijk})^2}} \\ &+ \Delta^z \frac{\Delta_+^z o_{ijk}}{\sqrt{(\Delta_+^z o_{ijk})^2 + m(\Delta_+^x o_{ijk}, \Delta_-^x o_{ijk})^2 + m(\Delta_+^y o_{ijk}, \Delta_-^y o_{ijk})^2}}, \end{aligned} \quad (7)$$

where

$$i = 1 \dots N_x, \quad j = 1 \dots N_y, \quad k = 1 \dots N_z,$$

$$\begin{aligned} \Delta_+^x o_{ijk} &= h_x^{-1} (\mp o_{ijk} \pm o_{(i\pm 1)jk}), \\ \Delta_{\pm}^y o_{ijk} &= h_y^{-1} (\mp o_{ijk} \pm o_{i(j\pm 1)k}), \\ \Delta_{\pm}^z o_{ijk} &= h_z^{-1} (\mp o_{ijk} \pm o_{ij(k\pm 1)}), \end{aligned} \quad (8)$$

$$m(a, b) = \frac{\text{sign } a + \text{sign } b}{2} \min(|a|, |b|), \quad (9)$$

and h_x, h_y, h_z are voxel dimensions. In boundary points, the following relations are used (Dey *et al.*, 2004):

$$\begin{aligned} o_{0jk} &= o_{1jk}, & o_{(N_x+1)jk} &= o_{N_xjk}, \\ o_{i0k} &= o_{i1k}, & o_{i(N_y+1)k} &= o_{iN_yk}, \\ o_{ij0} &= o_{ij1}, & o_{ij(N_z+1)} &= o_{ijN_z}. \end{aligned} \quad (10)$$

Determination of the PSF

The accuracy of any deconvolution algorithm depends on the quality of used PSF. The PSF can be computed from the optical properties of a microscope system or estimated from the measurements of microspheres. Also, a third option exists where the PSF is estimated from recorded images together with observed objects (blind deconvolution) but for this paper we assume that PSF is known before executing the deconvolution process.

From the deconvolution quality point of view the estimation of PSF is preferred over the computed PSF because all optical aberrations of the given microscope system are taken into account. By contrast, in estimating PSF from microspheres measurements, the problem of suppressing noise must be tackled. In Lai *et al.* (2005), a PSF denoising method is introduced that is based on singular value decomposition. The method has disadvantage that it produces small but visible artificial ripples to the denoised PSF.

In this paper, the PSF is estimated from the microscope images of fluorescent microspheres using the following algorithm:

- (1) Determine the location of microspheres and extract their intensity profiles.

- (2) Sum the intensity profiles, to form the PSF function h . The SNR ratio will increase with the increase of the number (M) of intensity profiles.

It turns out that further denoising procedures on the summed PSF function is not required when M is sufficiently large: the SNR of a single PSF measurement increases approximately \sqrt{M} times when summing up M different PSF measurements. In our PSF cases, typical values for M are within range 4–12.

For this paper, two PSFs for a confocal microscope are estimated for laser lines 473 and 633 nm. For laser line 473 nm, we used microspheres (green) with excitation maximum at 505 nm and emission maximum at 540 nm. Emission was collected through a bandpass filter 550 ± 44 nm (FF01-550/88-25, Semrock). For laser line 633 nm, we used microspheres (deep red) with excitation maximum at 633 nm and emission maximum at 660 nm. Emission was collected through a bandpass filter 725 ± 75 nm (FF01-725/150-25, Semrock).

In addition, a PSF for a widefield microscope was obtained by exciting microspheres (orange – excitation maximum at 540, emission maximum at 560 nm) with fluorescent light through a bandpass filter 543 ± 22 nm (Semrock, Rochester, NY, U.S.A.) and emission was collected through a bandpass filter 593 ± 40 nm (Semrock).

PSFs that were used in this study are shown in Fig. 1 in the upper row. The lower row in Fig. 1 shows the corresponding optical transfer functions for all PSFs.

All types of microspheres have diameter $0.175 \mu\text{m}$ (PS-Speck, Molecular Probes, Invitrogen, Eugene, OR, U.S.A.).

The slides of microspheres for measuring PSFs were prepared as follows. A 1000-fold dilution in water was made from the original suspension. A small drop of the dilution was placed on a cover glass of 0.17 mm in thickness and let it dry in air. When the sample was dry a small drop of immersion oil with refractive index 1.334 at 23° (Carl Zeiss ImmersolTM W, Oberkochen, Germany) was added on the spot and fixed with a glass slide.

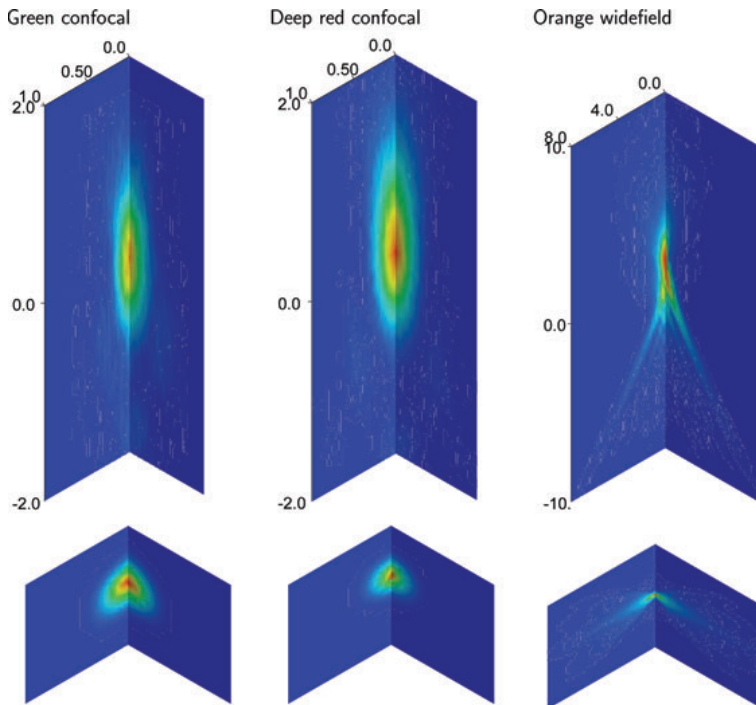


Fig. 1. The PSFs of the confocal and the widefield microscope used in this study. The upper row shows three PSFs estimated from the measurements of microspheres; two confocal PSFs and a widefield PSF. The axes in the subplots show distance in μm ; note the difference in scales used for confocal and widefield PSFs. Voxel sizes for PSF were as follows: green confocal $0.019 \times 0.019 \times 0.138 \mu\text{m}$, deep red confocal $0.027 \times 0.027 \times 0.120 \mu\text{m}$ and orange widefield $0.132 \times 0.132 \times 0.276 \mu\text{m}$, respectively. The lower row shows the corresponding optical transfer functions. Note that the PSF of widefield microscope is larger than the PSFs for confocal microscope.

Imaging of confocal images was carried out with custom confocal laser scanning microscope with a digital photon counter (avalanche photodiode, Perkin Elmer, SPCM-AQRH-13, Vaudreuil, Canada) and $60\times$ water-immersion objective (Olympus, UPLSAPO 60XW/1.2, Hamburg, Germany). Imaging of widefield images was carried out with Nikon TiU microscope (Nikon, Amstelveen, the Netherlands), equipped with Andor EMCCD camera (iXon 885, Andor, Belfast, Ireland), $60\times$ water-immersion objective (Nikon, Plan Apo VC $60\times/1.2$ WI, Amstelveen, the Netherlands). Optical sectioning was carried out by piezoelectric objective positioning system (Piezosystem Jena GmbH, MIPOS 250SG M25, Jena, Germany).

Obtaining experimental data for examples

Rat cardiomyocytes were isolated as in Sepp *et al.* (2010). Live cells were imaged using the approach similar to Birkedal *et al.* (2006) and Vendelin & Birkedal (2008). In short, the cells were kept and imaged in solution consisting of (mM): KH_2PO_4 3, MgCl_2 3, sucrose 110, K-lactobionate 60, taurine

20, HEPES 20, EGTA 0.5, DTT 0.5, malate 2, glutamate 5 and 5 mg mL^{-1} BSA. pH was adjusted to 7.1 with KOH at 25° . Mitochondria were visualized by staining isolated cells with MitoTracker Green FM with the final concentration of 200 nM; for sarcolemma we used di-8-ANEPPS with the final concentration of $1 \mu\text{M}$ (both from Invitrogen). After incubation for 15 min at the room temperature, cells were washed and inserted to imaging chamber that consisted of a FlexiPERM silicone insert (Vivascience, Hanau, Germany) attached to a cover slip glass of 0.17 mm in thickness.

For acquisition of images, the same microscope set-ups were used as described earlier for measuring PSF.

Analysis of the deconvolution process

To study the effects of deconvolution, we created two types of synthetic images with different textures from the microscope images of mitochondria and sarcolemma of rat cardiomyocytes. The image of mitochondria gives a typical example of blocky like textures. By contrast, the image of sarcolemma gives a typical example of honeycomb-like

textures. The synthetic images were obtained from confocal microscope images as follows. A microscope image was convolved and deconvolved several times using the following algorithm:

$$\begin{aligned}
 i^{(0)} &= i, \\
 i^{(j)} &= (i^{(j-1)} \otimes h) \otimes_{\lambda,S}^{-1} h, \quad j = 1, \dots, N, \\
 i_{\text{smooth}} &= i^{(N)} \otimes_{\lambda,S}^{-1} h.
 \end{aligned}
 \tag{11}$$

Note that the number of deconvolutions is larger by 1 compared to the number of convolutions in Eq. (11) to obtain small details in i_{smooth} that would be of similar size to the small details in the object image o [Eq. (1)]. Our smooth synthetic images were obtained using the following parameters: $N = 4$, $S = 200$, $\lambda = 0$.

We prefer using such synthetic images over traditional artificial images, which represent various geometrical shapes, because synthetic images allow us to tune the deconvolution algorithm parameters for microscope images that biologists need to deconvolve. An example of a synthetic image with blocky-like texture is shown in the first row of the second column of Fig. 2.

Two sets of test images were generated by convolving the synthetic image with PSF and degrading with Poisson noise. Various SNRs (13 different SNR values in total) were obtained by scaling the values of the synthetic image before degrading. For example of degraded image, see the first column of Fig. 2. The sets of test images were deconvolved using different regularization parameter λ values (100 different λ values in total) and compared with the synthetic image.

To quantify the quality of the deconvolution, we use mean squared error (MSE) between original object (e.g. synthetic image) and deconvolved images

$$\text{MSE} = \frac{\sum_v (o_v - o_v^{(s)})^2}{\sum_v o_v^2}.
 \tag{12}$$

In addition, we follow deconvolution process by computing relative changes between two estimates

$$\tau_d^{(s+d)} = \frac{\sum_v |o_v^{(s+d)} - o_v^{(s)}|}{\sum_v o_v^{(s)}},
 \tag{13}$$

where d shows the distance between the two estimates in iteration steps. In this paper, we consider only τ_1 and τ_2 .

Results

The RL deconvolution algorithm with TV regularization has been shown to give good deconvolution results with a carefully chosen regularization parameter λ . Because finding good parameter value to the algorithm is difficult, our aim is to estimate this value from microscope images. To test the effectiveness of the deconvolution method, we deconvolved synthetic images that were degraded with various Poisson noise levels. Following this, deconvolution

of images acquired on confocal and widefield microscopes are shown to demonstrate the effectiveness of the algorithm in practice.

Deconvolving synthetic images

The effectiveness of the deconvolution method can be assessed with the use of a synthetic image which is convolved and degraded with different Poisson noise levels. To ensure that this synthetic image represents similar textures as in cells, we used images of mitochondria and sarcolemma in rat cardiomyocyte where the noise was smoothed out by robustly convolving and deconvolving the image several times [Eq. (11)].

For example, the synthetic image from mitochondria recording is presented in the first row of the second column of Fig. 2. The blocky-like texture in this synthetic image consists of different geometrical shapes and intensities: spherical shapes, lines, homogeneous and heterogeneous areas. Two test images with different SNRs are shown in the first column of Fig. 2. The second and third columns of Fig. 2 show images deconvolved using our λ estimation procedure [Eq. (5)] and optimal regularization parameter λ_{opt} , respectively. The procedure for determining λ_{opt} is described later. Because for synthetic images the original image is known, the actual efficiency of the deconvolution algorithm can be assessed directly by using the MSE [Eq. (12)]. The MSE provides a mean to measure the difference between the deconvolved and original image. The larger MSE value corresponds to larger difference between images.

Fig. 3A shows the MSE between the original and estimated image for each iteration of the deconvolution process. The MSE was computed from the results which were obtained by deconvolving degraded original image with Poisson noise such that SNR = 22.7 using the λ estimation formula Eq. (5) and various fixed λ values. In the presence of noise, we see that the MSE is smaller when using the RL algorithm with TV regularization rather than the traditional RL algorithm ($\lambda = 0$). Looking at Fig. 3A, we see that when λ is small, the MSE between the original and deconvolved images decreases and reaches its minimum in a small number of iterations, after which the MSE starts to increase monotonically. When the regularization parameter value is larger (e.g. $\lambda = 4.0$), the deconvolution process stabilizes shortly after passing the MSE minimum. However, at larger λ values ($\lambda = 7.0$), the deconvolution process is not able to enhance image considerably which is clear from observation of MSE. Although deconvolving the test image with SNR = 22.7, the lowest MSE = 0.00528 was obtained at the 15th iteration step with regularization parameter $\lambda = 2.5$. When using our estimated λ , the deconvolution process reached its best result at the 25th iteration step with MSE = 0.000593. The results of 0th, 3rd, 8th, . . . , 103th, iterations are given in Fig. 4. Note that λ_{lsq} achieves its maximum at third iteration and MSE achieves its minimum at 25th iteration. Our stopping criterion suggests

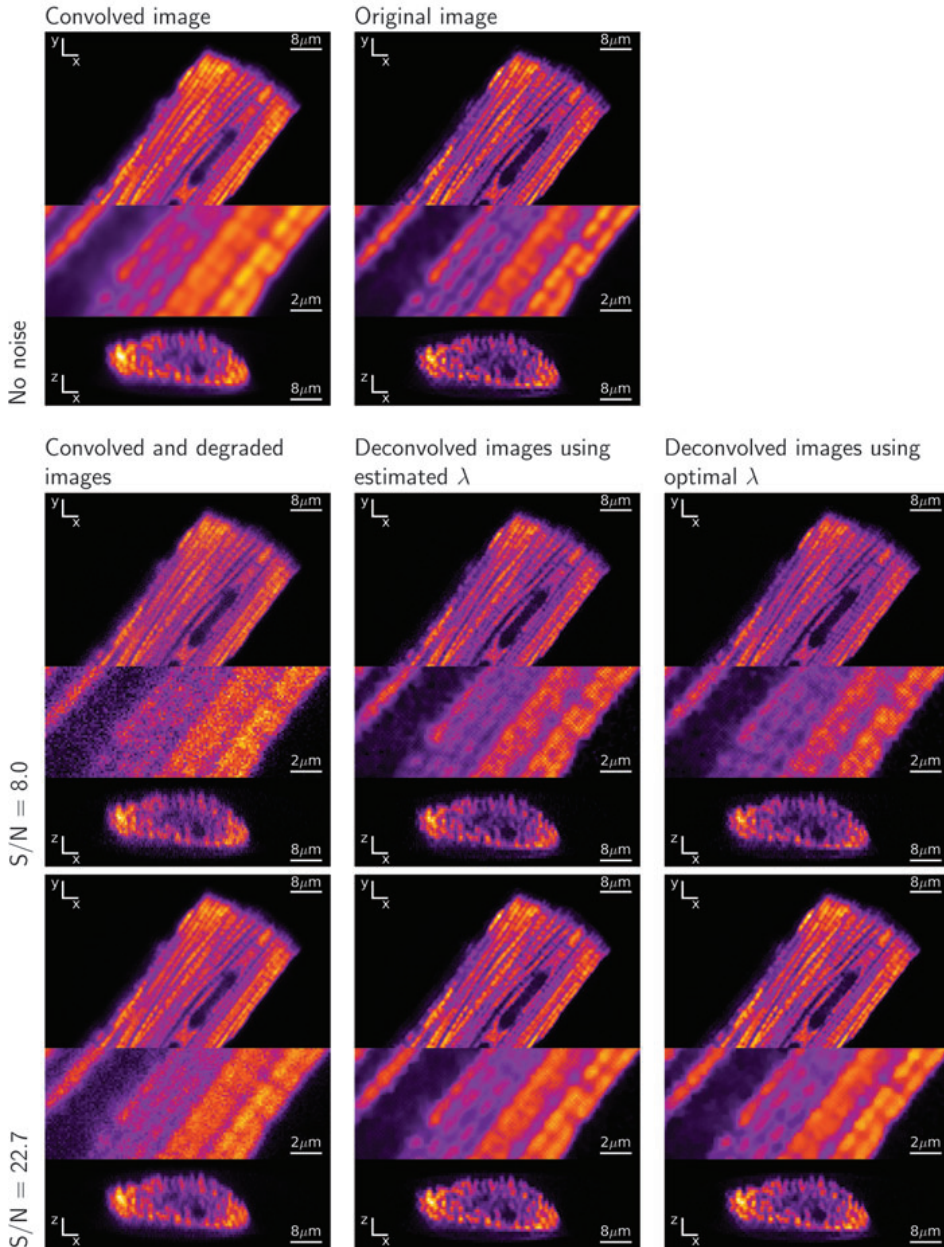


Fig. 2. The results of deconvolving synthetic 3D images with the voxel size $0.136 \mu\text{m} \times 0.136 \mu\text{m} \times 0.707 \mu\text{m}$. The first row shows convolved and original images, respectively. The original synthetic image is obtained from the confocal image of mitochondria in cardiac cell and has typical blocky like texture. The first column shows degraded images with different signal-to-noise ratios (SNR); the second column represents degraded images that are deconvolved using estimated λ ; and the last column shows degraded images that are deconvolved using an optimal value for λ . Test images with different SNR and the deconvolution results are shown in rows, starting from second, in decreasing order according to SNR. Deconvolution results correspond to minimal MSE value.

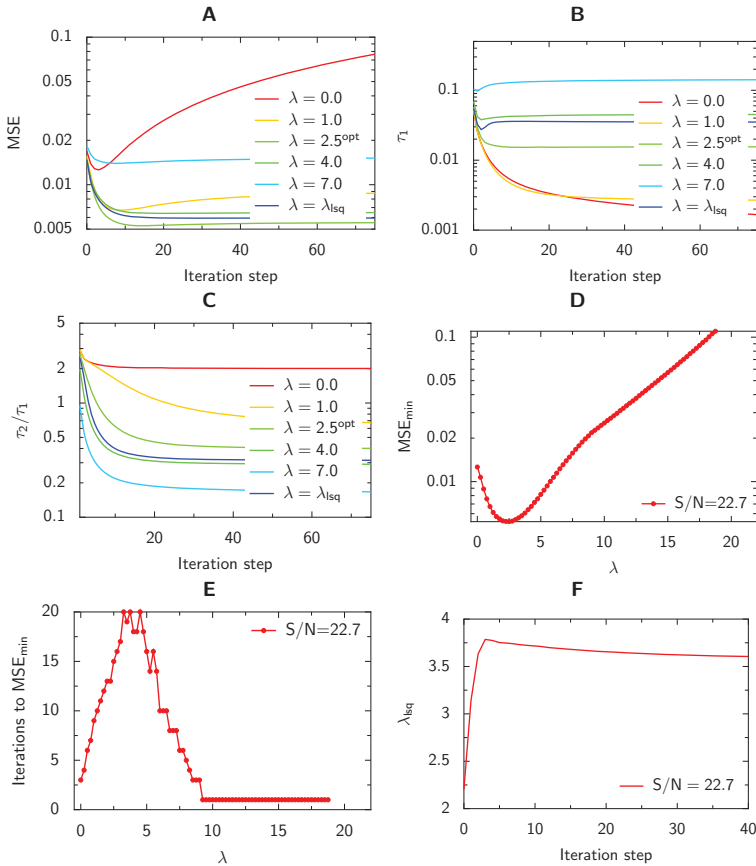


Fig. 3. The analysis of deconvolution for degraded image of blocky-like texture with Poisson noise, SNR = 22.7. (A) The evolution of the mean squared error (MSE) during iteration. The deconvolution process converges to a solution that is slightly different from the original image: MSE stabilizes to a certain nonzero level. The nearest result to original image is achieved with $\lambda = 2.5$ at iteration step 15 when MSE is minimal. (B) The evolution of convergence of MSE whereas smaller τ_1 does not mean smaller MSE. (C) The evolution of the ratio between two relative changes. Symbol τ_2 denotes the relative change between iterations s and $s + 2$. (D) Minimal MSE as a function of λ . The minimum point of the graph defines optimal λ value for that case. (E) The number of iteration steps required to achieve minimal MSE for different λ values. (F) The evolution of estimated λ during iteration. Note that estimated λ obtains its maximum at third iteration.

stopping iteration at 8th step when $MSE = 0.00635$ for this particular case.

The behaviour of the deconvolution process was tracked using the relative change between two successive estimates [Eq. (13)], which is shown in Fig. 3B. Frequently, the relative change between two successive estimates τ_1 is used as a stopping criterion (Cannell *et al.*, 2006; Dey *et al.*, 2006). According to that criterion, if τ_1 falls down to a given threshold the deconvolution process is stopped. However, there are at least two problems when using this criterion in practice, as indicated later.

First notice that, ideally, the stopping criterion should finish the deconvolution process when the deconvolved image is closest to 'true' image. From the analysis of MSE and τ_1 evolutions, it is clear that this is not always true (Figs 3A and B). Namely, as it is shown in the figure, there is no τ_1 value that can be used as an universal threshold for all regularization parameter values. Although it is theoretically possible to choose a threshold value for each trace individually so that deconvolution will be stopped at minimum of MSE, finding such threshold value in practice is very difficult, if impossible.

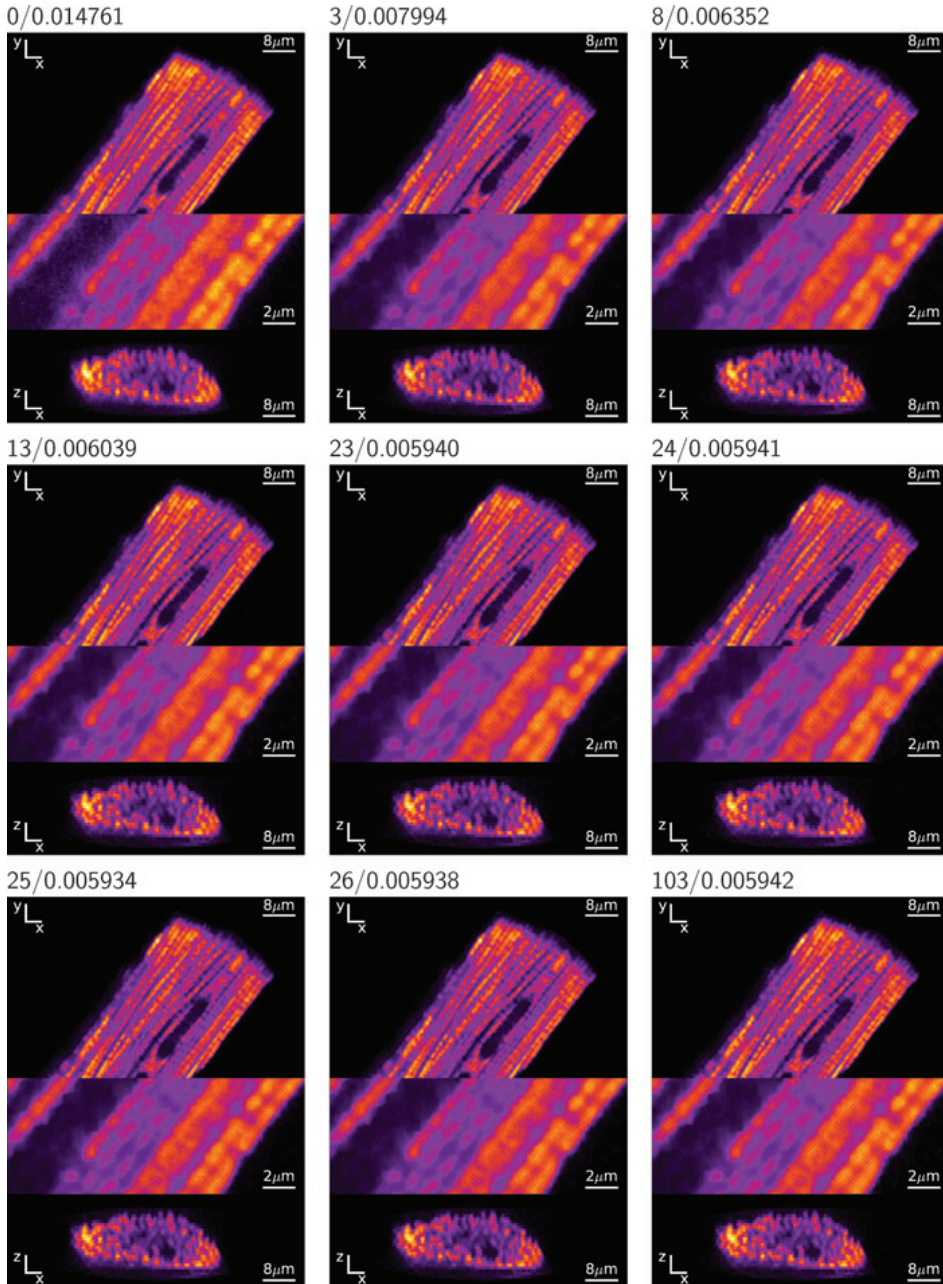


Fig. 4. The results of deconvolving synthetic 3D images with SNR = 22.7. The numbers above images show the iteration step and MSE between original object and deconvolved image. On the iteration step $s = 3$, the λ_{lsq} has maximal value and on the iteration step $s = 25$ the MSE has minimal value for this specific case. Note that there is no visible differences between results from the iteration step $s = 25$ and $s \geq 3$.

Secondly, from the comparison of deconvolution processes with different TV regularization parameter values reveals that the convergence of deconvolution is not always related to small τ_1 values. Namely, lower τ_1 value would indicate stabilization of the deconvolution process and we would expect the MSE to stabilize as well. Comparison of Figs 3A and B at $\lambda = 1.0$ shows that the relative change τ_1 is monotonically decreasing but MSE starts to increase after the sixth iteration. In contrast to that, at $\lambda = 2.5$, the relative change τ_1 has higher values than at $\lambda = 1.0$, but from the trace of the MSE (Fig. 3A), the deconvolution process seems to be converged because the MSE remains relatively constant at $\lambda = 2.5$. So, there exists no such threshold value for τ_1 that would be applicable for both cases.

It turns out that the behaviour where τ_1 is relatively large and MSE is stationary, indicates oscillations between several successive iteration steps. To demonstrate that, let us define the ratio between two different relative changes τ_2/τ_1 , where τ_1 denotes the relative change between s and $s + 1$ and τ_2 denotes the change between s and $s + 2$ iteration steps. Following the evolution of τ_2/τ_1 in Fig. 3C at $\lambda = 2.5$, the ratio decreases and stabilizes to a level smaller than 1. By contrast, using $\lambda = 0$ (Fig. 3A), the ratio stabilizes at a level above 1 while the MSE increases during iteration. Thus, for the cases where the ratio falls under 1 and stabilizes, we can assume that the deconvolution process starts to oscillate between several successive iteration steps. However, for the case where τ_2/τ_1 is larger than 1, we can assume that the changes in the images are progressive during deconvolution leading to changes in the MSE, as for $\lambda = 0$.

Optimal TV regularization parameter value and stopping criterion

As it is shown in Fig. 3A, the minimal MSE value is different for each λ value. Fig. 3D shows minimal MSE as a function of λ . Note that the minimal point defines the value of optimal λ for the particular case. So, the procedure for determining λ_{opt} consists of finding the minimum point of the minimal MSE and λ graph.

The optimal number of steps is defined as the number of steps needed to reach a minimal MSE value. In Fig. 3E, we see that the optimal number of steps varies between different λ values. For example, if λ is fixed and close to λ_{opt} (2.5 for this particular case), the deconvolution process requires more steps to reach the minimal MSE.

In practice, the original image is unknown and we cannot use MSE as a measure of the quality of deconvolved images. So, appropriate stopping criterion that does not depend on the original image is needed. For this we used the evolution of λ_{lsq} during iteration (Fig. 3F). The general behaviour of λ_{lsq} during the deconvolution process can be described as follows. In the beginning, λ_{lsq} values are small, increase to the maximum after which the value stabilizes to a certain nonzero level. We notice that the points where MSE is minimal and where λ_{lsq}

obtains a maximum value are correlated (Fig. 3A and 3F). Thus, the evolution of λ_{lsq} can be used as a stopping criterion.

Similar analysis was performed on test images with different SNR values as well as for honeycomb-like texture cases. Overall, there were 13 different test cases with various SNRs. From our simulations it is clear that for different SNR the value of λ_{opt} is not the same. In Fig. 5A where the MSE_{min} is displayed as a function of λ , we see that the minimum points of graphs are shifting towards zero as the SNR increases. Therefore, the value of λ_{opt} is decreasing with the increase of SNR. Note that when deconvolving images without noise ($\text{SNR} = \infty$) and taking $\lambda = 0$, the original image is obtained ($\text{MSE} \rightarrow 0$). By contrast, when deconvolving images with noise, the iteration process never converges to the original image. Furthermore, from the analysis of the values of λ_{opt} and SNR in Fig. 5B, we notice an inverse relation between λ_{opt} and SNR: $\lambda_{\text{opt}} \sim \frac{1}{\text{SNR}}$. As a robust estimate, we suggest using $\lambda = 50/\text{SNR}$.

For microscope images we use λ_{lsq} because finding the optimal λ is a tedious and nontrivial process. By comparing the deconvolution results for synthetic images that use λ_{lsq} , λ_{opt} and $\lambda = 0$ at different noise levels, we assessed the performance of the λ estimating formula. Figs 5C and E summarize the deconvolution results in terms of minimal MSE for different noise levels and λ selections. From the graphs we conclude that using optimal regularization always gives better results (smaller MSE), and generally, using regularization is necessary in the presence of noise. In addition, there exist a range of SNR values (5–100) where using λ_{lsq} gives the same order of magnitude for minimal MSE as using λ_{opt} .

As it was suggested earlier, evolution of λ_{lsq} can be used as a stopping criterion. We suggest to stop the iteration process after five steps of obtaining λ_{lsq} maximum value. According to our simulations, such stopping criteria leads to deconvolved image with the resulting MSE close to minimal MSE (Figs 5D and F). In addition, long and converging iterations (100 iterations after λ_{lsq} maximum) cause MSE to diverge from the minimal MSE. This clearly shows that converging iteration does not guarantee more accurate results.

Deconvolving microscope images

As an example, we applied RL algorithm with TV regularization to experimentally recorded images. First, confocal images of mitochondria and sarcolemma in rat cardiomyocytes were deconvolved. Secondly, to test the performance of the algorithm, we deconvolved confocal image with the punctated stain and a widefield image.

In Fig. 6A, where the cell was labelled with MitoTracker Green FM, cross-sections xy and yz are displayed from the middle of cell. At upper left corner, an enlarged view from the middle part of the xy cross-section is shown. From the comparison of the recorded and deconvolved image using λ_{lsq} , we can clearly see significant improvement in the quality of

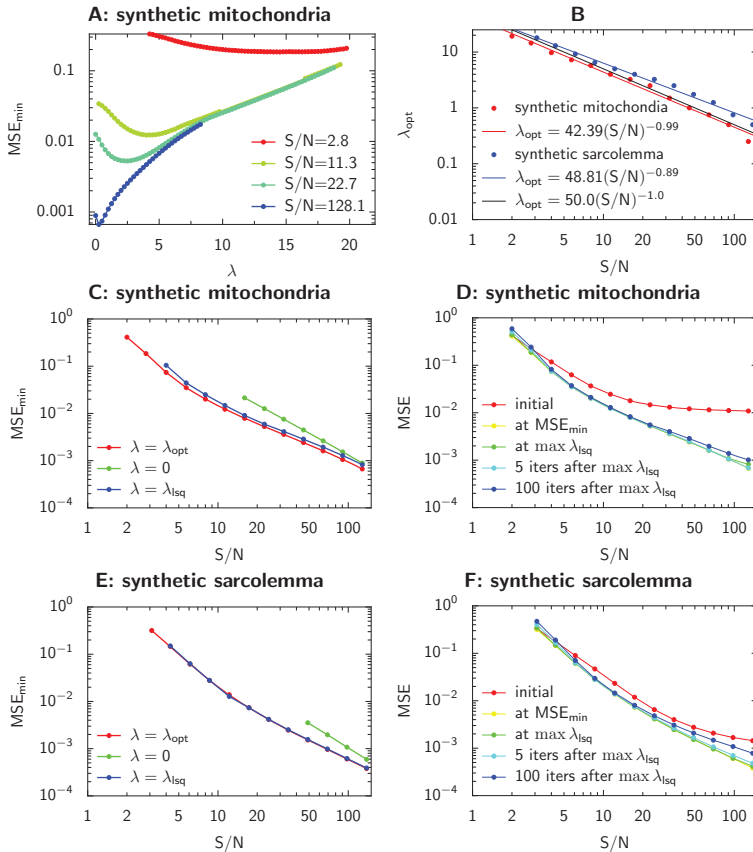


Fig. 5. The analysis of deconvolution at different SNR. (A) Minimal MSE as a function of λ for various SNR values. Note that the optimal λ (defined as the minimum point of MSE_{\min}) is smaller for higher SNR. The original image is achieved only when noise is not present and the TV term is disabled ($\lambda = 0$). (B) The relations between SNR and optimal λ for two different types of image textures. The confocal images of mitochondria and sarcolemma in cardiac cells are used to obtain synthetic image with blocky- and honeycomb-like textures, respectively. Note the approximate exponential relations $\lambda_{\text{opt}} \sim 1/\text{SNR}$, see text for details. (C) The relation between SNR and minimal MSE for disabled TV, estimated λ and optimal λ values, respectively. Restored image contains blocky-like textures. (D) MSE as a function of SNR and stopping iteration step. (E) Same as C, restored image contains honeycomb-like texture. (F) Same as D, restored image contains honeycomb-like texture.

the deconvolved image (compare Figs 6A and B). For example, the noise is reduced considerably on the whole image and mitochondria can be more easily distinguished from each other. Note the significant contrast enhancement on yz plane.

On the basis of our analysis, we estimated that the optimal λ value for deconvolving the image of the cell with stained mitochondria (Fig. 6A) is 2.5. This estimation was made assuming that the relationship between the SNR and λ_{opt} (Fig. 5B) is valid for this recording as well. Comparing the result to one obtained using λ_{lsq} , there are no visible differences (results not shown).

Fig. 7A shows a sarcolemma in rat cardiomyocyte labelled with di-8-ANEPPS. Lines seen in this image correspond to t -

tubules. As in the previous example, two cross-sections and an enlarged view from the middle of the image are shown. From the comparison of recorded image and restored image (Figs 7A and B), we see an improvement in contrast and reduction of noise.

To test the performance of the algorithm, we deconvolved a confocal image of a cluster of microspheres. Such cluster is similar to punctated stain which can occur in live cells when imaging distribution of ryanodine receptors, for example. As it is shown in Fig. 8, experimental images can be successfully deconvolved for such texture as well.

Although the considered deconvolution algorithm is designed for confocal microscopy where Poisson noise

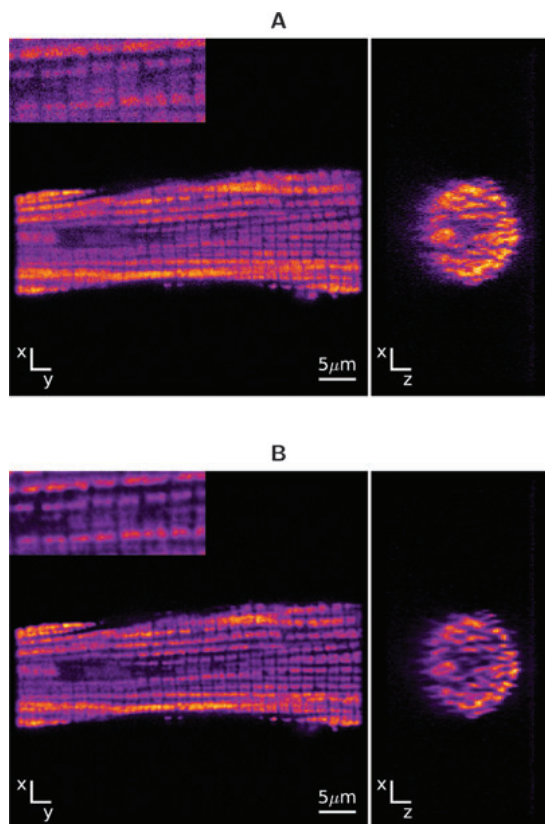


Fig. 6. The image of mitochondria in rat cardiomyocyte before and after deconvolution algorithm was applied (voxel size $0.095 \mu\text{m} \times 0.095 \mu\text{m} \times 0.343 \mu\text{m}$). The recorded confocal microscope image of rat cardiomyocyte mitochondria labelled with MitoTracker Green FM, note the blocky texture. (A) xy and yz cross-sections of the recorded image. At upper left corner, a zoomed region from the middle of xy cross-section is shown. (B) The seventh iteration of deconvolved recorded image A using estimated λ . Note the improvement in contrast. Noise is smoothed out and space between mitochondria has cleared.

is dominating, we have applied it to images of stained mitochondria of rat cardiomyocytes (Fig. 9A) acquired with a widefield fluorescence microscope. The deconvolution of such images reduces considerably out-of-focus light and reduces noise, as shown in Fig. 9B. However, further research is needed to improve the deconvolution result by taking into account other noise properties as well as gradients in the background field of widefield images.

Discussion

In this work, we derived a formula to estimate the TV regularization parameter for regularized RL deconvolution

algorithm and developed an open source software platform IOCBio Microscope where other deconvolution algorithms can be introduced easily. In addition, we illustrated that over a certain range of SNR, the estimated λ gives as good results as with the optimal regularization parameter. As a result, we propose a practical method to deconvolve confocal microscope images that uses estimated regularization parameter depending on the input image.

Deconvolving synthetic images

We analysed the behaviour of the deconvolution algorithm on a synthetic image. Usually, synthetic images that are used in the analysis of deconvolution contain various geometrical shapes with different intensities. In this paper, we use synthetic images that are constructed from actual microscope images as described in the Materials and Methods section. Usage of such synthetic images gives us an opportunity to study the deconvolution algorithms under more realistic conditions.

The RL algorithm with TV regularization requires the selection of an appropriate regularization parameter value for each image that is being deconvolved. In practice, the selection of this parameter value is based on an educated guess. However, the analysis of synthetic images (Fig. 5A) shows that the errors can be an order of magnitude smaller with appropriate λ value than with arbitrary λ values. In addition, Fig. 5B shows that the optimal λ depends on the SNR exponentially: $\lambda_{\text{opt}} \approx 50/\text{SNR}$.

Recently, methods for estimating the regularization parameter have been introduced to avoid the tedious work needed for finding the appropriate λ value. For this, Gilboa *et al.* (2003) use an adaptive variational scheme and Liao *et al.* (2009) make use of a generalized cross-validation technique. In this paper, we derived a formula Eq. (5) that is based on a least squares method and is related to findings of Gilboa *et al.* (2003). The usage of our formula gives as good results as with optimal λ value for a certain range of SNRs (Figs 5C–F).

Estimated regularization parameter as stopping criteria

As a stopping criterion, several authors have used the relative change between two estimates (τ_1) and the stopping point is determined when the relative change falls below a given threshold (van Kempen *et al.*, 1997; Dey *et al.*, 2004; Pankajakshan *et al.*, 2008). We could not use this approach for multiple reasons. First, we could not identify τ_1 threshold value that would fit deconvolution processes with different TV regularization parameter values. Secondly, the value of τ_1 was not always related to convergence of deconvolution process. Namely, we have shown (Figs 3A and B) that MSE can stabilize at relatively high values of τ_1 in some cases and the opposite can be true as well (evolving MSE at small values of τ_1). The discrepancy between stable MSE and relatively large τ_1 was related to oscillations between several estimates

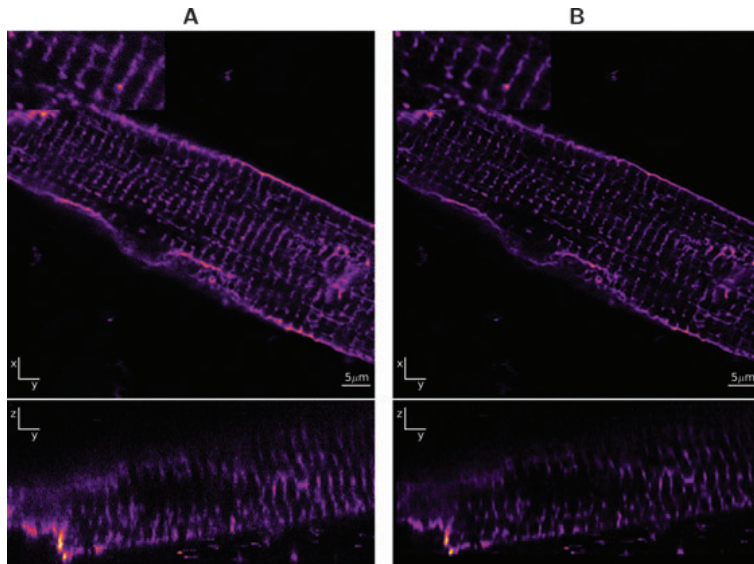


Fig. 7. The image of sarcolemma in rat cardiomyocyte before and after deconvolution algorithm was applied (voxel size $0.063 \mu\text{m} \times 0.063 \mu\text{m} \times 0.387 \mu\text{m}$). The recorded confocal microscope image of rat cardiomyocyte sarcolemma labelled with di-8-ANEPPS, note the honeycomb-like texture. (A) xy and yz cross-sections of recorded image. (B) The eighth iteration of deconvolved recorded image A with estimated λ . Note the improvement in contrast, noise is smoothed out, and t -tubules are more visible.

obtained in successive deconvolution steps, as shown using τ_2/τ_1 relationship in the Results. Thus, according to our analysis, the use of τ_1 for stopping deconvolution process would not lead to the best possible estimation of the 'true' image.

Our approach uses the evolution of λ_{lsq} that is computed from Eq. (5) as a stopping criterion – the deconvolution process is stopped after five iterations of λ_{lsq} has obtained its maximum value. The analysis of MSE confirms that the minimum point of MSE is well correlated with the point where λ_{lsq} obtains maximum value. By contrast, if the deconvolution process is prolonged, visually identifiable artefacts will be produced. This effect is well seen in Figs 5D and F where the results of long iterations (100 iterations after λ_{lsq} maximum has been obtained) have noticeably larger MSE compared to the results that are stopped after λ_{lsq} maximum point.

Deconvolving confocal microscope images

Although the quality of deconvolution result strongly depends on the quality of the input data, the deconvolution can improve the quality of image, even if the data is greatly corrupted by noise.

However, to ensure a realistic result using iterative deconvolution algorithms, the process needs to be stopped before artefacts are created. For deconvolving microscope images, we used the RL algorithm with TV regularization

using estimated λ . The optimal solution with noticeable improvements is achieved with a rather small number of iteration steps. However, prolonged iteration starts to produce artefacts. When using our λ estimation formula, the deconvolution process can be stopped at the right iteration step by monitoring the evolution of λ_{lsq} . By contrast, when visually examining the estimates around λ_{lsq} maximum, they look equally acceptable (Fig. 4). Furthermore, when using this criterion with experimental data, we noted that at higher SNRs in the initial data, the optimal number of iteration steps is larger than for smaller SNRs. This is in accordance to the results obtained from the analysis of deconvolution of synthetic images.

The input for estimating the regularization parameter of the RL deconvolution algorithm is the peak SNR of a recorded image. With confocal microscopes that use photon counting detectors, the peak SNR can be directly estimated as a square of largest count value in image data. In practice, use of peak SNR can be problematic. First, staining artefacts leading to small cluster of bright pixels would determine the estimate of the ratio. Secondly, when non-photon counting confocal microscopes are used, the use of a square of largest count value in image data as an estimate of SNR is questionable. Indeed, confocal microscopes equipped with analogue light detectors record intensity in arbitrary units that depend on user settings of detector gain and offset. The both problems can be resolved if more general SNR estimate is used. For example, SNR

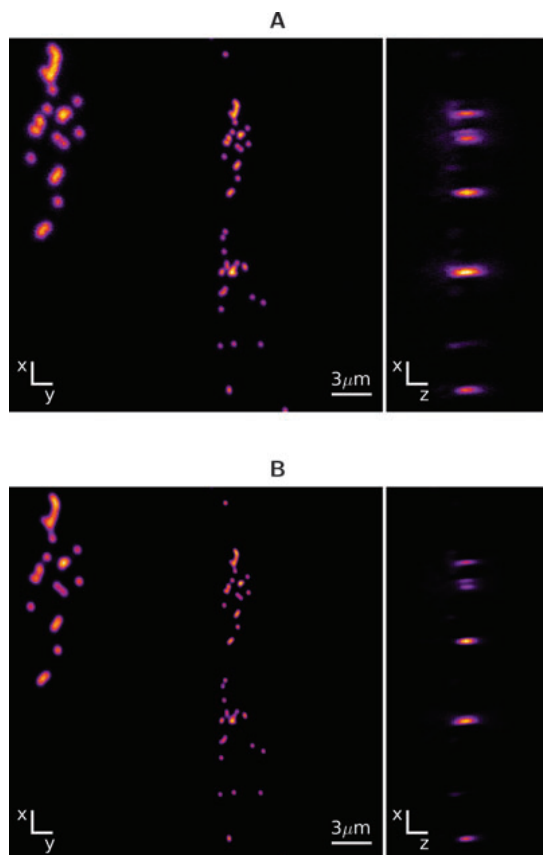


Fig. 8. The image of microspheres cluster before and after deconvolution algorithm was applied (voxel size $0.054 \mu\text{m} \times 0.054 \mu\text{m} \times 0.188 \mu\text{m}$). The recorded confocal microscope image of microspheres is also used for estimating PSFs, note punctuated texture. (A) xy and yz cross-sections of the recorded image. At upper left corner, a zoomed region from the middle of xy cross-section is shown. (B) The eighth iteration of deconvolved recorded image A using estimated λ .

estimate based on the variations of neighbouring voxels takes into account information from the whole image (de Monvel *et al.*, 2001). This would dampen the effect of small bright clusters in an image to SNR and, in addition, is applicable to images recorded using analogue detectors. How such estimate of SNR is related to the regularization parameter of the RL deconvolution algorithm is a subject of further studies.

In addition to difficulties in estimating SNR, confocal microscopes equipped with analogue detectors can have noise properties that are different from Poisson noise. However, that can be altered by user in practice by selecting lower gain of the detector. As it has been shown earlier, with lower gain settings, Poisson noise is dominating in images (Cho & Lockett, 2006).

Furthermore, by averaging image during acquisition, user can improve general SNR (Conchello & Lichtman, 2005) leading to a better deconvolution of the image.

Another important element in deconvolution is the PSF which should be determined as accurately as possible to account for imperfections in the optical pathway. In this paper, we used PSFs obtained from the measurements of microspheres. Such PSFs account for imperfections such as asymmetry. Including asymmetry to computed PSF is not trivial because the source of the asymmetry is hard to determine. The accurate PSF is important because deconvolving with a incorrect PSF can result misleading conclusions (Cannell *et al.*, 2006). The quality of PSF plays a critical role in obtaining a high quality result, and to this end, we recommend using a measured PSF.

IOCBio Microscope – a software for deconvolving microscope images

In this work, our contribution includes the development of an open source software package IOCBio Microscope that collects all necessary elements for deconvolution using the RL algorithm with TV variation regularization (Peterson, 2010a). This includes, reading microscope images of various formats (TIFF, RAW and LSM files), estimating PSF from the measurements of microspheres, deconvolving images with different algorithm options, etc. The software is implemented in Python which has proven itself as an excellent prototype language for testing algorithms. The computationally expensive parts are implemented in C and FFTW library is used with multiple threads to reduce CPU time for deconvolution considerably. For example, deconvolving an image stack of size $32 \times 512 \times 512$ with 100 iterations takes about 10 min on a standard desktop computer. We anticipate that this deconvolution software package becomes a platform for testing different deconvolution algorithms. Furthermore, the software has reasonable graphical user interface that makes it easy to use for enhancing microscope images. The software can be run in a computer cluster environment such as Sun Grid Engine to parallelize deconvolution tasks.

In future, we plan to implement Poisson noise removal algorithm by Le *et al.* (2007) that can be applied to estimated PSF as well as to the first estimate of deconvolution process. Application of such a noise removal can improve the efficiency of deconvolution algorithms even further. In addition, we plan to add interfaces to existing C/C++ deconvolution libraries such as Clarity and Deconv so that these algorithms could be used from the Python based IOCBio Microscope package. The availability of semi-automatic wrapper generation tools like SWIG (Beazley, 2003) and F2PY (Peterson, 2009) as well as the standard Python ctypes module makes wrapping C, C++ or Fortran software libraries to Python-based platform particularly easy. See Peterson (2010c) for an example of wrapping the Deconv library to Python.

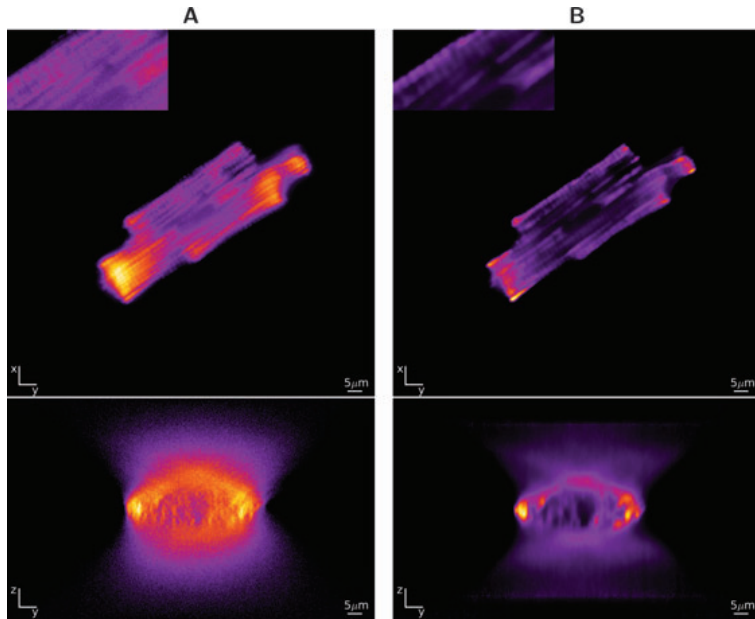


Fig. 9. The image of mitochondria in rat cardiomyocyte before and after deconvolution algorithm was applied (voxel size $0.132 \mu\text{m} \times 0.132 \mu\text{m} \times 0.398 \mu\text{m}$). The recorded widefield fluorescence microscope image (A) of rat cardiomyocyte mitochondria labelled with MitoTracker Green FM, note the blocky texture and extensive out-of-focus light. The image is improved by deconvolution (B) leading to the reduction of out-of-focus light and reducing noise. Note that deconvolution was not able to fully remove out-of-focus light.

Although this paper deals with confocal microscopy and deconvolving its images, the IOCBio Microscope software has extensions to apply deconvolution algorithms to the images of widefield microscopy as well. In particular, the algorithm for estimating PSF from the measurements of microspheres is adapted to deal with specific properties of widefield microscopy recordings such as relatively high level and nonuniform background field, different noise model, etc. The software can be used for testing deconvolution algorithms on recordings of widefield microscopy, similarly to what we have done in this paper for recordings of confocal microscopy. However, as seen in Fig. 9, more work is required to improve further the deconvolution results of widefield images by using the RL algorithm. It must take into account more appropriate image formation model for a widefield microscope that have other noise properties and more dominant background field gradients than in confocal microscope.

Conclusions

To conclude, we have developed an open source software package IOCBio Microscope that can be used for deconvolving images in practice. The developed software package can be also used as a platform for testing new deconvolution algorithms. We have derived a formula to estimate the TV regularization parameter for regularized RL deconvolution

algorithm and shown that over a certain range of noise levels the estimated regularization parameter gives as good results as the optimal regularization parameter. Inverse relation between the optimal TV regularization parameter and image SNR is shown and taken into account in the regularization estimation. In addition, new stopping criterion for deconvolution process has been proposed.

Acknowledgements

The authors thank Rikke Birkedal, Mervi Sepp who provided us with cardiomyocytes for collecting experimental data. the authors acknowledge David Schryer for his suggestion on improving the paper.

The research was supported by Wellcome Trust Fellowship no. WT081755MA and the Estonian Science Foundation grant no. ETF8041 (Ph.D. stipend for M.L.).

References

- Abdelhak, B. & Sedki, M. (1992) Filtering capabilities and convergence of the van-Cittert deconvolution technique. *IEEE Trans. Instrum. Meas.* **41**, 246–250.
- Agard, D.A. (1984) Optical sectioning microscopy: cellular architecture in three dimensions. *Annu. Rev. Biophys. Bio.* **13**, 191–219.

- Avinash, G. (1996) Data-driven, simultaneous blur and image restoration in 3-D fluorescence microscopy. *J. Microsc.* **183**, 145–167.
- Beazley, D. (2003) SWIG: an extensible compiler for creating scriptable scientific software. *Future Generat. Comput. Syst. (FGCS)*, Elsevier **19**, 599–609.
- Birkedal, R., Shiels, H.A. & Vendelin, M. (2006) Three-dimensional mitochondrial arrangement in ventricular myocytes: from chaos to order. *Am. J. Physiol. Cell. Physiol.* **291**, C1148–C1158.
- Cannell, M.B., McMorland, A. & Soeller, C. (2006) Image enhancement by deconvolution. *Handbook of Biological Confocal Microscopy* (ed. by J.B. Pawley), 3 edn., pp. 488–497. Springer, New York.
- Carrington, W., Lynch, R., Moore, E., Isenberg, G., Fogarty, K. & Fay, F. (1995) Superresolution three-dimensional images of fluorescence in cells with minimal light exposure. *Science* **268**, 1483–1487.
- Cho, E.H. & Lockett, S.J. (2006) Calibration and standardization of the emission light path of confocal microscopes. *J. Microsc.* **223**, 15–25.
- Conchello, J.-A. (1998) Superresolution and convergence properties of the expectation-maximization algorithm for maximum-likelihood deconvolution of incoherent images. *J. Opt. Soc. Am. A* **15**, 2609–2619.
- Conchello, J.-A. & Lichtman, J.W. (2005) Optical sectioning microscopy. *Nat. Methods* **2**, 920–931.
- Dey, N., Blanc-Feraud, L., Zimmer, C., Roux, P., Kam, Z., Olivo-Marin, J.-C. & Zerubia, J. (2004) 3D microscopy deconvolution using Richardson-Lucy algorithm with total variation regularization. *Technical Report 5272*. INRIA.
- Dey, N., Blanc-Feraud, L., Zimmer, C., Roux, P., Kam, Z., Olivo-Marin, J.-C. & Zerubia, J. (2006) Richardson-Lucy algorithm with total variation regularization for 3D confocal microscope deconvolution. *Microsc. Res. Techniq.* **69**, 260–266.
- Frigo, M. & Johnson, S.G. (2005) The design and implementation of FFTW3. *Proc. IEEE* **93**, 216–231.
- Gilboa, G., Zeevi, Y.Y. & Sochen, N. (2003) Texture preserving variational denoising using an adaptive fidelity term. *Proceedings of the VLSM*, pp. 137–144. Nice, France.
- Holmes, T. (1992) Blind deconvolution of quantum-limited incoherent imagery: maximum-likelihood approach. *J. Opt. Soc. Am. A* **9**, 1052–1061.
- Inoué, S. (2006) Foundations of confocal scanned imaging in light microscopy. *Handbook of Biological Confocal Microscopy* (ed. by J.B. Pawley), 3 edn., pp. 1–19. Springer, New York.
- Jones, E., Oliphant, T., Peterson, P. et al. (2001) SciPy: Open source scientific tools for Python. <http://www.scipy.org/>.
- Lai, X., Lin, Z., Ward, E. & Ober, R. (2005) Noise suppression of point spread functions and its influence on deconvolution of three-dimensional fluorescence microscopy image sets. *J. Microsc.* **217**, 93–108.
- Le, T., Chartrand, R. & Asaki, T. (2007) A variational approach to reconstructing images corrupted by Poisson noise. *J. Math. Imaging Vis.* **27**, 257–263.
- Liao, H., Li, F. & Ng, M. (2009) Selection of regularization parameter in total variation image restoration. *J. Opt. Soc. Am. A* **26**, 2311–2320.
- Lucy, L. (1974) An iterative technique for the rectification of observed distributions. *Astron. J.* **79**, 745–754.
- Markham, J. & Conchello, J. (1999) Parametric blind deconvolution of microscopic images: a robust method for the simultaneous estimation of image and blur. *J. Opt. Soc. Am. A* **16**, 2377–2391.
- de Monvel, J.B., Calvez, S.L. & Ulfendahl, M. (2001) Image restoration for confocal microscopy: improving the limits of deconvolution, with application to the visualization of the mammalian hearing organ. *Biophys. J.* **80**, 2455–2470.
- de Monvel, J.B., Scarfone, E., Calvez, S.L. & Ulfendahl, M. (2003) Image-adaptive deconvolution for three-dimensional deep biological imaging. *Biophys. J.* **85**, 3991–4001.
- Neelamani, R., Choi, H. & Baraniuk, R. (2004) ForWaRD: Fourier-wavelet regularized deconvolution for ill-conditioned systems. *IEEE Trans. Signal Process.* **52**, 418–433.
- Oliphant, T.E. (2007) Python for scientific computing. *Comput. Sci. Eng.* **9**, 10–20.
- Pankajakshan, P., Blanc Féraud, L., Zhang, B., Kam, Z., Olivo Marin, J.-C. & Zerubia, J. (2008) Parametric blind deconvolution for confocal laser scanning microscopy (CLSM) – proof of concept. *Research Report RR-6493*. INRIA.
- Peterson, P. (2009) F2PY: a tool for connecting Fortran and Python programs. *IJCSE* **4**, 296–305.
- Peterson, P. (2010a) IOCBio Microscope software. <http://iocbio.googlecode.com/>.
- Peterson, P. (2010b) List of open-source deconvolution software. <http://code.google.com/p/iocbio/wiki/DeconvolutionSoftware>.
- Peterson, P. (2010c) PyLibDeconv – a Python wrapper of the Deconv library. <http://pylibdeconv.googlecode.com/>.
- Preza, C. & Conchello, J.-A. (2004) Depth-variant maximum-likelihood restoration for three-dimensional fluorescence microscopy. *J. Opt. Soc. Am. A* **21**, 1593–1601.
- Preza, C., Miller, M., Thomas, I. & McNally, J. (1992) Regularized linear method for reconstruction of three-dimensional microscopic objects from optical sections. *J. Opt. Soc. Am. A* **9**, 219–228.
- Preza, C., Miller, M. & Conchello, J.-A. (1993) Image reconstruction for 3D light microscopy with a regularized linear method incorporating a smoothness prior. *Proc. SPIE* **1905**, 129–139.
- Quammen, C. (2007) Clarity – a C++ open-source deconvolution software library. <http://cismm.cs.unc.edu/downloads/>.
- Richardson, W. (1972) Bayesian-based iterative method of image restoration. *J. Opt. Soc. Am.* **62**, 55–59.
- Sepp, M., Vendelin, M., Vija, H. & Birkedal, R. (2010) ADP compartmentation analysis reveals coupling between pyruvate kinase and ATPases in heart muscle. *Biophys. J.* **98**, 2785–2793.
- Shaw, P.J. (2006) Comparison of widefield/deconvolution and confocal microscopy for three-dimensional imaging. *Handbook of Biological Confocal Microscopy* (ed. by J.B. Pawley), 3 edn., pp. 453–467. Springer, New York.
- Shaw, P.J. & Rawlins, D.J. (1991a) The point-spread function of a confocal microscope: its measurement and use in deconvolution of 3-D data. *J. Microsc.* **163**, 151–165.
- Shaw, P.J. & Rawlins, D.J. (1991b) Three-dimensional fluorescence microscopy. *Prog. Biophys. Mol. Biol.* **56**, 187–213.
- Sun, Y., Davis, P., Kosmacek, E.A., Ianzini, F. & Mackey, M.A. (2009) An open-source deconvolution software package for 3-D quantitative fluorescence microscopy imaging. *J. Microsc.* **236**, 180–193.
- Valdimarsson, E. & Preza, C. (2007) Computational optical sectioning microscopy open source (COSMOS) software package. <http://cirl.memphis.edu/cosmos/>.
- van Kempen, G. & van Vliet, L.J. (2000) The influence of the regularization parameter and the first estimate on the performance of Tikhonov

- regularized non-linear image restoration algorithms. *J. Microsc.* **198**, 63–75.
- van Kempen, G., van Vliet, L., Verveer, P. & van der Voort, H. (1997) A quantitative comparison of image restoration methods for confocal microscopy. *J. Microsc.* **185**, 354–365.
- van Rossum, G. (1991) Python programming language. <http://www.python.org/>.
- Vendelin, M. & Birkedal, R. (2008) Anisotropic diffusion of fluorescently labeled ATP in rat cardiomyocytes determined by raster image correlation spectroscopy. *Am. J. Physiol. Cell Physiol.* **295**, C1302–C1315.

PUBLICATION II

Illaste A, **Laasma M**, Peterson P, and Vendelin M
**Analysis of molecular movement reveals latticelike obstructions to diffusion
in heart muscle cells**
Biophysical Journal, 102(4), 739–748, 2012

Analysis of Molecular Movement Reveals Latticelike Obstructions to Diffusion in Heart Muscle Cells

Ardo Illaste, Martin Laasmaa, Pearu Peterson, and Marko Vendelin*

Laboratory of Systems Biology, Institute of Cybernetics, Tallinn University of Technology, Tallinn, Estonia

ABSTRACT Intracellular diffusion in muscle cells is known to be restricted. Although characteristics and localization of these restrictions is yet to be elucidated, it has been established that ischemia-reperfusion injury reduces the overall diffusion restriction. Here we apply an extended version of raster image correlation spectroscopy to determine directional anisotropy and coefficients of diffusion in rat cardiomyocytes. Our experimental results indicate that diffusion of a smaller molecule (1127 MW fluorescently labeled ATTO633-ATP) is restricted more than that of a larger one (10,000 MW Alexa647-dextran), when comparing diffusion in cardiomyocytes to that in solution. We attempt to provide a resolution to this counterintuitive result by applying a quantitative stochastic model of diffusion. Modeling results suggest the presence of periodic intracellular barriers situated $\sim 1 \mu\text{m}$ apart having very low permeabilities and a small effect of molecular crowding in volumes between the barriers. Such intracellular structuring could restrict diffusion of molecules of energy metabolism, reactive oxygen species, and apoptotic signals, enacting a significant role in normally functioning cardiomyocytes as well as in pathological conditions of the heart.

INTRODUCTION

Of the different processes active in a functioning cell, there are not many that are unaffected by diffusion. The composition, geometry, and solvent properties of the intracellular environment determine the characteristics of diffusion for everything from the smallest signaling molecules to enzymes to DNA/RNA. Three restrictions for diffusion are generally considered: viscosity of the fluid phase, binding of the diffusing molecule to other molecules or structures, and molecular crowding that effectively reduces the volume available for diffusion (1). In heart and oxidative skeletal muscle cells diffusion of smaller molecules, such as ADP, has been found to be severely restricted when analyzing kinetics of respiration in permeabilized fibers or cells in respirometer (2,3), autofluorescence of single cells (4), sarcoplasmic reticulum Ca^{2+} ATPase (5), and response of ATP-sensitive K^+ channel (6). Diffusion restrictions estimated from mitochondrial respiration kinetics have partially been attributed to mitochondrial outer membrane (3,7,8).

In addition to outer membrane and submembrane diffusion restrictions (6), there are diffusion obstacles in cardiomyocytes that group ATPases and mitochondria (5). Those diffusion obstacles have been attributed to the regular arrangement of intracellular organelles such as mitochondria (9,10) leading to anisotropic diffusion in rat cardiomyocytes (11) as well as dependence of apparent diffusion coefficient (DC) on diffusion time in lobster muscle fibers (12). The

role of diffusion obstacles in heart regulation is not clear. However, it has been established that ischemia-reperfusion injury reduces the overall diffusion restriction regardless of whether ischemia is induced globally (13) or regionally (14), an effect that can be reduced by ischemic preconditioning (15). Such correlation between the state of the heart muscle and diffusion obstacles suggests that obstacles to diffusion play an important role in regulation of intracellular processes and could be a target of therapies in heart failure treatment.

So far, diffusion restrictions have been suggested from indirect measurements such as kinetics of mitochondrial respiration in permeabilized cells and fibers. Although for larger molecules, diffusion has been found to be significantly restricted (1,16–18), direct assessment of diffusion in muscle cells has not confirmed the existence of large diffusion restrictions for smaller molecules, for which intracellular DC was found to be $\sim 2\times$ smaller than in water (19). In experiments performed using ^{31}P -NMR, a small reduction of DC was observed for ATP and phosphocreatine (PCr) when compared to DC in solution at short diffusion distances. It was found, however, that the transverse DC was dependent on diffusion time (12,20). To reproduce ^{31}P -NMR data, it was suggested that the diffusion is mainly restricted by intracellular structures with overall cylindrical orientation (12,20), such as sarcoplasmic reticulum (12). Such intracellular diffusion obstacles were not identified in a recent ^{31}P -NMR study of the human calf muscle (21). Large influence of intracellular structures on diffusion of smaller molecules in cytoplasm has not been demonstrated using fluorescence-based methods either.

Recently, we extended raster image correlation spectroscopy (RICS) (22–24) to take into account possible anisotropy of diffusion and determined the diffusion coefficient for fluorescently labeled ATP (11). We found only a small

Submitted October 9, 2011, and accepted for publication January 13, 2012.

*Correspondence: markov@ioc.ee

This is an Open Access article distributed under the terms of the Creative Commons-Attribution Noncommercial License (<http://creativecommons.org/licenses/by-nc/2.0/>), which permits unrestricted noncommercial use, distribution, and reproduction in any medium, provided the original work is properly cited.

Editor: Michael Stern.

© 2012 by the Biophysical Society. Open access under [CC BY-NC-ND license](https://creativecommons.org/licenses/by-nc-nd/4.0/). 0006-3495/12/02/0739/10

doi: 10.1016/j.bpj.2012.01.012

reduction of the DC attributable to anisotropy. In that study, however, several limitations emanated from using a commercial confocal microscope. In particular, using an analog photomultiplier tube as a detector demands that long pixel acquisition times be used to avoid interference between pixels (23,11). As a result, only a small amount of pixels is acquired at relatively slow laser scanning speeds, limiting correlation analysis to pixels in the same image line.

In this article, we custom-built a confocal microscope that allowed us to significantly increase the precision of DC estimation. We determined DCs for two different molecules of different size and found that the diffusion of a larger molecule (Alexa647-dextran 10K) was hindered less than that of a smaller one (ATTO633-ATP). To explain such a counterintuitive result, we composed a mathematical model that mimics the diffusion pathway in the heart muscle cell and found parameters describing intracellular diffusion obstacles. Although our main results are discussed in this text, we provide extensive [Supporting Material](#) giving an introduction to the RICS method, which includes extended experimental and mathematical method descriptions and a section on statistical analysis of model parameter estimates.

MATERIALS AND METHODS

Experimental procedures

Adult outbred Wistar rats of both sexes weighing 300–500 g were used in the experiments. Animal procedures were approved by Estonian National Committee for Ethics in Animal Experimentation (Estonian Ministry of Agriculture). Cardiomyocytes (CMs) were isolated as described in Sepp et al. (3).

Solutions and chemicals

The following fluorescent dyes were used in this work: ATTO633-ATP (catalogue No. NU-808-633; Jena Bioscience, Jena, Germany), Alexa647-dextran 10K (catalogue No. D-22914; Invitrogen, Carlsbad, CA), ATTO655-COOH (catalogue No. AD655-21; ATTO-TEC, Siegen, Germany), and MitoTracker Green (catalogue No. M-7514; Invitrogen). Mitotracker Green was used in concentration of 0.25 μM . Dyes for which DCs were estimated were used in a concentration of 8 nM and 16 nM for ATTO633-ATP and Alexa647-dextran 10K, respectively. Solutions are described in detail in the [Supporting Material](#).

Determination of diffusion coefficients using RICS

To perform imaging for RICS, we designed and built a confocal microscope. This allowed us to automate image acquisition under varying laser scanning angles and frequencies. For analysis, triplet states and experimentally obtained point-spread function (PSF) were taken into account. See the [Supporting Material](#) for the mathematical and experimental details of RICS analysis and for the setup of the confocal microscope.

Statistics

Raw data were analyzed using homemade software. All results are shown as mean \pm SD.

Mathematical model

Stochastic diffusion simulations and data analysis were performed using custom-written Python and C++ code on a computational cluster (96 dual-core AMD Opteron 2216 CPUs). Diffusion in three dimensions was simulated to establish independence of DCs in x , y , and z directions. A faster one-dimensional model was then used for each spatial direction separately. Diffusion was simulated inside a $20 \mu\text{m} \times 20 \mu\text{m} \times 5 \mu\text{m}$ region for the three-dimensional model and a $20\text{-}\mu\text{m}$ region for the one-dimensional model. Possible intracellular structures in direction α (α represents any of the directions x , y , and z) were approximated with periodically placed barriers $d_\alpha \mu\text{m}$ apart, having permeabilities p_α (probability for a particle to traverse the wall after an interaction). Diffusion in direction α in the interbarrier space (IBS) was assumed to be reduced by a factor of $0 < \lambda_\alpha \leq 1$ compared to that in free intracellular solution. Reduction factors λ were considered to be different for ATTO633-ATP and Alexa647-dextran 10K and for distinct spatial directions.

At each timestep $\Delta t = 1 \mu\text{s}$, every simulated particle undertook a random displacement in all of the directions x , y , and z , drawn from a normal distribution $\mathcal{N}(0, \sqrt{2D_\alpha\Delta t})$, where D_α is the DC in direction α . Timestep value $1 \mu\text{s}$ was chosen to match pixel acquisition timestep in experiments so as to obtain similar images from the stochastic model. Also, a timestep of $1 \mu\text{s}$ ensured that diffusing particles would have a very low probability of diffusing out of the PSF during acquisition. This was estimated by using the relation of root mean-square displacement to time and diffusion coefficient of the dye in water. If a particle's trajectory intersected with a barrier, it had a probability p_α of passing that barrier and $1-p_\alpha$ of bouncing back elastically.

Concurrent to simulating diffusion, confocal microscope image acquisition with various scanning speeds and pixel sizes was simulated to obtain images for use in RICS analysis. For the three-dimensional model, we used analysis methods identical to those employed for analyzing experimental data. For the one-dimensional model, theoretical one-dimensional autocorrelation functions used in fitting were derived (see the [Supporting Material](#) for details). Obtained apparent DCs in direction α were functions of barrier parameters p_α , d_α , and λ_α values. Comparison of simulated and experimental results yielded sets of model parameters with which simulations for both molecules simultaneously matched experimental data. In subsequent analysis, permeability values were reinterpreted as η -pores of radius R per μm^2 of barrier surface. This interpretation required knowledge of radii of the diffusing molecules. These were estimated from DCs in salt solution using the Stokes-Einstein relationship, yielding 0.92 nm for the radius of ATTO633-ATP and 4.1 nm for Alexa647-dextran 10K.

RESULTS

RICS extensions

RICS was extended by using multiple scanning speeds and angles during imaging with the aim of altering the contribution of diffusional anisotropy in acquired images. For image acquisition, we used 19 angles uniformly spanning the range from 0 to 360° . Scanning resolution was altered in tandem with scanning axes rotation. This was all done in a random sequence to eliminate bias. As explained in the [Supporting Material](#), these additions were done to maximize the amount of data for fitting with theoretical correlation curves.

We tested the method by estimating DCs of ATTO633-ATP, Alexa647-dextran 10K, and ATTO655-COOH in water and measurement solution. The estimated DC for

ATTO655-COOH in water, $454 \pm 3 \mu\text{m}^2/\text{s}$ at 26°C , is in good agreement with published data: $426 \pm 8 \mu\text{m}^2/\text{s}$ at 25°C (25). Full results are given in Table 1. According to our results, small anisotropy of diffusion (<20%) is not resolvable with this method. Further technical details concerning our extension to RICS can be found in the Supporting Material.

Experimental results

To determine the intracellular DCs of ATTO633-ATP and Alexa647-dextran 10K, the dye has to be present inside the cell. For both our dyes, which are not able to permeate intact sarcolemma, we used a poking procedure demonstrated in Fig. 1, A–E. In short, we introduced small holes (of diameter $\sim 1 \mu\text{m}$) into the cell membrane with a glass pipette, leading to diffusion of the dye from the surrounding solution into the cell. These small holes were open throughout the experiment, resulting in constant exchange of solution with the intracellular environment. For Alexa647-dextran 10K, a higher concentration had to be used to get a sufficient signal for RICS analysis.

Representative correlation functions (CFs) estimated for ATTO633-ATP in the cell and the fit with two components are shown in Fig. 1, F–I. The two components represent a slower, bound form of the dye and the freely diffusing form. In case of one component, only the free form is present. See the Supporting Material on how the number of components modifies the form of the theoretical CF. Slower diffusion in the cell can be seen from the relatively high correlation (especially when comparing to CFs in

water; see the Supporting Material) between pixels in adjacent lines (*inset*, Fig. 1, F and G). A slight lack of fit observable in Fig. 1, F and G, is caused by the fact that the fit for only one of the 19 angles recorded in experiment is shown. The optimization process attempts to fit all angles simultaneously (Fig. 1, H and I), resulting in slight per-angle deviations.

Summary of the DCs determined by anisotropic models is presented in Table 1. Note that, when fitting ATTO633-ATP data using a single-component model, the triplet-state time constant increases to $>40 \mu\text{s}$ and has a large contribution to the CF (39%). Such triplet-state parameters in the fit can be explained by an additional diffusing component that is not accounted for in the single-component model. When a two-component model is used, more acceptable triplet-state parameters are obtained. In the two-component model, contribution of the very slow fraction (probably bound fraction) is $\sim 30\%$, with the rest attributed to freely moving ATTO633-ATP.

As can be seen from Table 1, the triplet-state time constant for Alexa647-dextran 10K in cells is not as large as obtained with a single-component model for ATTO633-ATP and the single-component fit is sufficient for Alexa647-dextran 10K data. Using saponin permeabilization in lieu of poking did not result in markedly different results from Table 1. DCs obtained with saponin permeabilization were $15 \pm 2 \mu\text{m}^2/\text{s}$ in the transverse and $19 \pm 1 \mu\text{m}^2/\text{s}$ in the longitudinal directions ($n = 7$).

On the basis of our analysis, we conclude that the DC of the freely moving fraction of ATTO633-ATP in CMs is $5.6\text{--}8.1\times$ reduced (depending on direction) compared to

TABLE 1 Diffusion constants (D_{TR} and D_L in transverse and longitudinal directions, respectively) obtained from raster image correlation spectroscopy at 26°C

Dye	Media	n	Cmp.	Diffusion			Triplet	
				Concentration	D_{TR}	D_L	T	τ
				nM	$\mu\text{m}^2/\text{s}$	$\mu\text{m}^2/\text{s}$	Relative	μs
ATTO655-COOH	Water	4		21 ± 2	454 ± 3		0.08 ± 0.01	3.3 ± 0.1
	Water	4		21 ± 2	442 ± 4	483 ± 7	0.08 ± 0.01	3.1 ± 0.1
	Solution	4		22 ± 4	362 ± 4		0.10 ± 0.01	4.3 ± 0.7
	Solution	4		22 ± 4	348 ± 2	403 ± 10	0.09 ± 0.01	3.8 ± 0.7
ATTO633-ATP	Water	4		16 ± 4	326 ± 13		0.10 ± 0.01	4.3 ± 0.1
	Water	4		16 ± 4	322 ± 15	337 ± 12	0.10 ± 0.01	4.2 ± 0.1
	Solution	4		21 ± 4	195 ± 8		0.14 ± 0.01	5.6 ± 0.3
	Solution	4		21 ± 4	183 ± 11	222 ± 3	0.14 ± 0.01	5.5 ± 0.3
	CM	5		86 ± 12	4.0 ± 0.6	4.6 ± 0.9	0.39 ± 0.10	45 ± 5
	CM	5	1	19 ± 4	0.7 ± 0.3	0.8 ± 0.2	0.23 ± 0.04	5.2 ± 2.5
Alexa647-dextran 10K	Water	4		41 ± 10	24 ± 6	35 ± 8		
	Water	4		12 ± 3	62 ± 1		0.23 ± 0.01	3.8 ± 0.7
	Water	4		12 ± 3	60 ± 2	65 ± 2	0.23 ± 0.01	3.8 ± 0.7
	Solution	4		12 ± 2	53 ± 1		0.23 ± 0.00	4.0 ± 0.2
	Solution	4		12 ± 2	51 ± 2	57 ± 1	0.23 ± 0.00	4.0 ± 0.2
	CM	7		13 ± 3	16 ± 2	19 ± 3	0.34 ± 0.02	6.6 ± 1.1

Listed values were obtained in water, measurement solution (solution), or CMs. On the basis of n experiments, several parameters were determined in addition to diffusion coefficient(s): concentration, triplet time constant τ , and triplet-state contribution T . Correlations between fluctuation of fluorescence signal were fitted by isotropic model (diffusion coefficient specified only as D_{TR}), anisotropic model (D_{TR} and D_L specified), or model with two components (Cmp).

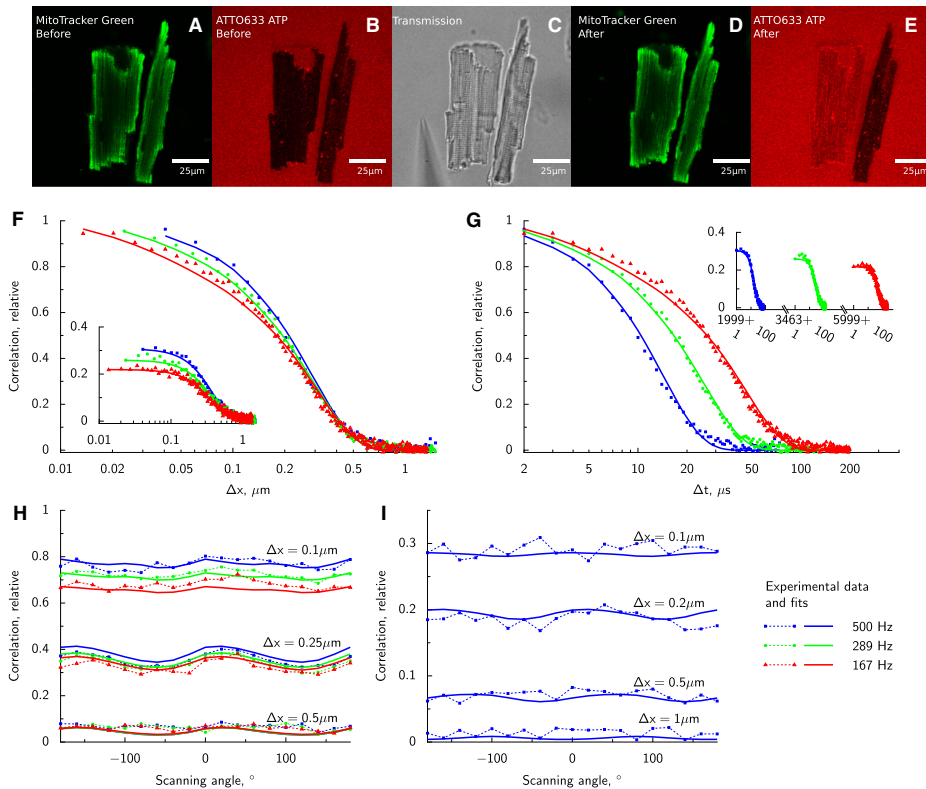


FIGURE 1 Diffusion of ATTO633-ATP in rat CM analyzed by RICS. In the beginning of the experiment, intact rat CMs labeled with Mitotracker Green are positioned into solution containing ATTO633-ATP (confocal images, *A* and *B*). Because cells are intact, ATTO633-ATP does not penetrate sarcolemma and fluorescence is recorded in solution surrounding the cells as well as T-tubules (*B*). Holes are introduced into sarcolemma by poking one of the cells with a glass pipette (*transmission image* of approaching pipette in *C*). As a result, ATTO633-ATP is able to diffuse into the cell (*E*) while the structure of the cell is intact (*D*). RICS analysis is presented in *F–I*. Experimental data (*points*) acquired at different laser scanning frequencies and directions are fitted by a model (*lines*). Spatial and temporal components of the correlation function are shown in panels *F* and *G*, respectively. On panels *F* and *G*, imaging was performed with the laser scanning along a line parallel to axis *x* at different frequencies (*frequencies* noted in *legend* on the *right bottom*). Correlation along the same line (*main graphs* of *F* and *G*); correlation of the signal between pixels in adjacent lines (*insets*). Due to the laser backtracking and variation in scan frequencies, temporal component has gaps visible (*inset* of panel *G*). Due to asymmetry of PSF, laser scanning in different directions leads to modification of correlation function between pixels in the same line (*H*) and in the adjacent lines (*I* and *insets* of *F* and *G*).

the coefficient in the measurement solution. For Alexa647-dextran 10K, reduction of the DC was considerably smaller: 2.8–3.5 times. Thus, our experimental results indicate that the diffusion of a smaller molecule is restricted more in the intracellular environment than the larger molecule.

Analysis by stochastic model

To find an explanation for our counterintuitive experimental results, we turned to computational modeling. Diffusion of ATTO633-ATP and Alexa647-dextran 10K was simulated in three dimensions with periodically placed permeable barriers in *x*, *y*, and *z* directions using a stochastic computational model (Fig. 2 *A*). This geometry

was chosen as the simplest and least computationally intensive approximation to intracellular diffusion restrictions. Concurrently with the processes of molecule diffusion and interaction with barriers, confocal microscope data acquisition was simulated and images similar to those in physical experiments were obtained. Apparent diffusion coefficients in the three dimensions were calculated from simulated results by applying numerical methods identical to those employed on experimental data. Our goal was to determine barrier parameters with which DC values obtained from the model coincide with those from experiments.

The apparent DC estimated by RICS is a macroscopic variable comprised of two components—diffusion in

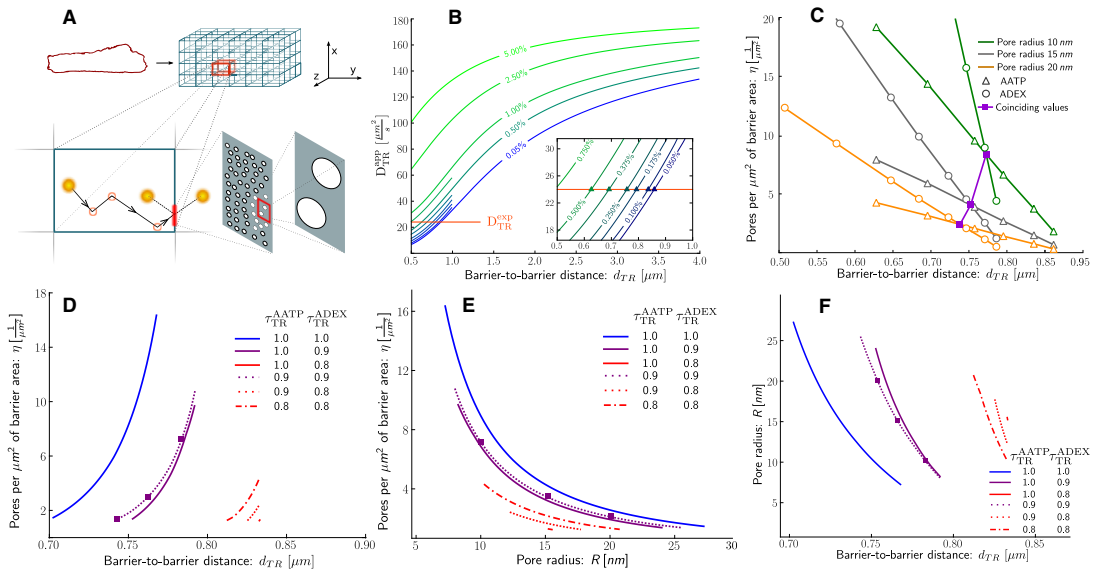


FIGURE 2 Analysis of diffusion in the cell using the stochastic model. (A) Scheme of the computational model. Intracellular structure of the cell (*top left*) is approximated by a three-dimensional lattice of barriers that hinder molecule diffusion (*top right*). Barriers are placed, depending on direction α , d_α μm apart and have permeabilities p_α . Diffusion coefficient in the space between barriers is reduced by a factor λ compared to solution ($0 < \lambda \leq 1$). Stochastically diffusing molecules interact with barriers and have a probability p_α of passing through (*bottom left*). Permeable barriers correspond to porous walls with η -pores of radius R per μm^2 of barrier area (*bottom right*). Apparent diffusion coefficients are estimated over the entire lattice. (B) Apparent diffusion constant values for ATTO633-ATP are obtained from simulations with varying barrier distances (*horizontal axis*) and permeabilities (indicated by values on curves). (*Horizontal solid line*) ATTO633-ATP diffusion coefficient estimated from experiment (D_{TR}^{exp}). (*Inset*) Region $0.5 \dots 1 \mu\text{m}$, where curves intersect with experimental data. (*Triangles*) Intersection points. (C) Points of intersection from panel B with permeability converted to pores per μm^2 for different pore radius values (10, 15, and 20 nm). Intersections of ATTO633-ATP (*open triangles*) and Alexa647-dextran 10K (*open circles*) curves of identical pore radius values signify points where model and experiment coincide for both molecules simultaneously (*solid squares*). Intersections are curves in three-dimensional space (barrier-to-barrier distance versus pore radius versus pores per μm^2). (D) View of intersection curves from panel C in barrier-to-barrier distance and pores per μm^2 axes. (*Lines*) Different λ_{TR}^{AATP} and λ_{TR}^{ADEX} values. (*Squares*) Example intersection points from panel C. (E) Same as panel D, but for pore radius and pores per μm^2 values. (F) Same as panel D, but for barrier-to-barrier distance and pore radius values. AATP and ADEX represent ATTO633-ATP and Alexa647-dextran 10K, respectively.

interbarrier space (IBS) and restrictions from barriers. We assume the x and z axis (both represented by the transverse TR direction) to have identical diffusion restrictions and, consequently, identical barrier parameters. The y axis corresponds to the longitudinal L direction and can have barrier parameters different from the transverse direction.

Barriers in spatial direction α (α is TR or L) are described by two parameters—their permeability (p_α) and barrier-to-barrier distance (d_α). DC in IBS is reduced compared to solution, $D_{IBS} = \lambda_\alpha \cdot D_{sol}$, where the reduction factor λ_α depends on the direction α and the diffusing molecule. In our simulations, we scan IBS diffusion reduction factors in the whole range $0 \dots 1$ for all directions and molecules.

We estimated apparent DC values (D_α^{app}) for various barrier distances, permeabilities, and IBS diffusion reduction factors. From calculations performed with the three-dimensional model, we determined that diffusion in any spatial direction is dependent on barrier parameters in that direction only and is not affected by the existence or prop-

erties of barriers in any orthogonal direction. This allowed us to derive and use a computationally faster one-dimensional RICS model to study diffusion in the transverse and longitudinal directions separately.

Results for simulations performed with $\lambda_{TR}^{AATP} = 0.9$ are shown in Fig. 2 B. Points where computational results intersect with the experimentally obtained D_{TR}^{exp} values give us a combination of barrier parameters in the transverse direction at which the stochastic model is able to reproduce experimental results. Surprisingly, for the model to match experimentally obtained D_{TR}^{app} values, very small permeabilities ($p < 0.1\%$) and closely spaced barriers ($d < 1 \mu\text{m}$) are necessary.

We performed analogous numerical experiments and analysis for Alexa647-dextran 10K with the intention of finding parameters where simulation results for both ATTO633-ATP and Alexa647-dextran 10K simultaneously match experimental data, and relating these values to physical barrier characteristics. Permeability values obtained for

ATTO633-ATP and Alexa647-dextran 10K are not directly comparable. They can, however, be related to the radius of the diffusing molecule (r), the radii of permeable pores in the barriers (R), and the number of pores per μm^2 (η) by: $p = \pi\eta(R-r)^2$ (see the Supporting Material for derivation).

Fixing a particular R value for the pore radius, we can convert p values to η and compare barrier characteristics obtained for ATTO633-ATP and Alexa647-dextran 10K (Fig. 2 C). Intersections between ATTO633-ATP and Alexa647-dextran 10K curves now indicate physical parameter values where computational and experimental constraints are satisfied for both molecules simultaneously. By varying R values we get a range of suitable parameters for a combination of λ^{ATP} and λ^{DEX} in both transverse and longitudinal directions. Some combinations of λ^{ATP} and λ^{DEX} do not result in intersections, and are therefore discarded as unsuitable. In addition, we assumed that $\lambda^{ATP} \geq \lambda^{DEX}$, as diffusion of larger molecules is restricted more by molecular crowding than the small ones (18).

The relationship between R - and η -values in the transverse direction is shown on Fig. 2, D–F, for λ_{TR}^{ATP} , λ_{TR}^{DEX} values where intersections occur. Summary of parameters satisfying all constraints is shown in Table 2. Error estimates for the table entries were obtained from Monte Carlo simulations detailed in the Supporting Material. Data in the table represent the mean \pm SDs obtained from Monte Carlo simulations. A number of parameter estimates do not follow a normal distribution. For those, the mean \pm SDs do not illustrate the actual distribution well and the histograms given in the Supporting Material should be consulted instead. For the DC reduction ratio, the maximum estimate for which no error is given as the result was always 100% of the DC in solution for both ATTO633-ATP and Alexa647-dextran 10K.

DISCUSSION

The major experimental finding of this study is that the diffusion of the freely moving fraction of a smaller molecule (ATTO633-ATP) is hindered considerably more by intracellular diffusion obstacles than the diffusion of a larger

molecule (Alexa647-dextran 10K). In general, fractional reduction of the diffusion coefficient is expected to be larger for larger molecules (18). To explain our counterintuitive result, we assumed that diffusion obstacles are formed by permeable barriers arranged in a three-dimensional lattice. The major finding from numerical simulations performed with this assumption is that such diffusion barriers can reproduce the overall DCs of ATTO633-ATP and Alexa647-dextran 10K estimated from experiments conducted on rat CMs. According to our simulations, the diffusion barriers are $\leq 1 \mu\text{m}$ apart with relatively few small openings ($\sim 1 \dots 30$ openings per μm^2 of radius $7 \dots 30 \text{ nm}$).

Intracellular structures acting as diffusion obstacles

Barrier parameters obtained from our computational model imply that only $\sim 0.3\%$ of barrier surface is covered with pores. Intuitively, this would appear a prohibitively small percentage for diffusion to be able to have a significant role in cellular metabolism. However, it can be shown that if there are $(4R \cdot d)^{-1}$ pores of radius R per unit area in a barrier that is at distance d from neighboring barriers, then the diffusion current through the barrier is half of what it would be if there was no barrier at all (26). Substituting our parameters, this means that just $\sim 1.2\%$ of the barrier would need to be penetrable to obtain half-maximal diffusion current.

The distances found between barriers are consistent with the morphology of rat CMs (Fig. 3). The predicted distance between barriers ($\sim 0.8 \mu\text{m}$) is in agreement with the reported transverse distance between T-tubules (27–30). In transversal direction, the distance between centers of adjacent mitochondria is $\sim 1.8 \mu\text{m}$ (9), indicating that there are two barriers at this distance. In longitudinal direction, two possible distances between adjacent mitochondria have been found ($\sim 1 \mu\text{m}$ and $\sim 1.8 \mu\text{m}$) due to the difficulty of distinguishing whether there is one or two mitochondria per sarcomere (9). It is possible to make this distinction, however, from following reactive oxygen species (ROS)-induced depolarization of mitochondria. Although ROS-induced mitochondrial depolarization typically occurs synchronously for mitochondria within the same sarcomere (31), depolarization of a single mitochondrion with half-sarcomere length can occasionally be observed (32). This suggests that there is a pair of mitochondria per sarcomere with $\sim 1 \mu\text{m}$ between the centers, similarly to the distance between barriers predicted for longitudinal direction in this work. Thus, distances between diffusion barriers are consistent with the internal periodicity of rat CM morphology.

It is not clear, however, which structures can cause such obstacles to diffusion. It has been shown that internal membranes can have an effect on intracellular diffusion

TABLE 2 Diffusion obstacles predicted by stochastic model on the basis of RICS measurements

Barrier	Direction			
	Transverse $TR(x,z)$		Longitudinal $L(y)$	
	Min	Max	Min	Max
Distance $d[\mu\text{m}]$	0.68 ± 0.10	0.87 ± 0.07	0.73 ± 0.13	1.02 ± 0.10
Pore radius $R[\text{nm}]$	7.4 ± 2.1	30 ± 8	6.7 ± 1.8	38 ± 10
Pore density $\eta[1/\mu\text{m}^2]$	1.2 ± 0.1	29 ± 23	1.1 ± 0.1	48 ± 37
λ_{α}^{ATP}	0.78 ± 0.13	1.0	0.78 ± 0.13	1.0
λ_{α}^{DEX}	0.77 ± 0.14	1.0	0.77 ± 0.14	1.0

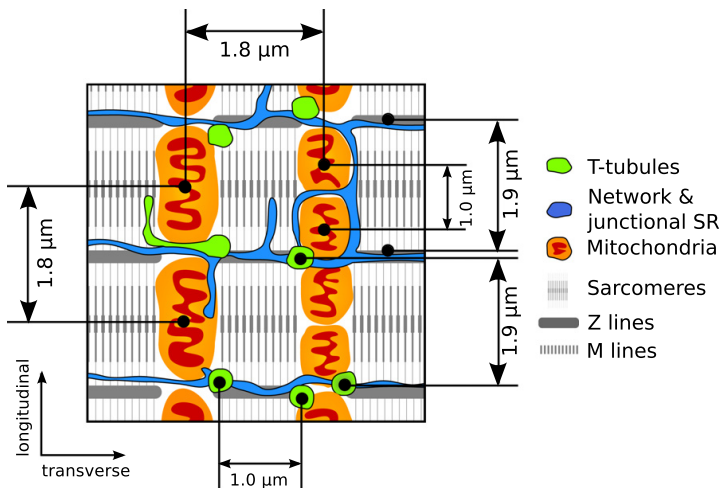


FIGURE 3 Internal structure of the cardiac muscle cell. A regular arrangement of intracellular structures and organelles is present (30,55,34). Mitochondria are separated 1.8 μm in the transverse direction and 1.0 or 1.8 μm (depending on whether there are one or two mitochondria per sarcomere) in the longitudinal direction (9). Sarcomere Z lines are separated by 1.9 μm in the longitudinal direction identically with T-tubules, whereas in the transverse direction T-tubules are 1.0 μm apart on average (27–29).

(33). This raises the possibility that, in restricting diffusion, a role is played by sarcoplasmic reticulum (SR) (that can form planular cisternae (30) and invaginate the space between sarcomeres (34)), or the T-tubular system. Both of these are found with periodicity (Fig. 3) similar to that determined by us. As we found very dense placement of diffusion barriers, we suggest that intracellular proteins in the heart cells could be associated with SR and other inner membrane structures leading to such profound diffusion obstacles. Additionally, enzymes can be associated with M and Z lines of sarcomeres (35,36). This suggestion is in line with our previous analysis of permeabilized fiber measurements using a three-dimensional mathematical model that predicted very small permeability for restrictions imposed by the SR (8).

Model geometry

The model geometry used by us is not the only one able to explain our experimental data. Other more complex geometries can be conceived and modeled. For example, a geometry with volumes accessible only to the smaller molecule could result in the apparent DC reducing more than the DC of a molecule that cannot access these volumes, leading to the same paradoxical smaller relative decrease in DC of a larger molecule. Our choice was motivated by the relative simplicity of the geometry employed and, stemming from this, relatively fast computation times. However, already for this basic model, calculations on our cluster of 96 dual-core machines took several months. More complex geometries would increase this time manifold. We consider our result not to be the definitive indication of wall-like porous barriers in cardiomyocytes, but a useful approximation presenting new questions to be investigated.

Diffusion between barriers

According to Shorten and Sneyd (37), the reduction factors of diffusion (λ -s) of the ATTO633-ATP-sized molecule in sarcomeres are 0.6 and 0.8 in the transverse and longitudinal directions, respectively. We consider IBS to contain sarcomeres, mitochondria, and free cytosolic space (up to 11% (38)) and, based on this, expect hindrance to diffusion in IBS to be less than or equal to that in sarcomeres. As in our study, viscosity in mitochondria has been found to be moderate when intramitochondrial structure with internal membranes is taken into account (39). Our results suggest moderate crowding in IBS, leading to a small influence of crowding on kinetics of reactions in the cell. Additionally, our results are in agreement with the small (5–15%) reduction of DC of unbound PCr and ATP in rat skeletal muscle compared to the value in solution, determined by ^{31}P -NMR diffusion spectroscopy (20).

Overall diffusion coefficient

The overall reduction of DC found in this work was larger than the DC reduction determined in Kushmerick and Podolsky (19). The reasons for the differences in results could be related to our use of larger molecules or the morphological differences between rat CMs and frog skeletal muscle. Reduction of ATTO633-ATP DC was considerably larger than the one we previously found for Alexa647-ATP (11). This is probably due to the use of dedicated confocal setup in this work, leading to a more accurate determination of CFs used in analysis.

In this article, we were able to use dedicated hardware. This allowed us to obtain data at a faster time resolution—making it possible to fit several lines of the CF, compared to just one line as it was done in Vendelin and

Birkedal (11). Additionally, the faster scan speeds that we can now obtain increase the amount of data that can be fitted. We have also included triplet states in the CF analysis, which were missing earlier. Furthermore, in our earlier study, saponin was kept in the solution throughout the experiment. We speculate that all these aspects contribute to the smaller reduction in DC obtained in Vendelin and Birkedal (11).

Although diffusion of ATP or PCr has been found to be anisotropic in skeletal muscle (20,12), diffusion of larger molecules has been found to be isotropic in rat CMs (16). Here, diffusion was found to be moderately anisotropic for both studied molecules. As a result, distances and permeabilities of diffusion barriers varied for different directions.

We found that ATTO633-ATP has two components when diffusing in the cell—a bound form and a freely diffusing form. This partitioning is indicated by a large triplet-state time constant when using only one component in the fit (Table 1). For Alexa647-dextran 10K only a single, freely diffusing component was necessary. Adding a second component resulted in the slow component having a small contribution to overall signal (~5% from total concentration, results not shown). Thus, although properties of the used dyes are different, to remove possible bias we compared only freely diffusing components in our analysis.

Technique used

In our analysis we fitted CFs found by RICS using a one- or two-component model, taking into account triplet states of the molecule. During measurements, we varied scanning speed and direction to determine how correlation relates to temporal and spatial components. With this approach, anisotropy of diffusion can be assessed and two DCs can be determined. However, there are several aspects that make the application of our technique nontrivial. For smaller molecules with fast diffusion rates, photon-counting detectors are required to increase the number of acquired data points used in fitting. When studying anisotropic diffusion, measurements have to be performed at different scanning angles. Due to the variation of scanning speeds and angles, measurements take a long time, with typical experiments lasting for 2–3 h.

Our measurements were performed on a dedicated microscope with a custom-built confocal detection unit that allowed us to automate measurements, to randomize scanning speed and angle sequences to avoid bias, and to track movements of the cell to acquire images in the same region. The main advantage of having a custom-built confocal arises from the ability to program it ourselves. Although some commercial confocal software allows the writing of macros, the extendibility of such solutions is limited. Although there are several solutions that allow automating aspects of image acquisition on commercial confocal microscopes, we are not aware of any solution

that allows the level of control we require. Furthermore, RICS analysis benefits greatly from having a photon counter instead of an analog detector (11,23). However, we expect that for studying diffusion of larger molecules, commercial microscopes with analog detectors can be adequate and would also allow us to determine DCs in an anisotropic case.

When analyzing the CFs found in RICS measurements, we used the actual PSF of the optical system (40), rather than approximate analytical functions, as PSF asymmetry was found to influence CF's dependence on scanning direction. In calculations of RICS analysis, knowledge of correlation of fluctuations in concentration is required. This information is conveyed by the so-called propagator, which determines the form of the diffusional correlation term G_D given in Eq. S2 in the Supporting Material. The propagator is a function that makes it possible to determine the probability of finding a diffusing particle at a distance from the starting position after a given time period. Although the propagator for the case pertinent to this work is described by simple analytical functions, it may not always be applicable. For example, when employing anomalous diffusion, one has to find solutions for the fractional Fokker-Planck equation or apply numerical approximations (41) to find the propagator. This may be an important limitation that has to be considered when applying our approach.

Physiological implications

Our results suggest small distances between intracellular barriers to diffusion and a limited amount of holes in them in rat CMs. Such partitioning of the cell may have important physiological and pathophysiological implications. Energy transfer can be influenced if the localization of the barriers is such that ATP-consuming and ATP-producing parts of the cell are separated. Such separation would indicate a prominent role for energy transfer systems, such as the creatine kinase shuttle. Because diffusion restrictions are expected to decrease after ischemia (13,14), such positioning of barriers could lead to a change in the role of the energy transfer system in pathologies. Whether it is consistent with modulation of energy transfer depending on the workload, as shown in the analysis of ^{31}P -NMR inversion and saturation transfer experiments (42), is not clear and requires further studies.

Alternatively, barriers could group ATP-producing and ATP-consuming parts of the cell together, as suggested by coupling between ATPases and mitochondrial respiration (3,5). In this case, barriers would influence synchronization between different parts of the cell and would restrict local ATP production to local consumption. Prominent diffusion obstacles separating the cell into smaller segments are also consistent with formation of clusters during mitochondrial oscillations (43,44) and may play an important role in pathologies by restricting diffusion of ROS, apoptosis signals, and Ca^{2+} waves (45).

SUPPORTING MATERIAL

A brief overview of the RICS method and our extensions to it; description of experimental methods, including confocal microscope setup; description of the analysis of RICS images and demonstration by analysis of diffusion of molecules in water and measurement solution; description of stochastic computational model together with derivations used to relate barrier permeability to physical parameters of the barrier and molecule size; statistical analysis of model parameters estimation; and references (46–54) are available at [http://www.biophysj.org/biophysj/supplemental/S0006-3495\(12\)00085-9](http://www.biophysj.org/biophysj/supplemental/S0006-3495(12)00085-9).

We thank Mervi Sepp and Natalja Jepihina for providing cardiomyocytes, Merle Mandel for technical assistance, and Rikke Birkedal, Hena R. Ramay, Päivo Simson (all from the Laboratory of Systems Biology, Institute of Cybernetics, Tallinn University of Technology, Estonia), and Peeter Illaste for discussions.

This work was supported by the Wellcome Trust (fellowship No. WT081755) and the Estonian Science Foundation (grants No. 7344 and 8041, PhD stipends for A.I. and M.L., respectively).

REFERENCES

- Verkman, A. S. 2002. Solute and macromolecule diffusion in cellular aqueous compartments. *Trends Biochem. Sci.* 27:27–33.
- Kümmel, L. 1988. Ca, Mg-ATPase activity of permeabilized rat heart cells and its functional coupling to oxidative phosphorylation of the cells. *Cardiovasc. Res.* 22:359–367.
- Sepp, M., M. Vendelin, ..., R. Birkedal. 2010. ADP compartmentation analysis reveals coupling between pyruvate kinase and ATPases in heart muscle. *Biophys. J.* 98:2785–2793.
- Jepihina, N., N. Beraud, ..., M. Vendelin. 2011. Permeabilized rat cardiomyocyte response demonstrates intracellular origin of diffusion obstacles. *Biophys. J.* 101:2112–2121.
- Kaasik, A., V. Veksler, ..., R. Ventura-Clapier. 2001. Energetic cross-talk between organelles: architectural integration of energy production and utilization. *Circ. Res.* 89:153–159.
- Abraham, M. R., V. A. Selivanov, ..., A. Terzic. 2002. Coupling of cell energetics with membrane metabolic sensing. Integrative signaling through creatine kinase phosphotransfer disrupted by M-CK gene knock-out. *J. Biol. Chem.* 277:24427–24434.
- Rostovtseva, T. K., K. L. Sheldon, ..., D. L. Sackett. 2008. Tubulin binding blocks mitochondrial voltage-dependent anion channel and regulates respiration. *Proc. Natl. Acad. Sci. USA.* 105:18746–18751.
- Ramay, H. R., and M. Vendelin. 2009. Diffusion restrictions surrounding mitochondria: a mathematical model of heart muscle fibers. *Biophys. J.* 97:443–452.
- Birkedal, R., H. A. Shiels, and M. Vendelin. 2006. Three-dimensional mitochondrial arrangement in ventricular myocytes: from chaos to order. *Am. J. Physiol. Cell Physiol.* 291:C1148–C1158.
- Vendelin, M., N. Béraud, ..., V. A. Saks. 2005. Mitochondrial regular arrangement in muscle cells: a “crystal-like” pattern. *Am. J. Physiol. Cell Physiol.* 288:C757–C767.
- Vendelin, M., and R. Birkedal. 2008. Anisotropic diffusion of fluorescently labeled ATP in rat cardiomyocytes determined by raster image correlation spectroscopy. *Am. J. Physiol. Cell Physiol.* 295:C1302–C1315.
- Kinsey, S. T., and T. S. Moerland. 2002. Metabolite diffusion in giant muscle fibers of the spiny lobster *Panulirus argus*. *J. Exp. Biol.* 205:3377–3386.
- Kay, L., V. A. Saks, and A. Rossi. 1997. Early alteration of the control of mitochondrial function in myocardial ischemia. *J. Mol. Cell. Cardiol.* 29:3399–3411.
- Boudina, S., M. N. Laclau, ..., P. Dos Santos. 2002. Alteration of mitochondrial function in a model of chronic ischemia in vivo in rat heart. *Am. J. Physiol. Heart Circ. Physiol.* 282:H821–H831.
- Laclau, M. N., S. Boudina, ..., P. Dos Santos. 2001. Cardioprotection by ischemic preconditioning preserves mitochondrial function and functional coupling between adenine nucleotide translocase and creatine kinase. *J. Mol. Cell. Cardiol.* 33:947–956.
- Papadopoulos, S., V. Endeward, ..., G. Gros. 2001. Radial and longitudinal diffusion of myoglobin in single living heart and skeletal muscle cells. *Proc. Natl. Acad. Sci. USA.* 98:5904–5909.
- Papadopoulos, S., K. D. Jürgens, and G. Gros. 2000. Protein diffusion in living skeletal muscle fibers: dependence on protein size, fiber type, and contraction. *Biophys. J.* 79:2084–2094.
- Muramatsu, N., and A. P. Minton. 1988. Tracer diffusion of globular proteins in concentrated protein solutions. *Proc. Natl. Acad. Sci. USA.* 85:2984–2988.
- Kushmerick, M. J., and R. J. Podolsky. 1969. Ionic mobility in muscle cells. *Science.* 166:1297–1298.
- de Graaf, R. A., A. van Kranenburg, and K. Nicolay. 2000. In vivo ³¹P-NMR diffusion spectroscopy of ATP and phosphocreatine in rat skeletal muscle. *Biophys. J.* 78:1657–1664.
- Gabr, R. E., A. M. El-Sharkawy, ..., P. A. Bottomley. 2011. High-energy phosphate transfer in human muscle: diffusion of phosphocreatine. *Am. J. Physiol. Cell Physiol.* 301:C234–C241.
- Digman, M. A., C. M. Brown, ..., E. Gratton. 2005. Measuring fast dynamics in solutions and cells with a laser scanning microscope. *Biophys. J.* 89:1317–1327.
- Brown, C. M., R. B. Dalal, ..., E. Gratton. 2008. Raster image correlation spectroscopy (RICS) for measuring fast protein dynamics and concentrations with a commercial laser scanning confocal microscope. *J. Microsc.* 229:78–91.
- Rossow, M. J., J. M. Sasaki, ..., E. Gratton. 2010. Raster image correlation spectroscopy in live cells. *Nat. Protoc.* 5:1761–1774.
- Müller, C. B., A. Loman, ..., J. Enderlein. 2008. Precise measurement of diffusion by multi-color dual-focus fluorescence correlation spectroscopy. *Europhys. Lett.* 83:46001.
- Berg, H. 1993. *Random Walks in Biology*. Princeton University Press, Princeton, NJ.
- Chen-Izu, Y., S. L. McCulle, ..., L. T. Izu. 2006. Three-dimensional distribution of ryanodine receptor clusters in cardiac myocytes. *Biophys. J.* 91:1–13.
- Salnikov, V., Y. O. Lukyanenko, ..., V. Lukyanenko. 2009. Distribution of ryanodine receptors in rat ventricular myocytes. *J. Muscle Res. Cell Motil.* 30:161–170.
- Soeller, C., and M. B. Cannell. 1999. Examination of the transverse tubular system in living cardiac rat myocytes by 2-photon microscopy and digital image-processing techniques. *Circ. Res.* 84:266–275.
- Hayashi, T., M. E. Martone, ..., M. Hoshijima. 2009. Three-dimensional electron microscopy reveals new details of membrane systems for Ca²⁺ signaling in the heart. *J. Cell Sci.* 122:1005–1013.
- Zorov, D. B., C. R. Filburn, ..., S. J. Sollott. 2000. Reactive oxygen species (ROS)-induced ROS release: a new phenomenon accompanying induction of the mitochondrial permeability transition in cardiac myocytes. *J. Exp. Med.* 192:1001–1014.
- Juhászova, M., D. B. Zorov, ..., S. J. Sollott. 2004. Glycogen synthase kinase-3β mediates convergence of protection signaling to inhibit the mitochondrial permeability transition pore. *J. Clin. Invest.* 113:1535–1549.
- Novak, I. L., P. Kraikivski, and B. M. Slepchenko. 2009. Diffusion in cytoplasm: effects of excluded volume due to internal membranes and cytoskeletal structures. *Biophys. J.* 97:758–767.
- Muir, A. R. 1967. The effects of divalent cations on the ultrastructure of the perfused rat heart. *J. Anat.* 101:239–261.
- Wegmann, G., E. Zanolla, ..., T. Wallimann. 1992. In situ compartmentation of creatine kinase in intact sarcomeric muscle: the acto-myosin

- overlap zone as a molecular sieve. *J. Muscle Res. Cell Motil.* 13: 420–435.
36. Sullivan, D. T., R. MacIntyre, ..., L. Ramizel. 2003. Analysis of glycolytic enzyme co-localization in *Drosophila* flight muscle. *J. Exp. Biol.* 206:2031–2038.
 37. Shorten, P. R., and J. Sneyd. 2009. A mathematical analysis of obstructed diffusion within skeletal muscle. *Biophys. J.* 96:4764–4778.
 38. Page, E. 1978. Quantitative ultrastructural analysis in cardiac membrane physiology. *Am. J. Physiol.* 235:C147–C158.
 39. Dieteren, C. E. J., S. C. A. M. Gielen, ..., W. J. Koopman. 2011. Solute diffusion is hindered in the mitochondrial matrix. *Proc. Natl. Acad. Sci. USA.* 108:8657–8662.
 40. Laasmaa, M., M. Vendelin, and P. Peterson. 2011. Application of regularized Richardson-Lucy algorithm for deconvolution of confocal microscopy images. *J. Microsc.* 243:124–140.
 41. Weiss, M., M. Elsner, ..., T. Nilsson. 2004. Anomalous subdiffusion is a measure for cytoplasmic crowding in living cells. *Biophys. J.* 87: 3518–3524.
 42. Vendelin, M., J. A. Hoerter, ..., J. L. Mazet. 2010. Modulation of energy transfer pathways between mitochondria and myofibrils by changes in performance of perfused heart. *J. Biol. Chem.* 285:37240–37250.
 43. Romashko, D. N., E. Marban, and B. O'Rourke. 1998. Subcellular metabolic transients and mitochondrial redox waves in heart cells. *Proc. Natl. Acad. Sci. USA.* 95:1618–1623.
 44. Kurz, F. T., M. A. Aon, ..., A. A. Armondas. 2010. Spatio-temporal oscillations of individual mitochondria in cardiac myocytes reveal modulation of synchronized mitochondrial clusters. *Proc. Natl. Acad. Sci. USA.* 107:14315–14320.
 45. Venetucci, L. A., A. W. Trafford, ..., D. A. Eisner. 2008. The sarcoplasmic reticulum and arrhythmogenic calcium release. *Cardiovasc. Res.* 77:285–292.
 46. Elson, E. L. 2011. Fluorescence correlation spectroscopy: past, present, future. *Biophys. J.* 101:2855–2870.
 47. Hausteiner, E., and P. Schwille. 2007. Fluorescence correlation spectroscopy: novel variations of an established technique. *Annu. Rev. Biophys. Biomol. Struct.* 36:151–169.
 48. Lakowicz, J. 2006. Principles of Fluorescence Spectroscopy. Springer, New York.
 49. Thompson, N. 2002. Fluorescence correlation spectroscopy. In Topics in Fluorescence Spectroscopy, Vol. 1. J. Lakowicz, C. D. Geddes, and J. R. Lakowicz, editors. Springer, New York. 337–378.
 50. Gröner, N., J. Capoulade, ..., M. Wachsmuth. 2010. Measuring and imaging diffusion with multiple scan speed image correlation spectroscopy. *Opt. Express.* 18:21225–21237.
 51. Krichevsky, O., and G. Bonnet. 2002. Fluorescence correlation spectroscopy: the technique and its applications. *Rep. Prog. Phys.* 65:251.
 52. Widengren, J., U. Mets, and R. Rigler. 1995. Fluorescence correlation spectroscopy of triplet states in solution: a theoretical and experimental study. *J. Phys. Chem.* 99:13368–13379.
 53. Moré, J. J., D. C. Sorensen, ..., B. S. Garbow. 1984. The MINPACK Project. In Sources and Development of Mathematical Software. W. J. Cowell, editor. Prentice-Hall, Englewood Cliffs, NJ. 88–111.
 54. Dertinger, T., V. Pacheco, ..., J. Enderlein. 2007. Two-focus fluorescence correlation spectroscopy: a new tool for accurate and absolute diffusion measurements. *ChemPhysChem.* 8:433–443.
 55. Fawcett, D. W., and N. S. McNutt. 1969. The ultrastructure of the cat myocardium. I. Ventricular papillary muscle. *J. Cell Biol.* 42:1–45.

Supporting material:

Analysis of molecular movement reveals latticelike obstructions to diffusion in heart muscle cells

Ardo Illaste, Martin Laasmaa, Pearu Peterson and Marko Vendelin

Laboratory of Systems Biology, Institute of Cybernetics, Tallinn University of Technology, Estonia

The supporting material is split into several sections. First, a brief overview of the RICS method and our extensions to it is given. Second, description of experimental methods, including confocal microscope setup is presented. Then, description of the analysis of RICS images is described and demonstrated by analyzing diffusion of molecules in water and measurement solution. Forth, description of stochastic computational model is given together with derivations used to relate barrier permeability to physical parameters of the barrier and molecule size. Lastly statistical analysis of model parameters estimation is presented.

Contents

1 Raster image correlation spectroscopy	S1
1.1 Basics	S1
1.2 Time delay between pixels	S3
1.3 Motivation for modifications	S3
1.4 Changes in scanning angle	S3
1.5 Scanning resolution	S3
1.6 Two diffusing species	S4
1.7 Triplet states	S4
1.8 Full form of correlation function	S4
2 Detailed methods	S4
2.1 Confocal setup	S4
2.2 Determination of diffusion coefficients using RICS	S6
2.3 Solutions	S6
3 Mathematical model	S6
3.1 Relation of barrier permeability to barrier and molecule properties	S6
3.2 Theoretical correlation function for 1D RICS	S8
4 Supporting results	S9
4.1 RICS extensions	S9
4.2 Diffusion obstacle parameter sensitivity	S11
Supporting references	S11

1 RASTER IMAGE CORRELATION SPECTROSCOPY

1.1 Basics

Raster image correlation spectroscopy (RICS) is based on merging the concepts of scanning confocal microscopy, FCS and image correlation spectroscopy (1, 2). While more detailed reviews are available covering the method and how it relates to other FCS-based methods (3, 4), we here present a brief overview of the concepts behind RICS and to our modification to this method.

The fundamental idea behind RICS is the realization that in an image obtained by a laser scanning confocal microscope, pixels on the image are not only separated in space but also in time (2). Photons emitted by excited fluorescent molecules are recorded as raster images as the mirrors scan the laser beam on the specimen. When recording a two dimensional raster image, the laser beam moves along one image axis (ξ), spending τ_d seconds acquiring each pixel on the line (dwell time), then flies back to the beginning of the line with flyback time τ_f , moves one pixel forward in the other axis (ψ) and records the second line. This sequential processes is repeated until the whole image has been scanned line by line (Fig. S1A), resulting in a rectangular grid of pixels separated in space and time. By calculating the correlation function (CF) of the scanned image it is possible to extract information about the space-time relationship between the pixels and to characterize, for example, reaction kinetics, translational and rotational diffusion, conformational dynamics, molecular flow, etc. (3–5). This can be done by fitting experimentally obtained CFs with theoretical CF curves derived for the phenomenon being observed. In this paper we focus on applying RICS on analysis of diffusion of fluorescent dyes.

The correlation function $G(\Delta\xi, \Delta\psi, \Delta\zeta)$ indicates the similarity of an image to a copy of itself shifted by $\Delta\xi$ in the ξ direction, $\Delta\psi$ in the ψ direction (see Fig. S1B) and, in case a 3D stack of images is analyzed, $\Delta\zeta$ in the ζ direction (otherwise $\Delta\zeta = 0$).

The CF for a given shift is calculated by multiplying the fluorescence values in the original image with values in the shifted image and averaging over all the pixels. The result is normalized to average image fluorescence squared:

$$G(\Delta\xi, \Delta\psi, \Delta\zeta) = \frac{\langle F(\xi, \psi, \zeta) \cdot F(\xi + \Delta\xi, \psi + \Delta\psi, \zeta + \Delta\zeta) \rangle_{\xi, \psi, \zeta}}{\langle F \rangle_{\xi, \psi, \zeta}^2} - 1, \quad (1)$$

where $\langle \dots \rangle$ signifies averaging over the whole image.

The CF can also be calculated in terms of fluorescence fluctuations from the average $\delta F = F - \langle F \rangle$ by substituting

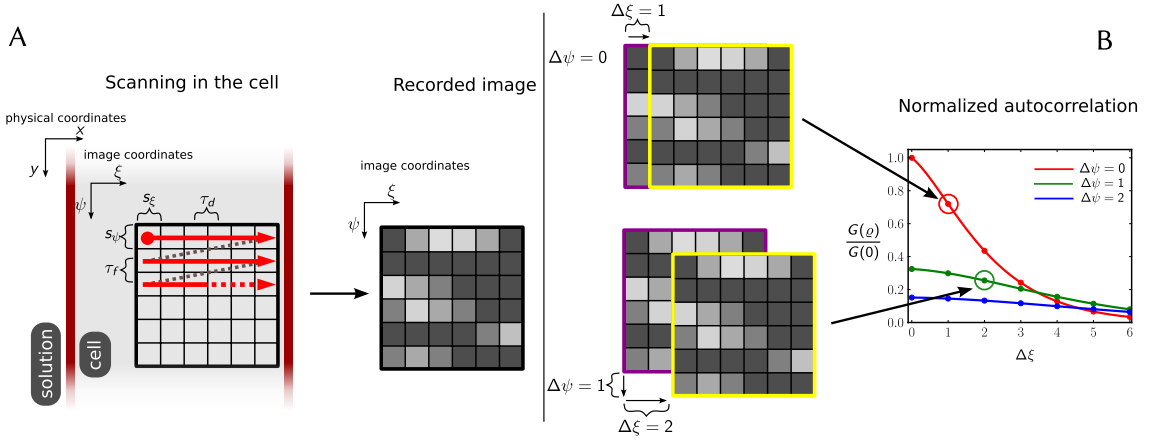


FIGURE S1: Explanation of the RICS protocol.(A) A raster image consisting of a grid of pixels is acquired within a cell. Pixels are separated by s_ξ, s_ψ μm spatially and by $\tau_d, n_\xi \times \tau_d + \tau_f$ μs temporally in the ξ and ψ directions, respectively. In the default case the image coordinates ξ, ψ align with the physical coordinates x, y . The image obtained shows traces of diffusing molecules within the cell. (B)The CF $G(\boldsymbol{\rho})$ for the shift $\boldsymbol{\rho} = (\Delta\xi, \Delta\psi)$ is calculated by shifting a copy of the original image, multiplying the fluorescence values and averaging over the entire image. Arrows indicate the location of the correlation value for the shifts shown. The CF here is normalized to the zero-shift correlation $G(0)$ from Eq.7

$F = \delta F + \langle F \rangle$ into Eq.1:

$$G(\Delta\xi, \Delta\psi, \Delta\zeta) = \frac{\langle \delta F(\xi, \psi, \zeta) \cdot \delta F(\xi + \Delta\xi, \psi + \Delta\psi, \zeta + \Delta\zeta) \rangle_{\xi, \psi, \zeta}}{\langle F \rangle_{\xi, \psi, \zeta}^2}.$$

It is more convenient to present the CF in vector form with image shift vector $\boldsymbol{\rho} = [\Delta\xi, \Delta\psi, \Delta\zeta]$ and position vector $\mathbf{h} = [\xi, \psi, \zeta]$:

$$G(\boldsymbol{\rho}) = \frac{\langle \delta F(\mathbf{h}) \cdot \delta F(\mathbf{h} + \boldsymbol{\rho}) \rangle_{\mathbf{h}}}{\langle F \rangle_{\mathbf{h}}^2}. \quad (2)$$

The physical coordinates corresponding to image coordinates \mathbf{h} are $\mathbf{p} = \mathbf{p}_0 + \mathbf{h}\mathbf{S}$. Here, \mathbf{p}_0 is the physical location at the 0-th pixel and $\mathbf{S} = \text{diag}(s_\xi, s_\psi, s_\zeta)$ is a diagonal matrix containing pixel sizes in each image dimension. Shift $\boldsymbol{\rho}$ in image coordinates converts to a shift $\mathbf{q} = [\Delta x, \Delta y, \Delta z]$ in the physical coordinate system:

$$\begin{aligned} \mathbf{q}(\boldsymbol{\rho}) &= \boldsymbol{\rho}\mathbf{S} = [\Delta\xi, \Delta\psi, \Delta\zeta] \begin{pmatrix} s_\xi & 0 & 0 \\ 0 & s_\psi & 0 \\ 0 & 0 & s_\zeta \end{pmatrix} \\ &= [\Delta\xi \cdot s_\xi, \Delta\psi \cdot s_\psi, \Delta\zeta \cdot s_\zeta] = [\Delta x, \Delta y, \Delta z]. \end{aligned}$$

For simplicity we consider that the fluorescence signal recorded at location \mathbf{p} is obtained from the convolution of the point spread function (PSF) of the microscope and the concentration of the fluorescent dye (c) in the PSF volume.

$$F(\mathbf{p}) = B \int W(\mathbf{r}) \cdot c(\mathbf{p} - \mathbf{r}) \, \text{dr},$$

where W is the PSF and B a parameter called brightness given by $B = q\sigma Q$ (5). Here q is the quantum efficiency of detecting emitted photons, σ the cross-section of absorption and Q

the emission quantum yield of the fluorescent molecule. Employing this relationship between recorded fluorescence and concentration, Eq.2 can be used to connect the fluctuations of fluorescence visible on the recorded image to fluctuations in concentration of the diffusing dye:

$$\begin{aligned} G(\boldsymbol{\rho}) &= \frac{\langle \delta F(\mathbf{p}) \cdot \delta F(\mathbf{p} + \mathbf{q}(\boldsymbol{\rho})) \rangle_{\mathbf{p}}}{\langle F(\mathbf{p}) \rangle_{\mathbf{p}}^2} \\ &= \frac{1}{\langle c(\mathbf{p}) \rangle_{\mathbf{p}}^2} \iint W(\mathbf{r})W(\mathbf{r}')G_D(\mathbf{r}, \mathbf{r}', \boldsymbol{\rho}) \, \text{dr} \, \text{dr}'. \quad (3) \end{aligned}$$

G_D is the correlation due to diffusion and can be calculated analytically (6):

$$\begin{aligned} G_D(\mathbf{r}, \mathbf{r}', \boldsymbol{\rho}) &= \langle \delta c(\mathbf{p} + \mathbf{r}) \cdot \delta c(\mathbf{p} + \mathbf{r}' + \mathbf{q}(\boldsymbol{\rho})) \rangle_{\mathbf{p}} \\ &= \langle c \rangle \prod_{i=1}^n (4\pi D_i)^{-\frac{1}{2}} \exp\left(-\frac{(r'_i + q_i - r_i)^2}{4D_i t(\boldsymbol{\rho})}\right), \quad (4) \end{aligned}$$

where $\delta c(\mathbf{p})$ is the fluctuation in concentration of the fluorescent dye at location \mathbf{p} , $\langle c \rangle$ is the average concentration, D_i are diagonal components of the diffusion tensor in the coordinate system composed of principal axes, collected here into $\mathbf{D} = [D_x, D_y, D_z]$. If diffusion is isotropic then all components in \mathbf{D} are equal. In the case of anisotropic diffusion, components of \mathbf{D} can have different values. The time delay $t(\boldsymbol{\rho})$ indicates how much time has passed between acquisition of two pixels separated by the shift $\boldsymbol{\rho}$. The number n indicates the number of dimensions and in general $n = 3$. The equations are still valid, however, for other n values as well.

Although the PSF is dependent on the microscope and should be measured experimentally, an analytic estimate is often used

(5, 6):

$$W(\mathbf{r}) = \prod_{i=1}^n \exp\left(-2\frac{r_i^2}{w_i}\right) \quad (5)$$

Here, \mathbf{w} is a vector describing the width of the PSF in spatial directions. It is customary to perform calibrations using a fluorescent molecule with a known concentration in order to determine the \mathbf{w} values. Furthermore, the x and y components of \mathbf{w} are often assumed to be equal.

Using the PSF definition from Eq.5 and G_D from Eq.4 the integrals in Eq.2 can be calculated and the following analytic form obtained:

$$G(\boldsymbol{\rho}) = \frac{1}{\langle c \rangle} \prod_{i=1}^n \left[\frac{1}{\sqrt{\pi(4D_i t(\boldsymbol{\rho}) + w_i^2)}} \cdot \exp\left(-\frac{q(\boldsymbol{\rho})_i^2}{4D_i t(\boldsymbol{\rho}) + w_i^2}\right) \right]. \quad (6)$$

From this result it can be seen that with zero shift (i.e., $\boldsymbol{\rho} = (0, 0, 0)$) the CF gives:

$$G(0) = \frac{1}{\langle c \rangle} \prod_{i=1}^n \frac{1}{\sqrt{\pi w_i}}. \quad (7)$$

As $G(0)$ is independent of the diffusion of the fluorescent molecule it can be used to determine the global concentration of the molecule or, knowing that, the properties of the PSF (i.e., components of \mathbf{w}).

1.2 Time delay between pixels

Scanning a 2D raster image with n_ξ pixels in the ξ direction, with τ_d seconds used as the dwell time for all pixels and τ_f being the time that it takes for the beam to move from the end of one line to the beginning of the next, the time delay between two pixels separated by the shift $\boldsymbol{\rho}$ used in Eqs. 6 and 9 is:

$$t(\boldsymbol{\rho}) = t(\Delta\xi, \Delta\psi) = \Delta\xi \cdot \tau_d + \Delta\psi \cdot (n_\xi \cdot \tau_d + \tau_f). \quad (8)$$

Inserting this relation in the CF Eqs. 6 and 9 will yield the function that can be used for fitting experimentally obtained data and obtaining diffusion coefficients.

1.3 Motivation for modifications

As we have demonstrated, RICS can be used to determine anisotropy of diffusion by varying the time delay between physical location in the sample during a scan. This can be achieved by altering the angle of scanning (7).

Also, diffusion dependent changes in the CF can be subtle, making them hard to detect and fit, especially with noisy data. Through changes in scanning resolution additional aspects of the CF can be estimated, leading to a larger amount of data-points available for fitting.

1.4 Changes in scanning angle

In order to detect anisotropy of diffusion, several scanning angles can be used to alter the time delay between pixels acquired

from the same location (7). When scanning is performed at an angle α relative to the physical coordinate axes, the CF equations need to be modified to account for this. For example, if scanning is performed under a 90° angle, the image ξ and ψ axes actually correspond to the physical y and x axes, respectively (see Fig. S2A). The CF that takes the scanning angle into account is:

$$G(\boldsymbol{\rho}, \alpha) = \frac{1}{\langle c \rangle} \prod_{i=1}^n \left[\frac{1}{\sqrt{\pi(4D_i t(\boldsymbol{\rho}) + w_i^2)}} \cdot \exp\left(-\frac{q(\boldsymbol{\rho}, \alpha)_i^2}{4D_i t(\boldsymbol{\rho}) + w_i^2}\right) \right], \quad (9)$$

where the physical shift \mathbf{q} is now a function of the rotation angle α :

$$\mathbf{q}(\boldsymbol{\rho}, \alpha) = \boldsymbol{\rho} \mathbf{S}(\mathbf{M}(\alpha))^T \quad (10)$$

$\mathbf{M}(\alpha)$ is the rotation matrix for rotation angle α . For rotating around the z axis, as is done in this paper, the rotation matrix is:

$$\mathbf{M}(\alpha) = \begin{pmatrix} \cos \alpha & -\sin \alpha & 0 \\ \sin \alpha & \cos \alpha & 0 \\ 0 & 0 & 1 \end{pmatrix}.$$

It is possible to do rotations around another axis or even multiple rotations around different axes by inserting a suitable rotation matrix in Eq.10 (assuming that the microscope employed is able to perform such scans).

The physical shift vector from Eq.10 for rotation α around the z axis is:

$$\begin{aligned} \mathbf{q}(\boldsymbol{\rho}, \alpha) &= [\Delta x, \Delta y, \Delta z] \\ &= \boldsymbol{\rho} \mathbf{S}(\mathbf{M}(\alpha))^T \\ &= \begin{pmatrix} \Delta\xi \cdot s_\xi \\ \Delta\psi \cdot s_\psi \\ \Delta\zeta \cdot s_\zeta \end{pmatrix}^T \begin{pmatrix} \cos \alpha & \sin \alpha & 0 \\ -\sin \alpha & \cos \alpha & 0 \\ 0 & 0 & 1 \end{pmatrix} \\ &= \begin{pmatrix} \Delta\xi \cdot s_\xi \cdot \cos \alpha - \Delta\psi \cdot s_\psi \cdot \sin \alpha \\ \Delta\xi \cdot s_\xi \cdot \sin \alpha + \Delta\psi \cdot s_\psi \cdot \cos \alpha \\ \Delta\zeta \cdot s_\zeta \end{pmatrix}^T. \end{aligned}$$

It is easy to verify that when $\alpha = 0$, \mathbf{M} reduces to the identity matrix and Eq.9 simplifies to Eq.6.

1.5 Scanning resolution

Changes in scanning resolution (7) or pixel dwell time τ_d (8) will alter the time delay function Eq.8 and result in different correlation curves. An example for scanning with double resolution but unchanged pixel dwell time τ_d in ξ axis is shown on Fig. S2B. An increased resolution increases the time taken to record a line and decreases pixel size. Therefore, in order to compare the CF for different resolutions it is more suitable to present them as functions of physical distance as is done in Fig. S2B.

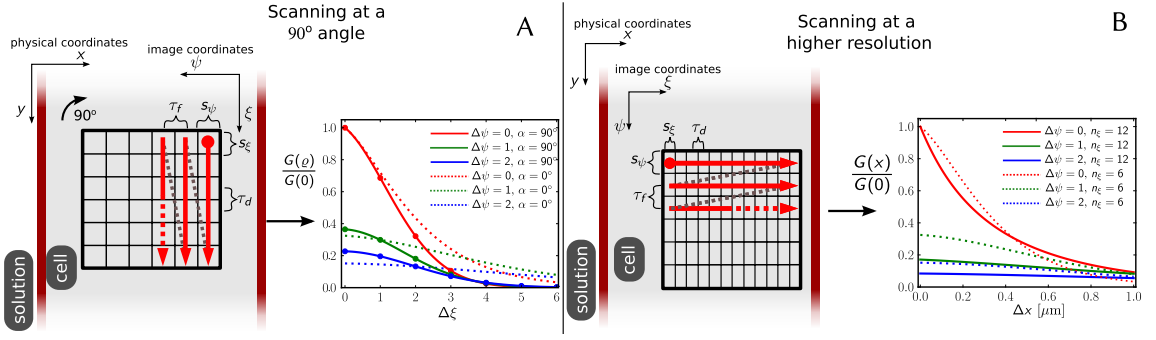


FIGURE S2: Modified scanning for RICS. (A) Scanning at an angle α rotates the image coordinates with respect to the physical coordinates and results in a different CF which can be used for determining anisotropy of diffusion. The CF for 0° angle scanning from Fig. S1B is shown in dotted lines and differs from the CF obtained for an image scanned at a different angle. In the shown example, scanning is performed at a 90° angle, effectively aligning the image ξ axis with the physical y axis and image ψ axis with physical x axis. (B) Changing the scanning resolution also alters the shape of the CF. In the example shown, the image is scanned at two times higher resolution resulting in the CF depicted with solid lines. Since the pixel dwell time τ_d is not changed, scanning one line takes two times longer. For comparison, the CF from Fig. S1B is shown in dotted lines. The horizontal axis now shows physical shift values in μm since the pixel size and count for the two CF-s is different.

1.6 Two diffusing species

It is possible for the fluorescent molecule to bind with other, larger, molecules in the intracellular solution. As a result, two subspecies of the fluorescent molecule would be diffusing in the cell: the faster unbound form and the slower bound form. Assuming that fluorescent properties of the dye are not altered as a result of binding and that the two species are non-interacting (i.e., the binding/unbinding is relatively slow), the CF for two species diffusing is (5, 9) :

$$G(\boldsymbol{\rho}, \alpha) = \frac{1}{\langle c_1(\mathbf{p}) + c_2(\mathbf{p}) \rangle_{\mathbf{p}}^2} \cdot \iint W(\mathbf{r})W(\mathbf{r}') (\langle c_1 \rangle \cdot g_{D1} + \langle c_2 \rangle \cdot g_{D2}) \, d\mathbf{r} \, d\mathbf{r}', \quad (11)$$

where $\langle c_1 \rangle$, $\langle c_2 \rangle$ are concentrations of the two components and g_{D1} and g_{D2} are given by $G_{Dk}(\mathbf{r}, \mathbf{r}', \boldsymbol{\rho}, \alpha) / \langle c_k \rangle$, ($k = 1, 2$). Inserting the gaussian PSF given in Eq.5 to calculate the CF for two components from Eq.11:

$$G(\boldsymbol{\rho}, \alpha) = \frac{1}{(\langle c_1 \rangle + \langle c_2 \rangle)^2} \cdot \left[\langle c_1 \rangle \prod_{i=1}^n \frac{\exp\left(-\frac{q(\boldsymbol{\rho}, \alpha)_i^2}{4D_{1,i}t(\boldsymbol{\rho}) + w_i^2}\right)}{\sqrt{\pi(4D_{1,i}t(\boldsymbol{\rho}) + w_i^2)}} + \langle c_2 \rangle \prod_{i=1}^n \frac{\exp\left(-\frac{q(\boldsymbol{\rho}, \alpha)_i^2}{4D_{2,i}t(\boldsymbol{\rho}) + w_i^2}\right)}{\sqrt{\pi(4D_{2,i}t(\boldsymbol{\rho}) + w_i^2)}} \right],$$

where $D_{1,i}$, $D_{2,i}$ are diffusion coefficients in direction i for the first and second component, respectively.

1.7 Triplet states

It is possible for a fluorescent molecule to go into a so-called triplet state from where it relaxes back to ground state after

a delay much longer than it takes for the normal excitation-emission cycle to complete. This phenomenon, if ignored, could cause diffusion coefficients to be overestimated. To account for this effect, we multiply the CF function (Eq.9 or Eq. 11) with a compensation factor (4, 8–10) :

$$1 + \frac{T}{1-T} \exp\left(-\frac{t}{\tau}\right), \quad (12)$$

where T is the fraction of molecules in triplet state and τ the triplet state relaxation time.

1.8 Full form of correlation function

In this work the experimentally measured PSF was used instead of the approximated one (Eq.5), necessitating numerical integration for each CF evaluation:

$$G(\boldsymbol{\rho}, \alpha) = \frac{1}{\langle F_1(\mathbf{p}) + F_2(\mathbf{p}) \rangle_{\mathbf{p}}^2} \left(1 + \frac{T}{1-T} \exp\left(-\frac{t}{\tau}\right) \right) \cdot \iint W(\mathbf{r})W(\mathbf{r}') (\langle c_1 \rangle \cdot g_{D1} + \langle c_2 \rangle \cdot g_{D2}) \, d\mathbf{r} \, d\mathbf{r}' \quad (13)$$

This is the CF form used for fitting experimental data in this work.

2 DETAILED METHODS

2.1 Confocal setup

To perform imaging for raster image correlation spectroscopy (RICS), we designed and built a confocal microscope. This allowed us to automate image acquisition under varying laser scanning angles and frequencies.

The confocal microscope was built around Olympus IX71-FVFS-2, using the left side port with the mounted scanning

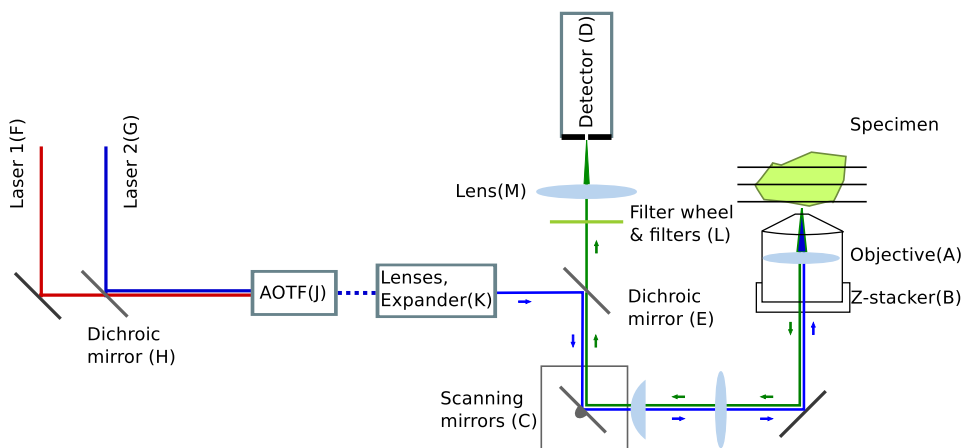


FIGURE S3: Scheme of the confocal microscope setup. See text for description of the parts.

lens (FV3-PLI2-2, Olympus). Images were acquired using water-immersion $60\times$ objective (UPLSAPO, NA 1.2, Olympus, indicated by *A* on Fig. S3) mounted on piezoelectric objective-lens positioning system (MIPOS 250 SG driven by 12V40 CLE piezo amplifier, Piezosystem Jena, Germany, *B* on Fig. S3). Excitation laser beam was guided and fluorescence signal descanned (i.e., emitted light from the sample returns along the path taken by excitation light, reflecting from the scanning mirrors (*C*) before heading to the detector (*D*) from the dichroic mirror *E*) on the image plane of the scanning lens using galvo mirrors (6210H 3mm 6121H 2-mirror system, Cambridge Technology, MA, USA; *C* on Fig. S3).

Two lasers were used in the experiments: 633 nm 05-LHP-151 (Melles Griot, USA; *F* on Fig. S3) and 473 nm SDL-473-LN-O1OT (Shanghai Dream Lasers Technology Co. Ltd, China, *G* on Fig. S3). Beams of the lasers were combined using LM01-503 dichroic (Semrock, Rochester, NY, USA; *H* on Fig. S3); all following dichroics and filters are from this company), passed through an acousto-optical tunable filter (AOTF; *J* on Fig. S3) to select the laser line and regulate power of the excitation (AOTFnc-VIS-TN, AA Sa Opto-Electronic Division, France). Laser beam was expanded and filtered by spatial filter KT310 using C220TME-A (FD 11mm) as focusing lens, P25S (25 μm) pinhole, and LA1608-A (FD 75mm) as a collimating lens (all from Thorlabs, NJ, USA, *K* on Fig. S3). After the spatial filter, the beam was passed through iris SM1D12C (Thorlabs) set at 2.4 mm. Excitation light and fluorescence emission were separated by dichroic FF500/646-Di01-25x36 (*E* on Fig. S3). Fluorescence signal passed an emission filter (FF01-550/88-25 or FF01-725/150-25 for 473 nm or 633 nm excitation, respectively) which was selected using motorized filter wheel FW102B (Thorlabs; *L* on Fig. S3). After passing the emission filter, fluorescence signal was focussed by AC254-500-A1-ML (FD 500 mm; *M* on Fig. S3) on photon counter SPCM-AQRH-13 (PerkinElmer, USA; *D* on Fig. S3). In this design, photon counter detector (nominal diameter 170 μm) was used as a pinhole. The optical scheme was mounted on honeycomb table top IHT12-15-20 positioned on pneumatic vibration isolation system 1VIS95-065-08-70 (Standa, Lithua-

nia). The scheme was covered by custom cover with internal wall separating excitation light processing before the dichroic that splits excitation and emission light. To avoid signal contamination from emitted radiation by galvo mirrors, a wall was mounted that prevented the radiation to reach the detector from mirror motors. In addition, filter wheel LED position indicator was turned off during acquisition to avoid emission signal contamination. Optical scheme was adjusted to optimize for maximal emission signal and symmetry of point spread function (PSF). Resulting PSF has been published earlier (11).

Confocal microscope was controlled using custom made software. Galvo mirrors, piezoelectric objective-lens positioning system and AOTF were driven by PCIe-6259 (National Instruments, Texas, USA) using analog (mirrors and piezomotor) and digital outputs (AOTF). Feedback from galvo mirrors and piezomotor was recorded via analog input channels of the same card. This feedback signal was used to optimize the driving signal to ensure that the specified region of interest was scanned. Photon counter pulses were counted using PCI-6602 card (National Instruments) and read out by the software with the specified pixel time (1 μs for RICS measurements, 25 μs or larger for imaging). Excitation light was reduced during flyback using AOTF ensuring that it fully recovered by the beginning of each imaged line. The cards and the software was running on Linux (OpenSUSE) PC with National Instruments cards interfaced using NI-DAQmx 8.0.1 driver (National Instruments).

Imaging for RICS was performed in a $\sim 20\times 20 \mu\text{m}$ region with line scanning frequencies 167, 289, and 500 Hz. The signal was acquired during half of the scan time with the other half used for flyback. Imaging was performed with different scan directions by changing the angle of acquisition from -180° to $+180^\circ$ with a step of 20° . Images were acquired in sets of 90 (scanning frequency 500 Hz), 60 (289 Hz), and 30 (167 Hz) frames. The order with with images with different scanning frequencies and directions were recorded was randomized.

“Poking” of cells was performed with 1.0 mm diameter glass pipettes (World Precision Instruments, USA) manufactured

into 0.5 μm diameter tips using a pipette puller (PC-10 puller, Narishige, Japan). Cell membranes were permeated by controlling the pipette with a micromanipulator (PatchStar Micromanipulator System PS-8300C, Scientifica, England).

2.2 Determination of diffusion coefficients using RICS

Measurements were performed using different laser scanning frequencies and directions, similar to our earlier study (12). Through variation of scanning speed and direction, we change $t(\varrho)$. As a result, several components of diffusion coefficients can be estimated and fits can be optimized against measurements obtained with different scan frequencies. In total we used 19 angles spanning the range from 0 to 360 degrees and 3 different scanning speeds. In our analysis, we assumed that the shape of rat cardiomyocyte can be approximated as a cylindrical rod. In experiments, cells were aligned along the y axis. Thus, D_y corresponded to longitudinal diffusion coefficient D_L and $D_x = D_z$ — to the transverse one D_{TR} .

DCs, concentrations, and triplet state parameters were determined by fitting Eq.13 with the correlation function estimated from measurements. Here, correlation between pixels on the same line as well as pixels on two adjacent lines was used. Fit was performed using the least squares method by the Levenberg-Marquardt algorithm (13). Integral in Eq.13 was determined numerically to take into account the asymmetry of the PSF, as in (12). PSF measurements were conducted regularly so as to verify that it remains stable throughout the experiment series. Fits were performed with the PSF obtained for the current alignment.

Effect of fluorophore photobleaching can be compensated for by using the approach applied in (8, 14). This involves correcting the correlation curves obtained for the i -th image by multiplying it with the ratio of average intensity of the i -th image to that of the first image. We did not apply this correction, however, as we perform RICS analysis only to an subsection of the recorded images where the average image intensity did not change over time. This selectivity effectively means that a separate compensation factor is not necessary. Due to the high photostability of the dyes employed (as indicated by long stable ranges in image sequences) we considered triplet states as the main cause for loss of fluorescence that would interfere with DC estimation.

For calibration, the PSF was scaled with the scaling factor that was optimized together with other parameters when fitting the measurements recorded in water and solution. The scaling factor was found to be 1.042 ± 0.014 ($n=24$). Value of 1.04 was used when analysing data recorded in cardiomyocytes.

When estimating DCs with RICS in cells, images are first processed by removing the immobile fraction of the signal using moving average, as in (2, 15). For that images were blurred with a 3×3 kernel (each pixel's value was taken as the average of the pixel together with its closest neighbors) to reduce interference with DC estimation (see *Supporting results*). This is similar to the approach used in (8).

2.3 Solutions

The measurement solution contained (in mM) 0.5 EGTA (Sigma, 03778), 3.0 KH_2PO_4 (Sigma, P0662), 3.0 MgCl_2 (Sigma, 63068), 20 HEPES (Sigma, H3375), 110 sucrose (Sigma, S1888), 20 taurine (Sigma, 86329), 0.5 dithiothreitol (Sigma, D0632) and 60 lactobionate (Sigma, L2398), 5 glutamate (Sigma, 49449), 2 malate (Sigma, M6413). In addition, 5 mg/ml BSA (Roche, 10 775 835 001) was added, and pH was adjusted at 25°C to 7.1 with KOH.

The simplified solution with reduced content of macromolecules contained (in mM) 0.5 EGTA, 3.0 KH_2PO_4 , 3.0 MgCl_2 , 20 HEPES, 0.5 dithiothreitol and 60 lactobionate. pH was adjusted at 25°C to 7.1 with KOH.

3 MATHEMATICAL MODEL

3.1 Relation of barrier permeability to barrier and molecule properties

Motivation. In our stochastic diffusion model we employ a permeability parameter p that describes the probability of a particle to traverse a barrier after coming into contact with it. This would, in reality, correspond to a distribution of permeable pores with a given radius on the surface of the barrier. If pore and particle dimensions are of the same order of magnitude then different particles would have different probabilities of being able to pass through the same pore, i.e., a permeability value of 1% for ATTO633-ATP would correspond to a smaller permeability for Alexa647-dextran 10K. Our goal is to determine the relative permeability values between particles of different sizes and to find a relationship between permeability and particle and pore dimensions.

Derivation. We take a circular object of radius r located at (x_r, y_r) . The object is diffusing with diffusion coefficient D_x . Centered at $(0, 0)$ is wall with an opening of radius R (see Fig. S4.)

The particle makes a random step, consisting of two independent steps in x and y directions : $dx \sim \mathcal{N}(0, \sigma)$ and $dy \sim \mathcal{N}(0, \sigma)$, where $\sigma = \sqrt{2D_x\tau}$. Total distance travelled $L = \sqrt{dx^2 + dy^2}$, follows the Rayleigh distribution:

$$L \sim \text{Rayleigh}(L, \sigma) = \frac{L}{\sigma^2} \exp\left(-\frac{L^2}{2\sigma^2}\right)$$

Probability of the particle passing through the hole is:

$$p_a = \frac{\int_{\alpha_1}^{\alpha_2} \int_0^{\frac{y_r}{\sin \alpha}} \text{Rayleigh}(L, \sigma) dL d\alpha}{\int_0^{\frac{y_r}{\sin \alpha}} \int_0^{\alpha_2} \underbrace{\text{Rayleigh}(L, \sigma) dL}_{=1} d\alpha} = \frac{\int_{\alpha_1}^{\alpha_2} \exp\left(-\frac{y_r^2}{2\sigma^2 \sin^2 \alpha}\right) d\alpha}{2\pi}, \quad (14)$$

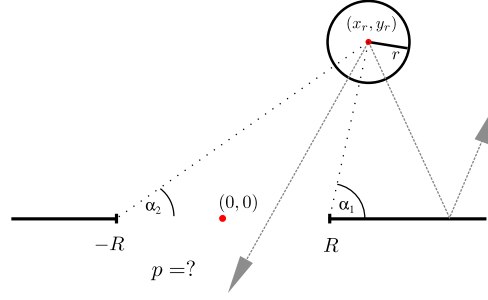


FIGURE S4: Probability p of particle of radius r located at x_r, y_r diffusing through a pore of radius R within timestep τ . α_1 and α_2 are the angles within which it is possible for the particle to permeate the pore (shown approximately on the figure)

where α_1 and α_2 are the minimum and maximum angles at which the object can still pass through the hole and $\frac{y_r}{\sin \alpha}$ is the minimal distance to pass through at angle α . From Fig. S4 it is visible that α_1 and α_2 change as x_r, y_r, r and R change. It is possible to calculate α values iteratively with increasing accuracy or by numerically solving the exact equation relating all the parameters. The integral in Eq.14 can not be represented in elementary functions and we must calculate the probabilities we seek numerically. Example probabilities for ATTO633-ATP and Alexa647-dextran 10K are shown on Fig. S5. As can be seen, the probabilities for ATTO633-ATP compared to Alexa647-dextran 10K to go through the pore are greater at all locations.

The probability for a particle to get out from the inside of a square D with side length d covered with n pores of radius R on each side is:

$$P_a = \frac{\overbrace{4n \cdot \iint_D p_a \, dx_r \, dy_r}^{\doteq Q}}{\iint_D dx_r \, dy_r} = \frac{4n \cdot Q}{d^2}, \quad (15)$$

where Q is the value of the numerically calculated surface integral of p_a .

Probability P_a from Eq.15 gives the combined probability of a particle reaching the wall from anywhere inside the square and then passing through a pore, i.e., $P_a = p \cdot P_b$, where P_b is the probability of the particle reaching the wall, and p is the probability of permeating the wall (the barrier permeability parameter used in our stochastic diffusion model). In order to calculate P_b we first need to find the probability of reaching the wall from a given position (x_r, y_r) . This is given by:

$$p_b = \frac{\int_0^\pi \exp\left(-\frac{y_r^2}{2\sigma^2 \sin^2 \alpha}\right) d\alpha}{\int_0^\pi \int_0^\infty \text{Rayleigh}(L, \sigma) dL d\alpha} = \text{erfc} \frac{y_r}{\sigma\sqrt{2}},$$

where erfc is the complementary error function. For P_b we get:

$$P_b = \frac{4 \cdot \iint_D p_b \, dx_r \, dy_r}{\iint_D dx_r \, dy_r} = \frac{4d\sigma\sqrt{\frac{2}{\pi}}}{d^2}. \quad (16)$$

Combining Eqs. 15 and 16 we get for permeability p :

$$p = \frac{P_a}{P_b} = \frac{nQ}{d\sigma\sqrt{\frac{2}{\pi}}}.$$

When we compare two molecules with different radii and diffusion coefficients (i.e., $r_1 \neq r_2$ and $\sigma_1 \neq \sigma_2$, whereby $Q_1 \neq Q_2$), then the ratio of their respective permeabilities is:

$$\frac{p_1}{p_2} = \frac{Q_1 \cdot \sigma_2}{Q_2 \cdot \sigma_1}. \quad (17)$$

The dependence of this ratio on pore radius R for ATTO633-ATP and Alexa647-dextran 10K is shown on Fig. S6. The fit depicted on the figure is: $\frac{p_1}{p_2} \approx \frac{R-r_1}{R-r_2}$. The fit can match the theoretical values closely and is trivial to calculate compared to finding exact theoretical values which require time consuming numerical calculations. The formula itself can be justified by the following: n pores of radius R on a otherwise impermeable line of length d gives $\frac{n \cdot R}{d}$ as the ratio of permeable to impermeable sections of the line i.e., permeability. For a particle with radius r the effective radius of a pore would be $R - r$, giving $\frac{n \cdot (R-r)}{d}$ as permeability. Introducing pore density $\eta = n/d$ we can write: $p = \eta(R - r)$. It is easy to see that using this result for two different particles and taking the ratio would yield the formula used for the fit in Fig. S6.

In two dimensions, total permeability for n circular pores of radius R on a surface with area A would be $\frac{n \cdot \pi R^2}{A}$. Again, for a particle this translates to effective permeability of $p = \frac{n \cdot \pi (R-r)^2}{A}$. Defining η as the number of pores per unit area, we get:

$$p = \eta \cdot \pi (R - r)^2,$$

which is the relationship between permeability, pore radius and particle radius used in our calculations.

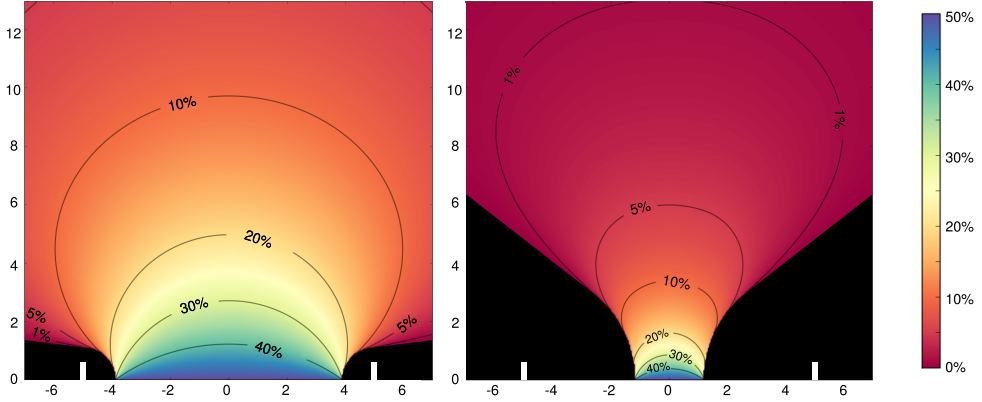


FIGURE S5: Probabilities for ATTO633-ATP (left) and Alexa647-dextran 10K (right) of going through a 10nm diameter pore (shown with white lines). Color at a given location indicates probability of the particle going through the pore in one random step. The area in black shows the region from where it is impossible for the particle to go through the pore.

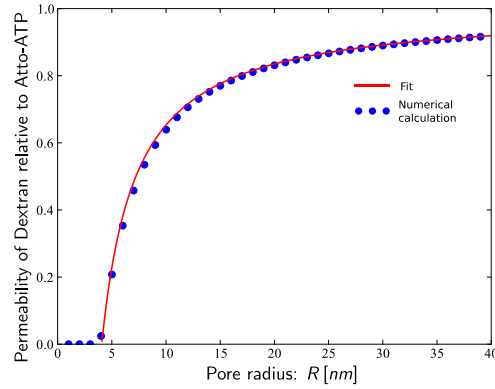


FIGURE S6: Ratio of probability of Alexa647-dextran 10K to ATTO633-ATP going through a pore of radius R . As pore radius increases, the ratio approaches 1, i.e., both particles are almost as like to permeate the pore. Dots indicate numerical calculations based on Eq.17, solid line is an approximate fit.

3.2 Theoretical correlation function for 1D RICS

In order to analyze images obtained from the simplified 1D stochastic diffusion model, an analytic expression for the correlation function is used in fitting. This is obtained for the 1D case from Eq.3. The correlation function showing correlation between pixels separated from each other by image shift $\Delta\xi$ and time t , can be calculated from:

$$G(\Delta\xi) = \frac{\int_{-\infty}^{\infty} \int_{-\infty}^{\infty} W(x_1)W(x_2)G_D(x_1, x_2, \Delta\xi) dx_1 dx_2}{\left(\langle c \rangle \int_{-\infty}^{\infty} W(x) dx \right)^2}.$$

Here, G_D is the correlation due to diffusion (from Eq.4 with $n = 1$)

$$G_D(x_1, x_2, \Delta\xi) = \frac{c}{\sqrt{4\pi D_x t}} \exp\left(-\frac{(x_2 + \Delta\xi \cdot s_\xi - x_1)^2}{4iD_x \cdot t}\right),$$

with $\langle c \rangle$ representing concentration. D_x the diffusion coefficient, s_ξ the pixel size in ξ direction and $t = t(\Delta\xi)$ is the delay time between acquisition of two pixels separated by $\Delta\xi$.

W is the 1D PSF (from Eq.5 with $n = 1$):

$$W(x) = \exp\left(-\frac{2x^2}{w_x^2}\right),$$

where w_x determines the width of the PSF.

After taking all the integrals and similar to Eq.6 with $n = 1$:

$$G(\Delta\xi) = \frac{\exp\left(-\frac{(s_\xi \cdot \Delta\xi)^2}{4D_x t + w_x^2}\right)}{\langle c \rangle \sqrt{\pi} \sqrt{4D_x t + w_x^2}}.$$

This formula was used to fit numerical experiments performed with the 1D stochastic model.

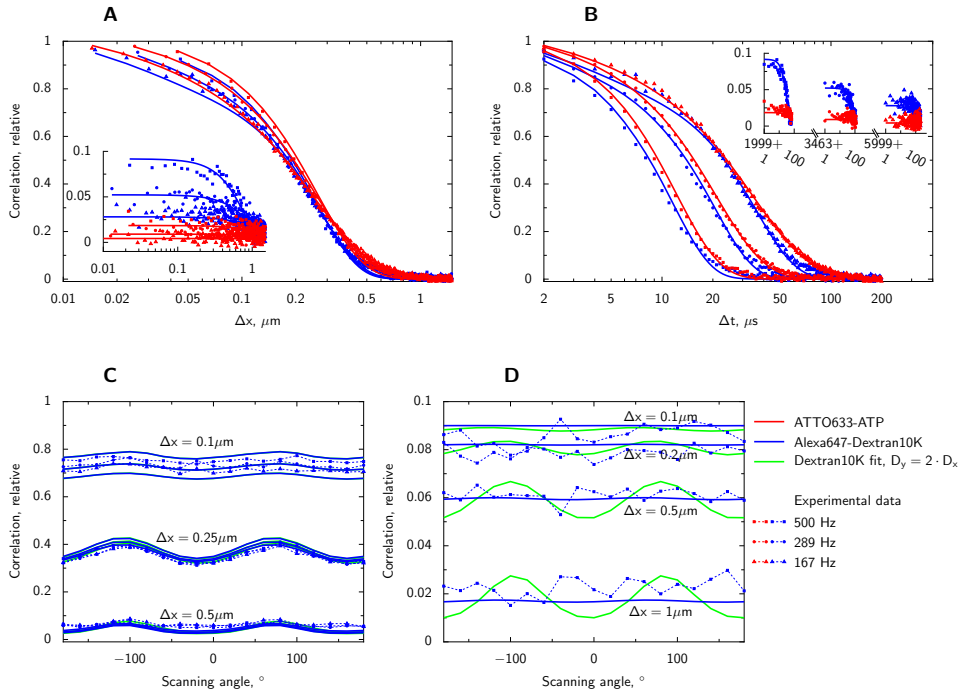


FIGURE S7: Diffusion of ATTO633-ATP (red) and Alexa647-dextran 10K (blue) in water analyzed by RICS. Experimental data (points) acquired at different laser scanning frequencies and directions are fitted with theoretical correlation curves given in Eq.13 (lines). By using dyes with different diffusion coefficients, we demonstrate the influence of diffusion coefficient on spatial (A) and temporal (B) components of correlation functions. Data and theoretical fits shown on A and B are identical. A is the classical way of presenting correlation functions in RICS analysis. As we use multiple scanning speeds, plotting correlation as a function of time (as in B) illustrates the differences caused by changes in scanning speed. Converting between A and B plots can be done by employing Eq.8. On A and B, imaging was performed with the laser scanning along a line parallel to axis x at different frequencies (frequencies noted in legend on the right bottom). Correlation along the same line is shown in the main graphs (A,B) while correlation of the signal between pixels in adjacent lines is shown in the insets. Due to the laser backtracking and variation in scan frequencies, temporal component has gaps visible in the inset of B. Due to asymmetry of PSF, laser scanning in different directions leads to modification of correlation function between pixels in the same line (C) and in the adjacent lines (D). This is demonstrated by showing correlation function estimated from the experiment (dots connected by dashed lines) and results of the fit (solid blue line) for Alexa647-dextran 10K. Correlation between pixels in the same line is not as sensitive to anisotropy of diffusion as correlation between neighbouring lines, resulting in an overlap between fits having a two time difference in diffusion coefficients in the y direction, as seen on C. Distinction between isotropic and anisotropic fits is mainly visible on correlation between pixels in adjacent lines (D).

4 SUPPORTING RESULTS

4.1 RICS extensions

To demonstrate the extended RICS protocol, we determined diffusion coefficients (DCs) of fluorescent dyes in water. Representative correlation functions (CF) calculated from measurements of ATTO633-ATP and Alexa647-dextran 10K are shown in Fig. S7. By varying the frequency of laser scanning while acquiring images in confocal microscope, we varied the relationship between spatial and temporal components of fluctuations of the signal (Fig. S7A and B). The plots in Fig. S7A and B contain the same data and theoretical fits. However, since we alter the scanning frequency it is easier to visually discern the differences in correlation if it is shown as a function of time (Fig. S7B) rather than space (Fig. S7A), which is the classical representation for RICS. In both cases Eq.13 was used for the theoretical fit. While for Alexa647-dextran 10K a

significant correlation of fluorescence fluctuations can be observed between pixels in two consecutive scan lines (Fig. S7A and B insets), the correlation is rather small for ATTO633-ATP. This is due to the larger DC of ATTO633-ATP leading to a smaller probability of a molecule staying in the same neighborhood while the laser is scanning two consecutive lines. For Alexa647-dextran 10K, correlation of fluctuations between pixels depends on laser scanning frequency, as demonstrated in Fig. S7A and B insets. By taking into account asymmetry of the point spread function (PSF), we can fit CFs obtained from measurements at different laser scanning frequencies and directions with a theoretical CF from Eq.13. The resulting fits are represented in Fig. S7 by solid lines. From analysis of the CFs for Alexa647-dextran 10K in water, dependence of CF on scanning angle in Fig. S7C and D demonstrates that asymmetry of PSF is mainly influencing correlation between pixels in the same line of an image. When fitting the CFs with a model that assumes a two time difference in DCs in x and y direc-

tions (green solid line in Fig. S7C and D), we observed that the model solution was different from isotropic case mainly in the signal correlation between pixels in adjacent lines (Fig. S7D). Correlation of the signal in the same line was not that much influenced by anisotropy (green and blue lines in Fig. S7C are very close to each other). Note that this observation can depend on the DCs.

Obtained diffusion coefficients, triplet time constants (τ) and triplet state contribution (T) to correlation functions for ATTO655-COOH, ATTO633-ATP, and Alexa647-dextran 10K are shown in Table 1 (main text). To test our method, we analyzed diffusion of ATTO655-COOH in water at 26°C. According to our measurements, the DC for ATTO655-COOH is $454 \pm 3 \mu\text{m}^2/\text{s}$. This is similar to the DC in water determined for the same dye using 2-focal fluorescence correlation spectroscopy measurements (16), $426 \pm 8 \mu\text{m}^2/\text{s}$ at 25°C. Taking into account the difference in temperatures, this would correspond to $\sim 437 \mu\text{m}^2/\text{s}$ in our conditions. DCs for ATTO633-ATP and Alexa647-dextran 10K which we used to study diffusion in cardiomyocytes (CM) were smaller in water as well as in the measurement solution (Table 1). Comparing DCs in water and solution, we can see that exposure to solution reduces the DC of Alexa647-dextran 10K and ATTO655-COOH to 80-85% of the value in pure water. For ATTO633-ATP, the reduction is considerably larger: DC in solution was only 60% of the value in water. We checked whether this reduction of DC could be attributed to the binding of a fraction of ATTO633-ATP to proteins in measurement solution. However, RICS analysis was not able to resolve two components (slow and fast) of ATTO633-ATP (both components had the same DC when the slow component's DC was not limited). However, when exposed to a simplified solution with a reduced amount of macromolecules (see *Detailed Methods* of Supporting Material for solution composition), we observed a reduction of the DC of ATTO633-ATP to $265 \pm 10 \mu\text{m}^2/\text{s}$ ($n = 4$), i.e., to $\sim 80\%$ of the value in water. In contrast, the DCs of Alexa647-dextran 10K and ATTO655-COOH in this simplified solution remained similar to their DCs in water: 60 ± 1 ($n = 4$) $\mu\text{m}^2/\text{s}$ and $451 \pm 10 \mu\text{m}^2/\text{s}$ ($n = 5$), respectively. This suggests that diffusion of ATTO633-ATP in the measurement solution is in-

fluenced in part by interaction of ATTO633-ATP salt with ions in the solution, leading to an increase in the apparent hydrodynamic radius of ATTO633-ATP. To avoid any bias induced by such interaction, we compared the DCs of dyes in the cell to the DCs in the measurement solution, not to the coefficients in water.

We fitted the CFs estimated from the measurements in water and solution using the anisotropic model. According to our fits, DCs in longitudinal y (L) direction was systematically overestimated (Table 1) leading to up to 22% difference in DCs (the largest anisotropy was estimated for ATTO633-ATP in solution). Thus, small differences in DCs due to anisotropy cannot be resolved with our method. We found that the predicted anisotropy can depend on the model used. In estimating DCs, we used a model where the x and z direction were taken to represent the transverse TR direction. When taking y and z as the transverse direction instead, the predicted anisotropy was much smaller. The exception was a relatively high anisotropy predicted for Alexa647-dextran 10K in water (25%). We think that such dependence on the model is induced by inaccuracies in the PSF.

When estimating DCs with RICS in cells, images are first processed by removing the immobile fraction of the signal using a moving average. We applied the same pre-processing to images recorded in water and solution. As a result, we found that such pre-processing affects RICS analysis. Influence on DC was found to be relatively small with DC estimated after removal of the average being $0.95\times$ to $1.13\times$ larger than DC estimated from the original images. However, triplet state characteristics were influenced more profoundly with triplet state time constant increasing by $1.17\times$ to $1.52\times$ and triplet state contribution increasing by $1.05\times$ to $1.36\times$. To reduce the influence of pre-processing on RICS analysis, we took advantage of sub-PSF pixel sizes and performed averaging by using images blurred with a 3×3 kernel (each pixel's value was taken as the average of the pixel together with its closest neighbors). Using such a kernel reduced the influence of average signal subtraction on DC ($1.02\times$ to $1.05\times$ larger than before pre-processing), triplet state time constant ($1.08\times$ to $1.16\times$),

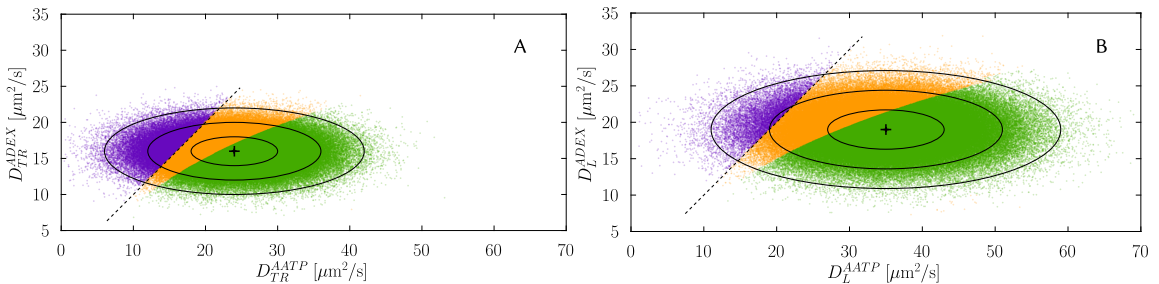


FIGURE S8: Distributions of random generated pairs of ATTO633-ATP and Alexa647-dextran 10K diffusion coefficients in transverse(A) and longitudinal directions (300000 values each). Pairs were randomly generated from normal distributions having the mean and standard deviation obtained from experiment (shown in Table 1 of the main text). Experimental mean values are shown with a cross. Ellipses indicate distances 1,2 and 3 standard deviations from the mean. Dotted line show DC values of ATTO633-ATP and Alexa647-dextran 10K are equal. As explained in the text, values left of this line are discarded and not included in analysis. The middle region (shown in yellow) contains DC value pairs where density of pores in barrier would be less than 1 per barrier. For the DC values in the green region intersections are found as in the main text and collected for statistics.

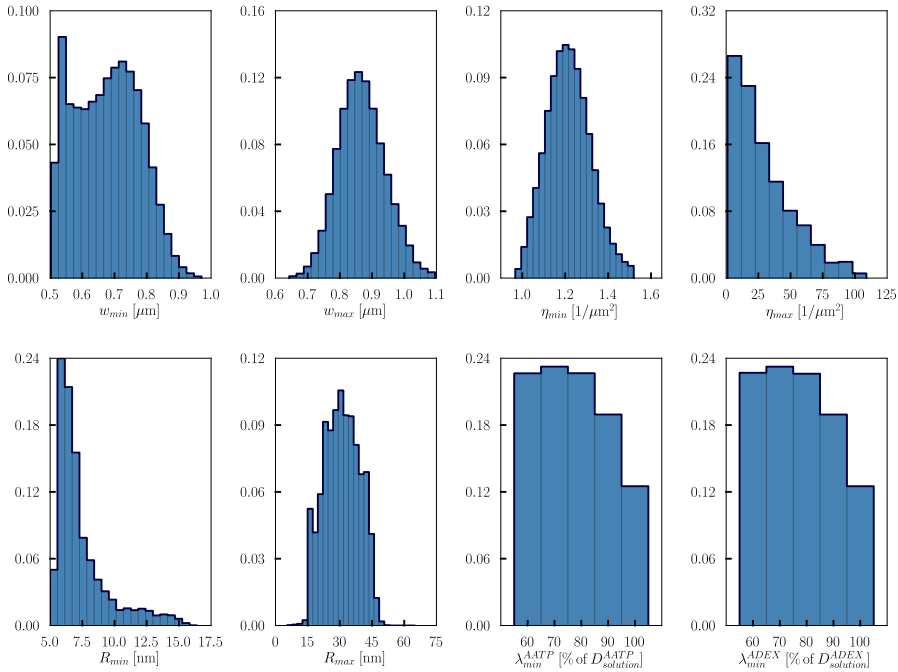


FIGURE S9: Histograms showing distributions of minimum and maximum model parameter values obtained from Monte Carlo simulations in the transverse direction.

and triplet state contribution ($0.92 \times$ to $1.04 \times$). On the basis of these observations, we used blurring by 3×3 kernel in analysis of diffusion in cardiomyocytes.

4.2 Diffusion obstacle parameter sensitivity

Parameters presented in Table 2 of the main text were obtained by finding intersections between curves of experimental and computational results. As visible from Figures 2C, 2D and 2E in the main text, a range of barrier-to-barrier distance, pore radius and pore density values satisfy the constraints of the model and computational results. The experimentally obtained DC values have a error associated with them. In order to estimate the uncertainties caused by measurement errors in the parameters we found, Monte Carlo analysis was applied. Similar to the procedure depicted on Figure 2B and 2C, random DC for ATTO633-ATP and Alexa647-dextran 10K were chosen from a normal distribution with the mean and standard deviation equal to the values from experiments presented in Table 1 (i.e., $\mathcal{N}(24, 6)$, $\mathcal{N}(16, 2)$ for ATTO633-ATP and Alexa647-dextran 10K in the transverse direction and $\mathcal{N}(35, 8)$, $\mathcal{N}(19, 3)$ in the longitudinal direction). For each randomly generated ATTO633-ATP Alexa647-dextran 10K DC value pair, intersections were found and from those a range of suitable parameter values determined. Random sampling was performed 300000 times for both transverse and longitudinal directions. The resulting distribution of random DC value pairs are shown on Fig. S8A and B for the transverse and longitudinal directions, respectively. Of possible combinations two types were discarded. First, cases where DC of Alexa647-dextran 10K

was larger than ATTO633-ATP (left of the dashed lines and on Fig. S8) and, secondly, cases where the pore density value was so low that less than one would be present on a single barrier element (the middle, light region on Fig. S8). For all other pairs model parameter maximum and minimum values were obtained and collected. Histograms for obtained maximum and minimum parameter values are presented in Figs. S9 and S10. Histograms for maximum estimate of DC reduction values are not shown as they were always 100% of the DC in solution. The results presented in Table 2 in the main text are the mean and standard deviations of these distributions.

SUPPORTING REFERENCES

1. Brown, C. M., R. B. Dalal, B. Hebert, M. A. Digman, A. R. Horwitz, and E. Gratton, 2008. Raster image correlation spectroscopy (RICS) for measuring fast protein dynamics and concentrations with a commercial laser scanning confocal microscope. *J Microsc* 229:78–91.
2. Digman, M. A., C. M. Brown, P. Sengupta, P. W. Wiseman, A. R. Horwitz, and E. Gratton, 2005. Measuring fast dynamics in solutions and cells with a laser scanning microscope. *Biophys J* 89:1317–1327.
3. Digman, M. A., and E. Gratton, 2011. Lessons in Fluctuation Correlation Spectroscopy. *Annu Rev Phys Chem* 62:645–668.
4. Haustein, E., and P. Schwille, 2007. Fluorescence correlation spectroscopy: novel variations of an established technique. *Annu. Rev. Biophys. Biomol. Struct.* 36:151–169.
5. Lakowicz, J., 2006. Principles of fluorescence spectroscopy. Springer.
6. Thompson, N., 2002. Fluorescence Correlation Spectroscopy. In J. Lakowicz, C. D. Geddes, and J. R. Lakowicz, editors, Topics

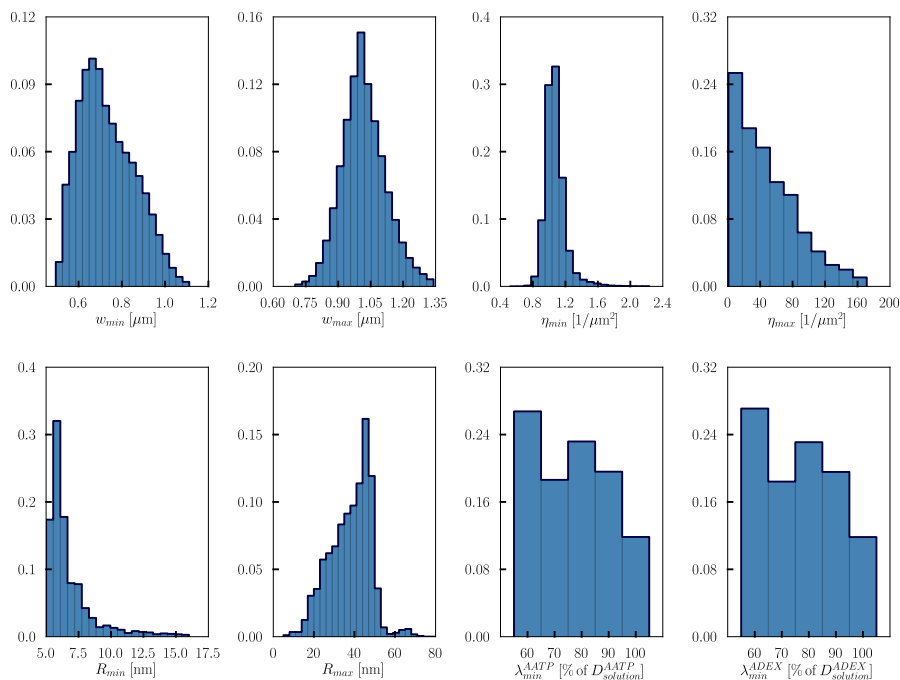


FIGURE S10: Histograms showing distributions of minimum and maximum model parameter values obtained from Monte Carlo simulations in the longitudinal direction.

in Fluorescence Spectroscopy, Springer US, volume 1 of *Topics in Fluorescence Spectroscopy*, 337–378.

7. Vendelin, M., and R. Birkedal, 2008. Anisotropic diffusion of fluorescently labeled ATP in rat cardiomyocytes determined by raster image correlation spectroscopy. *Am. J. Physiol. Cell. Physiol.* 295:C1302–1315.
8. Gröner, N., J. Capoulade, C. Cremer, and M. Wachsmuth, 2010. Measuring and imaging diffusion with multiple scan speed image correlation spectroscopy. *Opt. Express* 18:21225.
9. Krichevsky, O., and G. Bonnet, 2002. Fluorescence correlation spectroscopy: the technique and its applications. *Reports on Progress in Physics* 65:251.
10. Widengren, J., U. Mets, and R. Rigler, 1995. Fluorescence correlation spectroscopy of triplet states in solution: a theoretical and experimental study. *J Phys Chem* 99:13368–13379.
11. Laasmaa, M., M. Vendelin, and P. Peterson, 2011. Application of regularized Richardson-Lucy algorithm for deconvolution of confocal microscopy images. *J Microsc* 243:124–140.
12. Vendelin, M., and R. Birkedal, 2008. Anisotropic diffusion of fluorescently labeled ATP in rat cardiomyocytes determined by raster image correlation spectroscopy. *Am J Physiol Cell Physiol* 295:C1302–C1315.
13. Moré, J. J., D. C. Sorensen, K. E. Hillstrom, and B. S. Garbow, 1984. The MINPACK Project. In W. J. Cowell, editor, Sources and Development of Mathematical Software, Prentice-Hall.
14. Brown, C. M., R. B. Dalal, B. Hebert, M. A. Digman, A. R. Horwitz, and E. Gratton, 2008. Raster image correlation spectroscopy (RICS) for measuring fast protein dynamics and concentrations with a commercial laser scanning confocal microscope. *J. Microsc.* 229:78–91.
15. Rossow, M. J., J. M. Sasaki, M. A. Digman, and E. Gratton, 2010. Raster image correlation spectroscopy in live cells. *Nat Protoc* 5:1761–1774.
16. Dertinger, T., V. Pacheco, I. von der Hocht, R. Hartmann, I. Gregor, and J. Enderlein, 2007. Two-focus fluorescence correlation spectroscopy: a new tool for accurate and absolute diffusion measurements. *Chemphyschem* 8:433–443.

PUBLICATION III

Simson P, Jepihhina N, **Laasma M**, Peterson P, Birkedal R, and Vendelin M
**Restricted ADP movement in cardiomyocytes: Cytosolic diffusion obstacles
are complemented with a small number of open mitochondrial voltage-dependent
anion channels**

Journal of Molecular and Cellular Cardiology, 97, 197–203, 2016



Original article

Restricted ADP movement in cardiomyocytes: Cytosolic diffusion obstacles are complemented with a small number of open mitochondrial voltage-dependent anion channels



Päivo Simson¹, Natalja Jepihhina¹, Martin Laasmaa, Pearu Peterson, Rikke Birkedal, Marko Vendelin^{*}

Laboratory of Systems Biology, Institute of Cybernetics, Tallinn University of Technology, Akadeemia Rd 21, 12618 Tallinn, Estonia

ARTICLE INFO

Article history:

Received 31 March 2016

Accepted 19 April 2016

Available online 31 May 2016

Keywords:

Oxidative phosphorylation

Regulation

Rat cardiomyocytes

Voltage-dependent anion channel VDAC

Intracellular diffusion obstacles

ABSTRACT

Adequate intracellular energy transfer is crucial for proper cardiac function. In energy starved failing hearts, partial restoration of energy transfer can rescue mechanical performance. There are two types of diffusion obstacles that interfere with energy transfer from mitochondria to ATPases: mitochondrial outer membrane (MOM) with voltage-dependent anion channel (VDAC) permeable to small hydrophilic molecules and cytoplasmic diffusion barriers grouping ATP-producers and -consumers. So far, there is no method developed to clearly distinguish the contributions of cytoplasmic barriers and MOM to the overall diffusion restriction. Furthermore, the number of open VDACS *in vivo* remains unknown. The aim of this work was to establish the partitioning of intracellular diffusion obstacles in cardiomyocytes. We studied the response of mitochondrial oxidative phosphorylation of permeabilized rat cardiomyocytes to changes in extracellular ADP by recording 3D image stacks of NADH auto-fluorescence. Using cell-specific mathematical models, we determined the permeability of MOM and cytoplasmic barriers. We found that only ~2% of VDACS are accessible to cytosolic ADP and cytoplasmic diffusion barriers reduce the apparent diffusion coefficient by 6–10×. In cardiomyocytes, diffusion barriers in the cytoplasm and by the MOM restrict ADP/ATP diffusion to similar extents suggesting a major role of both barriers in energy transfer and other intracellular processes.

© 2016 Elsevier Ltd. All rights reserved.

1. Introduction

The intracellular environment in the heart muscle is highly compartmentalized with not only intracellular organelles determining the compartments, but a high level of compartmentalization in the cytosol as well [1]. In this compartmentalized environment, energy transfer between ATPases and ATP-producing mitochondria plays a vital role in cardiac function. In failing hearts, energy transfer is compromised and the resulting energy starvation limits cardiac performance [2].

Several mechanisms of energy transfer have been proposed. Based on diffusion coefficients measured in frog skeletal muscle [3], direct ATP/ADP and P_i diffusion between ATPases and mitochondria seems to be sufficient to cover short diffusion distances [4,5]. To facilitate direct diffusion, the creatine kinase shuttle may form a parallel energy transfer

system [6]. Furthermore, on the basis of a study of skeletal muscle, it has been proposed that diffusion distances required by energy transfer systems can be minimized by formation of a mitochondrial reticulum [7]. Such a reticulum would provide proton-motive force conduction from cell periphery to the cell interior leading to the reduction of diffusion distances for oxygen and substrates. The importance of adequate energy transfer is obvious in failing hearts and hearts injured by ischemia-reperfusion, where the overexpression of muscle creatine kinase increases energy transfer via the creatine kinase system and is able to rescue mechanical performance [8].

In cardiomyocytes, adequate energy transfer seems to be intimately connected to the compartmentation of the intracellular environment. The formation of a mitochondrial reticulum throughout the cell [7], local mitochondrial networks [9], and the existence of intracellular compartments in the cytosol [10–14] suggests that there are barriers causing significant restriction of diffusion and forming compartments of variable size in oxidative muscle cells. The origin of this diffusion restriction is, however, not fully understood. In the studies of heart energetics, there are two types of experiments demonstrating restricted movement of ATP/ADP in cardiomyocytes. First, it has been demonstrated that 20× larger ADP concentration is required to

Abbreviations: CK, creatine kinase; DC, diffusion coefficient; GAMT, GuanidinoAcetate MethylTransferase; MOM, mitochondrial outer membrane; VDAC, voltage-dependent anion channel.

^{*} Corresponding author.

E-mail address: markov@ioc.ee (M. Vendelin).

¹ Authors contributed equally to this work.

stimulate respiration in permeabilized cardiomyocytes and fibers to reach parity of respiration in isolated mitochondria [15–17]. This indicates that there are significant diffusion restrictions on the way of ADP from solution, through the cytosol of the permeabilized cell, to the mitochondrial inner membrane where it is picked up by the adenine nucleotide translocase. Earlier, we have shown that these diffusion restrictions are of intracellular nature [18,19]. The second type of experiments demonstrate strong coupling between ATPases and ATP synthesis by mitochondria [20–22] or glycolysis [23]. Crucially, coupling between ATP synthesis in mitochondria and ATPases shows that there is a diffusion obstacle grouping mitochondria and ATPases together [24,25].

The compartmentalization of cardiomyocytes is expected to play a major role in regulation of energy transfer and, possibly, in other processes such as signaling and apoptosis in the healthy and diseased heart. There is a clear link between the level of compartmentalization and the state of cardiomyocytes. In pathological conditions, diffusion restrictions were severely reduced after acute ischemia and chronic heart failure when assessed by analyzing respiration kinetics [26–28]. On the other hand, preconditioning the heart with a brief period of ischemia reduced this effect and kept the sensitivity of respiration to ADP in permeabilized fibers low [29]. Such correlation between the state of the heart muscle and diffusion restrictions suggests that these restrictions play an important role in the regulation of intracellular processes and could be a target of therapies in the treatment of heart disease.

The overall diffusion restriction identified on the basis of respiration kinetics measurements has been suggested to be due to restricted permeability of mitochondrial outer membrane, MOM [30–33]. MOM permeability to ADP can be regulated by modulation of VDAC permeability by voltage, or by external factors, such as tubulin, for example. Indeed, on single channel experiments, tubulin has been demonstrated to reduce permeability for ADP [30]. In certain conditions, and in the presence of tubulin, a fraction of mitochondria showed a reduced apparent affinity to ADP similar to the reduction in the affinity demonstrated in permeabilized cardiomyocytes [30]. However, while tubulin can reduce VDAC permeability, to our knowledge, it has never been established what MOM permeability in cardiomyocytes is. Note that the tubulin-dependent closure of VDAC to ADP would not lead to the coupling between ATPases and mitochondrial ATP synthesis demonstrated in the absence of creatine [20–22]. To reproduce this type of experiment, diffusion restrictions surrounding ATPases and mitochondria are required [34]. Shielding of the MOM by sarcoplasmic reticulum wrapping around the mitochondria could also explain the restricted diffusion of exogenous ADP and would be in agreement with the coupling between sarcoplasmic reticulum Ca^{2+} -ATPase and mitochondria [35]. Intriguingly, this second type of diffusion restriction is consistent with the intracellular diffusion barriers forming a lattice in the cardiomyocytes, as indicated on the basis of raster image correlation microscopy data analysis [36] and 3D mathematical model of cardiomyocytes [37].

While two types of diffusion restrictions have been shown, to our knowledge, there has been no experimental method that would allow to simultaneously quantify both diffusion restrictions in a single cell. The aim of this work is to establish the partitioning of intracellular diffusion obstacles in the heart muscle. In particular, we determine the number of VDACS that allow movement of ADP through MOM and the apparent diffusion coefficient (DC) in cardiomyocytes.

2. Methods

2.1. Experimental procedures

Adult outbred Wistar rats of both sexes weighing 250–500 g were used in the experiments. Animal procedures were approved by the Estonian National Committee for Ethics in Animal Experimentation (Estonian Ministry of Agriculture). Before the experiments, animals were anesthetized with 0.5 mg/kg ketamine (Bioketan, Vetoquinol Biowet,

Gorzów Wielkopolski, Poland) and 125 mg/kg dexmedetomidine (Dexdomitor; Orion, Espoo, Finland).

2.2. Cell isolation and measurements

Cardiomyocytes were isolated as described in [38]. Cardiomyocytes were put into a diamond-shaped fast-exchange chamber (15×6 mm, RC-24N; Warner Instruments, Harvard Apparatus, March-Hugstetten, Germany) on the fluorescence microscope. Cells were allowed to sediment (5–10 min) and then they were permeabilized with Mitomed solution containing 100 $\mu\text{mol/L}$ ADP and 25 $\mu\text{g/mL}$ of saponin. Then ADP concentration was increased stepwise from 100 to 300, 500, 1000, and 2000 $\mu\text{mol/L}$. The cells were superfused for at least 5 min at each step. Next, 3D image of a cell was taken. At the end of each experiment, the precise geometry of each cell was determined by a z-stack with the step size of 1 μm in the presence of 10 $\mu\text{mol/L}$ oligomycin and 5 mmol/L sodium cyanide. Next, the cell was exposed to the uncoupler FCCP (Carbonyl cyanide 4-(trifluoromethoxy) phenylhydrazone) to determine the baseline fluorescence. Note that the experiment was performed in the flow chamber with solutions in each condition flowing through chamber to ensure the replacement of the solution used in the previous condition. Only those cells located in the middle of the chamber were used for measurements. According to the manufacturer and our simulations [18], the geometry of the chamber provided laminar flow of solutions during experiments at the used flow rate of 0.5 mL/min. For detailed descriptions of cardiomyocyte isolation, used solutions, and the fluorescence microscope see Supporting Information

2.3. Mathematical model

The mathematical model was composed to describe reaction-diffusion system with ADP/ATP diffusion inside the cardiomyocyte, and two reactions: ATPase and ATP synthase. For each studied cardiomyocyte, the 3D geometry was constructed. Boundary contours for the cell and for the nuclei were found manually from recorded image stacks and custom made software was used to generate three-dimensional surfaces representing the shape of the cell and the shapes of the nuclei. Netgen mesh generator [39] was then used to create the finite element mesh for numerical calculations. External ADP concentration was considered constant and the outer boundary of the cell was assumed to be permeable to ADP. The model equations included five parameters in total: ADP/ATP diffusion coefficient D in cytosolic and myofibrillar compartments (cytosolic for short), reaction rates $V_1 = V_{\max}(\text{ATPsyn})$, $V_2 = V_{\max}(\text{ATPase})$ and Michaelis constants $K_1 = K_m(\text{ADP})$, $K_2 = K_m(\text{ATP})$ for ATP synthase and ATPase respectively. Here K_1 is an apparent Michaelis constant for mitochondrial ATP synthesis in respect to local cytosolic ADP. In calculations we assumed the reaction rates V_1 , V_2 and the Michaelis constant K_2 to be known and varied the diffusion constant D and the apparent Michaelis constant K_1 . If looked from the point of view of the ADP/ATP diffusion restrictions, D describes the cytosolic part and K_1 the mitochondrial outer membrane part of the restrictions. The stationary state solutions were calculated numerically for various external ADP concentrations using finite element software package FEniCS [40]. As a result, ADP and ATP concentration fields inside the modeled cardiomyocyte were obtained. A linear relation between the respiration rate VO_2 and NADH fluorescence intensity was assumed, as an approximation to the measured relationship [18]. Since the respiration rate is linearly related to ATP synthase activity, we could directly link ADP concentration to local NADH fluorescence. To simulate widefield microscope imaging the theoretical fluorescence field was convolved with experimentally measured point spread function [41]. By analyzing the results for various D and K_1 combinations, the best fit for experimental data was found. See Supporting Information for formal description of the model.

2.4. Data fitting

A detailed description of image processing and data fitting is given in Supporting Information. Data is shown as mean \pm SEM.

2.5. Relationship between apparent mitochondrial affinity and VDAC permeability

The apparent Michaelis constant K_1 of mitochondrial ATP synthesis is closely related to the mitochondrial outer membrane permeability and therefore to the number of open VDACs during the experiment. This relation can be estimated from the balance of the mean ATP synthase rate inside the mitochondrion to the ADP flow through the mitochondrial outer membrane (see Supporting Information for detailed calculations). The total number of VDACs on the mitochondrial outer membrane was estimated from general data available for intracellular water and dry mass distribution in intact rat heart [42], mitochondrial positioning [43], VDAC fraction among mitochondrial proteins [44], and VDAC molecular weight [45], as shown in Supporting Information.

3. Results

To establish the distribution of intracellular diffusion obstacles in the cardiomyocytes, we turned to analysis of the response of permeabilized cardiomyocytes to variation of extracellular ADP. Earlier, we have demonstrated that the NADH-induced autofluorescence is linearly related to respiration rate of cardiomyocytes in our conditions [18]. Note that this linear relationship (see Fig. S1) was found in the conditions used in our experiments and is not an universal property of the mitochondrial respiration in the heart. Here, we assumed that by determining local NADH autofluorescence in cardiomyocytes, we can estimate respiration rate in that part of the cell. In our study we considered the following processes: ADP diffusion from extracellular solution into the permeabilized cardiomyocyte, mitochondrial oxidative phosphorylation, and endogenous ATPase activity (Fig. 1A and B). As a reporter of mitochondrial oxidative phosphorylation activity, we recorded NADH-induced fluorescence under a fluorescence microscope. As expected, variation of ADP concentration induced changes in fluorescence (Fig. 1C). The fluorescence was normalized by exposing cells to oligomycin and

cyanide (blocking oxidative phosphorylation, maximal NADH fluorescence) or uncoupling mitochondria by FCCP (all NADH oxidized, minimal fluorescence). By recording 3D image stacks under the microscope, we obtained the distribution of intracellular fluorescence (Fig. 1D). To analyze the experimental data obtained from a single cell, we composed a mathematical model that took into account the geometry of a particular cell. For that, a 3D image stack recorded in the presence of oligomycin and cyanide were used to manually mark the boundary of the cell as well the location of the nuclei (Fig. 1E) allowing us to generate a finite element mesh (Fig. 1F). By solving reaction-diffusion equations, we determined the distribution of ADP in the cell (Fig. 1G), local respiration rate, and, taking into account the relationship between NADH-induced fluorescence and respiration as well as the microscope point spread function, we calculated the distribution of intracellular fluorescence predicted by the model (Fig. 1H).

In general, measured NADH fluorescence distribution heterogeneity is induced by the heterogeneity of the mitochondrial response, cell geometry (thickness of the cell) and mitochondrial distribution (see example in Supporting Information, Fig. S3). To study the intracellular heterogeneity of the mitochondrial response and reduce the effects induced by cell geometry on measured fluorescence, we normalized the fluorescence at each location to the fluorescence recorded in the same location in the presence of oligomycin and cyanide. This normalization was performed after subtracting the fluorescence recorded in the uncoupled case (in the presence of FCCP). As it is clear from the comparison of normalized fluorescence, in the experiment (Fig. 2, left column) and in the simulations taking into account the diffusion restrictions induced by MOM and cytoplasmic obstacles, there is a similar heterogeneity within the cell (Fig. 2, middle column). In contrast, when we assumed that the intracellular diffusion in cytosolic and myofibrillar compartments is fast as in [3], the normalized fluorescence was homogeneous (Fig. 2, right column). Thus, we can conclude that closure of VDAC in the MOM is not the only diffusion obstacle leading to a high apparent K_m of mitochondrial respiration in permeabilized cardiomyocytes.

To determine the distribution of diffusion obstacles between cytoplasm and MOM, we found the least square residual between the normalized measured fluorescence and the calculated images. The diffusion restriction induced by MOM was simulated by increasing

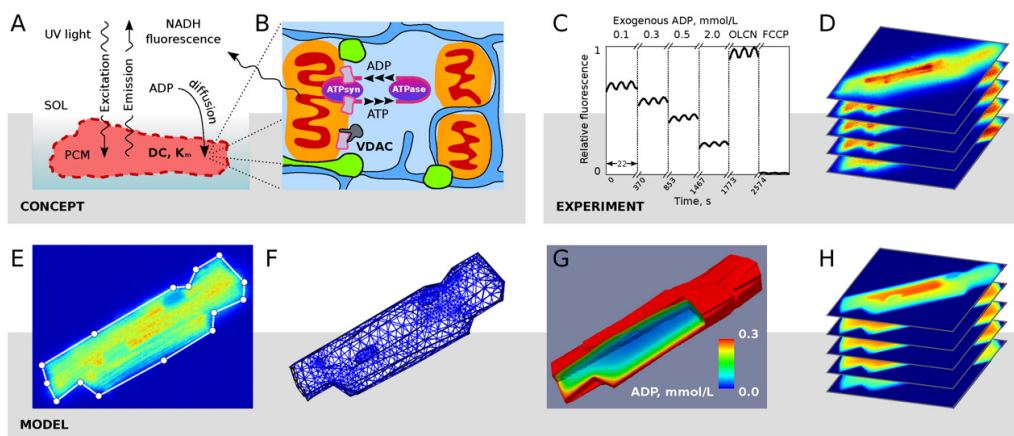


Fig. 1. Overall design of the study. To determine the DC and the number of open VDACS for ADP in mitochondrial outer membrane, we permeabilized the cardiomyocytes (PCM) and recorded NADH-induced fluorescence (A). The distribution of fluorescence in PCM is expected to be influenced by the distance of mitochondria from the permeabilized sarcolemma, intracellular DC, mitochondrial ATP synthase exposure to cytosol through open VDACS, and intracellular ATPases (B). The heterogeneity of the fluorescence was determined by recording images at different focal planes (D) for several extracellular ADP concentrations (C). Several image stacks were recorded in each condition and normalized by maximal and minimal fluorescence obtained in the presence of oligomycin and cyanide (OLCN) and FCCP, respectively (C). The experimental data obtained from PCM was analyzed by constructing cell-specific finite element model. Geometry of PCM was found manually from recorded image stacks (E) and mesh was generated (F). For given parameter set, the model calculated ADP concentration distribution within the cell (G) and corresponding NADH-induced fluorescence (H). By fitting the calculated (H) to the measured (D) fluorescence images, the DC and apparent K_m of mitochondria was found. On the basis of the apparent K_m , number of open VDACS was calculated.

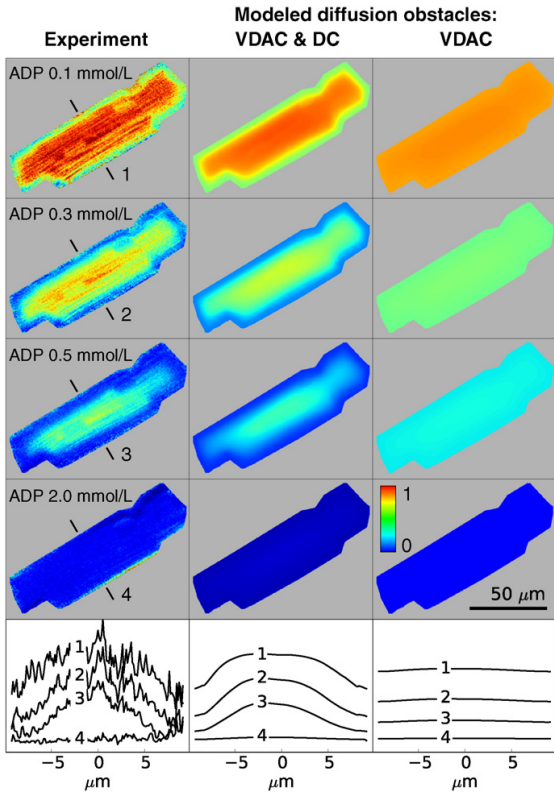


Fig. 2. NADH autofluorescence of a single permeabilized cardiomyocyte was varied by changing extracellular ADP concentrations. The fluorescence images recorded by a camera and normalized in each location by maximal fluorescence obtained in the presence of mitochondrial respiration inhibitors, oligomycin and cyanide (left column), are compared with the images calculated by the model (middle and right columns). The normalized fluorescence intensity is encoded by color, as shown on the bar. Model results are shown here for two cases: diffusion restriction between extracellular solution and mitochondrial inner membrane is either partitioned between cytosolic diffusion obstacles and mitochondrial outer membrane (middle column, $DC = 15 \mu\text{m}^2/\text{s}$, $K_m(\text{ADP}) = 0.1 \text{ mmol/L}$) or exclusively induced by closure of VDAC in mitochondrial outer membrane (right column, $DC = 200 \mu\text{m}^2/\text{s}$, $K_m(\text{ADP}) = 0.28 \text{ mmol/L}$). Note the similar intracellular heterogeneity in experiment and simulation results in the middle column. This is in sharp contrast with the results in the right column that show no significant gradients in relative autofluorescence, compared to the experimental data.

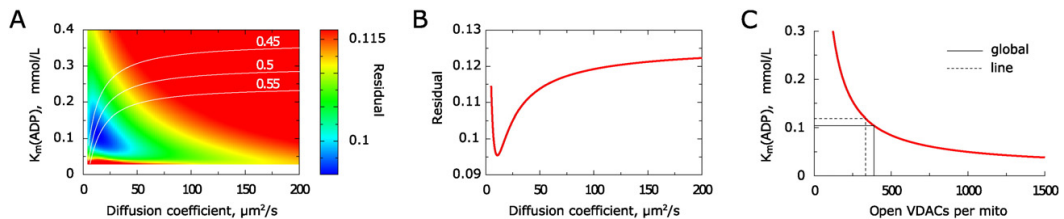


Fig. 3. Representative analysis of the model fit against the measurements. **A:** The least square residual (encoded in color) of the model fit for different combinations of cytosolic diffusion coefficient and apparent mitochondrial $K_m(\text{ADP})$. The white lines correspond to the relationship between the DC and K_m that would lead to respiration rate of 0.45, 0.5, or 0.55 times smaller than the maximal respiration rate in the presence of 0.3 mmol/L ADP in extracellular solution. Note that the minimum of the residual is next to the relationship corresponding to apparent $K_m(\text{ADP})$ of 0.3 mmol/L of a permeabilized cell. **B:** The least square residual of the fit found along the line in **A** corresponding to apparent $K_m(\text{ADP})$ of 0.3 mmol/L of a permeabilized cell (line marked by 0.5). **C:** Relationship between apparent $K_m(\text{ADP})$ of mitochondria and number of open VDACS. According to simulations performed in this case, there are 400–450 VDACS open for ADP per mitochondrion, marked by lines corresponding to the global minimum (as in **A**) or minimum found along the line (as in **B**).

apparent K_m of mitochondrial respiration to ADP in vicinity of the mitochondria [$\text{Mito } K_m(\text{ADP})$]. In the example shown in the Fig. 3A, there is a global minimum in residual at cytosolic DC $14.8 \mu\text{m}^2/\text{s}$ and $\text{Mito } K_m(\text{ADP})$ 0.108 mmol/L. This minimum is close to the line depicting the relationship between the cytosolic DC and $\text{Mito } K_m(\text{ADP})$ corresponding to the apparent K_m of permeabilized cell respiration to ADP in solution equal to 0.3 mmol/L. The corresponding relationship is shown in Fig. 3A by a white line marked with 0.5. When we calculate the residual along this relationship (i.e. along the line), the constrained minimum is at the DC equal to $10.8 \mu\text{m}^2/\text{s}$ and $\text{Mito } K_m(\text{ADP})$ equal to 0.120 mmol/L (Fig. 3B). The summary of performed experiments is shown in Table 1 with the results obtained using global minima (as in Fig. 3A) or the minima found along the relationship corresponding to the cellular $K_m(\text{ADP})$ of 0.3 mmol/L (as in Fig. 3B). As it is clear from Fig. 3C and Table 1, roughly a half of the apparent K_m of permeabilized cell respiration (0.3 mmol/L to extracellular ADP) is caused by closure of VDAC ($\sim 0.16 \text{ mmol/L}$, Table 1) with the second half contributed by cytoplasmic diffusion obstacles.

To estimate the number of open VDACS in MOM, we found the relationship between MOM permeability and $\text{Mito } K_m(\text{ADP})$. For that, we related the permeability of a single VDAC to ADP [46] to respiration rate of a single mitochondria assuming that the flux through MOM is in balance with ATP synthesis (see Supporting Information). As shown in Fig. 3C, in that example, there are about 400 VDACS accessible to ADP from cytosol in each mitochondria. On average, we found that the number of VDACS open for cytosolic ADP is approximately 300 per mitochondrion, $n = 7$. When compared to the total amount of VDACS in the membrane (around 14,000 per mitochondrion, see Supporting Information), the number of VDACS open for ADP is rather small, about 2% from all VDACS.

4. Discussion

The main result of our work is that we demonstrate and quantify two significant intracellular diffusion restrictions in cardiomyocytes. As suggested earlier on the basis of tubulin-VDAC interaction [30], we demonstrate that a significant number of VDACS are closed in cardiomyocytes and create a large diffusion obstacle for ADP diffusion through MOM. However, reduction of open VDAC by interaction with tubulin [30] or some other mechanism, such as wrapping by sarcoplasmic reticulum [35], contributes only to half of the observed diffusion restriction between mitochondrial inner membrane and the surrounding solution in permeabilized rat cardiomyocytes. The other half of the overall diffusion restriction is clearly positioned not on the MOM but on some other location in the cell, on the way between the solution and the MOM. The contribution of this diffusion obstacle is as large as VDAC closure. However, the specific location and the role of these diffusion obstacles in intracellular energetics, signaling, and apoptosis is uncertain.

Table 1
Number of open VDACS and cytosolic diffusion coefficient.

Residual minimum	D $\mu\text{m}^2/\text{s}$	$K_m(\text{ADP})$ mmol/L	Open VDACS per mito
Global	29.2 ± 3.5	0.156 ± 0.013	308 ± 31
On the 0.5-line	22.8 ± 3.4	0.183 ± 0.014	256 ± 26

Many suggested, assuming a relatively fast diffusion in muscle cells [3], that the MOM is a major diffusion obstacle [30–33]. Such obstruction of ATP/ADP diffusion by MOM gathered general support from the demonstration that tubulin interacts with VDAC and reduces VDAC permeability to ATP/ADP. Indeed, in the presence of tubulin there is a population of mitochondria with a high apparent K_m (ADP) for respiration [30]. In addition, in cancer cells, it has been demonstrated that interaction of VDAC and tubulin modulates mitochondrial oxidative phosphorylation [47]. But, to our knowledge, it has not been shown whether tubulin–VDAC interaction is indeed leading to significant diffusion obstacle *in vivo* in the heart. In addition, the strong preference of sarco-plasmic reticulum Ca^{2+} -ATPase to ATP provided by oxidative phosphorylation instead of ATP provided from solution surrounding permeabilized cardiomyocytes [21], and the demonstration of a coupling between ATPases and mitochondrial oxidative phosphorylation [48] clearly suggests that the diffusion between ATPases and MOM is relatively fast, and that there are diffusion obstacles which group ATPases and mitochondria together. In contrast, large diffusion restriction on MOM level would split them apart [37]. In this work, we resolve the controversy by demonstrating the partitioning of intracellular diffusion restrictions into two parts: one is shown to co-localize with MOM and the second is found in the cytoplasm.

The contribution of the cytosolic diffusion obstacles is clearly demonstrated in this work, where we find that they reduce the DC by 6–10 \times compared to those found in skeletal muscle using isotope traces and nuclear magnetic resonance methods [3,49]. Such a difference in the estimation of the DCs in skeletal and cardiac muscle is remarkable and can cause cell-specific properties of local intracellular signaling as well as metabolic regulation. Earlier, on the basis of raster image correlation measurements analysis, we suggested that cytosolic diffusion obstacles are not distributed uniformly within the cytoplasm but are formed by lattice-like structures with the distance between obstacles being in the range of 1 μm [36]. Here, we could not distinguish the homogenous distribution of diffusion obstacle from the lattice-like structures due to the relatively small spatial resolution of our approach. To find the specific spatial distribution of cytosolic diffusion obstacles, some other methods allowing to visualize local diffusion must be employed in future. There is a remarkable similarity in the estimated DC values when comparing our results with earlier estimates. To reduce the number of parameters fitted by the model, we neglected the anisotropy of intracellular diffusion [50]. As shown earlier, depending on the fluorescent dye, the DC in transversal direction is 60–85% of the DC in longitudinal direction [36,50]. Due to the elongated shape of the cells, the DC estimated in this work should mainly correspond to that in the transversal direction. The value of the cytosolic DC found from the analysis of fluorescence heterogeneity in the cardiomyocytes in this work ($\sim 30 \mu\text{m}^2/\text{s}$) is remarkably close the DC of fluorescently labeled ATP ($\sim 24 \mu\text{m}^2/\text{s}$) estimated using raster image correlation spectroscopy [36]. In skeletal muscle, the diffusion coefficient is 6 to 10 \times larger than the diffusion coefficient found in this work for cardiomyocytes. This difference suggests that, in skeletal muscle, the diffusion is mainly restricted on mitochondrial outer membrane level. However, further detailed studies are needed to test this suggestion.

The predicted small number of open or accessible VDACS in mitochondria lead to a significant diffusion restriction for movement of ADP through MOM. Taking into account that the present experiments

were performed at 25 °C, temperature dependence of mitochondrial respiration [51] and larger channels conductivity [52,53], the apparent K_m of oxidative respiration for cytosolic ADP in the vicinity of mitochondria would be ~ 0.25 mmol/L at 37 °C. Assuming that ADP concentration in the cell is about 0.05 mmol/L [54], this indicates an important role of energy transfer systems such as the creatine kinase (CK) shuttle in order to meet the metabolic demands of the working heart. However, a major role of CK shuttle contradicts some recent data. First, on the basis of ^{31}P -NMR magnetization transfer analysis, it has been shown that the CK shuttle can be bypassed by direct ADP diffusion at higher workloads [55]. Second, GuanidinoAcetate MethylTransferase (GAMT) knockout mice lacking a functional CK shuttle, exhibit the same cardiac performance as their wild-type littermates at basal level [56], have unaltered maximal exercise capacity and response to chronic myocardial infarction, and no obvious metabolic adaptations [57]. Intracellular diffusion restrictions and mitochondrial positioning was shown to be the same in cardiomyocytes isolated from GAMT knockouts and their wild-type littermates [19]. Thus, there is a contradiction between a small number of open VDACS found in this study and the non-exclusive role of the CK shuttle in energy transfer suggested earlier. If part of the diffusion restriction at the MOM found in our study on resting cardiomyocytes was due to shielding by the sarcoplasmic reticulum, then this would ensure energy transfer between sarcoplasmic reticulum Ca^{2+} -ATPase and the mitochondria. The sarcoplasmic reticulum would, however, still shield the mitochondria from myosin ATPase, which is the main energy consumer in working heart [58]. Thus, irrespective of the identity of the diffusion barrier at the MOM, the large restriction seems to call for a facilitation of energy transfer between myosin ATPase and mitochondria.

Our finding that only 2% of VDACS are open leads to the question on physiological role of the rest of VDACS in mitochondria. At present, we can only speculate on why 98% of VDACS are closed. Taking into account that VDAC is the main gateway for small molecules into mitochondria, we have to consider that VDAC conductivity may be enhanced in the closed state for some molecules. For example, calcium conductivity was found to be higher at closed state than in the open state [59]. Thus, closure of VDAC may enhance calcium uptake by mitochondria. Additionally, having most of VDACS closed can allow the cardiomyocytes to regulate energy transfer from direct transfer by ATP/ADP diffusion to the CK shuttle, as discussed above. Taking into account the large relative changes in ADP concentrations expected during a beat [54] due to oscillatory nature of acto-myosin ATPase [60,61], reduction of MOM conductivity to ADP would reduce influence of oscillations on mitochondrial oxidative phosphorylation regulation. The large number of closed VDACS could be also used as a reserve that is recruited at some specific conditions, for example during excessive mechanical work. All these questions are still open and are subjects of future research that should find whether more VDACS are open *in vivo*, whether VDAC permeability is significantly different from the one estimated by us at 37 °C, and whether VDAC state is modulated as the cell performs mechanical work.

In summary, we have developed a method and demonstrated as well as quantified two principal intracellular diffusion restrictions in cardiomyocytes to ADP: mitochondrial outer membrane induced by closure of a large number of VDACS and cytosolic diffusion restriction grouping ATPases and mitochondria into a single unit. These diffusion restrictions are expected to play a major role in the regulation of energy transfer and, possibly, in other processes such as signaling and apoptosis in the healthy and diseased heart.

Sources of funding

This work was supported by the European Union through the European Regional Development Fund (CENS Estonian Center of Excellence in Research) and Estonian Research Council (IUT33-7).

Appendix A. Supplementary data

Supplementary data to this article can be found online at <http://dx.doi.org/10.1016/j.yjmcc.2016.04.012>.

References

- [1] J.N. Weiss, P. Korge, The cytoplasm: no longer a well-mixed bag, *Circ. Res.* 89 (2001) 108.
- [2] R. Ventura-Clapier, A. Garnier, V. Veksler, F. Joubert, Bioenergetics of the failing heart, *BBA-Mol. Cell Res.* 1813 (2011) 1360–1372.
- [3] M.J. Kushmerick, R.J. Podolsky, Ionic mobility in muscle cells, *Science* 166 (80-) (1969) 1297–1298.
- [4] R.A. Meyer, H.L. Sweeney, M.J. Kushmerick, A simple analysis of the “phosphocreatine shuttle”, *AJP: Cell Physiol.* 246 (1984) C365–C377.
- [5] S. Kinsey, B. Locke, R. Dillaman, Molecules in motion: influences of diffusion on metabolic structure and function in skeletal muscle, *J. Exp. Biol.* 214 (2011) 263–274.
- [6] S.P. Bessman, P.J. Geiger, Transport of energy in muscle: the phosphocreatine shuttle, *Science* 211 (1981) 448–452.
- [7] B. Glancy, L. Hartnell, D. Malide, Z. Yu, C. Combs, P. Connelly, S. Subramaniam, R. Balaban, Mitochondrial reticulum for cellular energy distribution in muscle, *Nature* 523 (2015) 617–620.
- [8] A. Akki, J. Su, T. Yano, A. Gupta, Y. Wang, M. Leppo, V. Chacko, C. Steenbergen, R. Weiss, Creatine kinase overexpression improves ATP kinetics and contractile function in postischemic myocardium, *Am. J. Physiol. Heart Circ. Physiol.* 303 (2012) H844–H852.
- [9] V. Eisner, G. Lenaers, G. Hajnóczy, Mitochondrial fusion is frequent in skeletal muscle and supports excitation–contraction coupling, *J. Cell Biol.* 205 (2014) 179–195.
- [10] S. Gudbjarnason, P. Mathes, K.G. Ravens, Functional compartmentation of ATP and creatine phosphate in heart muscle, *J. Mol. Cell. Cardiol.* 1 (1970) 325–339.
- [11] R. Fischmeister, L.V. Castro, A. Abi-Gerges, F. Rochais, J. Jurevičius, J. Leroy, G. Vandecasteele, Compartmentation of cyclic nucleotide signaling in the heart: the role of cyclic nucleotide phosphodiesterases, *Circ. Res.* 99 (2006) 816–828.
- [12] G. Csordás, C. Hajnóczy, Sr/er–mitochondrial local communication: calcium and rds, *BBA-Bioenerg.* 1787 (2009) 1352–1362.
- [13] B.Z. Silverman, A. Warley, J.I. Miller, A.F. James, M.J. Shattock, Is there a transient rise in sub-sarcolemmal Na and activation of Na/K pump current following activation of I(Na) in ventricular myocardium? *Cardiovasc. Res.* 57 (2003) 1025–1034.
- [14] M.R. Abraham, V. Selivanov, D. Hodgson, D. Pucar, L. Zingman, B. Wieringa, P. Dzeja, A. Alekseev, A. Terzic, Coupling of cell energetics with membrane metabolic sensing, *J. Biol. Chem.* 277 (2002) 24427–24434.
- [15] V.I. Veksler, A.V. Kuznetsov, V.G. Sharov, V.I. Kapelko, V.A. Saks, Mitochondrial respiratory parameters in cardiac tissue: a novel method of assessment by using saponin-skinned fibers, *BBA* 892 (1987) 191–196.
- [16] L. Kümmel, Ca,Mg-ATPase activity of permeabilized rat heart cells and its functional coupling to oxidative phosphorylation of the cells, *Cardiovasc. Res.* 22 (1988) 359–367.
- [17] A. Kuznetsov, V. Veksler, F. Gellerich, V. Saks, R. Margreiter, W. Kunz, Analysis of mitochondrial function in situ in permeabilized muscle fibers, tissues and cells, *Nat. Protoc.* 3 (2008) 965–976.
- [18] N. Jephthina, N. Beraud, M. Sepp, R. Birkedal, M. Vendelin, Permeabilized rat cardiomyocyte response demonstrates intracellular origin of diffusion obstacles, *Biophys. J.* 101 (2011) 2112–2121.
- [19] J. Branovets, M. Sepp, S. Kotlyarova, N. Jephthina, N. Sokolova, D. Aksentijevic, C. Lygate, S. Neubauer, M. Vendelin, R. Birkedal, Unchanged mitochondrial organization and compartmentation of high-energy phosphates in creatine-deficient *GAMT*^{−/−} mouse hearts, *Am. J. Physiol. Heart Circ. Physiol.* 305 (2013) H506–H520.
- [20] E.K. Seppet, T. Kaambre, P. Sikk, T. Tiivel, H. Vija, M. Tonkonogi, K. Sahlin, L. Kay, F. Appaix, U. Braun, M. Eimre, V.A. Saks, Functional complexes of mitochondria with Ca,MgATPases of myofibrils and sarcoplasmic reticulum in muscle cells, *BBA* 1504 (2001) 379–395.
- [21] A. Kaasik, V. Veksler, E. Boehm, M. Novotova, A. Minajeva, R. Ventura-Clapier, Energetic crosstalk between organelles: architectural integration of energy production and utilization, *Circ. Res.* 89 (2001) 153–159.
- [22] V. Saks, T. Kaambre, P. Sikk, M. Eimre, E. Orlova, K. Paju, A. Piirsoo, F. Appaix, L. Kay, V. Regitz-Zagrosek, E. Fleck, E. Seppet, Intracellular energetic units in red muscle cells, *Biochem. J.* 356 (2001) 643–657.
- [23] M. Sepp, N. Sokolova, S. Jugai, M. Mandel, P. Peterson, M. Vendelin, Tight coupling of Na⁺/K⁺-ATPase with glycolysis demonstrated in permeabilized rat cardiomyocytes, *PLoS One* 9 (2014), e99413.
- [24] V. Saks, A. Kuznetsov, T. Andrienko, Y. Usson, F. Appaix, K. Guerrero, T. Kaambre, P. Sikk, M. Lemba, M. Vendelin, Heterogeneity of adp diffusion and regulation of respiration in cardiac cells, *Biophys. J.* 84 (2003) 3436–3456.
- [25] M. Vendelin, M. Eimre, E. Seppet, N. Peet, T. Andrienko, M. Lemba, J. Engelbrecht, E. Seppet, V. Saks, Intracellular diffusion of adenosine phosphates is locally restricted in cardiac muscle, *Mol. Cell. Biochem.* 256 (257) (2004) 229–241.
- [26] L. Kay, V.A. Saks, A. Rossi, Early alteration of the control of mitochondrial function in myocardial ischemia, *J. Mol. Cell. Cardiol.* 29 (1997) 3399–3411.
- [27] L. Kay, Z. Daneshrad, V.A. Saks, A. Rossi, Alteration in the control of mitochondrial respiration by outer mitochondrial membrane and creatine during heart preservation, *Cardiovasc. Res.* 34 (1997) 547–556.
- [28] S. Boudina, M. Laclau, L. Tariosse, D. Daret, G. Gouverneur, S. Bonoron-Adèle, V. Saks, P. Dos Santos, Alteration of mitochondrial function in a model of chronic ischemia in vivo in rat heart, *Am. J. Physiol. Heart Circ. Physiol.* 282 (2002) H821–H831.
- [29] M.N. Laclau, S. Boudina, J.B. Thambo, L. Tariosse, G. Gouverneur, S. Bonoron-Adèle, V.A. Saks, K.D. Garlid, P. Dos Santos, Cardioprotection by ischemic preconditioning preserves mitochondrial function and functional coupling between adenosine nucleotide translocase and creatine kinase, *J. Mol. Cell. Cardiol.* 33 (2001) 947–956.
- [30] T. Rostovtseva, K. Sheldon, E. Hassanzadeh, C. Monge, V. Saks, S. Bezrukov, D. Sackett, Tubulin binding blocks mitochondrial voltage-dependent anion channel and regulates respiration, *PNAS* 105 (2008) 18746–18751.
- [31] P. Gurnev, T. Rostovtseva, S. Bezrukov, Tubulin-blocked state of VDAC studied by polymer and ATP partitioning, *FEBS Lett.* 585 (2011) 2363–2366.
- [32] M. Gonzalez-Granillo, A. Grichine, R. Guzun, Y. Usson, K. Tepp, V. Chekulayev, I. Shevchuk, M. Karu-Varikmaa, A. Kuznetsov, M. Grimm, V. Saks, T. Kaambre, Studies of the role of tubulin beta II isotype in regulation of mitochondrial respiration in intracellular energetic units in cardiac cells, *J. Mol. Cell. Cardiol.* 52 (2012) 437–447.
- [33] R. Guzun, M. Karu-Varikmaa, M. Gonzalez-Granillo, A. Kuznetsov, L. Michel, C. Cotten-Rousselle, M. Saaremaa, T. Kaambre, M. Metsis, M. Grimm, C. Auffray, V. Saks, Mitochondria–cytoskeleton interaction: distribution of beta-tubulins in cardiomyocytes and HL-1 cells, *BBA* 1807 (2011) 458–469.
- [34] M. Vendelin, M. Eimre, E. Seppet, N. Peet, T. Andrienko, M. Lemba, J. Engelbrecht, E. Seppet, V. Saks, Intracellular diffusion of adenosine phosphates is locally restricted in cardiac muscle, *Mol. Cell. Biochem.* 256–257 (2004) 229–241.
- [35] R. Birkedal, M. Laasmaa, M. Vendelin, The location of energetic compartments affects energetic communication in cardiomyocytes, *Front. Physiol.* 5 (2014) 376.
- [36] A. Illaste, M. Laasmaa, P. Peterson, M. Vendelin, Analysis of molecular movement reveals lattice-like obstructions to diffusion in heart muscle cells, *Biophys. J.* 102 (2012) 739–748.
- [37] H. Ramay, M. Vendelin, Diffusion restrictions surrounding mitochondria: a mathematical model of heart muscle fibers, *Biophys. J.* 97 (2009) 443–452.
- [38] M. Sepp, M. Vendelin, H. Vija, R. Birkedal, ADP compartmentation analysis reveals coupling between pyruvate kinase and ATPases in heart muscle, *Biophys. J.* 98 (2010) 2785–2793.
- [39] J. Schöberl, Netgen an advancing front 2d/3d-mesh generator based on abstract rules, *Comput. Vis. Sci.* 1 (1997) 41–52.
- [40] A. Logg, K. Mardal, G. Wells, Automated Solution of Differential Equations by the Finite Element Method, Springer, Berlin Heidelberg, 2012.
- [41] M. Laasmaa, M. Vendelin, P. Peterson, Application of regularized Richardson-Lucy algorithm for deconvolution of confocal microscopy images, *J. Microsc.* 243 (2011) 124–140.
- [42] M. Aliev, P. Santos, J. Hoerter, S. Soboll, A. Tikhonov, V. Saks, Water content and its intracellular distribution in intact and saline perfused rat hearts revisited, *Cardiovasc. Res.* 53 (2002) 48–58.
- [43] R. Birkedal, H.A. Shiels, M. Vendelin, Three-dimensional mitochondrial arrangement in ventricular myocytes: from chaos to order, *Am. J. Physiol. Cell. Physiol.* 291 (2006) C1148.
- [44] T. Rostovtseva, M. Colombini, ATP flux is controlled by a voltage-gated channel from the mitochondrial outer membrane, *J. Biol. Chem.* 271 (1996) 28006.
- [45] J. Lemasters, E. Holmuhamedov, Voltage-dependent anion channel (VDAC) as mitochondrial governor—thinking outside the box, *BBA-Mol. Basis Dis.* 2006 (1762) 181–190.
- [46] T. Rostovtseva, M. Colombini, VDAC channels mediate and gate the flow of ATP: implications for the regulation of mitochondrial function, *Biophys. J.* 72 (1997) 1954–1962.
- [47] E. Maldonado, K. Sheldon, D. Dehart, J. Patnaik, Y. Manevich, D. Townsend, S. Bezrukov, T. Rostovtseva, J. Lemasters, Voltage-dependent anion channels modulate mitochondrial metabolism in cancer cells regulation by free tubulin and erastin, *J. Biol. Chem.* 288 (2013) 11920–11929.
- [48] E. Seppet, T. Kaambre, P. Sikk, T. Tiivel, H. Vija, M. Tonkonogi, K. Sahlin, L. Kay, F. Appaix, U. Braun, M. Eimre, V. Saks, Functional complexes of mitochondria with Ca,MgATPases of myofibrils and sarcoplasmic reticulum in muscle cells, *BBA-Bioenerg.* 1504 (2001) 379–395.
- [49] R. de Graaf, A. van Kranenburg, K. Nicolay, In vivo 31P-NMR diffusion spectroscopy of ATP and phosphocreatine in rat skeletal muscle, *Biophys. J.* 78 (2000) 1657–1664.
- [50] M. Vendelin, R. Birkedal, Anisotropic diffusion of fluorescently labeled ATP in rat cardiomyocytes determined by raster image correlation spectroscopy, *Am. J. Physiol. Cell. Physiol.* 295 (2008) C1302–C1315.
- [51] V.N. Samartsev, S.A. Chezanova, L.S. Polishchuk, A.P. Paydyganov, O.V. Vidyakina, I.P. Zeldi, Temperature dependence of rat liver mitochondrial respiration with uncoupling of oxidative phosphorylation by fatty acids. Influence of inorganic phosphate, *Biochem. Mosc.* 68 (2003) 618–626.
- [52] I. Biró, S. Pezeshki, H. Weingart, M. Winterhalter, U. Kleinekathöfer, Comparing the temperature-dependent conductance of the two structurally similar *E. coli* porins OmpC and OmpF, *Biophys. J.* 98 (2010) 1830–1839.
- [53] E. Nestorovich, V. Karginov, A. Berezhkovskii, V.A. Parsegian, S. Bezrukov, Kinetics and thermodynamics of binding reactions as exemplified by anthrax toxin channel blockage with a cationic cyclodextrin derivative, *PNAS* 109 (2012) 18453–18458.
- [54] M. Vendelin, O. Kongas, V. Saks, Regulation of mitochondrial respiration in heart cells analyzed by reaction-diffusion model of energy transfer, *Am. J. Physiol. Cell. Physiol.* 278 (2000) C747–C764.
- [55] M. Vendelin, J. Hoerter, P. Mateo, S. Soboll, B. Gillet, J. Mazet, Modulation of energy transfer pathways between mitochondria and myofibrils by changes in performance of perfused heart, *J. Biol. Chem.* 285 (2010) 37240–37250.
- [56] J. Schneider, L. Stork, J. Bell, M. Hove, D. Isbrandt, K. Clarke, H. Watkins, C. Lygate, S. Neubauer, Cardiac structure and function during ageing in energetically compromised guanidinoacetate N-methyltransferase (*GAMT*)-knockout mice – a one year longitudinal mri study, *J. Cardiovasc. Magn. Reson.* 10 (2008) 9.
- [57] C. Lygate, D. Aksentijevic, D. Dawson, M. ten Hove, D. Phillips, J. de Bono, D. Medway, L. Sebag-Montefiore, I. Hunyor, K. Channon, K. Clarke, S. Zervou, H. Watkins, R.

- Balaban, S. Neubauer, Living without creatine: unchanged exercise capacity and response to chronic myocardial infarction in creatine-deficient mice, *Circ. Res.* 112 (2013) 945–955.
- [58] H. Suga, Ventricular energetics, *Physiol. Rev.* 70 (1990) 247–277.
- [59] W. Tan, M. Colombini, Vdac closure increases calcium ion flux, *Biochim. Biophys. Acta Biomembr.* 1768 (2007) 2510–2515.
- [60] M. Vendelin, P.H.M. Bovendeerd, T. Arts, J. Engelbrecht, D.H.v. Campen, Cardiac mechanoenergetics replicated by cross-bridge model, *Ann. Biomed. Eng.* 28 (2000) 629–640.
- [61] M. Kalda, P. Peterson, M. Vendelin, Cross-bridge group ensembles describing cooperativity in thermodynamically consistent way, *PLoS One* 10 (2015), e0137438.

Supporting Information:

Restricted ADP movement in cardiomyocytes: cytosolic diffusion obstacles are complemented with a small number of open mitochondrial voltage-dependent anion channels

Päivo Simson*, Natalja Jephina*, Martin Laasmaa, Pearu Peterson, Rikke Birkedal, and Marko Vendelin
Laboratory of Systems Biology, Institute of Cybernetics, Tallinn University of Technology, Akadeemia Rd 21, 12618 Tallinn, Estonia

* Authors contributed equally to this work

This Supporting Information presents the detailed experimental methods, model and simulation description. In addition, example case is shown where fluorescence was normalized globally, instead of local normalization as presented in the main text. Finally, analysis results for each considered cell are summarized in the table.

1 ISOLATION OF CARDIOMYOCYTES

Cardiomyocytes were isolated as described in [1]. The animals received an i.p. injection of 2500 U heparin and were anesthetized with 0.5 mg/kg ketamine (Bioketan, Vetoquinol Biowet, Gorzów Wielkopolski, Poland) and 125 mg/kg dexmedetomidine (Dexdomitor; Orion, Espoo, Finland). The excised heart was swiftly placed in ice-cold wash solution (see composition below) to minimize ischemic damage. The heart was Langendorff perfused with wash solution at constant pressure of 80 cm H₂O for 5 minutes before the perfusate was changed to digestion solution containing 0.75 – 1 mg/ml of liberase TH (Roche; see composition below). This solution was recirculated with a rate of 5.1 ml/min until the pressure was 0 mm Hg (approx. 40 min). After this, the ventricle was cut into four pieces and transferred into 10 ml digestion solution. It was incubated with gentle shaking in waterbath at 37°C for additional 10 – 20 minutes. When the ventricular tissue pieces began to disassemble, they were transferred to sedimentation solution (see composition below), cut a few times with a scissor and the cells were suspended with a pipette. The cell suspension was passed through a nylon mesh and viable cells separated by sedimentation. Calcium concentration in the cell suspension was increased gradually to 1 mmol/L with repeated wash-sedimentation cycles after which the cells were washed three times with large volumes of Ca²⁺-free solution. The cells were stored in this solution at room temperature until use.

2 SOLUTIONS AND CHEMICALS

Solutions used in isolation of cardiomyocytes. Wash solution contained (in mmol/L): 117 NaCl, 5.7 KCl, 4.4 NaHCO₃, 1.5 KH₂PO₄, 1.7 MgCl₂, 21 HEPES, 20 taurine, 11.7 glucose, and pH was adjusted at 25°C to 7.4 with NaOH. Digestion solution had the same composition as the wash solution with the addition of 3 mg/ml BSA (Roche, 10 775 835 001), 0.25 mg/ml liberase TH (Roche). In some cases, 0.0125 % trypsin was added to the digestion solution. Sedimentation solution had the same composition as the wash solution with the addition of 2 mg/mL BSA (Roche, 10 775 835 001), 10 μmol/L leupeptine (Roche, 11 034 626 001), 2 μmol/L soybean trypsin inhibitor (Fluka, 93619).

Measurements were performed in Mitomed solution. It contained (in mmol/L): 3 KH₂PO₄, 3 MgCl₂, 20 HEPES, 0.5 EGTA, 20 taurine, 0.5 dithiothreitol and 60 lactobionate, 110 sucrose, 5 glutamate and 2 malate, and pH was adjusted at 25°C to 7.1 with KOH. For cell membrane permeabilization 25 μg/mL saponin and 100 μmol/L ADP were added to Mitomed solution.

Concentrations of the uncoupler and respiration blockers were: 10 μmol/L FCCP (Carbonyl cyanide 4-(trifluoromethoxy)phenylhydrazone), 10 μmol/L oligomycin A (Tebu-bio, bia-01059-1) and 5 mmol/L sodium cyanide.

All chemicals were obtained from Sigma-Aldrich if not mentioned otherwise.

3 FLUORESCENCE MICROSCOPY

Experiments were performed on an inverted Nikon Eclipse Ti-U microscope (Nikon, Japan) equipped with two tiers of motorized filter turrets. 60x water-immersion objective (Nikon, Plan Apo VC 60x/1.2 WI, Amstelveen, the Netherlands) was used in the experiments. For images of NADH autofluorescence, light from a Prior Lumen 200 with a 200W metal halide lamp with extended wavelength (Prior Scientific, Cambridge, United Kingdom) was passed via a liquid guide into the upper filter turret. For NADH recordings, the light was passed through a 340/26 nm excitation filter onto a 400 nm long pass dichroic mirror, which deflected the light onto the specimen. Light emitted from the specimen passed back through the upper filter cube to a 510 XR dichroic in the lower filter cube and was reflected through a 460/80 nm emission filter to an Andor Ixon EMCCD camera (Andor Technologies, Belfast, United Kingdom). All filters were obtained from AHF Analysentechnik AG, Germany. Optical sectioning was carried out by a piezoelectric objective positioning system (Piezosystem Jena GmbH, MIPOS 250SG M25, Jena, Germany). To reduce photobleaching through limitation of light exposure, Uniblitz shutter (VCM-D1, Vincent Associates, Rochester, USA) was used. Image acquisition and microscope control during experiments were performed using the software written in our laboratory.

At each experimental condition, such as ADP concentration, exposure to FCCP, or OL+CN, at least three 3D image stacks were acquired. Each 3D stack consisted of 5 images acquired

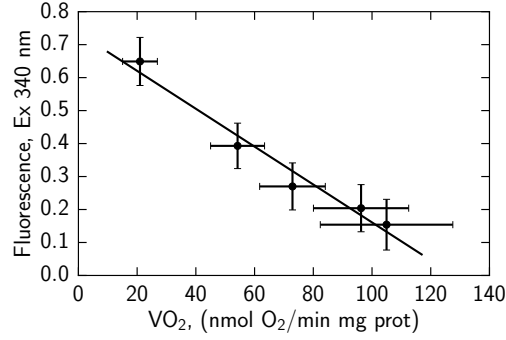


FIGURE S1: Relationship between relative NADH fluorescence and mitochondrial respiration rate in permeabilized cardiomyocytes exposed to the different amount of ADP in solution to stimulate mitochondrial respiration. The experimental points are fitted using linear regression. Data from [2].

at different focal planes. The acquired 3D stacks were averaged leading to 3D image of NADH fluorescence for the corresponding condition. In the analysis, these averaged 3D images were used.

4 REACTION-DIFFUSION MODEL FOR ADP AND ATP

To describe the changes in ADP and ATP concentrations we consider a reaction-diffusion model. We introduce the following notation for the concentrations:

$$u = [ADP], \quad v = [ATP],$$

for the associated maximal reaction rates:

$$V_1 = V_{max}^{ATPsyn}, \quad V_2 = V_{max}^{ATPase},$$

and for the Michaelis constants:

$$K_1 = K_m^{ATPsyn}, \quad K_2 = K_m^{ATPase}.$$

As has been done for representing cardiac electric activation propagation simulations using bidomain models [3], we use continuum approximation of intracellular environment and, in the model, follow changes in ATP and ADP concentrations within cytosol and myofibrils. The model equations, describing ADP/ATP diffusion, ATPase and ATP synthase inside the cytosolic and myofibrillar compartments, are

$$\frac{\partial u}{\partial t} - D\nabla^2 u = V_{ATPase}(v) - V_{ATPsyn}(u), \quad (1)$$

$$\frac{\partial v}{\partial t} - D\nabla^2 v = V_{ATPsyn}(u) - V_{ATPase}(v), \quad (2)$$

where the ATP synthase and ATPase reaction rates are given by Michaelis–Menten formulæ:

$$V_{ATPsyn}(u) = V_1 \frac{u}{u + K_1}, \quad V_{ATPase}(v) = V_2 \frac{v}{v + K_2}.$$

Here we assumed the intracellular diffusion constants for ADP and ATP to be equal, e.g. $D_{ADP} = D_{ATP} = D$. Notice that

the apparent Michaelis constant K_1 reflects stimulation of mitochondrial respiration by cytosolic ADP in the vicinity of the mitochondrion, Mito $K_m(ADP)$ in the main text.

The sum of ADP and ATP concentrations is governed by

$$\frac{\partial}{\partial t}(u + v) + D\nabla^2(u + v) = 0,$$

which is linear and homogeneous diffusion equation. The stationary state solution corresponding to the boundary conditions

$$u|_S = u_{out} = const, \quad v|_S = v_{out} = const,$$

where S denotes the surface of the cell, is

$$u + v = u_{out} + v_{out} = const.$$

Since there is a flow in the chamber, we assume that there is no ATP buildup in the solution ($v_{out} = 0$), and we have

$$v = u_{out} - u.$$

Substituting this relationship into the equation [1], we get a single nonlinear partial differential equation for ADP concentration u inside the cell:

$$D\nabla^2 u = V_1 \frac{u}{u + K_1} - V_2 \frac{u_{out} - u}{u_{out} - u + K_2}.$$

Variational form of this equation is

$$\begin{aligned} -D \int_{\Omega} \nabla u \cdot \nabla v^* d\Omega + \int_S \frac{\partial u}{\partial n} v^* dS \\ = \int_{\Omega} \left[V_1 \frac{u}{u + K_1} - V_2 \frac{u_{out} - u}{u_{out} - u + K_2} \right] v^* d\Omega, \quad (3) \end{aligned}$$

where Ω is the volume of the modeled cell. v^* is the test function required to vanish on the parts of the boundary where u is known. In the present problem this implies that $v^* = 0$ on the whole boundary S , and thus the second term on the left side of the equation [3] vanishes everywhere.

NADH fluorescence is related to respiration rate using a linear approximation of the relationship between respiration rate and the fluorescence [2]. The linear fit through the data points

is shown in Fig.S1 with the coefficient of determination $r^2 = 0.97$. Note that this linear relationship was found in the conditions used in our experiments and is not an universal property of the mitochondrial respiration in the heart.

In our model, NADH fluorescence F_{NADH} at position \mathbf{r} is calculated from local ATP synthesis rate:

$$F_{NADH}(\mathbf{r}) = \gamma \cdot \left(1 - \frac{u(\mathbf{r})}{u(\mathbf{r}) + K_1} \right),$$

where γ is a normalization constant. By convolving the fluorescence signal F_{NADH} with experimentally determined point spread function of the used fluorescence microscope, the images were calculated that were later compared with the measurements (see below).

5 SOLVING THE REACTION-DIFFUSION PROBLEM

Equation [3] was solved numerically by the finite element software package FEniCS [4]. Solutions for each modeled cell for 0.1 mmol/L, 0.3 mmol/L, 0.5 mmol/L and 2.0 mmol/L of exogenous ADP (u_{out}) were calculated for a large set of D and K_1 combinations. The results were compared to experiment and the best fit was found using the methods described below (section Image analysis and data fitting).

6 MODEL PARAMETER VALUES

The maximal mitochondrial ATP synthase activity in the cell, when normalized to cytosolic together with myofibrillar fraction, was $V_1 = 0.54$ mmol/L ATP/s. This was found taking into account ADP/O₂ ratio 6, maximal mitochondrial respiration rate 13.5 $\mu\text{mol O}_2/\text{min}\cdot\text{g dw}$ [5], total dry mass, cellular, and myofibrillar and sarcoplasmic volumes in 1 kg of heart tissue [6].

The maximal ATPase rate, $V_2 = 0.18$ mmol/L/s, was calculated on the basis of the maximal mitochondrial ATP synthase activity taking into account that, in our conditions, the exogenous ATP-stimulated respiration in permeabilized cardiomyocytes was 1/3 from the maximal ADP-stimulated respiration rate [1]. The apparent Michaelis constant for bulk ATPases was taken $K_2 = 0.3$ mmol/L, the upper limit used in [5, 7] on the basis of the fits in [1].

7 EMPIRICAL EQUATION CONNECTING D AND K_1

Regional ATP synthesis rate is approximated by Michaelis-Menten relationship and is dependent on cytosolic ADP concentration in the vicinity of mitochondria:

$$V_{ATPsyn}(u) = V_1 \frac{u}{u + K_1}.$$

Since ATP synthesis rate can be related to respiration rate through linear relationship [8], the found relationships for respiration rate can be directly applied to ATP synthesis rate. For permeabilized cells, the exogenous ADP has to be

~ 0.3 mmol/L to reach half-maximal respiration rate [1]. In the model terms, it can be expressed as

$$\frac{1}{\Omega} \int_{\Omega} V_{ATPsyn}(u^*(\mathbf{r})) d\Omega = \frac{1}{\Omega} \int_{\Omega} \frac{1}{2} V_{max}(\mathbf{r}) d\Omega,$$

where $u^*(\mathbf{r})$ is a solution of the equation [3] that satisfies the boundary condition $u^*|_S = 0.3$ mmol/L. Since in the model we assumed that $V_{max}(\mathbf{r})$ is constant in the cell, we get

$$\frac{1}{\Omega} \int_{\Omega} \frac{u^*(\mathbf{r})}{u^*(\mathbf{r}) + K_1} d\Omega = \frac{1}{2}. \quad (4)$$

This non-linear equation can be solved with respect to D for given K_1 . For that, at each iteration, for given D and K_1 , ADP concentration and average ATP synthesis rate was found by solving Eq. [3] with exogenous [ADP] is 0.3 mmol/L as an boundary condition. By comparing calculated ATP synthesis rate with the expected half-maximal rate, non-linear solver adjusted D until the solution satisfied Eq. [4]. This solution corresponds to D and K_1 values lying on the 0.5-line of Fig.3 A.

8 TOTAL NUMBER OF VDACS PER MITOCHONDRION

To estimate the number of VDACS per mitochondrion, we took into account mitochondrial distribution in rat cardiomyocytes [9] as well as the following morphological data for the heart:

- Total volume of mitochondria, $\Omega_{all\ mitos} = 32.7\%$ of cell volume = 248 ml = $248 \cdot 10^{12} \mu\text{m}^3$ per kg wet weight [6];
- Dry mass of mitochondria, $m_{all\ mitos;dry} = 89.4$ g per kg wet weight [6];
- Total mass of mitochondrial protein $\approx 75\%$ of mitochondrial dry mass [6];
- Total mass of VDACS $\approx 0.3\%$ of all mitochondrial protein [10].

We have earlier shown that mitochondria in rat are distributed in highly ordered pattern along the parallel strands with the longitudinal distance between mitochondrial centers $d \approx 0.95 \mu\text{m}$ and transversal distance $a \approx 1.8 \mu\text{m}$ [9]. Here, we assume that transversally mitochondria are aligned along a hexagon, as in Fig.S2. Assuming that all the mitochondria have the same shape (Fig.S2B, dashed circles denoting the mitochondria), it is clear that the numbered volumes inside the hexagon occupy three times the volume of one mitochondrion. Since the total area of the equilateral triangle is $\sqrt{3}/4 a^2$, the relative volume occupied by mitochondria (32.7% in heart) can be expressed as

$$\frac{\Omega_{all\ mitos}}{\Omega_{cell}} = \frac{3 \times \Omega_{mito} \frac{1}{d}}{6 \times \frac{\sqrt{3}}{4} a^2}.$$

From here, the volume of one mitochondrion equals

$$\Omega_{mito} = 0.327 \frac{\sqrt{3}}{2} a^2 d = 0.872 \mu\text{m}^3.$$

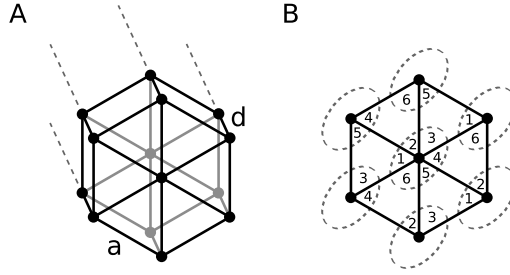


FIGURE S2: Hexagonal arrangement of mitochondria.

Notice that the calculated volume does not depend on the exact shape of the mitochondrion. If the mitochondria can be considered identical, the volume of one mitochondrion is determined by the volume ratio and the spatial arrangement only.

From a single mitochondrion volume, we can get the number of mitochondria per kg of wet weight

$$N_{mitos} = \frac{\Omega_{all\ mitos}}{\Omega_{mito}} = \frac{248 \cdot 10^{12}}{0.872} = 285 \cdot 10^{12},$$

as well as the mass of a single mitochondrion

$$m_{mito;dry} = \frac{m_{all\ mitos;dry}}{N_{mitos}} = \frac{89.4}{285 \cdot 10^{12}} = 0.314 \cdot 10^{-12} g.$$

Thus, the total mass of VDACS per one mitochondrion is therefore

$$\begin{aligned} m_{all\ vdacs\ per\ mito} &= m_{mito;dry} \cdot 75\% \cdot 0.3\% \\ &= 0.314 \cdot 10^{-12} \cdot 0.75 \cdot 0.003 = 0.707 \cdot 10^{-15} g, \end{aligned}$$

and, taking into account VDAC molecular weight [30 kDa = $5 \cdot 10^{-20}$ g, [11]], the number of VDACS per mitochondrion is

$$N_{vdacs\ per\ mito} = \frac{m_{all\ vdacs\ per\ mito}}{m_{vdac}} = \frac{0.707 \cdot 10^{-15}}{5 \cdot 10^{-20}} \approx 14000.$$

Assuming the surface area of the mitochondrion to be $5 \mu m^2$ we get approximately 2800 VDACS per μm^2 and the mean distance between VDAC centers on the mitochondrial outer membrane around 20 nm. Note that the diameter of the VDAC's aqueous channel is 2.6-3 nm [11].

9 NUMBER OF OPEN VDACS

The number of open VDACS is found by taking into account that, at steady state, ADP flux through mitochondrial outer membrane is equal to ATP synthesis rate inside the mitochondrion. At half-maximal respiration rate, for a single mitochondrion, we have

$$p_{mito}(u_{cyto} - u_{mito}) = \frac{V_1 \Omega_{cyto} + \Omega_{myo}}{2 N_{mitos}},$$

where p_{mito} is the permeability of mitochondrial outer membrane, u_{cyto} and u_{mito} are ADP concentrations in cytosol and

in the mitochondrial inter membrane space, respectively; Ω_{cyto} and Ω_{myo} are volumes of sarcoplasmic and myofibrillar compartments per kg wet weight, respectively; and N_{mitos} is number of mitochondria per kg wet weight. At half-maximal respiration rate, ADP concentrations would be the corresponding Michaelis-Menten constants leading to

$$p_{mito} = \frac{V_1 \Omega_{cyto} + \Omega_{myo}}{2 N_{mitos}} \frac{1}{K_1 - K_m^{ANT}},$$

where K_m^{ANT} is an apparent K_m for adenine nucleotide translocase. From here, assuming that VDAC conductance for ATP and ADP in closed state is negligible, we can get the number of open VDACS N_{vdac}^{open} in single mitochondrion by dividing total mitochondrial outer membrane permeability p_{mito} with a single VDAC permeability $p_{vdac} = 1.1 \times 10^{-2} \mu m^3/s$ [12]:

$$N_{vdac}^{open} = \frac{1}{p_{vdac}} \frac{V_1 \Omega_{cyto} + \Omega_{myo}}{2 N_{mitos}} \frac{1}{K_1 - K_m^{ANT}}. \quad (5)$$

For example, for $K_1 = 0.156$ mmol/L found as an average apparent K_m for cytoplasmic ADP of mitochondrial respiration (Table S1), taking into account the myofibrillar and sarcoplasmic volumes in 1 kg of heart tissue [6], assuming that $K_m^{ANT} = 0.015$ mmol/L, we get $N_{vdac}^{open} = 291$ VDACS open for ADP per single mitochondria. This is only 2% of the total number of VDACS on the mitochondrial outer membrane, which was calculated above.

10 IMAGE ANALYSIS AND DATA FITTING

The measured (E) and computed (T) images for each condition s are expressed by three-dimensional arrays:

$$E^s = E_{ijk}^s, \quad T^s = T_{ijk}^s(D, K_1),$$

$$i = 0 \dots 1003, \quad j = 0 \dots 1001, \quad k = 0 \dots 4,$$

where i, j, k are the pixel indexes in x, y, z direction, respectively, and s denotes one of the following conditions: exogenous ADP 0.1 mmol/L, 0.3 mmol/L, 0.5 mmol/L, or 2 mmol/L; inhibitors oligomycin and cyanide OLCN; and uncoupler FCCP.

To correct for the camera image offset and changes in background fluorescence induced by flowing solution, the mean

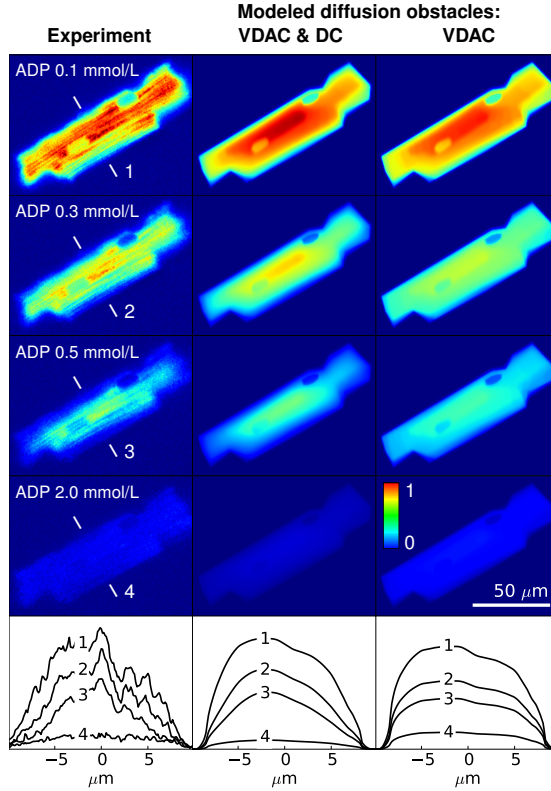


FIGURE S3: NADH autofluorescence of a single permeabilized cardiomyocyte was varied by changing exogenous ADP concentration. The fluorescence images recorded by a camera (left column) on a focal plane are compared with the images calculated by the model (middle and right columns). In the images, the fluorescence intensity is encoded by color, as shown on the bar. The model simulations were performed assuming that diffusion restriction between extracellular solution and mitochondrial inner membrane is either partitioned between cytosolic diffusion obstacles and mitochondrial outer membrane (middle column) or exclusively induced by closure of VDAC in mitochondrial outer membrane (right column). As it is clear from the comparison of the images as well as the intensity profiles shown on the bottom for different ADP concentrations (see experimental images for location of the profile and corresponding ADP concentration), the images calculated by the model for two different diffusion restriction distributions give similar result.

background offset level per pixel is defined for every two-dimensional image:

$$b_k^s = \frac{1}{(i_1 - i_0)(j_1 - j_0)} \sum_{i=i_0}^{i_1} \sum_{j=j_0}^{j_1} E_{ijk}^s,$$

were the indices i_0 , i_1 and j_0 , j_1 define a subregion on the experimental images. This subregion is chosen from outside the cell, appropriately for each experiment.

In addition to the background fluorescence correction, we assumed that, in the presence of FCCP, there is no mitochondrial NADH-induced fluorescence (NADH concentration was expected to be zero in mitochondria). Thus, all experimental images were normalized as in

$$\bar{E}_{ijk}^s = E_{ijk}^s - b_k^s - (E_{ijk}^{\text{fccp}} - b_k^{\text{fccp}}).$$

These level-corrected experimental images were used for comparison with the images calculated by the model.

10.1 Image norm

Let A be an arbitrary array of any dimensions. We define the norm $\|A\|$ as the square root of the sum of the squares of all the array elements. If $A = A_{ijk}$ then

$$\|A\| = \left[\sum_{i,j,k} |A_{ijk}|^2 \right]^{\frac{1}{2}}.$$

10.2 Fitting locally normalized images

Fluorescence distribution heterogeneity is induced by heterogeneity in mitochondrial response, geometry (thickness of the cell) and mitochondrial distribution. To demonstrate the superposition of these effects, experimental and calculated fluorescence image stacks are shown in Fig.S3.

Calculated image stacks corresponding to two different sets of parameters are presented: diffusion is obstructed either mainly

by MOM (Fig.S3, right column) or by combination of MOM and cytoplasmic diffusion obstacles (Fig.S3, middle column). In the both parameter sets used, the diffusion obstacles are such that the apparent K_m of mitochondrial respiration to ADP in solution is 0.3 mmol/L, in accordance with the experimental data [1]. Thus, in the simulation with the combination of two diffusion obstructions (the middle column), the contribution of MOM is reduced when compared to the simulation where only MOM is contributing to overall diffusion restriction.

As in the experiment, the calculated overall fluorescence reduced with the increase of extracellular ADP (Fig.S3). In the both model solutions, there is a marked heterogeneity in fluorescence induced by the heterogeneity of mitochondrial respiration and the differences in thickness of the cell in that particular location (see colormaps and intensity profiles in Fig.S3). However, in the solution with diffusion obstacles mainly attributed to MOM (Fig.S3, right column), the heterogeneity of mitochondrial response is minimal with the differences in calculated fluorescence mainly induced by the differences in cell thickness. Due to the superposition of the heterogeneity of mitochondrial respiration and the differences in thickness of the cell in that particular location leading to the heterogeneity in fluorescence, comparison of the calculated and measured fluorescence heterogeneity poorly differentiated between different combinations of intracellular diffusion obstacles.

To highlight the heterogeneity in mitochondrial response, we found that the sensitivity of the method increases if experimental and calculated data sets are normalized by local maximum fluorescence determined in the presence of oligomycin and cyanide.

Here, for any given (K_1, D) combination, we first determined the gains α^s by minimizing

$$\|\bar{E}^s - \alpha^s T^s\|$$

for each condition separately. Second, we normalized the arrays as follows:

$$\tilde{E}_{ijk}^s = \bar{E}_{ijk}^s N_{ijk}, \quad \tilde{T}_{ijk}^s = \alpha^s T_{ijk}^s M_{ijk},$$

where

$$N_{ijk} = \begin{cases} 1/\bar{E}_{ijk}^{\text{olcn}} & \text{if } \bar{E}_{ijk}^{\text{olcn}}/\alpha^{\text{olcn}} \geq \epsilon \text{ and } T_{ijk}^{\text{olcn}} \geq \epsilon \\ 0 & \text{otherwise} \end{cases}$$

$$M_{ijk} = \begin{cases} 1/(\alpha^{\text{olcn}} T_{ijk}^{\text{olcn}}) & \text{if } \bar{E}_{ijk}^{\text{olcn}}/\alpha^{\text{olcn}} \geq \epsilon \text{ and } T_{ijk}^{\text{olcn}} \geq \epsilon \\ 0 & \text{otherwise} \end{cases}$$

with the cut-off parameter $\epsilon > 0$ was taken equal to 0.01.

The goodness of the fit for any (K_1, D) combination was given by

$$r = \sum_s \|\tilde{E}^s - \tilde{T}^s\|,$$

where s corresponded to exogenous ADP concentrations 0.1 mmol/L, 0.3 mmol/L, 0.5 mmol/L, and 2 mmol/L. As shown in the main text, the calculated normalized image intensities depended on K_1 and D (Fig.2 in the main text, compare to Fig.S3) and r minimum was well determined in parameter space (K_1, D) , Fig.3 in the main text.

10.3 Detailed results

Estimated diffusion coefficient and mitochondrial outer permeability for each studied cell is shown in Table S1.

References

1. M. Sepp, M. Vendelin, H. Vija, and R. Birkedal. Adp compartmentation analysis reveals coupling between pyruvate kinase and atpases in heart muscle. *Biophys. J.*, 98:2785–2793, 2010. ISSN 0006-3495.
2. N. Jephthina, N. Beraud, M. Sepp, R. Birkedal, and M. Vendelin. Permeabilized rat cardiomyocyte response demonstrates intracellular origin of diffusion obstacles. *Biophys. J.*, 101(9):2112–2121, 2011. ISSN 0006-3495.
3. C. S. Henriquez. Simulating the electrical behavior of cardiac tissue using the bidomain model. *Crit. Rev. Biomed. Eng.*, 21(1): 1–77, 1993. ISSN 0278-940X.
4. A. Logg, K. Mardal, and G. Wells. *Automated Solution of Differential Equations by the Finite Element Method*. Springer Berlin Heidelberg, 2012.
5. M. Vendelin, M. Eimre, E. Seppet, N. Peet, T. Andrienko, M. Lemba, J. Engelbrecht, E. Seppet, and V. Saks. Intracellular diffusion of adenosine phosphates is locally restricted in cardiac muscle. *Mol. Cell. Biochem.*, 256-257(1):229–241, 2004. ISSN 0300-8177.
6. M. Aliev, P. Santos, J. Hoerter, S. Soboll, A. Tikhonov, and V. Saks. Water content and its intracellular distribution in intact and saline perfused rat hearts revisited. *Cardiovasc. Res.*, 53(1):48–58, 2002. ISSN 0008-6363.
7. H. Ramay and M. Vendelin. Diffusion restrictions surrounding mitochondria: A mathematical model of heart muscle fibers. *Biophys. J.*, 97(2):443–452, 2009. ISSN 0006-3495.
8. M. Vendelin, O. Kongas, and V. Saks. Regulation of mitochondrial respiration in heart cells analyzed by reaction-diffusion model of energy transfer. *Am. J. Physiol. Cell. Physiol.*, 278(4): C747–C764, 2000. ISSN 0363-6143.
9. R. Birkedal, H. A. Shiels, and M. Vendelin. Three-dimensional mitochondrial arrangement in ventricular myocytes: from chaos to order. *Am. J. Physiol. Cell. Physiol.*, 291(6):C1148, 2006. ISSN 0363-6143.
10. T. Rostovtseva and M. Colombini. Atp flux is controlled by a voltage-gated channel from the mitochondrial outer membrane. *J. Biol. Chem.*, 271(45):28006, 1996. ISSN 0021-9258.
11. J. Lemasters and E. Holmuhamedov. Voltage-dependent anion channel (vdac) as mitochondrial governor—thinking outside the box. *BBA-Mol. Basis Dis.*, 1762(2):181–190, 2006. ISSN 0925-4439.
12. T. K. Rostovtseva and S. M. Bezrukov. Atp transport through a single mitochondrial channel, vdac, studied by current fluctuation analysis. *Biophys. J.*, 74(5):2365–2373, 1998. ISSN 0006-3495.

Table S1: Number of VDACs open for ADP and cytosolic diffusion coefficient.

Experiment No.	Global minimum			Minimum on the 0.5 line		
	D $\mu\text{m}^2/s$	$K_m(ADP)$ mmol/L	Open VDACs per mitochondrion	D $\mu\text{m}^2/s$	$K_m(ADP)$ mmol/L	Open VDACs per mitochondrion
1.	14.8	0.108	440	10.7	0.120	390
2.	42.0	0.163	276	30.2	0.219	201
3.	22.6	0.141	325	16.1	0.178	251
4.	24.5	0.133	347	18.6	0.152	299
5.	32.3	0.152	299	22.2	0.189	235
6.	30.3	0.178	251	23.6	0.208	212
7.	38.1	0.219	201	38.1	0.218	201
Average value \pm standard error of the mean						
	29.2 \pm 3.5	0.156 \pm 0.013	306 \pm 29	22.8 \pm 3.4	0.184 \pm 0.014	256 \pm 26

PUBLICATION IV

Laasma M, Birkedal R, and Vendelin M

Revealing calcium fluxes by analyzing inhibition dynamics in action potential clamp

Journal of Molecular and Cellular Cardiology, 100, 93–108, 2016



Original article

Revealing calcium fluxes by analyzing inhibition dynamics in action potential clamp



Martin Laasma, Rikke Birkedal*, Marko Vendelin*

Laboratory of Systems Biology, Institute of Cybernetics, Tallinn University of Technology, Akadeemia Rd 21, Tallinn 12618, Estonia

ARTICLE INFO

Article history:

Received 4 April 2016

Received in revised form 19 July 2016

Accepted 22 August 2016

Available online 1 October 2016

Keywords:

Calcium fluxes

Cardiac excitation-contraction coupling

Action potential clamp

Sarcoplasmic reticulum

Rainbow trout

ABSTRACT

In cardiac excitation-contraction coupling (ECC), calcium enters the cytosol via L-type Ca^{2+} channels (LTCC) and reverse $\text{Na}^+/\text{Ca}^{2+}$ -exchange (NCX_{rev}), or is released from the sarcoplasmic reticulum (SR) by Ca^{2+} -induced Ca^{2+} -release (CICR). The magnitude of Ca^{2+} influx via the different pathways varies with the state of the cell and is difficult to assess quantitatively, because changes in Ca^{2+} influx through one pathway affect the others. In rainbow trout ventricular myocytes, the role of the SR has been uncertain for decades. The aim of this work was therefore two-fold: 1) to develop a method to quantify the Ca^{2+} influx pathways, and 2) to determine the role of CICR from the SR in trout ventricular myocytes. The novelty of our developed method lies in the mathematical analysis of measured transsarcolemmal Ca^{2+} currents and their impact on the corresponding Ca^{2+} transient during gradual inhibition of the currents in action potential (AP) clamp. We tested the developed method using an excitation-contraction model and showed that the method was able to recover calcium fluxes from noisy synthetic data. We applied the approach to trout ventricular myocytes and quantified the relative contributions of different Ca^{2+} influx pathways in ECC and determined the kinetics of these fluxes. Under baseline conditions, NCX_{rev} is the main transmembrane Ca^{2+} influx pathway contributing $29 \pm 6\%$ (of the Ca^{2+} influx), LTCC $18 \pm 7\%$, and CICR $53 \pm 10\%$ to overall Ca^{2+} transient. Thus, NCX_{rev} is an important regulator of contractility and probably plays a role in the negative force-frequency relationship of trout ventricular preparations. These results demonstrate that trout and neonatal mammalian cardiomyocytes resemble each other not only in terms of morphology and energetics but ECC as well. In summary, the developed method resolves the major problem how to separate highly interconnected fluxes in AP clamp and allows to study Ca^{2+} fluxes in cardiomyocytes under conditions close to *in vivo*.

© 2016 Elsevier Ltd. All rights reserved.

1. Introduction

In cardiac excitation-contraction coupling (ECC), an action potential (AP) leads to formation of the Ca^{2+} transient by initiating sarcolemmal Ca^{2+} influx via L-type Ca^{2+} channels, LTCC, and the $\text{Na}^+/\text{Ca}^{2+}$ -exchange running in reverse, NCX_{rev} . This transsarcolemmal Ca^{2+} influx in turn triggers Ca^{2+} -induced Ca^{2+} -release, CICR, from the sarcoplasmic reticulum (SR). In steady state, Ca^{2+} influx via LTCC and NCX_{rev} is pumped out of the cells via the NCX operating in forward mode, and the Ca^{2+} released by CICR is pumped back into the SR via the sarcoendoplasmic reticulum Ca^{2+} -ATPase, SERCA.

Abbreviations: AP, action potential; CICR, Ca^{2+} -induced Ca^{2+} -release; ECC, excitation-contraction coupling; LTCC, L-type Ca^{2+} channel; NCX, $\text{Na}^+/\text{Ca}^{2+}$ -exchange; NCX_{rev} , $\text{Na}^+/\text{Ca}^{2+}$ -exchange in reverse mode; NIF, nifedipine; SERCA, sarcoendoplasmic reticulum Ca^{2+} -ATPase; SR, sarcoplasmic reticulum.

* Corresponding authors.

E-mail addresses: rikke@sysbio.ioc.ee (R. Birkedal), markov@ioc.ee (M. Vendelin).

The contribution of the three Ca^{2+} influx pathways (LTCC, NCX_{rev} and CICR) to the Ca^{2+} transient is dynamic and varies with species and conditions. The contribution of NCX_{rev} is considered negligible in rabbit cardiomyocytes [1], whereas in mouse cardiomyocytes it participates in the regulation of Ca^{2+} release and contractility [2–4]. Whether triggered by LTCC alone or together with NCX_{rev} , CICR from the SR plays a large role in mammalian ECC. In rat heart, it was estimated to contribute 80% to the Ca^{2+} transient [5]. In contrast, in some fish species, LTCC and NCX_{rev} contribute more or less equally to the Ca^{2+} transient, and CICR does not take place [6]. There is a trend that in more active fish, the SR plays a larger role in cardiac ECC [7]. However, in one of the most studied ectothermic vertebrates, the rainbow trout, the contribution of the three Ca^{2+} influx pathways is still not settled. Some studies suggest that in trout ventricle, CICR from the SR does play a minor role, although this depends on temperature and pacing frequency [8–10]. A more recent study suggested that CICR is only recruited under adrenergic stimulation [11]. The importance of NCX_{rev} under physiological conditions is uncertain,

but it is expected to be significant due to the high intracellular sodium concentration [12].

Within an individual, the contribution of the different Ca^{2+} pathways also varies with life stage and fitness of the animal. For example, NCX_{rev} contributes to the Ca^{2+} transient in cardiomyocytes of neonatal rabbits. As the animals mature, the contribution of NCX_{rev} decreases, and the contribution of CICR increases [13,14]. Failing cardiomyocytes of adult mammals return to an “immature ECC” with diminished CICR and enhanced flow through NCX_{rev} [15]. Thus, a quantitative assessment of the Ca^{2+} influx pathways can give important information about cardiac health.

Quantification of the Ca^{2+} influx pathways is, however, far from trivial. Currents through LTCC, NCX and CICR can be measured using a combination of patch clamp and fluorescence microscopy on cells loaded with a Ca^{2+} indicator. It is common to assess the importance of one pathway by inhibiting it and recording the effect on the Ca^{2+} transient. Unfortunately, the inhibition of one pathway will affect the contribution of the others. For example, CICR is proportional to the size of the trigger [16] and will diminish if LTCC or NCX_{rev} current is inhibited. Inhibition of LTCC and/or CICR affects the Ca^{2+} balance across the sarcolemma and the shape of the AP, which in turn affects the NCX current. Therefore, quantification of the Ca^{2+} influx pathways requires an integrated approach where these relationships are taken into account.

The present study was undertaken with the aim to develop a method to quantify the Ca^{2+} influxes in rainbow trout cardiomyocytes. For this, we used AP clamp of individual cells and recorded how inhibition of LTCC and NCX elicited a compensatory current and reduced the Ca^{2+} transient. The recorded data was analyzed by a simple mathematical model of Ca^{2+} dynamics to reveal Ca^{2+} fluxes through LTCC, NCX, and SR.

2. Methods

2.1. Animals

Female rainbow trout (270 ± 54 g, $n = 12$) (*Oncorhynchus mykiss*) were purchased from a local fish farm (SK Trade OÜ, Staadioni 11–4, Juuru Parish, Rapla County, 79401, Reg: 11187349). Before experiments, the fish were acclimated at least three weeks in a 1600 liter fresh water tank at 15 ± 1 °C under 12:12 h light-dark photoperiod. They were fed commercial fish food on a daily basis. All procedures were approved by the Estonian National Committee for Ethics in Animal Experimentation (Estonian Ministry of Agriculture).

2.2. Cell isolation

Trout ventricular cardiomyocytes were isolated using a standard enzymatic technique as in [17–19]. In brief, the animal was killed with a single blow to the head followed by a cut of the spine. The heart was removed and placed in ice cold isolation solution containing (mM): 100 NaCl, 10 KCl, 1.2 KH_2PO_4 , 4 MgSO_4 , 50 taurine, 20 glucose, 10 HEPES and pH adjusted to 6.9 with NaOH. The heart was cannulated through the bulbus arteriosus and perfused 8–10 min with cell isolation solution at a flow rate of 0.6–0.8 ml/min. After this, 0.5 mg/ml trypsin (Type IX-S), 0.75 mg/ml collagenase (Type IA), and 0.75 mg/ml fatty-acid-free bovine serum albumin (BSA) was added to the isolation solution and perfusion was continued with the same flow rate for 16–20 min. After the perfusion, the heart was taken off the cannula and cut into a few pieces. The cells were suspended with a Pasteur pipette and the suspension was then filtered through nylon tissue. The cells were left to sediment for 5 min, after which the supernatant was replaced with fresh isolation solution. This washing procedure was repeated 3 times. All this was carried out at room temperature. Isolated cells were kept in isolation solution at 4 °C and used for experiments within 5 h

after the cell isolation. Before each experiment, the cells were incubated 20 min in external solution (see below) at 4 °C with 1 μM of the calcium indicator Fluo-4 AM (Invitrogen, OR, USA). In the experiments with inhibited SR, ryanodine receptors (RyRs) and SERCA were inhibited by pre-incubating cells for 20 min with 10 μM ryanodine (Ascent) and 2 μM thapsigargin (Ascent), respectively, as in [9].

2.3. Electrophysiological measurements

All electrophysiological recordings were conducted in the perforated patch clamp configuration. We used an Optopatch patch clamp amplifier (Cairn Research, UK), connected to a computer via an NI PCI-6221 data acquisition board (National Instruments, USA). The amplifier was controlled and data were recorded at a frequency of 10 kHz by custom-made software. All experiments were performed at room temperature (22 °C, temperature controlled by air conditioner).

The pipette solution contained (mM): 6 KCl, 124 K-glutamate, 1 MgCl_2 , 14 NaCl, 10 CaCl_2 and pH adjusted to 7.2 with KOH. Perforation was achieved by front-filling with pipette solution containing additional 240 $\mu\text{g/ml}$ amphotericin B (Sigma-Aldrich, MO, USA). Having 10 mM CaCl_2 in pipette solution ensured that amphotericin perforated patch was permeable only for monovalent ions, otherwise Ca^{2+} in pipette induced hypercontraction of the cell and experiment was discarded. In practice, about 20% of cells were discarded due to the faulty perforation or rupture of the patch. In the used cells, no hypercontraction was observed nor slow increase of Ca^{2+} fluorescence suggesting a leak from pipette to the cell. The external solution for control measurements contained (mM): 130 NaCl, 5.4 KCl, 1.5 MgSO_4 , 0.4 NaH_2PO_4 , 2 CaCl_2 , 10 glucose, 10 HEPES and pH was adjusted to 7.6 with NaOH. The total Ca^{2+} concentration in trout plasma is around 2.4 mM [20]. It is, however, highly buffered, and the free Ca^{2+} concentration is ~ 1.4 mM [20]. For our experiments, we used 2 mM Ca^{2+} in the extracellular solution in order to compare with previous studies [11,21–23].

A batch of cells was placed in a diamond-shaped fast-exchange chamber (15 \times 6 mm, RC-24N; Warner Instruments, Harvard Apparatus, March-Hugstetten, Germany) under a Nikon Eclipse Ti-U microscope (Nikon, Japan) equipped with a 40 \times objective (CFI Super Plan Fluor ELWD 40x NA 0.60, Nikon, Japan). The cells were allowed to attach to the glass for 5 min before starting the perfusion of the chamber with extracellular solution at a flow rate of ~ 0.5 ml/min. A cell in the middle of the chamber was approached with a patch pipette (resistance 2–3 M Ω). After gigaseal formation (>3 G Ω) in voltage clamp, the pore formation in the patch was monitored by following the current response to a square voltage pulse with baseline -80 mV, width of 10 ms, height 5 mV and pulse period 25 ms. When the current response had reached steady state, cell capacitance and series resistance was noted.

For later analysis, a short series of transmission images were acquired with a CCD camera (IPX-VGA210-LMCN, Imperx Inc., FL, USA). From these images, cell width and length was measured, and cell volume was calculated as in [24]. Namely, cells were considered as a cylinder with an elliptical cross section, where the semi-major and semi-minor axes of the ellipse are taken as 1/2 and 1/4 of cell's width, respectively. The cell volume was found using following equation: $V = \pi \cdot w/2 \cdot w/4 \cdot l$, where w is width and l is length of a cell. To estimate cytosolic volume, we assumed that non-mitochondrial cell volume in trout cardiomyocytes is 55% of total cell volume [19].

After acquisition of the transmission images, the configuration was switched to current clamp, and the minimal current square pulse triggering an AP was found. This pulse had a width of 1–2 ms and height of 600–900 pA, depending on the cell. The minimum pulse was used to record the cell-specific AP at 1.1 Hz for 90 s. This corresponds to 66 bpm, which is close to the routine heart rate at the

temperature at which the experiments were conducted (22 °C) [25]. We averaged the last 50 APs at the end of the measured sequence. This averaged AP was used as the input in voltage clamp, where the cell was stimulated with its intrinsic AP at 1.1 Hz for 2.5 min to verify that the current trace was flat. Then, 1 or 5 mM NiCl₂ or 10 μM nifedipine (Ascent) was added to the external solution to inhibit NCX and/or LTCC, respectively. Calculations of the flow in our chamber suggest that the solution containing inhibitor hits the cell rather abruptly with the flow component dominating diffusion if the cell is lifted from the coverslip [26], as it was done in our work. These recordings were performed in control and SR-inhibited cells.

2.4. Fluorescence measurements

Fluorescence was measured throughout the experiment with an Andor Ixon EMCCD camera, at a frame rate of 85 Hz and binning 4×4 that was mounted on a Nikon Eclipse Ti-U microscope. The optical scheme of the microscope is the same as described in [27]. At continuous illumination, excitation light from a Prior Lumen 200 with a 200 W metal halide lamp was passed through a 482/35 nm filter and reflected onto the specimen by a long-pass 506 nm dichroic mirror. Emission light was directed through the same dichroic mirror, and reflected by a 580 XR dichroic mirror through a 536/40 nm filter to be recorded by the EMCCD camera.

To convert the fluorescence signal to Ca²⁺ concentration, the maximum fluorescence at 2 mM extracellular Ca²⁺ was measured by rupturing the cell membrane at the end of each experiment. The background was estimated from a region of interest in surrounding solution.

We assumed that the minimum fluorescence measured from the resting cell in control and SR inhibited case before addition of transmembrane Ca²⁺ current inhibitors corresponded to a cytosolic Ca²⁺ concentration of 100 nM. To determine whether the diastolic calcium concentration is different between control and SR inhibited case, we compared the ratios of the fluorescence before the inhibitors were applied at cell rest and fluorescence at maximum after cell membrane rupture. In control case the mean ratio and standard deviation was 0.370±0.099 (n = 10) and SR inhibited case 0.304±0.128 (n = 9). Using Welch's *t*-test we did not find statistically significant difference between these groups (p = 0.213) and assumed, in the following analysis, that the diastolic calcium concentration is the same in both cases.

Fluorescence was converted to Ca²⁺ concentration using the following equation:

$$F_{Ca} = \alpha \frac{F_t[Ca^{2+}]_i}{K_f + [Ca^{2+}]_i} + \beta, \quad (1)$$

where F_{Ca} is fluorescence induced by the free cytosolic $[Ca^{2+}]_i$ bound to the fluorescence agent with total concentration F_t and with dissociation constant K_f ; α and β are gain and offset of the recorded fluorescence signal, respectively. The value for K_f was set to 1048 nM as in [28].

2.5. Analysis of the measurements

To estimate the contributions and kinetics of Ca²⁺ fluxes via LTCC, NCX, and CICR in cardiomyocytes we used the following data: measured compensatory currents and corresponding Ca²⁺ transients in the presence of nickel (Ni²⁺) and nifedipine (NIF) (see overall method scheme Fig. 1 and example data in Fig. 2). In general, from the electrophysiological measurements we determined the contribution of transmembrane currents to Ca²⁺ concentration changes in the cell and the remaining changes in Ca²⁺ concentration were

attributed to movement of Ca²⁺ to and from SR. To separate contributions of different Ca²⁺ fluxes, we composed a simple mathematical model of Ca²⁺ dynamics that relates transmembrane Ca²⁺ fluxes via LTCC and NCX with Ca²⁺-induced Ca²⁺ transient in the cell during ECC. The formal description of all analysis steps is given in Supporting Material.

To relate estimated currents to the changes in Ca²⁺ concentration in the cell, we had to estimate buffering capacity B_t . For that we used the data from cardiomyocytes where Ca²⁺ release and uptake by SR was inhibited. In this case, all changes in Ca²⁺ concentration are induced by transmembrane currents. In the analysis of the data, we made the following assumptions: 1) $[Ca^{2+}]_i$ at rest is 100 nM before NIF or Ni²⁺ was applied, 2) NIF inhibits LTCC ≥ 99%, 3) Ni²⁺ inhibits Ca²⁺ fluxes via NCX (J_{NCX}) and LTCC (J_{LTCC}), 4) the shape of J_{LTCC} stays the same and only the amplitude can change during inhibition, 5) J_{NCX} is determined by $[Ca^{2+}]_i$ and membrane potential, 6) half saturation concentration (K_b) of B_t is 2380 nM [29]. Having experimental data of compensatory currents and corresponding Ca²⁺ transients in the presence of Ni²⁺ and NIF and the assumptions described before, we used least square fitting of the data to estimate following parameters: 1) B_t , 2) inhibition extents of J_{LTCC} , J_{NCX} in the presence of Ni²⁺, 3) inhibition time constants of J_{LTCC} , J_{NCX} , 4) shapes of J_{LTCC} , J_{NCX} , 5) conductances of J_{LTCC} , J_{NCX} . The analysis required combining the data recorded from cells in the presence of different inhibitors. As a result, the analysis was performed for combinations of recordings performed in the presence of Ni²⁺ and NIF.

After determining B_t , we were able to estimate Ca²⁺ fluxes in cardiomyocytes where CICR was not inhibited. The same assumptions were used as above to fit the data. The fit was performed for all combinations of the recordings performed in the presence of Ni²⁺ and NIF.

The relative contribution of different Ca²⁺ pathways was found by calculating the integral of the respective Ca²⁺ flux (for influx positive and efflux negative part of flux) and dividing it with the total Ca²⁺ (free and buffered) concentration change during a beat.

2.6. Uniqueness of the model solution

The uniqueness of the fit of the model solution to experimental recordings has been verified as follows. As described in the Supporting Material in details, in the optimization procedure, we start with a scan of several parameters describing inhibition of the currents. Within this scan, an optimization was performed for such parameters as spline nodal values describing LTCC current. To analyze the optimization result obtained through such brute force scan in 6-dimensional space, we produced heat maps of residuals found as a projections from 6-dimensional space to 2-dimensional space. We observed that for all combinations of 2 scanned parameters, the heat map was smooth with one minimum, a global one. The following steps in the optimization procedure were applied around this global minimum. The existence of only one minimum in the scan stage and the smoothness of the residual heat maps suggest that the solution was unique within the given optimization procedure.

2.7. Testing method against synthetic data

In order to test the developed method, we used a published model of ECC to generate synthetic data. For synthetic data generation we used Pandit–Hinch–Niederer et al. (PHN) cell model [30], an integrative model of rat electromechanics that combines three separate models of rat cardiomyocyte function. The initial source code in C of the model was obtained from CellML repository (<http://www.cellml.org>). To solve the model and apply inhibition of different transmembrane currents at the conditions resembling AP clamp, we wrote a custom driver in C++. The model equations were numerically solved by using *nlsolve* solver from the FORTRAN library *odepack* [31].

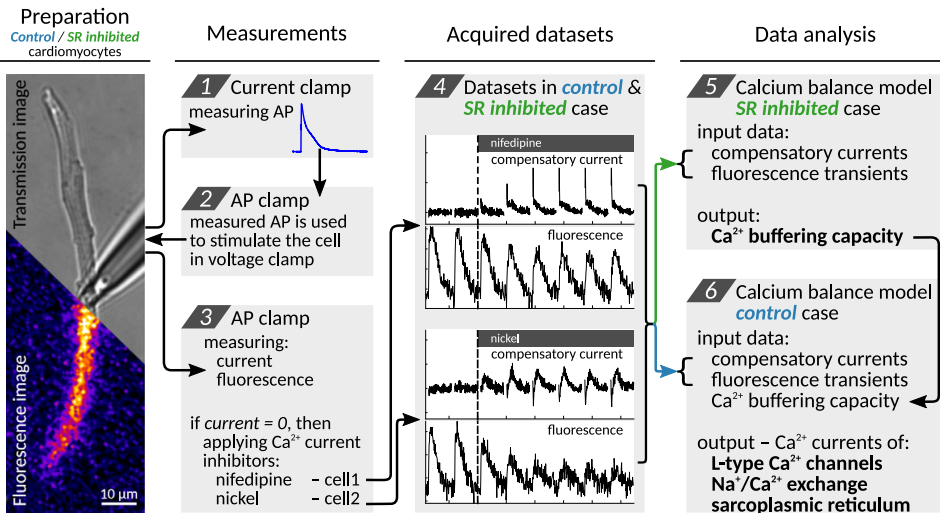


Fig. 1. Overall scheme of the method: from data acquisition to analysis.

The simulations were performed as follows:

First, we found a minimal current pulse that triggered an AP (5 ms, -600 pA). Then we used this stimulus pulse at 1 Hz until the model solution reached steady state. Steady state was considered reached when all model variables (either followed by differential or algebraic equations) were the same at the ends of two consecutive periods with given absolute or relative tolerance (10^{-6}). After a stable model solution was found, we calculated 20 additional periods. This procedure corresponds to the experimental condition of current clamp where a stable AP was found.

Second, the AP of the last calculated period was extracted and, on the basis of it, a function of AP in time was created in the form of a spline. Next, we replaced the PHN model's membrane potential equation with the AP function and continued the calculations using the values of the variables found in the end of the first part as an initial condition in these simulations. This corresponds to the experimental condition where the cell is voltage clamped with its intrinsic AP. After five periods, we started to gradually decrease Ca^{2+} flux via NCX and/or LTCC to obtain synthetic data that would correspond to the experimental conditions when Ni^{2+} or NIF is applied, respectively. To decrease the NCX Ca^{2+} flux, we decreased the pump rate of NCX ("g_NCX in component Na_Ca_Exchange" in the PHN model). To decrease the LTCC flux, we decreased the number of Ca^{2+} release units ("N in component CaRU" in the PHN model). For the gradual inhibition we used the function given by Eq. 6 in Supporting Material. We continued calculations for 15 more pulses.

Third, we used this data to create synthetic experimental data. Namely, calculated Ca^{2+} transients ("Ca_i in component intracellular_ion_concentrations" in the PHN model) were extracted from the model solution at a sampling rate similar to the experimental one (85 Hz). Compensatory current was found as a total transmembrane current difference between the current period and the period before inhibition. For currents, the sampling rate was taken equal to 10 kHz, as in the experiments.

Finally, we applied Gaussian noise to the synthetic data at different levels that was similar, $2\times$, $5\times$ or $10\times$ the noise level observed in our experimental data.

The generated synthetic data were analyzed in the same way as the experimental data, except total Ca^{2+} buffering was estimated using the PHN cell model (see Results section for details) and the

kinetic constant, K_{Pi} , of our J_{NCX} function (Eq. 3 in Supporting Material) was found by fitting our J_{NCX} function against the function in the PHN model. The found value for K_{Pi} was fixed in further calculations. The method did not allow to fit K_{Pi} for synthetic data, due to the small NCX current, opposite to recorded data from trout cardiomyocytes.

2.8. Statistics and numerical methods

2.8.1. Statistics

Values are presented as average \pm standard deviation and Welch's t -test was used to assess statistical differences if not mentioned otherwise.

2.8.2. Numerical methods

For splines, we used GNU Scientific Library. The mathematical model equation was numerically solved by using *Isoda* from the FORTRAN library odepack that automatically switches between stiff and non-stiff integration routines [31]. Least squares optimizing was carried out by the Levenberg-Marquardt algorithm from MINPACK [32]. The programs were implemented in programming language Python. C++ functions were called using Cython.

3. Results

The overall scheme of the developed method with the data measurements and analysis is shown in Fig. 1. The results are presented as follows. First, the experimental recordings are described. Second, the developed method is tested against synthetically generated data. Third, the method is applied to analyze the recordings performed on trout cardiomyocytes to determine the intracellular Ca^{2+} buffering capacity and calcium fluxes.

3.1. Electrophysiological and fluorescence recordings

To determine intracellular Ca^{2+} fluxes, we combined AP clamp with recordings of intracellular free Ca^{2+} using the Ca^{2+} sensitive dye Fluo-4. General electrophysiological properties of the used cardiomyocytes are given in Supporting Material. Representative examples of two recordings are shown in Fig. 2. When the cell was voltage clamped with its specific AP (shown in insert), the measured

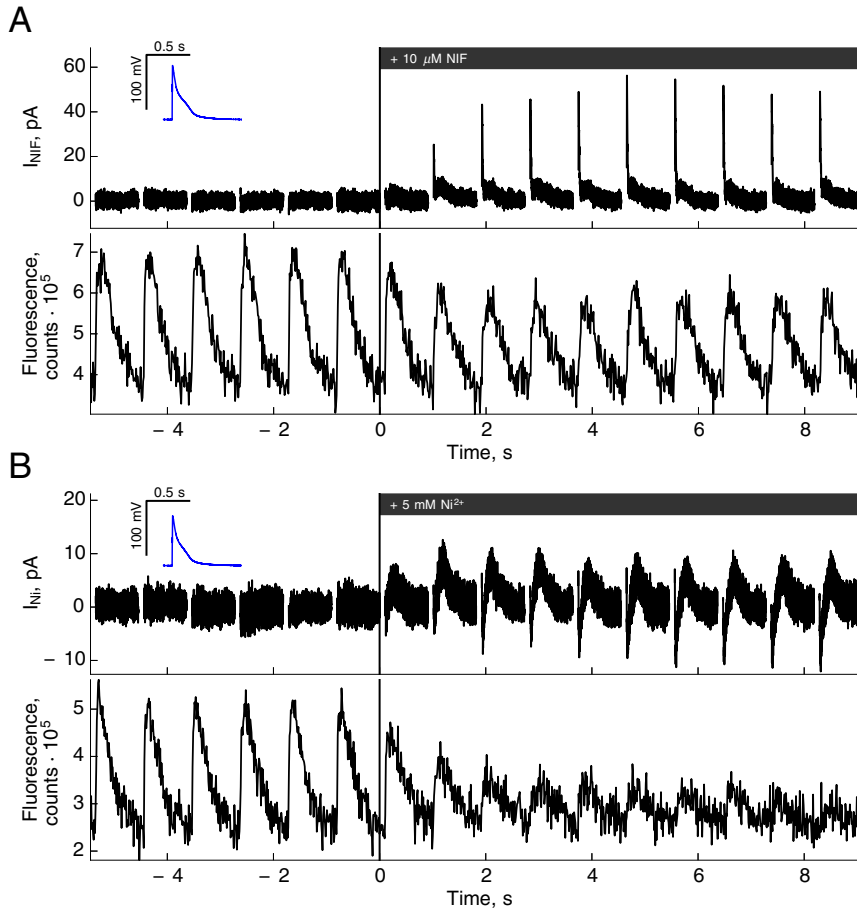


Fig. 2. Representative data measured on two control cells in the presence of NIF (A) or Ni^{2+} (B). Introduction of the inhibitor resulted in the appearance of the compensation current (upper traces in A and B) and changes in calcium sensitive fluorescence indicator Fluo-4 (lower traces in A and B). For the both cells, the inset in blue shows cell-specific AP that was used as stimulus of the cell in voltage clamp. In the current traces, we excluded the spike in the current that corresponds to activation with current square pulse having width of 1–2 ms and height of 600–900 pA, depending on the cell used in AP measurements. Note that in the beginning of the experiment, the compensation current is zero under cell-specific AP in voltage clamp mode. Only after inhibition of transmembrane currents, the corresponding compensation current appears and, after few beats, the new calcium dynamics with new currents distribution develops in the cell. (For interpretation of the references to color in this figure legend, the reader is referred to the web version of this article.)

currents were zero as expected when the applied AP matches the cellular response to stimulation [33,34]. When a channel or transporter is inhibited, its current is missing from this cellular response. Hence, the missing current has to be injected by the amplifier leading to the appearance of a compensatory current. As a result, the compensatory current appears upon inhibition and is the inverse of the inhibited current. Please note that, in Fig. 2 and the following figures, the compensatory current is shown and not the current that was inhibited. As the inhibition is not instant, the compensatory current appears gradually after the inhibitor is applied at time 0. In A, the cell was exposed to NIF, which inhibits LTCC. As LTCC is inward, the compensatory current representing LTCC is outward. In B, the cell was exposed to Ni^{2+} , which inhibits both NCX and LTCC, and a biphasic compensatory current appeared. At first, the compensatory current is inward because the reverse NCX-current is larger than LTCC-current. Then, as NCX switches to forward mode, the outward compensatory current represents a combination of NCX and LTCC.

To reveal the influence of LTCC, NCX on SR fluxes, we complemented the current recordings with fluorescence measurements of intracellular free Ca^{2+} . Introduction of the inhibitors of NCX and LTCC influenced Ca^{2+} release and uptake by SR. This influence is visible in the lower traces in Fig. 2. As the compensatory current appears, the amplitude of the Ca^{2+} transient reduces. Notice that inhibition of LTCC with NIF only leads to a slight reduction of the Ca^{2+} transient (Fig. 2A). Not surprisingly, as Ni^{2+} inhibits LTCC as well as NCX and thus significantly reduces the Ca^{2+} trigger of CICR, the Ca^{2+} transient was nearly abolished (Fig. 2B). Statistical analysis of the Ni^{2+} inhibition is given in Supporting Material.

3.2. Test against synthetic data

To test the method, we used a mathematical model of rat cardiomyocyte ECC and generated a set of synthetic data that correspond to the recordings in Fig. 2. For that, we found a periodic

solution of the PHN model and, at a given time moment, started inhibition of NCX and/or LTCC channels while keeping the dynamics of the AP unchanged. Such a protocol corresponds to the AP clamp used in our experiments. The changes in transmembrane currents induced by inhibition were calculated and, together with the calculated dynamics of intracellular calcium concentration, were used for further analysis by the developed method. Note that we applied noise at a level similar to the level of noise that was in our experimental data. In addition, the currents were cut out at the beginning of each stimulation to reproduce the exclusion of the activation spike in the experimental data. The resulting synthetic data are shown in Fig. 3.

After application of the developed method, as described in detail in Supporting Material, we were able to fit the synthetic data set (Fig. 4). In these fits, we used a single buffer, as opposed to two buffering components used in the PHN model: calmodulin and troponin C. Despite this simplification as well as several other simplifications, the fitted solution captures the dynamics of Ca^{2+} and the appearance of compensatory currents well (Fig. 4).

The contribution of different Ca^{2+} fluxes and the changes in the Ca^{2+} influx are shown in Fig. 5. In Fig. 5A and B, each point corresponds to the Ca^{2+} influx through LTCC, NCX or SR during an AP. Fig. 5C–E shows the fluxes during the time of a single AP before inhibition. As it is clear from the fit results (Fig. 5A and B), the amount of Ca^{2+} entering the cytoplasm during a beat from SR is somewhat

overestimated, while the contributions of LTCC and NCX are reproduced very accurately. At the same time, the dynamics of LTCC, NCX, and SR fluxes as well as free Ca^{2+} are quite well captured by the fit (Fig. 5C, D, E, and F). Note that there are two fits corresponding to two studied cells – one for the cell inhibited with NIF (blue in Fig. 5D–F) and one for the cell inhibited with Ni^{2+} (red in Fig. 5D–F). As described in Methods, the LTCC current was exactly the same for both cells and is shown in Fig. 5C. We noticed that the PHN model predicts a large Ca^{2+} influx spike at the beginning of the AP leading to a small oscillation in the Ca^{2+} concentration (see inset in Fig. 5F). Due to the relatively large time-step used in the splines describing LTCC and SR fluxes, this spike was not reproduced in our fits.

In the synthetic data calculated by rat cardiomyocyte electrophysiological model, Ca^{2+} influxes were dominated by LTCC (~10%) and CICR (~90%), see Table 1 for details. To describe the sensitivity of the developed method, we analyzed the fits at different noise levels and different buffering capacities. In general, we found that the developed method is rather robust. When comparing the estimated total Ca^{2+} influx and relative contributions of different influx pathways, we observed that the changes in noise level had only a minor effect on these parameters (Table 1). However, the dynamics of Ca^{2+} fluxes recovered by the fits with high noise levels (5× and 10× “experimental”) was significantly disturbed and very noisy (results not shown). In contrast to noise, changes in the buffering capacity had more significant effects (Table 1). When we increased

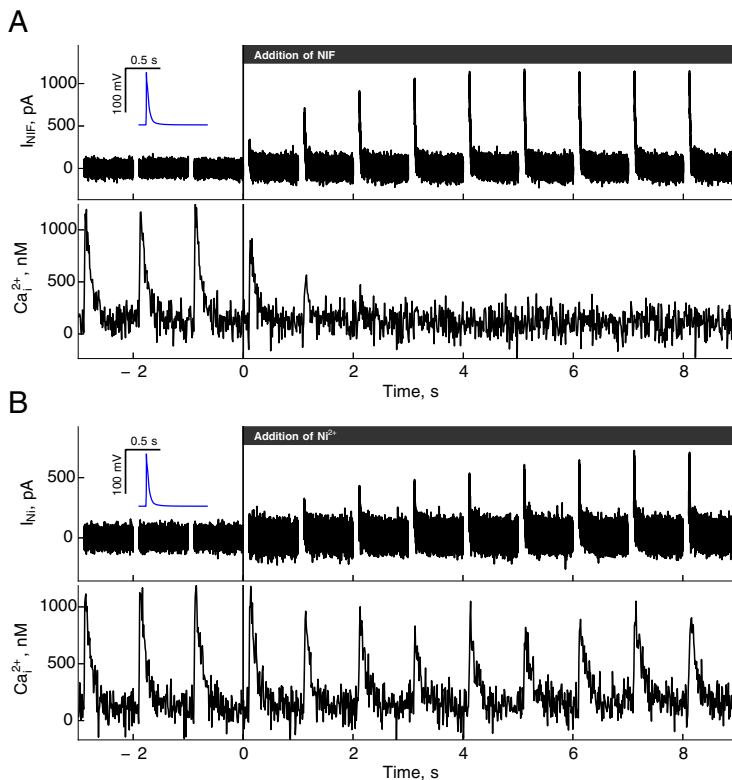


Fig. 3. Synthetic experimental data using the PHN rat cell model where Ca^{2+} flux was restricted 99% via LTCC (A) or 30% via LTCC and 95% via NCX (B). This, as shown in the experimental part, imitates using either 10 μM NIF or 5 mM Ni^{2+} as transmembrane Ca^{2+} current inhibitors, respectively. The insets in blue in both figures show APs used for stimulus of the cells in voltage clamp. Note that, as for experimental data, the compensatory currents appear only after the inhibition of transmembrane currents that in turn is reflected in the decrease of Ca^{2+} transients. (For interpretation of the references to color in this figure legend, the reader is referred to the web version of this article.)

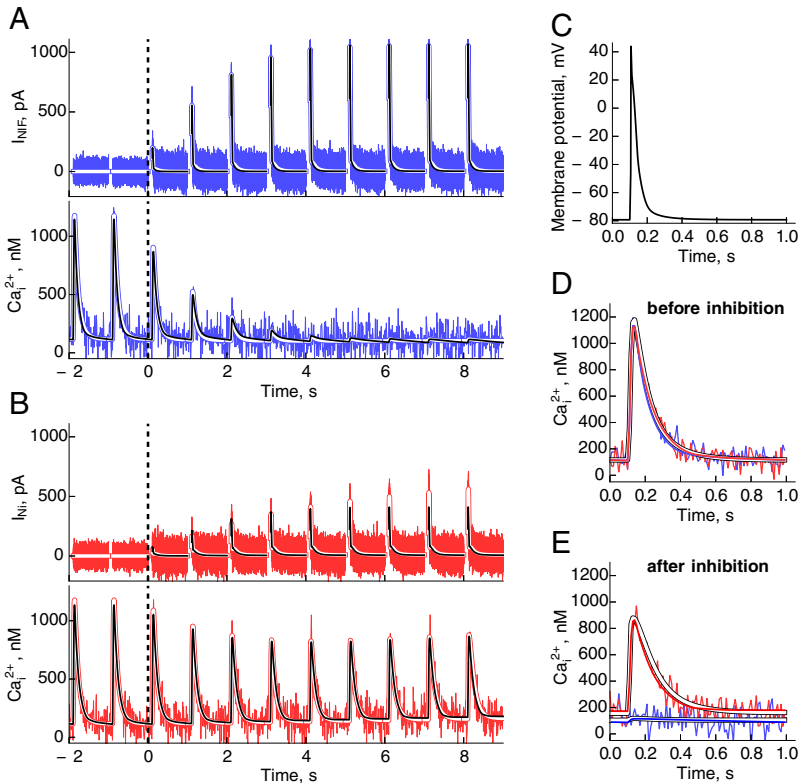


Fig. 4. Representative results of synthetic data. In A and B the compensatory currents and corresponding Ca²⁺ transients of synthetic NIF and Ni²⁺ experiment are shown, respectively. Here the reference data from the PHN cell model, without applied noise, are marked in white and our model fits are shown in black. In both cases, our model solution fits the shape and beat-to-beat changes of the simulated compensatory currents and the Ca²⁺ transients perfectly as well restores the reference data. In C, membrane potential is shown that was used to stimulate the cells. The changes in Ca²⁺ transients during a beat induced by “application” of NIF (blue) or Ni²⁺ (red) is clear from the average of three beats of Ca²⁺ transients before (D) and after (E) of inhibition. (For interpretation of the references to color in this figure legend, the reader is referred to the web version of this article.)

or decreased the buffering capacity (113 μM , fit shown below) by 16 μM , *i.e.* the relative standard deviation of the buffering estimated below for trout, the total influx of Ca²⁺ found by the developed method changed by $\sim 15\%$. Thus, estimating buffering capacity is an important step in the application of the developed method.

We found that description of the Ca²⁺ buffering can be further improved by taking into account non-stationary state of the buffer during a beat. Namely, the buffering in cardiomyocytes is dynamic during a beat with a fast (calmodulin) and slow (troponin C) components. The interplay between these components and the dynamics of Ca²⁺ fluxes during a beat leads to relationship between total Ca²⁺ and free Ca²⁺ in cytoplasm that is significantly different from the relationship in equilibrium (Fig. 6). The earlier analysis (Figs. 4, 5) was performed using the buffering capacity found by fitting the relationship obtained in equilibrium (Fig. 6A, blue line). This would correspond to estimating the buffering capacity during a slow experiment, such as following Ca²⁺ efflux through NCX from the cell with depleted SR Ca²⁺. When we estimated the buffering capacity of the cardiomyocyte using Ca²⁺ dynamics during a beat (Fig. 6A, black line), the fitted Ca²⁺ fluxes reproduced the PHN solution without overestimating the influx through SR (Fig. 6B and C, last line in Table 1). In addition, the dynamics of Ca²⁺ concentration changes and the fluxes were reproduced very well (results not shown). Note that all these fits were performed using only a single buffer with fast

kinetics, *i.e.* without taking into account the dynamics of Ca²⁺ and troponin C association. Thus, on the basis of these tests, the developed method is able to recover the distribution of Ca²⁺ fluxes in the cell even from noisy experimental data with somewhat biased buffering capacity (Fig. 5). By improving the description of Ca²⁺ buffering, the estimates of Ca²⁺ fluxes can be improved further (Fig. 6).

3.3. Intracellular Ca²⁺ buffering capacity

To determine Ca²⁺ buffering capacity in trout cardiomyocytes, we recorded the transmembrane currents in AP-clamp mode and related them to the Ca²⁺ transient in cardiomyocytes where SR release and uptake was inhibited (SR inhibited case). As a result, we could assume that all changes in Ca²⁺ concentration were induced by LTCC and NCX only, and modulated by Ca²⁺ buffering. The estimation of buffering from such measurements would correspond to the dynamic approach in Fig. 6, since we follow Ca²⁺ dynamics during a beat with the same frequency as later used in the control measurements. In addition, for simplicity, we assumed that the inhibitors influenced LTCC and NCX as follows (see Supporting Material for details). First, NIF inhibited LTCC only and changed NCX dynamics through changes in intracellular Ca²⁺ concentration. We assumed that 10 μM NIF, as used in the experiments, inhibits LTCC

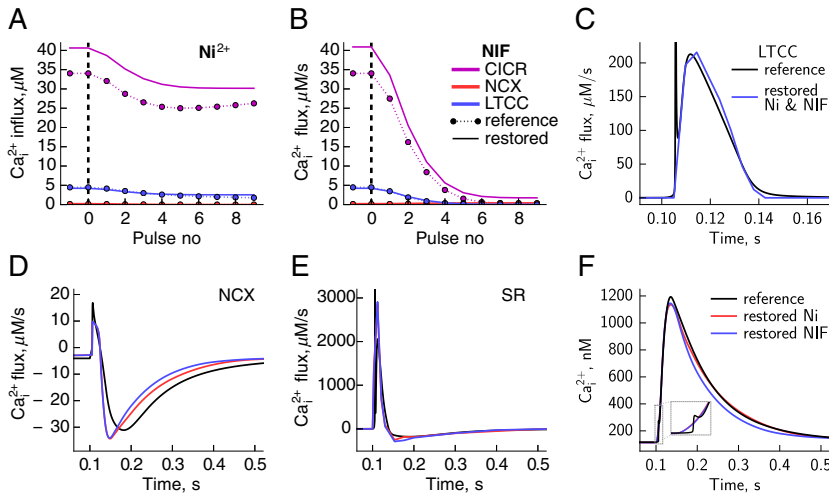


Fig. 5. Analysis of Ca²⁺ fluxes of synthetic data. The changes of different Ca²⁺ influxes per beat induced by synthetic Ni²⁺ (A) or NIF (B) experiment are shown. Here, solid lines indicate the restored influxes and dashed lines correspond to the respective reference influxes from the PHN cell model. Comparison of reference (black) and restored (blue & red) dynamics of different Ca²⁺ fluxes per beat are shown in C–E and respective Ca²⁺ transients in F. (For interpretation of the references to color in this figure legend, the reader is referred to the web version of this article.)

fully at the end of the measurements. This is in agreement with the full suppression of LTCC by NIF at 2.5 μM NIF in trout ventricular cardiomyocytes [19]. In rat ventricular cardiomyocytes, it has been shown that the half maximal effective concentration for NIF is 130 nM and at μM concentration I_{LTCC} is practically absent [35]. Note that inhibition of K⁺ currents by NIF is assumed to be insignificant in trout (see discussion for further details). Second, Ni²⁺ inhibited LTCC and NCX to different extents, but along the same time-course. Third, the time-course of inhibition was assumed to follow an exponential relationship. In the model, the LTCC current scaled in accordance with its inhibition keeping its shape unchanged. This was in contrast to NCX, which was inhibited by reduction of its conductivity only and could change the shape induced by changes in intracellular Ca²⁺ concentration.

The buffering capacity is determined knowing the Ca²⁺ influx through LTCC and NCX, and these were recorded on different cells. Therefore, the analysis was performed for combinations of 4 Ni²⁺- and 5 NIF-inhibited cells (20 pairs of cells in total). Representative

measurements and mathematical model solutions are shown in Fig. 7. Here, the currents were inhibited by addition of 10 μM NIF in Fig. 7A and 1 mM Ni²⁺ in Fig. 7B. Use of 1 mM Ni²⁺ induced moderate inhibition of the currents as indicated by the relatively large amplitude of the Ca²⁺ transient after inhibition (Fig. 7B and E). In this example, the data recorded on the two different cells were fitted very well by the model solution even in the case where there were large differences in AP and Ca²⁺ transients. This particular cell pair demonstrates the cell variability, with the cell used in the Ni²⁺ inhibition protocol having a relatively large peak Ca²⁺, as opposed to the cell used for NIF inhibition (see Table 2 for statistics). Note that the shapes of the compensatory currents I_{NIF} and I_{Ni} and the transitions during inhibition matched the measured data as well as the calculated Ca²⁺ transients. In this example (Fig. 7), the buffering capacity found by the fitting of measured data by model solution was 43.8 μM.

Not all cell combinations led to satisfying fits as judged by visual comparison. More specifically, in some cases, the model was not capable to reproduce the Ca²⁺ transients and fit the inhibition

Table 1
Comparison of the analysis of synthetic data at different noise levels and buffering capacities. Here, the “experimental” denotes a noise level similar to the relative noise observed in real experiments.

	Influx via SR		Influx via LTCC		Influx via NCX		Total influx	
	Rel contrib., %	Δ, %	Rel contrib., %	Δ, %	Rel contrib., %	Δ, %	μM/beat	Δ, %
Reference PHN model	88.1		11.6		0.4		38.7	
<i>Restored influxes at different noise levels</i>								
0	91.2	3.1	8.5	−3.0	0.3	−0.1	45.4	17.5
Experimental	90.4	2.3	9.4	−2.2	0.3	−0.1	45.1	16.7
2× experimental	91.2	3.1	8.6	−2.9	0.2	−0.2	46.1	19.4
5× experimental	89.4	1.3	10.5	−1.0	0.1	−0.3	45.9	18.7
10× experimental	91.1	3.0	8.9	−2.7	0.0	−0.4	51.0	32.0
<i>Restored influxes at different buffer conditions</i>								
Buffering increased	92.2	4.1	7.6	−4.0	0.2	−0.1	51.5	33.2
Buffering decreased	88.9	0.9	10.7	−0.8	0.3	−0.1	39.3	1.6
Buffering estimated from Ca dynamics	89.3	1.2	10.4	−1.2	0.3	−0.1	37.5	−3.0

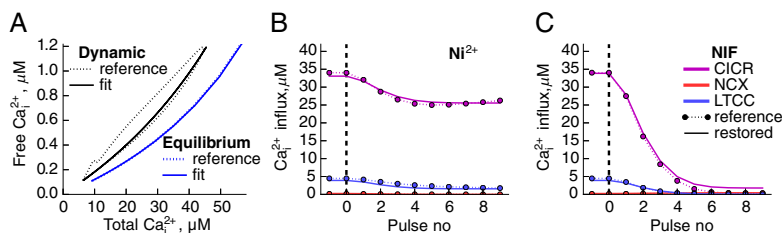


Fig. 6. Analysis of Ca^{2+} buffering in case of synthetic data. To analyze synthetic data, we used two different approaches to estimate total buffering concentration and respective affinities (A). Namely, shown in blue, the Ca^{2+} buffering was estimated from the equilibrium state of the relationship between total and free Ca^{2+} , where as, in black, the buffering was estimated using Ca^{2+} dynamics from the PHN cell model during one cardiac beat. Using buffering derived from Ca^{2+} dynamics gave better estimates for Ca^{2+} influxes in synthetic Ni^{2+} (B) and NIF (C) experiments compared to the results using buffering estimated from the equilibrium state of Ca^{2+} (A and B in Fig. 5, respectively). (For interpretation of the references to color in this figure legend, the reader is referred to the web version of this article.)

dynamics. It may have been due to the too large cell-to-cell variation in those particular combinations, though the exact reason remains unknown. In this part of the analysis, only 5 pairs out of the 20 pairs were discarded, and 15 pairs gave satisfying model fits of the recorded currents and Ca^{2+} transients. In SR inhibited cells, NCX contributed $60 \pm 7\%$ and LTCC $40 \pm 7\%$ to the Ca^{2+} transient.

On average, we found that total intracellular buffering capacity is $51.2 \pm 15.6 \mu\text{M}$. While, to the best of our knowledge, trout buffering capacity has not been directly measured, it is expected to be similar to mammalian cardiomyocytes [36,37], which is ~ 110 – $120 \mu\text{M}$ [38,39]. Thus, while of the same order of magnitude, the buffering capacity in trout is $\sim 2\times$ smaller than in mammalian cardiomyocyte. It could, in part, be due to the smaller relative volume of myofibrils in trout (40% [19]) compared to rat ($\sim 55\%$ [40]).

3.4. Determining cell specific Ca^{2+} fluxes and average contributions

After determining the buffering capacity of trout cardiomyocytes, we proceeded with the analysis of Ca^{2+} fluxes in control cells, where the SR was not inhibited. A representative data set and model solution is shown in Fig. 8. In these experiments, we used 5 mM Ni^{2+} which almost fully inhibited all Ca^{2+} fluxes. As a result, the amplitude of the Ca^{2+} transient was severely reduced (compare Fig. 8D and E). This is in contrast to the application of NIF (Fig. 8A), where inhibition of LTCC did not produce any significant drop in Ca^{2+} transient amplitude. Taking into account that LTCC inhibition reduces the Ca^{2+} transient significantly when it is a dominant Ca^{2+} transmembrane influx, as in the synthetic data Fig. 4, the LTCC inhibition experiments in trout suggest that the role of LTCC in trout is either small or can be compensated by other currents during inhibition.

As before, the data were fitted for pairs of cells, where one was exposed to NIF to inhibit LTCC and the other was exposed to 5 mM Ni^{2+} to inhibit NCX and LTCC. To simulate the recorded data, we used the same assumptions as for the SR-inhibited case. Additionally, we assumed that the difference between calculated changes in Ca^{2+} concentration on the basis of estimated LTCC and NCX currents was induced by SR fluxes. As a result, we could fit the measured data and estimate the fluxes through LTCC, NCX and SR. Furthermore, Ca^{2+} release from SR was assumed to be triggered by the transmembrane currents. Thus, at zero transmembrane current, no Ca^{2+} release from SR was permitted and all model parameter values leading to residual SR Ca^{2+} release at zero transmembrane current were not considered.

Fig. 8 shows the data set and how well the model fits the Ca^{2+} transient. The calculated Ca^{2+} fluxes are shown in Fig. 9. In Fig. 9A and C, each point corresponds to the Ca^{2+} influx through LTCC, NCX or SR during an AP. Fig. 9B and D shows the fluxes during the time

of a single AP before inhibition. The positive Ca^{2+} flux indicates the Ca^{2+} influx through all three pathways at the beginning of AP. Then, less than 100 ms after the beginning of an AP, the Ca^{2+} flux turns negative, indicating that Ca^{2+} is pumped out of the cell via NCX and back into the SR. In both Fig. 9A and C, before the application of inhibitor (i.e. before pulse 0), the distribution of Ca^{2+} influx was as follows: $\sim 1 \mu\text{M}$ through LTCC, $\sim 3 \mu\text{M}$ through NCX, and 5 – $6 \mu\text{M}$ Ca^{2+} is released from the SR. These numbers are the positive, integrated areas in Fig. 9B and D. During relaxation Ca^{2+} removal from cytosol is mediated mainly by NCX and SR. In this case the efflux through NCX and SR was $\sim 4 \mu\text{M}$ and 5 – $6 \mu\text{M}$ respectively. Note that the Ca^{2+} fluxes are given as Ca^{2+} amounts normalized to non-mitochondrial cellular volume.

We analyzed the data obtained from 6 Ni^{2+} - and 4 NIF-inhibited cells by pairing the cells with different inhibitors and fitting the measured data with the model solution (24 pairs). The example shown in Fig. 8 fits very well. However, as in SR-inhibited cells, not all pairs of cells gave satisfying fits. In the following, the results from 15 pairs are summarized. The average shape of Ca^{2+} fluxes via LTCC, NCX and SR, is shown in Fig. 10. According to our analysis of trout ECC, the contributions to Ca^{2+} influx are SR $53 \pm 10\%$, NCX $29 \pm 6\%$, and LTCC $18 \pm 7\%$. The average Ca^{2+} effluxes by SR was $53 \pm 10\%$ and by NCX $47 \pm 10\%$. In addition, transmembrane Ca^{2+} influx and efflux during a beat was in balance in all fitted pairs. Namely, the maximum absolute relative difference of transmembrane Ca^{2+} in- and efflux was less than 2% ($0.8 \pm 0.6\%$). For SR, the difference was zero.

The relatively large contribution of the SR is in agreement with the impact that SR inhibition has on the Ca^{2+} transient. Characteristics of the Ca^{2+} transients in control and SR inhibited cells are given in Table 2. In SR inhibited cells, the transient amplitude is 45% lower, and it rises and falls with significantly slower rates. Extrapolated to the situation *in vivo*, the involvement of the SR results in a much more powerful contraction.

4. Discussion

In this paper we developed a new method to assess the Ca^{2+} dynamics via different pathways during ECC under physiological conditions. The method is based on mathematical analysis of transsarcolemmal Ca^{2+} currents and intracellular Ca^{2+} transients during AP clamp. It allows to quantify the Ca^{2+} fluxes through LTCC, NCX and the SR during a beat. The method was tested against synthetic data generated by a rat ECC model and was able to recover the intracellular Ca^{2+} fluxes from noisy data. While we developed the method using trout cardiomyocytes, it is applicable to other species. We found a large contribution of the SR to the Ca^{2+} transient in trout ventricular myocytes. Around 50% of the Ca^{2+} transient is attributable to CICR from the SR, and the main transmembrane

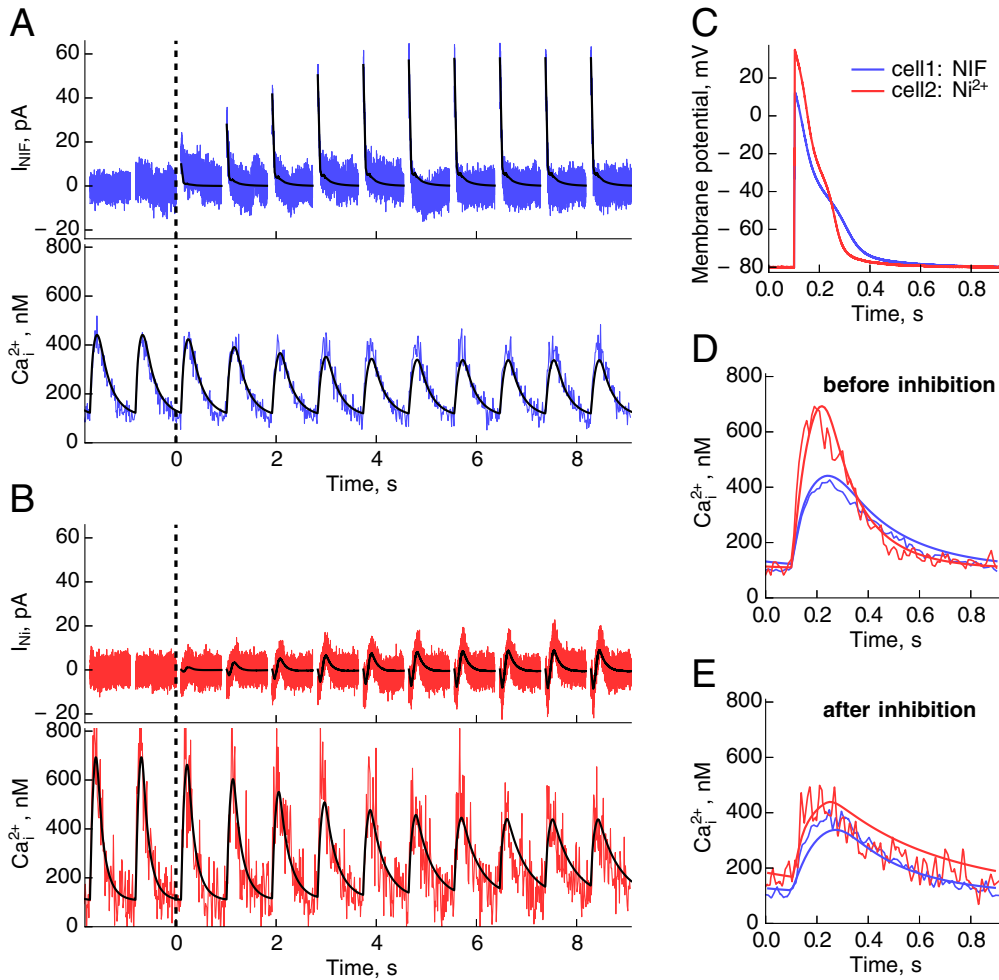


Fig. 7. Representative results for SR inhibited case. Measured compensatory current and corresponding Ca^{2+} transient in the presence of NIF (A) or 1 mM Ni^{2+} (B) and respective model fits (black). The vertical dashed line indicates the moment when NIF (A) or Ni^{2+} (B) starts to take effect and compensatory currents appear. In both cases, model solution fits the shape and beat-to-beat changes of the compensatory currents perfectly. Furthermore, calculated Ca^{2+} transients fit the measured data. Membrane potentials (C) that were used to stimulate cells had a significant cell to cell variability. Change in Ca^{2+} transients during a beat induced by application of NIF (blue) or Ni^{2+} (red) is clear from average of three beats of Ca^{2+} transients before (D) and after (E) of inhibition. As demonstrated in this example, even in the presence of large cell-to-cell variation in the measurements, the data is fitted well by the model solution. Note that inhibition of LTCC by NIF induces only minor changes in calcium concentration dynamics (A). (For interpretation of the references to color in this figure legend, the reader is referred to the web version of this article.)

influx of Ca^{2+} is provided by NCX operating in reverse mode. From our results, we conclude that the SR plays an important role in ECC even under basal conditions in ventricular cardiomyocytes from the

trout. This is in contrast to rat where, according to our simulations using the PHN model [30], the main Ca^{2+} influx is through SR and it is induced by LTCC.

Table 2
Comparison of SR inhibited and control case.

	Control		SR inhibited		p-Value
	Mean \pm SD	n	Mean \pm SD	n	
Ca^{2+} influx via LTCC, μM	2.1 ± 0.7	4	2.9 ± 0.8	5	<0.03
Ca^{2+} influx via NCX, μM	3.5 ± 0.8	6	4.3 ± 1.3	5	0.081
Ca^{2+} transient peak (before inhibition), nM	880 ± 139	10	480 ± 114	9	< 10^{-5}
LTCC inactivation time, ms	21.3 ± 2.6	4	31.0 ± 9.5	5	0.083
Rate of rise of Ca^{2+} transient, $\mu\text{M}/\text{s}$	19.9 ± 5.5	10	7.5 ± 2.4	9	< 10^{-4}
Time to peak of Ca^{2+} transient, ms	71.0 ± 20.0	10	111.2 ± 32.1	9	<0.01
Relaxation time of Ca^{2+} transient, ms	200.4 ± 52.8	10	254.8 ± 55.5	9	<0.05

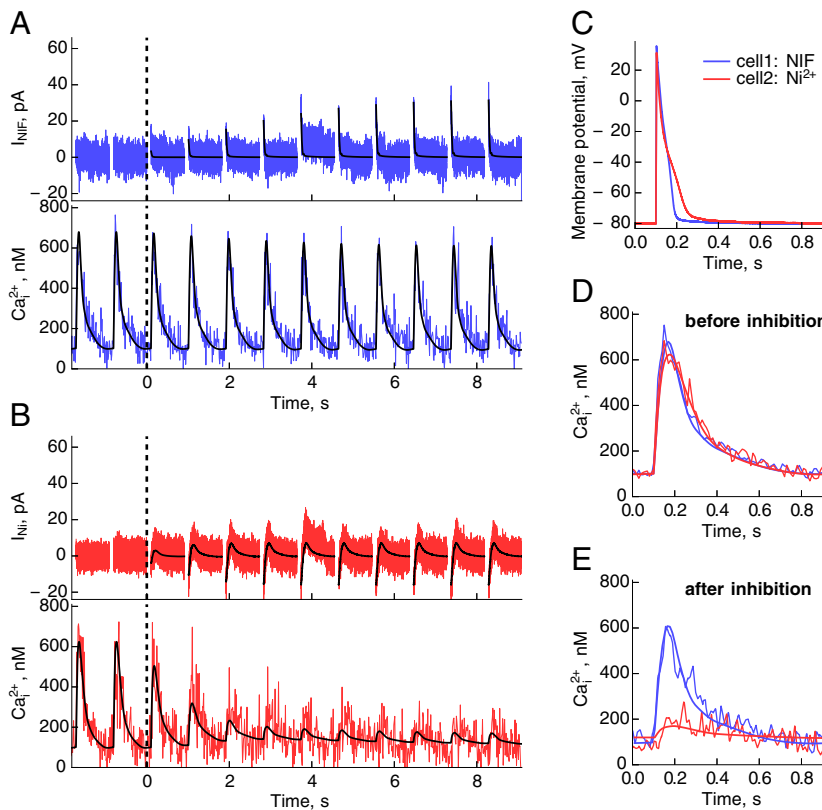


Fig. 8. Representative results for control case with active SR. The notation and subplots are the same as in Fig. 7. Here, 5 mM Ni^{2+} concentration was used leading to a negligible Ca^{2+} transient after inhibition. This is in contrast to the smaller influence of 1 mM Ni^{2+} in Fig. 7. Note that the model solution is able to reproduce the measured compensatory currents and Ca^{2+} transients for both cells.

4.1. Measurement of Ca^{2+} currents and dynamics

In the standard AP clamp approach, the current is measured by exposing the cell to a current-specific inhibitor during AP voltage clamp. The application of inhibitors can be continued with the currents estimated one after another, similar to peeling the layers of an onion [34]. In this approach, there are two major assumptions: the inhibitors are specific for the currents in question, and inhibition of a current does not alter other currents. While these assumptions are reasonable for many currents, none of them are satisfying for Ca^{2+} current studies. First, specific inhibition of NCX has been proven to be problematic [41]. Second, any changes in one of the currents lead to changes in CICR and/or the Ca^{2+} transient that influences NCX. As a result, an estimation of Ca^{2+} fluxes is impossible using the AP clamp approach directly.

The major novelty of our approach is in analyzing the inhibition dynamics occurring at the beginning of the cells' exposure to the inhibitor. By following the transition from non-inhibited to inhibited case, we avoid the problems that arise from the vastly changed intracellular ionic composition at the steady state after inhibition. In the beginning of the inhibition, this effect is secondary and the changes are primarily induced by the inhibited currents. As a result, we can estimate the currents and intracellular fluxes that are deeply interconnected and cannot be altered without influencing each other. More specifically, we followed the transition of

Ca^{2+} currents and Ca^{2+} transients in the cell during inhibition, made some simple assumptions of the underlying processes and, on the basis of these assumptions, constructed a Ca^{2+} balance mathematical model. With this, we were able to estimate the Ca^{2+} currents through sarcolemma and the Ca^{2+} flux from and into the SR during a beat, and their changes during inhibition. As we demonstrate in this work, it is possible even without a specific inhibitor for one of the currents—NCX. This new approach allows to determine Ca^{2+} fluxes in cardiomyocytes in health and disease, and compare the fluxes in different animals and conditions. For its development and as a first example of its use, we applied this approach to resolve the long standing issue on the contribution of SR to the Ca^{2+} transient in trout ventricular myocytes and demonstrated that Ca^{2+} release from the SR is significant under physiological conditions.

4.2. Novel method advantages and outlook

When compared to the approaches that rely on determining Ca^{2+} current properties to estimate Ca^{2+} fluxes, our method has the advantage of disturbing the cell as little as possible. We conducted the measurements in a solution that mimics the extracellular environment and the currents of interest are induced by adding a single chemical compound. Moreover, the data used for fitting is taken shortly before and after inhibition started (± 10 beats). The advantages of keeping the experimental measurements as close to in

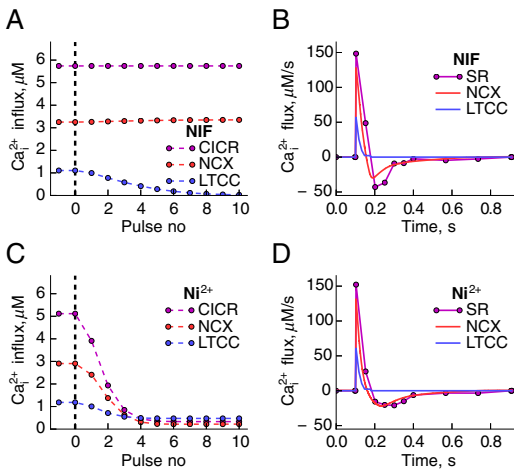


Fig. 9. Analysis of Ca^{2+} fluxes in trout. Top and bottom rows correspond to the data in Fig. 8 obtained from experiments where NIF and Ni^{2+} were used, respectively. The changes of different Ca^{2+} influxes per beat induced by NIF (A) or Ni^{2+} (C) are shown. Dynamics of estimated Ca^{2+} fluxes by SR (purple), NCX (red) and LTCC (blue) during a beat before inhibition are shown for the cell inhibited by NIF (B) or Ni^{2+} (D). (For interpretation of the references to color in this figure legend, the reader is referred to the web version of this article.)

in vivo as possible were clearly demonstrated earlier [42]. That study revealed novel features of I_{LTCC} and showed a much smaller I_{LTCC} magnitude than found before using traditional voltage-clamp data. By following the dynamics of inhibitor-induced current and fluorescence changes, we measure under conditions that are even closer to *in vivo* than standard AP clamp, where the changes induced by inhibitor are measured at steady state and have to be accounted for, as in [42].

The traditional way of estimating contributions of the different Ca^{2+} fluxes would be to determine the properties of all involved channels and compose a mathematical model to estimate the currents *in vivo*. The application of this traditional approach has several challenges. First, channel properties are measured under conditions that are rather far from *in vivo*. For example, LTCC would be characterized by recording currents during square pulses after inhibition of Na^+ channels with tetrodotoxin, K^+ channels with tetraethylammonium and by replacing K^+ with cesium in all solutions. Second, a mathematical model fitting the experimental data would have to be composed and used to predict the currents' dynamics *in vivo*, i.e. under conditions that are far from the experimental conditions used

to calibrate the model. While one can record the channel activity using voltage clamp with an AP, as in [43], to get conditions closer to *in vivo*, the use of a large number of inhibitors to isolate the channel would still disturb the cell. With the proposed method, we perform the recordings while the cell is minimally disturbed.

The developed approach, while relatively complex (Fig. 1), allows to study Ca^{2+} fluxes in cells where detailed electrophysiological models are lacking. The mathematical model used to analyze the data is very simple with LTCC and SR fluxes described by splines. Thus, there is no *a priori* CICR mechanism incorporated into the model that could introduce a bias in the analysis. As a result, the estimated fluxes can be used in formulating and testing the biophysical models of the studied cells.

We envision that our approach could be further developed by combining it with state-of-the-art mathematical models and, through this combination, allow to study details of Ca^{2+} dynamics *in vivo*. As demonstrated by the test against synthetic data, the accurate description of some key processes, such as Ca^{2+} buffering, can improve the accuracy of the method. In this work, inhibition dynamics was described by a simple mathematical model of Ca^{2+} balance. One could replace this mathematical model with the full electrophysiological model allowing to test the model assumptions by fitting the experimental data that is close to *in vivo*. For example, guinea-pig rapid delayed rectifier K^+ current model was recently refined by combined use of traditional AP clamp and dynamic clamp techniques [44]. We expect that the combination of analysis of inhibition dynamics used in this work with dynamic clamp would allow to reveal properties of Ca^{2+} fluxes that have eluded researchers so far.

4.3. Method limitations

When compared to the standard AP clamp, the proposed method is experimentally more time-consuming inasmuch as recordings from one cell provides only the current from one channel/transporter at one stimulation frequency. Taking into account the interactions between currents, as in the case of Ca^{2+} currents, we cannot apply inhibitor after inhibitor to sequentially determine currents in the same cell, as has been done for Na^+ and K^+ currents [34]. Furthermore, the experimental data have to be analyzed by the model, which is an additional step.

The model analysis relies on several parameters that have to be estimated separately. One critical part is the description of Ca^{2+} buffering. As we demonstrated in the test against synthetic data, estimating the buffering capacity using slow measurements leads to overestimation of the buffering capacity. In the case of the synthetic data generated by the rat cardiomyocyte model, this overestimation was below 20% for SR Ca^{2+} influx. Thus, the estimations of the buffering capacity based on similar dynamics as in the measurements are preferable. Alternatively, a more accurate description of

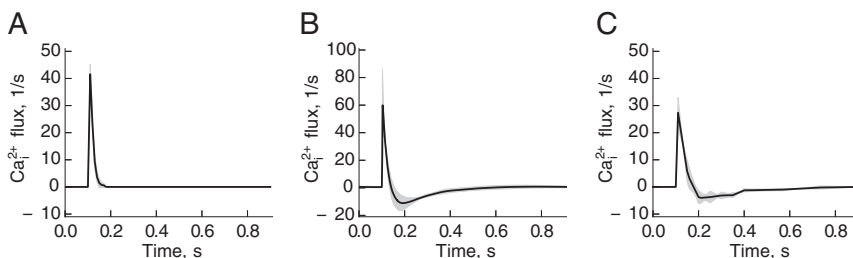


Fig. 10. Average shapes of Ca^{2+} fluxes in trout ventricular cardiomyocytes via LTCC (A), NCX (B) and SR (C). The area in gray indicates a standard deviation of a given Ca^{2+} flux. Here, each flux was normalized to lead to an influx of 1 Ca^{2+} molecule in a second. Notice a small variation in shape among all cells, indicated by small standard deviation in gray.

the buffering could be used that takes into account fast buffers and the buffers that have slower kinetics.

It is essential to note that if there are side-effects of the inhibitors, then these side-effects have to be taken into account. For example, if some Ca^{2+} current inhibitor influences a K^+ current, then one has to inhibit that current before applying Ca^{2+} current inhibitor. That way, the onion peeling approach [34] can be used to overcome side-effects of Ca^{2+} current inhibitors. While such side-effects were not identified in trout cardiomyocytes used in this work (see discussion below), these side-effects are expected when applying the developed method to other cell types and/or species.

More specific method limitations come from the used assumptions. While some of the assumptions have been addressed earlier (Ca^{2+} concentration in rest, NIF inhibition extent of LTCC), others are addressed below.

During the analysis, we assumed that J_{LTCC} shape is unchanged during inhibition with NIF and Ni^{2+} and only the amplitude of the current changes. As we have seen in simulations of cardiac electrophysiology for synthetic data, there is some change in the J_{LTCC} profile during a beat through inhibition. However, we are mainly interested in LTCC kinetics before inhibition, in control. As we demonstrate in our analysis of synthetic data, it can be recovered very well with this assumption (see Fig. 5C). Note that in our analysis we did not wait for a formation of a new steady-state after inhibition, but followed the progress of inhibition during several beats. This is in contrast to the SR inhibited case, where new Ca^{2+} transient dynamics were formed leading to significant changes in currents, as demonstrated in Table 2.

We assumed that the time-constants for NCX and LTCC inhibition were the same. This was a simplification that allowed us to reduce the number of optimized parameters. While there may be differences in the inhibition time constants for NCX and LTCC, this simplification in our analysis, did not cause major issues with the calcium balance model solution. For example, in SR inhibited case (Fig. 7), we were able to fit the compensatory currents and Ca^{2+} transients in a way that total transmembrane Ca^{2+} net flux was zero during each fitted beat. In addition, note that the inhibition curve was given for each flux through inhibition time constant and extent. By setting the two time constants equal, we let the optimizer choose the extent of inhibition by Ni^{2+} of NCX and LTCC. Thus, through the changes in the inhibition extent, the optimizer was able to somewhat compensate for the time-constant differences between the currents.

For simplicity, and as a result of significant reduction in optimization, we took the Ca^{2+} buffer affinity from the literature [29]. The bias in K_b would have influenced the estimation of total Ca^{2+} buffering capacity B_t . Thus, if the used K_b was incorrect that would influence B_t estimated from the analysis of the data in SR-inhibited case. However, in this work, we were interested Ca^{2+} fluxes, not estimation of Ca^{2+} buffering. Taking into account that the model fits were good in the SR-inhibited case, a case where the fits would be influenced the most by wrong Ca^{2+} dynamics, the overall behavior of Ca^{2+} buffering is captured reasonably well with the found buffering constants. In future, by using additional experimental data describing the buffering, this step in the developed method could be improved.

In our analysis, we did not consider the contribution of mitochondria to Ca^{2+} dynamics and, in the present form, the method cannot be used to resolve the debate regarding mitochondrial Ca^{2+} dynamics in the heart [45]. This is a limitation of the current implementation of the method. However, we think that it is possible to incorporate Ca^{2+} fluxes to and from mitochondria by loading mitochondria with a Ca^{2+} -sensitive dye, for example as in [46], and observing its fluorescence changes during a beat. Such extension of the developed method is not trivial and would require an additional calibration of the mitochondrial Ca^{2+} fluorescence signal. When the developed method is used as it is, mitochondrial Ca^{2+} dynamics would be incorporated into the estimated fluxes as follows. The

possible flux between SR and mitochondria through direct coupling between organelles would not be incorporated into any of the fluxes since it does not influence Ca^{2+} in cytosol. The flux between mitochondria and cytosol would be incorporated into the flux from and to SR. So, when analyzing the data from cells with significant Ca^{2+} fluxes to and from mitochondria, these limitations of the current implementation of the method have to be taken into account when interpreting the estimated fluxes.

In trout, our analysis points to a rather small direct Ca^{2+} flux between mitochondria and cytosol. This conclusion is based on the fact that we were able to fit the Ca^{2+} dynamics and AP clamp current measurements relatively well in SR-inhibited case (Fig. 7). There is a small deviation of the model fit from the center of the measured currents suggesting that the model did not recover all the currents, for example a smaller current by sarcolemmal Ca-ATPase pump (see below for discussion). However, taking into account that the deviations are relatively small, these fits suggest that there are no significant fluxes missing from the mathematical model. Notice that in SR-inhibited case, there were no fluxes from and to SR in the model with only transmembrane currents and a buffer influencing the model solution. Since the fluxes from and to mitochondria are expected to be relatively slow (not as fast as fast buffer kinetics), we would expect significant deviations between model solution and experimental data if mitochondrial fluxes to/from cytosol would be large. However, it has to be pointed out that, as discussed above, our data does not allow us to estimate the direct flux between SR and mitochondria in trout.

The last specific limitation of the method is the absence of the contribution of the sarcolemmal Ca-ATPase pump. The contribution of this pump is expected to be small [47] and it would be difficult to estimate it against the other, large fluxes. As demonstrated in the analysis of synthetic data, which included Ca-ATPase pump in the underlying mathematical model [30], the absence of the pump contribution in our analysis did not influence the estimated Ca^{2+} fluxes significantly and allowed us to recover the main fluxes (Fig. 5). To be able to estimate the flux induced by the pump, we think that the detailed biophysical model has to be used as a part of the analysis of the inhibition data. Through iterative adjustment of the model when comparing its solution to the measured data, it may be possible to estimate the contribution of the pump to overall Ca^{2+} dynamics.

4.4. Nifedipine interaction with potassium currents

It has previously been shown that NIF can inhibit not only the LTCC current but K^+ currents as well. For example, transient outward currents (I_{to}) in rat ventricular myocytes [48], I_{to} and ultra rapid potassium currents (I_{Kur}) in human atrial myocytes [49], and potassium channel Kv2.1 in HEK293 cells [50]. In fish cardiomyocytes, the two major K^+ currents are the rapid delayed rectifier current (I_{Kr}) and the background inward rectifier current (I_{K1}) [51,52]. I_{K1} is responsible for maintaining the resting membrane potential and is activated in the final AP repolarization phase [53]. The compensatory current measured in the presence of NIF is zero at that AP phase (Fig. 8B) demonstrating that NIF did not inhibit I_{K1} . Trout APs of ventricular cardiomyocytes lack the phase-1 repolarization suggesting that the contribution of I_{to} is marginal or even absent as in zebrafish [54]. Even if there is I_{to} present, then 10 μM NIF would lead to a reduction of only 20% of that current [49]. Moreover, if there would have been a significant effect of NIF on any K^+ currents then fitting the Ca^{2+} transients with transmembrane Ca^{2+} fluxes, J_{LTCC} and J_{NCX} , derived from the measured compensatory currents would have been unsuccessful. Namely, Ca^{2+} influx to the cell via LTCC and NCX_{rev} was extruded from the cell by NCX to ensure the balance of Ca^{2+} influx and efflux during a beat. If NIF would inhibit any K^+ currents significantly, J_{LTCC} estimation from AP clamp would be

significantly different from the real J_{LTCC} ensuring that the Ca^{2+} balance would not be kept by NCX. As shown in our fits (Figs. 7 and 8), the Ca^{2+} balance is kept in the simulations describing control and SR-inhibited cardiomyocytes. This demonstrates that NIF does not significantly alter K^+ currents in trout cardiomyocytes.

4.5. With NCX_{rev} as the main transsarcolemmal Ca^{2+} -source, CICR from the SR is responsible for about 50% of the Ca^{2+} influx in trout ventricular myocytes

The importance of the SR in trout ventricular myocytes has been studied for a long time. The situation is complex as SR function depends on temperature and pacing frequency. Studies on ventricular strips, where the SR was inhibited with ryanodine, suggest that the SR is more important at high temperatures and low pacing frequencies [8,55]. From a comparison of different studies [8,55,56], it seems that the SR mainly participates in ECC at temperatures above 20 °C. But, although the SR may be functional in trout ventricle, most studies conclude that its role is minor under physiological, baseline conditions, and the main Ca^{2+} influx pathway is LTCC [11,55,56].

The present results give a different picture. We kept the conditions close to physiological and found that the ECC in trout ventricular myocytes is largely controlled by Ca^{2+} influx via NCX_{rev} . Ca^{2+} influx via LTCC was ~ 2 times smaller than the influx via NCX_{rev} . These transmembrane fluxes triggered a significant CICR from the SR, which was responsible for about half of the total Ca^{2+} influx. This is in agreement with the data of Shiels et al. [55]. At conditions similar to ours (22 °C and stimulation frequencies of 1–1.2 Hz), they found that SR inhibition of ventricular strips resulted in a decrease in peak tension that was of similar magnitude as the decrease of the Ca^{2+} transient measured in this work. It has been shown before that both J_{LTCC} and NCX_{rev} can trigger CICR [57], and a large Ca^{2+} influx through NCX_{rev} was expected on basis of the high intracellular Na^+ concentration found in trout cardiomyocytes [12]. The relatively small contribution of LTCC to the transsarcolemmal Ca^{2+} fluxes fits well with the results of Cros et al. [11]. They used Na^+ -free solution to block NCX and found that LTCC alone only triggers CICR during adrenergic stimulation, but not under baseline conditions. Our results show that the larger, combined Ca^{2+} influx through NCX and LTCC under baseline, physiological conditions triggers a significant CICR.

The major impact of our study is in the *quantitative* measurements of the flux distributions *in vivo*. This is in contrast with earlier works which *qualitatively* suggest an importance of SR in trout ECC [21,23,36,58,59]. As an example of qualitative data on the SR role, in [21], the Ca^{2+} transients of trout cardiomyocytes are compared before and after SR calcium depletion. The large difference in Ca^{2+} transients in the two studied cases demonstrates importance of SR in Ca^{2+} dynamics, but does not provide a quantitative measure. As we have seen in our analysis, there are significant changes in the Ca^{2+} currents induced by inhibition of SR Ca^{2+} uptake and release (Table 2). These changes occur even if the AP stimulating the cardiomyocyte is kept the same as before inhibition, a condition that is not met when using field stimulation as in [21]. The changes in Ca^{2+} currents demonstrate that estimating the role of SR by inhibiting SR fluxes has to take into account that all other Ca^{2+} fluxes can change as well. For example, in our measurements, while the Ca^{2+} transients were reduced in the SR inhibited case, this reduction was partially offset by an increase in LTCC. This can be explained by Ca^{2+} dependent inactivation of LTCC that is clear when comparing LTCC inactivation times (see Table 2). Thus, Ca^{2+} flux estimates based on comparison of steady states before and after inhibition give a qualitative but not quantitative estimate of the fluxes.

4.6. Physiological implications

The importance of NCX in trout ventricular myocytes may provide an explanation for the negative force-frequency relationship [60]. The shape of the AP depends on the heart rate, and its duration increases as the frequency decreases. This will result in a larger Ca^{2+} influx via NCX_{rev} , which in turn will provide a larger trigger of CICR from the SR. When changes in temperature are taken into account, the situation becomes more complex, as the triggering of the SR seems to depend on temperature as well.

The large contribution of the SR in ventricular myocytes may explain the relatively high SR Ca^{2+} load in ventricular myocytes [61]. Neither the SR Ca^{2+} load nor the ryanodine receptor expression or localization change with temperature acclimation [61,62]. However, SERCA expression increases with cold-acclimation in atrium as well as ventricle [63]. Thus, although there are temperature dependent adaptations, it seems that the SR is always ready to be recruited. This may explain why rainbow trout can manage relatively large, acute shifts in temperature.

4.7. Trout cardiomyocytes as a model for neonatal mammalian cardiomyocytes

There are several similarities between trout cardiomyocytes and neonatal mammalian cardiomyocytes. Morphologically, both are long and slender with no t-tubules [18,64]. Energetically, both are more hypoxia-tolerant and have a higher glycolytic capacity [65], and lack functional coupling of mitochondrial creatine kinase to respiration [18,66]. With the present results, we can finally demonstrate what was expected on basis of the high Na^+ concentration in trout ventricular myocytes [12] that the similarities extend to ECC as well. Neonatal rabbit cardiomyocytes have a relatively large Ca^{2+} influx via NCX_{rev} , which triggers CICR from the SR [13], and ryanodine receptors which co-localize with NCX rather than L-type Ca^{2+} channels [64,67]. Although co-localization studies are lacking, we have now shown that, in functional terms, trout ECC is similar. The situation is of course more complex than just stated, and the contributions of the Ca^{2+} influx pathways are expected to range with species and conditions. But there is a trend that cardiomyocyte morphology, energetics and ECC are all interconnected and adapted to the conditions.

5. Conclusions

The aim of this work was two-fold: 1) to develop a method to quantify the Ca^{2+} influx pathways during ECC *in vivo*; 2) to determine the role of CICR from the SR in trout ventricular myocytes.

AP clamp was already established over two decades ago by Doerr et al., [33] and not so long ago an extension of this method to record multiple ionic currents in the single cell was proposed [34]. We, in turn, combined the AP clamp technique, intracellular calcium imaging and mathematical modeling. Our novel approach allows us to quantitatively assess contributions and kinetics of different Ca^{2+} pathways on single cell level by analyzing the changes in measured Ca^{2+} transients and corresponding compensatory currents on beat-to-beat basis during gradual inhibition with transmembrane Ca^{2+} current blockers.

Here, we quantified the contribution and show the dynamics of different Ca^{2+} pathways in trout ventricular cardiomyocytes during a single beat. To our knowledge, this is done for the first time for intact cardiomyocytes. Moreover, our findings quantify the significant role of SR and NCX_{rev} under basal conditions in trout ventricular cardiomyocytes.

Author contributions

Designed research: RB, ML, MV; performed research: ML; analyzed data: ML, RB, MV; drafted the manuscript: ML, RB, MV.

Disclosures

None.

Sources of funding

This work was supported by Estonian Science Foundation (Grant No. 8041), European Union through the European Regional Development Fund (CENS Estonian Center of Excellence in Research), and Estonian Research Council (IUT33-7).

References

- D.M. Bers, Excitation-Contraction Coupling and Cardiac Contractile Force, Kluwer Academic Publishers, 2001.
- A. Yao, Z. Su, A. Nonaka, I. Zubair, L. Lu, K. Philipson, J.B. Bridge, W. Barry, Effects of overexpression of the Na⁺-Ca²⁺ exchanger on [Ca²⁺]_i transients in murine ventricular myocytes, *Circ. Res.* 82 (6) (1998) 657–665.
- C. Terracciano, A. De Souza, K. Philipson, K. Macleod, Na⁺-Ca²⁺ exchange and sarcoplasmic reticular Ca²⁺ regulation in ventricular myocytes from transgenic mice overexpressing the Na⁺-Ca²⁺ exchanger, *J. Physiol. (Lond.)* 512 (Pt 3) (1998) 651–667.
- R. Larbig, N. Torres, J. Bridge, J. Goldhaber, K. Philipson, Activation of reverse Na⁺-Ca²⁺ exchange by the Na⁺ current augments the cardiac Ca²⁺ transient: evidence from NCX knockout mice, *J. Physiol. (Lond.)* 588 (Pt 17) (2010) 3267–3276. ISSN 0022-3751.
- M. Vornanen, Excitation-contraction coupling of the developing rat heart, *Mol. Cell. Biochem.* 163–164 (1996) 5–11.
- M. Vornanen, Na⁺/Ca²⁺ exchange current in ventricular myocytes of fish heart: contribution to sarcolemmal Ca²⁺ influx, *J. Exp. Biol.* 202 (Pt 13) (1999) 1763–1775.
- H. Shiels, G.J. Galli, The sarcoplasmic reticulum and the evolution of the vertebrate heart, *Physiology* 29 (6) (2014) 456–469.
- L. Hove-Madsen, The influence of temperature on ryanodine sensitivity and the force-frequency relationship in the myocardium of rainbow trout, *J. Exp. Biol.* 167 (1992) 47–60.
- C.L. Harwood, F.C. Howarth, J.D. Altringham, E. White, Rate-dependent changes in cell shortening, intracellular Ca²⁺ levels and membrane potential in single, isolated rainbow trout (*Oncorhynchus mykiss*) ventricular myocytes, *J. Exp. Biol.* 203 (2000) 493–504.
- H.A. Shiels, M. Vornanen, A.P. Farrell, Effects of temperature on intracellular Ca²⁺ in trout atrial myocytes, *J. Exp. Biol.* 205 (2002) 3641–3650.
- C. Cros, L. Salle, D.E. Warren, H.A. Shiels, F. Brette, The calcium stored in the sarcoplasmic reticulum acts as a safety mechanism in rainbow trout heart, *AJP: Regul. Integr. Comp. Physiology* 307 (2014) R1493–R1501.
- R. Birkedal, H.A. Shiels, High [Na⁺]_i in cardiomyocytes from rainbow trout, *Am. J. Physiol. Regul. Integr. Comp. Physiol.* 293 (2007) R861–R866.
- J. Huang, L. Hove-Madsen, G.F. Tibbitts, Ontogeny of Ca²⁺-induced Ca²⁺ release in rabbit ventricular myocytes, *Am. J. Physiol. Cell. Physiol.* 294 (2008) C516–C525.
- T. Klitzner, W.F. Friedman, Excitation-contraction coupling in developing mammalian myocardium: evidence from voltage clamp studies, *Pediatr. Res.* 23 (1988) 428–432.
- D.M. Bers, S. Despa, Cardiac myocytes Ca²⁺ and Na⁺ regulation in normal and failing hearts, *J. Pharmacol. Sci.* 100 (2006) 315–322.
- J.W. Bassani, W. Yuan, D.M. Bers, Fractional SR Ca release is regulated by trigger Ca and SR Ca content in cardiac myocytes, *Am. J. Physiol.* 268 (1995) C1313–C1319.
- H.A. Shiels, E.V. Freund, A.P. Farrell, B.A. Block, The sarcoplasmic reticulum plays a major role in isometric contraction in atrial muscle of yellowfin tuna, *J. Exp. Biol.* 202 (Pt 7) (1999) 881–890.
- N. Sokolova, M. Vendelin, R. Birkedal, Intracellular diffusion restrictions in isolated cardiomyocytes from rainbow trout, *BMC Cell Biol.* 10 (2009) 90.
- M. Vornanen, L-type Ca²⁺ current in fish cardiac myocytes: effects of thermal acclimation and beta-adrenergic stimulation, *J. Exp. Biol.* 201 (1998) 533–547.
- P. Andreasen, Free and total calcium concentrations in the blood of rainbow trout, *Salmo gairdneri*, during 'stress' conditions, *J. Exp. Biology* 118 (1985) 111–120.
- A. Llach, C. Molina, E. Alvarez-Lacalle, L. Tort, R. Benítez, L. Hove-Madsen, B. Launikonis, Detection, properties, and frequency of local calcium release from the sarcoplasmic reticulum in teleost cardiomyocytes, *PLoS ONE* 6 (2011) e23708.
- C.E. Molina, H. Gesser, A. Llach, L. Tort, L. Hove-Madsen, Modulation of membrane potential by an acetylcholine-activated potassium current in trout atrial myocytes, *Am. J. Physiol. Regul. Integr. Comp. Physiol.* 292 (2007) R388–R395.
- H.A. Shiels, E. White, Temporal and spatial properties of cellular Ca²⁺ flux in trout ventricular myocytes, *Am. J. Physiol. Regul. Integr. Comp. Physiol.* 288 (2005) R1756–R1766.
- M. Vornanen, Sarcolemmal Ca influx through L-type Ca channels in ventricular myocytes of a teleost fish, *AJP: Regul. Integr. Comp. Physiology* 272 (1997) R1432–R1440.
- A.P. Farrell, A.K. Gamperl, J.M. Hicks, H.A. Shiels, K.E. Jain, Maximum cardiac performance of rainbow trout (*Oncorhynchus mykiss*) at temperatures approaching their upper lethal limit, *J. Exp. Biol.* 199 (1996) 663–672.
- N. Jephthina, N. Beraud, M. Sepp, R. Birkedal, M. Vendelin, Permeabilized rat cardiomyocyte response demonstrates intracellular origin of diffusion obstacles, *Biophys. J.* 101 (2011) 2112–2121.
- P. Simson, N. Jephthina, M. Laasmaa, P. Peterson, R. Birkedal, M. Vendelin, Restricted ADP movement in cardiomyocytes: cytosolic diffusion obstacles are complemented with a small number of open mitochondrial voltage-dependent anion channels, *J. Mol. Cell. Cardiol.* 97 (2016) 197–203.
- H.A. Shiels, A.D. Maio, S. Thompson, B.A. Block, Warm fish with cold hearts: thermal plasticity of excitation-contraction coupling in bluefin tuna, *Proc. Royal Soc. B: Biological Sci. NA* (2010).
- J. Greenstein, R. Winslow, An integrative model of the cardiac ventricular myocyte incorporating local control of Ca²⁺ release, *Biophys. J.* 83 (2002) 2918–2945.
- J. Terkildsen, S. Niederer, E. Crampin, P. Hunter, N. Smith, Using physiome standards to couple cellular functions for rat cardiac excitation-contraction, *Exp. Physiol.* 93 (2008) 919–929.
- A. Hindmarsh, ODEPACK, a systematized collection of ODE solvers, *Sci. Comput.* 1 (1983) 55–64.
- J.J. More, D.C. Sorensen, K.E. Hillstrom, B.S. Garbow, The MINPACK Project, in: W.J. Cowell (Ed.), Sources and Development of Mathematical Software, Prentice-Hall, 1984.
- T. Doerr, R. Denger, W. Trautwein, Calcium currents in single SA nodal cells of the rabbit heart studied with action potential clamp, *Pflugers Arch.* 413 (1989) 599–603.
- T. Banyasz, B. Horvath, Z. Jian, L. Izu, Y. Chen-Izu, Sequential dissection of multiple ionic currents in single cardiac myocytes under action potential-clamp, *J. Mol. Cell. Cardiol.* 50 (2011) 578–581.
- J. Wegener, H. Meyer, J. Rupp, H. Nawrath, Barnidipine block of L-type Ca²⁺ channel currents in rat ventricular cardiomyocytes, *Br. J. Pharmacol.* 130 (2000) 2015–2023.
- L. Hove-Madsen, A. Llach, L. Tort, Quantification of Ca²⁺ uptake in the sarcoplasmic reticulum of trout ventricular myocytes, *Am. J. Physiol.* 275 (1998) R2070–R2080.
- M. Vornanen, H.A. Shiels, A.P. Farrell, Plasticity of excitation-contraction coupling in fish cardiac myocytes, *Comp. Biochem. Physiol. A Mol. Integr. Physiol.* 132 (2002) 827–846.
- A.W. Trafford, M.E. Diaz, D.A. Eisner, A novel, rapid and reversible method to measure Ca buffering and time-course of total sarcoplasmic reticulum Ca content in cardiac ventricular myocytes, *Pflugers Arch.* 437 (1999) 501–503.
- J.R. Berlin, J.W. Bassani, D.M. Bers, Intrinsic cytosolic calcium buffering properties of single rat cardiac myocytes, *Biophys. J.* 67 (1994) 1775–1787.
- M. Aliev, P. Santos, J. Hoerster, S. Soboll, A. Tikhonov, V. Saks, Water content and its intracellular distribution in intact and saline perfused rat hearts revisited, *Cardiovasc. Res.* 53 (2002) 48–58.
- M.S. Amran, N. Homma, K. Hashimoto, Pharmacology of KB-R7943: a Na⁺-Ca²⁺ exchange inhibitor, *Cardiovasc Drug Res* 21 (2003) 255–276.
- T. Banyasz, B. Horvath, Z. Jian, L. Izu, Y. Chen-Izu, Profile of L-type Ca²⁺ current and Na⁺/Ca²⁺ exchange current during cardiac action potential in ventricular myocytes, *Heart Rhythm* 9 (2012) 134–142.
- H.A. Shiels, M. Vornanen, A.P. Farrell, Temperature-dependence of L-type Ca²⁺ channel current in atrial myocytes from rainbow trout, *J. Exp. Biol.* 203 (2000) 2771–2780.
- C. Bartolucci, C. Altomare, M. Bennati, S. Furini, A. Zaza, S. Severi, Combined action potential- and dynamic-clamp for accurate computational modelling of the cardiac I_{Kr} current, *J. Mol. Cell. Cardiol.* 79 (2015) 187–194.
- G.B. Williams, L. Boyman, A. Chikando, R. Khairallah, W.J. Lederer, Mitochondrial calcium uptake, *PNAS* 110 (2013) 10479–10486.
- X. Lu, K. Ginsburg, S. Kettlewell, J. Bossuyt, G. Smith, D. Bers, Measuring local gradients of intramitochondrial [Ca²⁺]_i in cardiac myocytes during sarcoplasmic reticulum Ca²⁺ release, *Circ. Res.* 112 (2013) 424–431.
- D. Bers, Calcium fluxes involved in control of cardiac myocyte contraction, *Circ. Res.* 87 (2000) 275–281.
- U. Jahnel, P. Klemm, H. Nawrath, Different mechanisms of the inhibition of the transient outward current in rat ventricular myocytes, *Naunyn-Schmiedeberg Arch. Pharmacol.* 349 (1994) 87–94.
- Z. Gao, H. Sun, S. Chiu, C. Lau, G. Li, Effects of diltiazem and nifedipine on transient outward and ultra-rapid delayed rectifier potassium currents in human atrial myocytes, *Br. J. Pharmacol.* 144 (2005) 595–604.
- X. Li, X. Li, X. Hu, X. Qiu, The inhibitory effects of Ca²⁺ channel blocker nifedipine on rat Kv2.1 potassium channels, *PLoS ONE* 10 (2015) e0124602.
- M. Vornanen, A. Ryokkynen, A. Nurmi, Temperature-dependent expression of sarcolemmal K⁺ currents in rainbow trout atrial and ventricular myocytes, *Am. J. Physiol. Regul. Integr. Comp. Physiol.* 282 (2002) R1191–R1199.

- [52] M. Hassinen, V. Paajanen, J. Haverinen, H. Eronen, M. Vornanen, Cloning and expression of cardiac Kir2.1 and Kir2.2 channels in thermally acclimated rainbow trout, *AJP: Regul. Integr. Comp. Physiology* 292 (2007) R2328–R2339.
- [53] J. Haverinen, M. Vornanen, Responses of action potential and K⁺ currents to temperature acclimation in fish hearts: phylogeny or thermal preferences? *Physiol. Biochem. Zool.* 82 (2009) 468–482.
- [54] M. Vornanen, M. Hassinen, Zebrafish heart as a model for human cardiac electrophysiology, *Channels (Austin)* 10 (2) (2016) 101–110.
- [55] H.A. Shiels, E.D. Stevens, A.P. Farrell, Effects of temperature, adrenaline and ryanodine on power production in rainbow trout *Oncorhynchus mykiss* ventricular trabeculae, *J. Exp. Biol.* 201 (Pt 19) (1998) 2701–2710.
- [56] E. Aho, M. Vornanen, Contractile properties of atrial and ventricular myocardium of the heart of rainbow trout *Oncorhynchus mykiss*: effects of thermal acclimation, *J. Exp. Biol.* 202 (Pt 19) (1999) 2663–2677.
- [57] L. Hove-Madsen, A. Llach, G.F. Tibbits, L. Tort, Triggering of sarcoplasmic reticulum Ca²⁺ release and contraction by reverse mode Na⁺/Ca²⁺ exchange in trout atrial myocytes, *Am. J. Physiol. Regul. Integr. Comp. Physiol.* 284 (2003) R1330–R1339.
- [58] L. Hove-Madsen, A. Llach, L. Tort, Quantification of calcium release from the sarcoplasmic reticulum in rainbow trout atrial myocytes, *Pflügers Arch.* 438 (1999) 545–552.
- [59] L. Hove-Madsen, A. Llach, L. Tort, Na⁺/Ca²⁺-exchange activity regulates contraction and SR Ca²⁺ content in rainbow trout atrial myocytes, *Am. J. Physiol. Regul. Integr. Comp. Physiol.* 279 (5) (2000) R1856–R1864.
- [60] W.R. Driedzic, H. Gesser, Ca²⁺ protection from the negative inotropic effect of contraction frequency on teleost hearts, *J. Comp. Physiol. [B]* 156 (1985) 135–142.
- [61] J. Haverinen, M. Vornanen, Comparison of sarcoplasmic reticulum calcium content in atrial and ventricular myocytes of three fish species, *AJP: Regul. Integr. Comp. Physiology* 297 (4) (2009) R1180–R1187.
- [62] R. Birkedal, J. Christopher, A. Thistlethwaite, H. Shiels, Temperature acclimation has no effect on ryanodine receptor expression or subcellular localization in rainbow trout heart, *J. Comp. Physiol. B, Biochem. Syst. Environ. Physiol.* 179 (2009) 961–969.
- [63] H. Korajoki, M. Vornanen, Expression of SERCA and phospholamban in rainbow trout (*Oncorhynchus mykiss*) heart: comparison of atrial and ventricular tissue and effects of thermal acclimation, *J. Exp. Biol.* 215 (2012) 1162–1169.
- [64] F. Sedarat, L. Xu, E.D. Moore, G.F. Tibbits, Colocalization of dihydropyridine and ryanodine receptors in neonate rabbit heart using confocal microscopy, *Am. J. Physiol. Heart Circ. Physiol.* 279 (2000) H202–H209.
- [65] B. Ostadal, I. Ostadalova, N. Dhalla, Development of cardiac sensitivity to oxygen deficiency: comparative and ontogenetic aspects, *Physiol. Rev.* 79 (1999) 635–659.
- [66] J.A. Hoerter, R. Ventura-Clapier, A. Kuznetsov, Compartmentation of creatine kinases during perinatal development of mammalian heart, *Mol. Cell. Biochem.* 133–134 (1994) 277–286.
- [67] P. Dan, E. Lin, J. Huang, P. Biln, G.F. Tibbits, Three-dimensional distribution of cardiac Na⁺-Ca²⁺ exchanger and ryanodine receptor during development, *Biophys. J.* 93 (7) (2007) 2504–2518.

Supporting material:

Revealing calcium fluxes by analyzing inhibition dynamics in action potential clamp

M. Laasmaa, R. Birkedal, and M. Vendelin

The supporting material consist of four parts. First, general electrophysiological parameters of the used cardiomyocytes and analysis of Ni^{2+} inhibition are given. Second, the mathematical model used for data analysis is described. Third, parameter optimization procedures for estimating total cellular calcium buffering capacity and estimating cell specific calcium fluxes are given. Finally, tables containing values of used constants and optimized parameters are presented.

Contents

1 Supporting results	S1
2 Mathematical model	S1
3 Optimization procedures	S2
3.1 Estimating total cellular calcium buffering capacity . .	S2
3.2 Estimating cell specific calcium fluxes and average contributions	S3
3.3 Minimized residuals	S3
4 Values of used constants and optimized parameters	S5
Supporting references	S5

1 SUPPORTING RESULTS

The myocytes used for the study had an average cell volume and capacitance of $5056 \pm 1017 \mu\text{m}^3$ and $21.9 \pm 3.7 \text{ pF}$ in control ($n=10$) and $4848 \pm 2010 \mu\text{m}^3$ and $19.2 \pm 4.2 \text{ pF}$ in SR-inhibited cells ($n=9$). Their series resistance was $21.8 \pm 8.2 \text{ M}\Omega$ and $25.5 \pm 3.6 \text{ M}\Omega$ in control and SR-inhibited cells, respectively. None of these electrophysiological parameters were significantly different between control and SR-inhibited cells.

Inhibition effect of Ni^{2+} . In our experiments we used two different Ni^{2+} concentrations: 1 mM and 5 mM. In these experiments, Ni^{2+} reduced the total flow through NCX significantly more ($p < 10^{-5}$) when the larger concentration of Ni^{2+} was used: by $59 \pm 5\%$ ($n=15$) at 1 mM or $97 \pm 3\%$ ($n=15$) at 5 mM. LTCC flux inhibition had the same tendency, but did not reach statistical significance ($p=0.12$): LTCC was inhibited by $21 \pm 9\%$ ($n=15$) at 1 mM Ni^{2+} or $29 \pm 15\%$ ($n=15$) at 5 mM Ni^{2+} . The reduction of the current by Ni^{2+} was always more profound for NCX than LTCC for both Ni^{2+} concentrations ($p < 0.001$).

2 MATHEMATICAL MODEL

To estimate the contributions and kinetics of LTCC, NCX, and CICR, we composed a simple mathematical model of Ca^{2+} dynamics before and during inhibition of Ca^{2+} fluxes.

Ca^{2+} balance model. To determine Ca^{2+} dynamics in cardiomyocytes, we simulated Ca^{2+} dynamics using a simple Ca^{2+} balance model. In the model, transmembrane and internal Ca^{2+} release and uptake induce changes in cytosolic Ca^{2+} concentration per beat that are modulated by intracellular buffer and the fluorescent dye:

$$\frac{d\text{Ca}}{dt} = \left(1 + \frac{F_t K_f}{(K_f + \text{Ca})^2} + \frac{B_t K_b}{(K_b + \text{Ca})^2} \right)^{-1} \cdot (J_{\text{LTCC}} + J_{\text{NCX}} + J_{\text{SR}}), \quad (1)$$

where Ca is intracellular free calcium concentration, B_t total intracellular Ca^{2+} buffer concentration, K_b is dissociation constant for intracellular buffer, F_t is the total concentration of the fluorescent agent, K_f its dissociation constant. J_{LTCC} , J_{NCX} and J_{SR} are Ca^{2+} fluxes induced by LTCC, NCX and SR, respectively. The fluxes are normalized by the non-mitochondrial cell volume. Representation of different Ca^{2+} fluxes are described below.

Approximation of J_{LTCC} . We used a first order periodic spline S_{LTCC} to determine J_{LTCC} . Within period p , the spline has six nodal points equally distributed between 0.1–0.18 s that can have values between 0 and 1. Everywhere else, $S_{\text{LTCC}}(t) = 0$ is assumed. Using this spline, J_{LTCC} is defined as

$$J_{\text{LTCC}} = H_{\text{LTCC}}(t) \cdot c \cdot C \cdot S_{\text{LTCC}}(t), \quad (2)$$

where $H_{\text{LTCC}}(t)$ determines inhibition of J_{LTCC} , c is a conductivity of J_{LTCC} that is normalized here and below by capacitance C and non-mitochondrial volume of the cell.

Approximation of J_{NCX} . For J_{NCX} , we assumed that the flux is dependent only on the corresponding electrochemical gradient Π :

$$J_{\text{NCX}} = H_{\text{NCX}}(t) \cdot c \cdot C \cdot g_{\text{NCX}} \cdot \begin{cases} \Pi, & \text{if } \Pi \leq 0, \\ \frac{K_{\Pi} \Pi}{K_{\Pi} + \Pi}, & \text{otherwise,} \end{cases} \quad (3)$$

and

$$\Pi = \exp\left(\frac{V_m(t)F}{RT}\right) [\text{Na}^+]_e^3 [\text{Ca}^{2+}]_e - [\text{Na}^+]_e^3 [\text{Ca}^{2+}]_i, \quad (4)$$

where $H_{\text{NCX}}(t)$ determines inhibition of J_{NCX} , c is a conductivity, C is capacitance of the cell, g_{NCX} is a scaling factor, K_{Π} is NCX kinetic constant, $V_m(t)$ is membrane potential measured at time-moment t , indexes e and i mark extracellular and

intracellular concentrations of corresponding free ions, respectively.

Approximation of J_{SR} . We used a first order periodic spline S_{SR} to determine J_{SR} . Within period p , spline has 9 nodal points between 0.1–0.906 s that are distributed as follows: in the range 0.1–0.4 s there are seven nodal points, in the range 0.4–0.906 s there are two nodal points. Within the specified ranges, the nodal points are equally distributed. Outside of the ranges, J_{SR} is taken equal to zero. Thus, J_{SR} is given by

$$J_{SR} = H_{SR}(t) \cdot S_{SR}(t), \quad (5)$$

where $H_{SR}(t)$ determines inhibition of J_{SR} .

Inhibition function. We used following step-wise function H_Y to apply inhibition to Ca^{2+} flux Y :

$$H_Y(t) = -A_Y \operatorname{erf}(t_{0.5p}(t)/\tau_Y) + 1, \quad (6)$$

$$t_{0.5p}(t) = \begin{cases} 0, & \text{if } t \leq 0, \\ p(\lfloor t/p \rfloor + 0.5), & \text{otherwise,} \end{cases}$$

where A_Y is the maximal inhibition extent (from 0 to 1), τ_Y is the inhibition time constant, $t_{0.5p}$ is a time-moment in the middle of the pulse, and t is the actual time for which inhibition extent H_Y is found, $\lfloor \cdot \rfloor$ is the floor function. In the simulations, we considered only $\tau_Y \in [0.5, 5]$. By using the floor function, we assumed that within one beat inhibition extent remained constant.

Transmembrane Ca^{2+} flux conversion to membrane current. We converted transmembrane Ca^{2+} flux Y to membrane current I_Y by multiplying flux with Faraday constant F , non-mitochondrial cell volume V_c , and charge z (for J_{LTCC} $z=2$, J_{NCX} $z=-1$ assuming NCX stoichiometry of $3Na^+ : 1Ca^{2+}$). Thus, taking into account current sign convention, flux J_Y specific transmembrane current I_Y can be represented with following equation:

$$I_Y = -FV_c z_Y \cdot J_Y. \quad (7)$$

Calculation of compensatory current. Inhibitor specific compensatory current of a cell $I_c(t)$ was calculated as a difference between the sum of channel/exchanger specific transmembrane currents after and before inhibition. This corresponds to the current that has to be injected by the amplifier to maintain AP. Time-moment $t=0$ was taken as a time-moment at the start of a period at which the first non-zero current was measured. The compensatory current is given by the following equation:

$$I_c(t) = [I_{NCX}(t) + I_{LTCC}(t)] - [I_{NCX}(t_r) + I_{LTCC}(t_r)], \quad (8)$$

$$t_r(t) = t - \lceil t/p \rceil p,$$

where flux specific transmembrane currents are calculated by Eq. 7, t_r is time-moment within the last beat before inhibition corresponding to the time-moment t and $\lceil \cdot \rceil$ is the ceiling function.

3 OPTIMIZATION PROCEDURES

We used a combination of parameter scan and least square optimization to estimate different parameters of the model. We

applied different optimization procedures for estimating total cellular Ca^{2+} buffering capacity and estimating cell specific calcium fluxes and average contributions.

The values of all used constants are presented in Table 1 and the mean values with their respective standard deviations of optimized parameters are shown in Table 2.

3.1 Estimating total cellular calcium buffering capacity

To estimate total cellular Ca^{2+} buffering capacity B_t , we used trout cardiomyocytes where SR Ca^{2+} release and uptake were inhibited. Using these myocytes, we measured compensatory currents and corresponding fluorescence transients in the presence of either NIF or Ni^{2+} . For analysis, we combined the measurements into pairs. In each pair, there was a measurement performed in the presence of NIF and a measurement performed in the presence of Ni^{2+} . For each pair of cells, the modeling was carried out in several steps:

(step 1) we performed a parameter scan totaling of 3600 different value combinations of the following parameters:

- inhibition time constants: τ_{LTCC}^{NIF} , τ_{LTCC}^{Ni} , τ_{NCX}^{Ni} , where $\tau_{LTCC}^{Ni} = \tau_{NCX}^{Ni}$,
- maximum inhibition extents: A_{LTCC}^{NIF} , A_{LTCC}^{Ni} , A_{NCX}^{Ni} ,
- NCX kinetic constant K_{II} .

Note that upper index of inhibition denotes experiment type and lower index channel/exchanger. For each parameter set, we found the following current parameters that minimized the difference between model solution and measured compensatory currents:

- shape of J_{LTCC} through values at nodal points of the spline,
- conductivities c_{NIF} and c_{Ni} ,
- J_{NCX} scaling factor g_{NCX} .

The minimized least square residual ε_c is given below (Eq. 9, *Fitting compensatory currents*). For J_{NCX} calculations, Ca^{2+} concentration determined from experiments was used.

(step 2) we used optimized parameter values found from the previous step for each parameter set, and optimized B_t value. For that, we minimized least square residual ε_{Ca} (Eq. 10, *Fitting calcium transients*) by varying B_t . Here, Ca^{2+} concentration changes during a beat before inhibition were considered only. To improve signal-to-noise ratio, we found average Ca^{2+} concentration changes by averaging measured fluorescence traces of 10 sequential beats before inhibition.

(step 3) for each optimized parameter set (step 1) and corresponding B_t (step 2), we found the least square residual ε_{Ca} (Eq. 10). Here, the measured and calculated Ca^{2+} transients for 10 beats before and after inhibition were used. Out of the calculated residuals, we considered only parameter sets corresponding to 5% percentile of the least square residual ε_{Ca} . From these parameter sets, we selected a set that fitted compensatory currents the best (minimal ε_c). The corresponding B_t found for this parameter set in step 2 determined the buffering capacity for an experimental pair.

3.2 Estimating cell specific calcium fluxes and average contributions

To estimate cell specific Ca^{2+} fluxes and their average contributions to overall flux, we used data obtained from Ni^{2+} and NIF inhibition experiments. As an input for all calculations performed in this estimation procedure, we used an average Ca^{2+} buffering capacity B_t found from analysis of the recordings performed on trout cardiomyocytes with inhibited SR Ca^{2+} release and uptake (see previous subsection). As for estimating total cellular Ca^{2+} buffering capacity, we combined the measurements into pairs. In each pair, there was a measurement performed in the presence of NIF and a measurement performed in the presence of Ni^{2+} . For each pair of cells the modeling was carried out in several steps with the result of each step used in the subsequent step:

(step 1) as in step 1 for estimating total cellular Ca^{2+} buffering capacity, we performed a parameter scan totaling of 3600 different value combinations of the following parameters:

- inhibition time constants: $\tau_{\text{LTCC}}^{\text{NIF}}, \tau_{\text{LTCC}}^{\text{Ni}}, \tau_{\text{NCX}}^{\text{Ni}}$, where $\tau_{\text{LTCC}}^{\text{Ni}} = \tau_{\text{NCX}}^{\text{Ni}}$,
- maximum inhibition extents: $A_{\text{LTCC}}^{\text{NIF}}, A_{\text{LTCC}}^{\text{Ni}}, A_{\text{NCX}}^{\text{Ni}}$,
- NCX kinetic constant K_{II} .

For each parameter set, we found the following current parameters that minimized the difference between model solution and measured compensatory currents:

- shape of J_{LTCC} through values at nodal points of the spline,
- conductivities c_{NIF} and c_{Ni} , assuming that $c_{\text{NIF}} = c_{\text{Ni}}$,
- J_{NCX} scaling factor g_{NCX} .

The minimized least square residual ε_c is given below (Eq. 9, *Fitting compensatory currents*). For J_{NCX} calculations, Ca^{2+} concentration determined from experiments was used.

(step 2) for further analysis, we selected the parameter sets corresponding to 5% percentile of the least square residual ε_c found for all parameter values combinations in step 1. The following steps 3–7 were performed for all selected parameter sets, some parameters sets were filtered out if they failed condition specified in step 8, and the best solution among the parameter sets was selected in step 9.

(step 3) we found the first estimate for J_{SR} . For that, we first calculated the contribution of transmembrane Ca^{2+} fluxes to overall Ca^{2+} transient. Second, we subtracted found transmembrane Ca^{2+} flux contribution from average of 10 sequential Ca^{2+} transient measured before inhibition started. Finally, to get first estimate for SR Ca^{2+} flux, we minimized least square residual $\varepsilon_{J_{\text{SR}}}$ (Eq. 11, *First estimate of J_{SR}*) by varying J_{SR} spline S_{SR} nodal values. For the pair of considered measurements, J_{SR} was found for each cell separately, *i.e.* one for the cell in the presence of Ni^{2+} and one for the cell in the presence of NIF.

(step 4) we found the estimates for inhibition curves of J_{SR} fluxes. Here, only maximum inhibition extents $A_{\text{SR}}^{\text{NIF}}$ and $A_{\text{SR}}^{\text{Ni}}$ were optimized and time constants remained the same as assigned for inhibition functions for J_{NCX} and J_{LTCC} in parameter scan. The minimized least square residual ε_h is given in Eq. 13 (*Estimating J_{SR} flux inhibition extent*).

(step 5) we optimized J_{SR} spline S_{SR} nodal points and its inhibition extents. Inhibition extents were split into two per J_{SR} . Namely, starting from inhibition of transmembrane currents, decrease of Ca^{2+} release and uptake from SR was separated. As a result, SR does not have to take up the same amount of Ca^{2+} than it releases per beat when inhibitor is applied. However, the balance of Ca^{2+} release and uptake by SR is enforced before application of inhibitor by including a term in minimized least square residual ε_f (Eq. 14, *Estimating J_{SR} flux*).

(step 6) we optimized only J_{SR} spline S_{SR} nodal points. The minimized least square residual ε_r is given in Eq. 17.

(step 7) with the found J_{SR} spline S_{SR} nodal points, we optimized only inhibition extents of J_{SR} . The minimized least square residual ε_f is given in Eq. 14 (*Estimating J_{SR} flux*).

(step 8) the found optimized model solution was checked to satisfy CICR condition. Namely, for solution representing cell response in the presence of Ni^{2+} , we calculated the relationship between Ca^{2+} influx through SR and through transmembrane channels (NCX and LTCC) during the inhibition phase of the experiment. Here, the influxes per each beat were calculated, as in Fig 4A and C in the main text. Assuming that Ca^{2+} influx to cytoplasm from SR is induced by CICR, we checked whether Ca^{2+} influx from SR would be zero when total Ca^{2+} influx through transmembrane currents was zero. For that, we extrapolated the relationship between SR and transmembrane fluxes during inhibition to condition at which transmembrane fluxes are zero. If extrapolated Ca^{2+} influx from SR was zero or below it, CICR condition was satisfied for this model parameters set and the set was used in the following step. If the influx through SR was larger than zero in the absence of transmembrane flux, the parameters set was discarded.

(step 9) the model solution of an experimental pair was determined as the solution that fits the best Ca^{2+} transients using the parameter values from the previous step, as judged by the least square residual ε_{Ca} in Eq. 10. As a result, the fluxes for each cell in the pair were found before and during the inhibition.

3.3 Minimized residuals

Fitting compensatory currents. Compensatory currents, I_{Ni} and I_{NIF} were fit in range of 10 beats starting with beat where compensatory current was first visible (Ni^{2+} or NIF started to take effect, respectively). The minimized residual is:

$$\varepsilon_c = \varepsilon_{c,\text{Ni}} + \varepsilon_{c,\text{NIF}}, \quad (9)$$

where $\varepsilon_{c,\text{Ni}}$ and $\varepsilon_{c,\text{NIF}}$ are least square residuals corresponding to compensatory currents recorded in Ni^{2+} and NIF inhibition experiments, respectively. The residual $\varepsilon_{c,X}$ for an experiment X is:

$$\varepsilon_{c,X} = \frac{1}{\sqrt{N_{c,X} \cdot \sigma_c}} \sum_{i=1}^{N_{c,X}} \left[I_{c,X}^{\text{calc}}(t_i) - I_{c,X}^{\text{expr}}(t_i) \right]^2,$$

where $N_{c,X}$ is a total number of data points of measured compensatory current during inhibition (10 beats of experiment X from the start of inhibition), σ_c is a penalty factor, $I_{c,X}^{\text{calc}}(t_i)$ is calculated compensatory current (see Eq. 8) and $I_{c,X}^{\text{expr}}(t_i)$ is measured compensatory current at time-moment t_i .

Fitting calcium transients. To fit Ca^{2+} transients, we calculated Ca^{2+} transients by solving Eq. 1 for Ni^{2+} and NIF inhibition experiment. The minimized residual is as follows:

$$\varepsilon_{\text{Ca}} = \varepsilon_{\text{Ca},\text{Ni}} + \varepsilon_{\text{Ca},\text{NIF}}, \quad (10)$$

where

$$\varepsilon_{\text{Ca},X} = \frac{1}{\sqrt{N_{\text{Ca},X} \cdot \sigma_{\text{Ca}}}} \sum_{i=1}^{N_{\text{Ca},X}} \left[\text{Ca}_X^{\text{calc}}(t_i) - \text{Ca}_X^{\text{expr}}(t_i) \right]^2,$$

$N_{\text{Ca},X}$ is a total number of data points of measured Ca^{2+} transient during inhibition (10 beats of experiment X from the start of inhibition), σ_{Ca} is a penalty factor, $\text{Ca}_X^{\text{calc}}$ is calculated intracellular free Ca^{2+} concentration using Eq. 1, and $\text{Ca}_X^{\text{expr}}$ is corresponding Ca^{2+} concentration derived from fluorescence measurements of experiment X . Here, Ca^{2+} concentration was found by the model, J_{NCX} in Eq. 1 was calculated using the model-provided intracellular Ca^{2+} concentration.

First estimate of J_{SR} . The minimized residual for estimating J_{SR} flux is as follows:

$$\varepsilon_{J_{\text{SR}}} = \varepsilon_{J_{\text{SR}},\text{Ni}} + \varepsilon_{J_{\text{SR}},\text{NIF}}, \quad (11)$$

where

$$\varepsilon_{J_{\text{SR}},X} = \frac{1}{\sqrt{N_{J_{\text{SR}},X} \cdot \sigma_{J_{\text{SR}}}}} \sum_{i=1}^{N_{J_{\text{SR}},X}} \left[J_{\text{SR},X}^{\text{calc}}(t_i) - J_{\text{SR},X}^{\text{expr}}(t_i, \text{Ca}_X) \right]^2.$$

Here, $N_{J_{\text{SR}},X}$ is a number of data points of derived intracellular free Ca^{2+} concentration Ca_X from fluorescence measurements of experiment X , $\sigma_{J_{\text{SR}}}$ is a penalty factor, $J_{\text{SR},X}^{\text{calc}}$ is calculated SR Ca^{2+} flux using Eq. 5, and $J_{\text{SR},X}^{\text{expr}}$ is SR Ca^{2+} flux using following equations:

$$\begin{aligned} J_{\text{SR},X}^{\text{expr}}(t_i, \text{Ca}_X) &= \frac{\Delta \text{Ca}_X}{\Delta t} \Big|_{t_i} \quad (12) \\ &\cdot \left(1 + \frac{F_t K_f}{[K_f + \text{Ca}_X(t_i)]^2} + \frac{B_t K_b}{[K_b + \text{Ca}_X(t_i)]^2} \right) \\ &- J_{\text{NCX},X}(t_i) - J_{\text{LTCC},X}(t_i), \\ \frac{\Delta \text{Ca}_X}{\Delta t} \Big|_{t_i} &= \frac{\text{Ca}_X(t_i) - \text{Ca}_X(t_i - t_{i-2})}{t_i - t_{i-2}}, \quad i \in \mathbb{N}[3, N_{J_{\text{SR}},X}], \\ \frac{\Delta \text{Ca}_X}{\Delta t} \Big|_{t_1, t_2} &= \frac{\Delta \text{Ca}_X}{\Delta t} \Big|_{t_3}, \end{aligned}$$

where $J_{\text{NCX},X}$ and $J_{\text{LTCC},X}$ are transmembrane Ca^{2+} fluxes determined on the bases of compensation currents for experiment performed in presence of inhibitor X .

Estimating J_{SR} flux inhibition extent. To estimate J_{SR} flux inhibition extent, we minimized the following residual:

$$\varepsilon_h = \varepsilon_{h,\text{Ni}} + \varepsilon_{h,\text{NIF}}, \quad (13)$$

where

$$\varepsilon_{h,X} = \frac{1}{\sqrt{N_{h,X} \cdot \sigma_{J_{\text{SR}}}}} \sum_{i=1}^{N_{h,X}} \left[J_{\text{SR},X}^{\text{calc}}(t_i) - J_{\text{SR},X}^{\text{expr}}(t_i, \text{Ca}_X) \right]^2,$$

$N_{h,X}$ is a number of data points of measured Ca^{2+} transients Ca_X from 10 beats before and after inhibition of experiment X , $J_{\text{SR},X}^{\text{calc}}$ is calculated SR Ca^{2+} flux using Eq. 5, and $J_{\text{SR},X}^{\text{expr}}$ is SR Ca^{2+} flux using Eq. 12.

Estimating J_{SR} flux. The minimized residual ε_f consist of compensation current residual ε_c , Ca^{2+} transient residual ε_{Ca} , Ca^{2+} periodicity residual $\varepsilon_{\text{Ca}^{\text{rest}}}$, and residual $\varepsilon_{\text{ClCR}}$ that ensures net Ca^{2+} flux from SR during a period is zero in the absence of inhibitors. The residual ε_f is given by

$$\varepsilon_f = \varepsilon_c + \varepsilon_{\text{Ca}} + \varepsilon_{\text{Ca}^{\text{rest}}} + \varepsilon_{\text{ClCR}}, \quad (14)$$

where ε_c is given by Eq. 9, ε_{Ca} is residual for Ca^{2+} transient 10 beats before and after inhibition (Eq. 10). Periodicity of $[\text{Ca}^{2+}]_i$ before inhibition is ensured by $\varepsilon_{\text{Ca}^{\text{rest}}}$:

$$\varepsilon_{\text{Ca}^{\text{rest}}} = \varepsilon_{\text{Ca}^{\text{rest}},\text{Ni}} + \varepsilon_{\text{Ca}^{\text{rest}},\text{NIF}} \quad (15)$$

where

$$\varepsilon_{\text{Ca}^{\text{rest}},X} = \frac{\text{Ca}_X^{\text{rest}} - \text{Ca}_X^{\text{calc}}(0)}{\text{Ca}_X^{\text{rest}}},$$

where $\text{Ca}_X^{\text{rest}}$ is resting intracellular Ca^{2+} concentration and $\text{Ca}_X^{\text{calc}}(0)$ is the calculated $[\text{Ca}^{2+}]_i$ at the time-moment $t=0$ of experiment X . The last term $\varepsilon_{\text{ClCR}}$ in Eq. 14 ensures that the amount of calcium released and accumulated by SR within a beat remains the same:

$$\varepsilon_{\text{ClCR}} = \left[\int_{-p}^0 J_{\text{SR},\text{Ni}}(t) dt \right]^2 + \left[\int_{-p}^0 J_{\text{SR},\text{NIF}}(t) dt \right]^2, \quad (16)$$

where $J_{\text{SR},\text{Ni}}$ and $J_{\text{SR},\text{NIF}}$ are SR Ca^{2+} flux approximation functions (Eq. 5).

Estimating J_{SR} flux 2. The following minimized residual for estimating J_{SR} flux is reduced form of ε_f (Eq. 14):

$$\varepsilon_r = \varepsilon_{\text{Ca}} + \varepsilon_{\text{Ca}^{\text{rest}}} + \varepsilon_{\text{ClCR}}. \quad (17)$$

4 VALUES OF USED CONSTANTS AND OPTIMIZED PARAMETERS

In the following tables values of used constants and optimized parameters are given.

TABLE 1: Values of used constants

Notation	Definition	Value
F	Faraday constant	96.487 C/mmol
R	universal gas constant	8.3145 J/(mol·K)
T	temperature	295 K
$[\text{Na}^+]_i$	intracellular sodium concentration	14 mM
$[\text{Na}^+]_e$	extracellular sodium concentration	130.4 mM
$[\text{Ca}^+]_e$	extracellular calcium concentration	2 mM
K_b	dissociation constant of B_t	2380 nM (1)
F_t	intracellular concentration of fluorescence agent	130 nM
K_f	dissociation constant of fluorescence agent	1048 nM (2)
p	pulse period	0.9091 s
σ_c	compensatory current penalty factor for optimization	5 pA
σ_{Ca}	measured Ca^{2+} transient penalty factor for optimization	125 nM
$\sigma_{J_{\text{SR}}}$	penalty factor for J_{SR} optimization	25 μM
$\text{Ca}_X^{\text{rest}}$	resting intracellular calcium concentration	100 nM

TABLE 2: Values of optimized parameters

Notation	Definition	Control	SR inhibited	Unit
		mean \pm SD	mean \pm SD	
B_t	Total cellular Ca^{2+} buffering capacity	51.2	51.2 ± 15.6	μM
$\tau_{\text{LTCC}}^{\text{NIF}}$	inhibition time constant	2.5 ± 1.1	3.5 ± 0.8	s
$\tau_{\text{LTCC}}^{\text{Ni}}$	inhibition time constant	2.5 ± 0.7	2.7 ± 1.4	s
$\tau_{\text{NCX}}^{\text{Ni}}$	inhibition time constant	2.5 ± 0.7	2.7 ± 1.4	s
c_{Ni}	conductivity of J_{LTCC} in Ni^{2+} experiment	5.5 ± 1.6	5.1 ± 1.8	$\mu\text{M}/(\text{s}\cdot\text{pF})$
c_{NIF}	conductivity of J_{LTCC} in NIF experiment	5.5 ± 1.6	5.0 ± 3.1	$\mu\text{M}/(\text{s}\cdot\text{pF})$
g_{NCX}	J_{NCX} scaling factor	0.28 ± 0.10	0.50 ± 0.16	$\cdot 10^{-3} \text{ mM}^{-4}$
K_{II}	NCX kinetic constant	10000 ± 6500	1600 ± 440	mM^4

SUPPORTING REFERENCES

1. Greenstein, J., and R. Winslow, 2002. An integrative model of the cardiac ventricular myocyte incorporating local control of Ca^{2+} release. *Biophys. J.* 83:2918–2945.
2. Shiels, H. A., A. D. Maio, S. Thompson, and B. A. Block, 2010. Warm fish with cold hearts: thermal plasticity of excitation–contraction coupling in bluefin tuna. *Proc. Royal Soc. B: Biological Sci.* NA.

**DISSERTATIONS DEFENDED AT
TALLINN UNIVERSITY OF TECHNOLOGY ON
NATURAL AND EXACT SCIENCES**

1. **Olav Kongas**. Nonlinear Dynamics in Modeling Cardiac Arrhythmias. 1998.
2. **Kalju Vanatalu**. Optimization of Processes of Microbial Biosynthesis of Isotopically Labeled Biomolecules and Their Complexes. 1999.
3. **Ahto Buldas**. An Algebraic Approach to the Structure of Graphs. 1999.
4. **Monika Drews**. A Metabolic Study of Insect Cells in Batch and Continuous Culture: Application of Chemostat and Turbidostat to the Production of Recombinant Proteins. 1999.
5. **Eola Valdre**. Endothelial-Specific Regulation of Vessel Formation: Role of Receptor Tyrosine Kinases. 2000.
6. **Kalju Lott**. Doping and Defect Thermodynamic Equilibrium in ZnS. 2000.
7. **Reet Koljak**. Novel Fatty Acid Dioxygenases from the Corals *Plexaura homomalla* and *Gersemia fruticosa*. 2001.
8. **Anne Paju**. Asymmetric oxidation of Prochiral and Racemic Ketones by Using Sharpless Catalyst. 2001.
9. **Marko Vendelin**. Cardiac Mechanoenergetics *in silico*. 2001.
10. **Pearu Peterson**. Multi-Soliton Interactions and the Inverse Problem of Wave Crest. 2001.
11. **Anne Menert**. Microcalorimetry of Anaerobic Digestion. 2001.
12. **Toomas Tiivel**. The Role of the Mitochondrial Outer Membrane in *in vivo* Regulation of Respiration in Normal Heart and Skeletal Muscle Cell. 2002.
13. **Olle Hints**. Ordovician Scolecodonts of Estonia and Neighbouring Areas: Taxonomy, Distribution, Palaeoecology, and Application. 2002.
14. **Jaak Nõlvak**. Chitinozoan Biostratigraphy in the Ordovician of Baltoscandia. 2002.
15. **Liivi Kluge**. On Algebraic Structure of Pre-Operad. 2002.
16. **Jaanus Lass**. Biosignal Interpretation: Study of Cardiac Arrhythmias and Electromagnetic Field Effects on Human Nervous System. 2002.
17. **Janek Peterson**. Synthesis, Structural Characterization and Modification of PAMAM Dendrimers. 2002.
18. **Merike Vaher**. Room Temperature Ionic Liquids as Background Electrolyte Additives in Capillary Electrophoresis. 2002.
19. **Valdek Mikli**. Electron Microscopy and Image Analysis Study of Powdered Hardmetal Materials and Optoelectronic Thin Films. 2003.
20. **Mart Viljus**. The Microstructure and Properties of Fine-Grained Cermets. 2003.
21. **Signe Kask**. Identification and Characterization of Dairy-Related *Lactobacillus*. 2003.
22. **Tiiu-Mai Laht**. Influence of Microstructure of the Curd on Enzymatic and Microbiological Processes in Swiss-Type Cheese. 2003.
23. **Anne Kuusksalu**. 2–5A Synthetase in the Marine Sponge *Geodia cydonium*. 2003.
24. **Sergei Bereznev**. Solar Cells Based on Polycrystalline Copper-Indium Chalcogenides and Conductive Polymers. 2003.

25. **Kadri Kriis.** Asymmetric Synthesis of C₂-Symmetric Bimorpholines and Their Application as Chiral Ligands in the Transfer Hydrogenation of Aromatic Ketones. 2004.
26. **Jekaterina Reut.** Polypyrrole Coatings on Conducting and Insulating Substrates. 2004.
27. **Sven Nõmm.** Realization and Identification of Discrete-Time Nonlinear Systems. 2004.
28. **Olga Kijatkina.** Deposition of Copper Indium Disulphide Films by Chemical Spray Pyrolysis. 2004.
29. **Gert Tamberg.** On Sampling Operators Defined by Rogosinski, Hann and Blackman Windows. 2004.
30. **Monika Übner.** Interaction of Humic Substances with Metal Cations. 2004.
31. **Kaarel Adamberg.** Growth Characteristics of Non-Starter Lactic Acid Bacteria from Cheese. 2004.
32. **Imre Vallikivi.** Lipase-Catalysed Reactions of Prostaglandins. 2004.
33. **Merike Peld.** Substituted Apatites as Sorbents for Heavy Metals. 2005.
34. **Vitali Syritski.** Study of Synthesis and Redox Switching of Polypyrrole and Poly(3,4-ethylenedioxythiophene) by Using *in-situ* Techniques. 2004.
35. **Lee Põllumaa.** Evaluation of Ecotoxicological Effects Related to Oil Shale Industry. 2004.
36. **Riina Aav.** Synthesis of 9,11-Secosterols Intermediates. 2005.
37. **Andres Braunbrück.** Wave Interaction in Weakly Inhomogeneous Materials. 2005.
38. **Robert Kitt.** Generalised Scale-Invariance in Financial Time Series. 2005.
39. **Juss Pavelson.** Mesoscale Physical Processes and the Related Impact on the Summer Nutrient Fields and Phytoplankton Blooms in the Western Gulf of Finland. 2005.
40. **Olari Ilison.** Solitons and Solitary Waves in Media with Higher Order Dispersive and Nonlinear Effects. 2005.
41. **Maksim Säkki.** Intermittency and Long-Range Structurization of Heart Rate. 2005.
42. **Enli Kiipli.** Modelling Seawater Chemistry of the East Baltic Basin in the Late Ordovician–Early Silurian. 2005.
43. **Igor Golovtsov.** Modification of Conductive Properties and Processability of Polyparaphenylene, Polypyrrole and polyaniline. 2005.
44. **Katrin Laos.** Interaction Between Furcellaran and the Globular Proteins (Bovine Serum Albumin β -Lactoglobulin). 2005.
45. **Arvo Mere.** Structural and Electrical Properties of Spray Deposited Copper Indium Disulphide Films for Solar Cells. 2006.
46. **Sille Ehala.** Development and Application of Various On- and Off-Line Analytical Methods for the Analysis of Bioactive Compounds. 2006.
47. **Maria Kulp.** Capillary Electrophoretic Monitoring of Biochemical Reaction Kinetics. 2006.
48. **Anu Aaspõllu.** Proteinases from *Vipera lebetina* Snake Venom Affecting Hemostasis. 2006.

49. **Lyudmila Chekulayeva.** Photosensitized Inactivation of Tumor Cells by Porphyrins and Chlorins. 2006.
50. **Merle Uudsemaa.** Quantum-Chemical Modeling of Solvated First Row Transition Metal Ions. 2006.
51. **Tagli Pitsi.** Nutrition Situation of Pre-School Children in Estonia from 1995 to 2004. 2006.
52. **Angela Ivask.** Luminescent Recombinant Sensor Bacteria for the Analysis of Bioavailable Heavy Metals. 2006.
53. **Tiina Lõugas.** Study on Physico-Chemical Properties and Some Bioactive Compounds of Sea Buckthorn (*Hippophae rhamnoides* L.). 2006.
54. **Kaja Kasemets.** Effect of Changing Environmental Conditions on the Fermentative Growth of *Saccharomyces cerevisiae* S288C: Auxo-accelerostat Study. 2006.
55. **Ildar Nisamedtinov.** Application of ^{13}C and Fluorescence Labeling in Metabolic Studies of *Saccharomyces* spp. 2006.
56. **Alar Leibak.** On Additive Generalisation of Voronoï's Theory of Perfect Forms over Algebraic Number Fields. 2006.
57. **Andri Jagomägi.** Photoluminescence of Chalcopyrite Tellurides. 2006.
58. **Tõnu Martma.** Application of Carbon Isotopes to the Study of the Ordovician and Silurian of the Baltic. 2006.
59. **Marit Kauk.** Chemical Composition of CuInSe_2 Monograin Powders for Solar Cell Application. 2006.
60. **Julia Kois.** Electrochemical Deposition of CuInSe_2 Thin Films for Photovoltaic Applications. 2006.
61. **Ilona Oja Açıık.** Sol-Gel Deposition of Titanium Dioxide Films. 2007.
62. **Tiia Anmann.** Integrated and Organized Cellular Bioenergetic Systems in Heart and Brain. 2007.
63. **Katrin Trummal.** Purification, Characterization and Specificity Studies of Metalloproteinases from *Vipera lebetina* Snake Venom. 2007.
64. **Gennadi Lessin.** Biochemical Definition of Coastal Zone Using Numerical Modeling and Measurement Data. 2007.
65. **Enno Pais.** Inverse problems to determine non-homogeneous degenerate memory kernels in heat flow. 2007.
66. **Maria Borissova.** Capillary Electrophoresis on Alkylimidazolium Salts. 2007.
67. **Karin Valmsen.** Prostaglandin Synthesis in the Coral *Plexaura homomalla*: Control of Prostaglandin Stereochemistry at Carbon 15 by Cyclooxygenases. 2007.
68. **Kristjan Piirimäe.** Long-Term Changes of Nutrient Fluxes in the Drainage Basin of the Gulf of Finland – Application of the PolFlow Model. 2007.
69. **Tatjana Dedova.** Chemical Spray Pyrolysis Deposition of Zinc Sulfide Thin Films and Zinc Oxide Nanostructured Layers. 2007.
70. **Katrin Tomson.** Production of Labelled Recombinant Proteins in Fed-Batch Systems in *Escherichia coli*. 2007.
71. **Cecilia Sarmiento.** Suppressors of RNA Silencing in Plants. 2008.
72. **Vilja Mardla.** Inhibition of Platelet Aggregation with Combination of Antiplatelet Agents. 2008.

73. **Maie Bachmann.** Effect of Modulated Microwave Radiation on Human Resting Electroencephalographic Signal. 2008.
74. **Dan Hivonen.** Terahertz Spectroscopy of Low-Dimensional Spin Systems. 2008.
75. **Ly Villo.** Stereoselective Chemoenzymatic Synthesis of Deoxy Sugar Esters Involving *Candida antarctica* Lipase B. 2008.
76. **Johan Anton.** Technology of Integrated Photoelasticity for Residual Stress Measurement in Glass Articles of Axisymmetric Shape. 2008.
77. **Olga Volobujeva.** SEM Study of Selenization of Different Thin Metallic Films. 2008.
78. **Artur Jogi.** Synthesis of 4'-Substituted 2,3'-dideoxynucleoside Analogues. 2008.
79. **Mario Kadastik.** Doubly Charged Higgs Boson Decays and Implications on Neutrino Physics. 2008.
80. **Fernando Perez-Caballero.** Carbon Aerogels from 5-Methylresorcinol-Formaldehyde Gels. 2008.
81. **Sirje Vaask.** The Comparability, Reproducibility and Validity of Estonian Food Consumption Surveys. 2008.
82. **Anna Menaker.** Electrosynthesized Conducting Polymers, Polypyrrole and Poly(3,4-ethylenedioxythiophene), for Molecular Imprinting. 2009.
83. **Lauri Ilison.** Solitons and Solitary Waves in Hierarchical Korteweg-de Vries Type Systems. 2009.
84. **Kaia Ernits.** Study of In₂S₃ and ZnS Thin Films Deposited by Ultrasonic Spray Pyrolysis and Chemical Deposition. 2009.
85. **Veljo Sinivee.** Portable Spectrometer for Ionizing Radiation "Gammamapper". 2009.
86. **Juri Virkepu.** On Lagrange Formalism for Lie Theory and Operadic Harmonic Oscillator in Low Dimensions. 2009.
87. **Marko Piirsoo.** Deciphering Molecular Basis of Schwann Cell Development. 2009.
88. **Kati Helmja.** Determination of Phenolic Compounds and Their Antioxidative Capability in Plant Extracts. 2010.
89. **Merike Somera.** Sobemoviruses: Genomic Organization, Potential for Recombination and Necessity of P1 in Systemic Infection. 2010.
90. **Kristjan Laes.** Preparation and Impedance Spectroscopy of Hybrid Structures Based on CuIn₃Se₅ Photoabsorber. 2010.
91. **Kristin Lippur.** Asymmetric Synthesis of 2,2'-Bimorpholine and its 5,5'-Substituted Derivatives. 2010.
92. **Merike Luman.** Dialysis Dose and Nutrition Assessment by an Optical Method. 2010.
93. **Mihhail Berezovski.** Numerical Simulation of Wave Propagation in Heterogeneous and Microstructured Materials. 2010.
94. **Tamara Aid-Pavlidis.** Structure and Regulation of BDNF Gene. 2010.
95. **Olga Bragina.** The Role of Sonic Hedgehog Pathway in Neuro- and Tumorigenesis. 2010.

96. **Merle Randrüüt.** Wave Propagation in Microstructured Solids: Solitary and Periodic Waves. 2010.
97. **Marju Laars.** Asymmetric Organocatalytic Michael and Aldol Reactions Mediated by Cyclic Amines. 2010.
98. **Maarja Grossberg.** Optical Properties of Multinary Semiconductor Compounds for Photovoltaic Applications. 2010.
99. **Alla Maloverjan.** Vertebrate Homologues of Drosophila Fused Kinase and Their Role in Sonic Hedgehog Signalling Pathway. 2010.
100. **Priit Pruunsild.** Neuronal Activity-Dependent Transcription Factors and Regulation of Human *BDNF* Gene. 2010.
101. **Tatjana Knjazeva.** New Approaches in Capillary Electrophoresis for Separation and Study of Proteins. 2011.
102. **Atanas Katerski.** Chemical Composition of Sprayed Copper Indium Disulfide Films for Nanostructured Solar Cells. 2011.
103. **Kristi Timmo.** Formation of Properties of CuInSe_2 and $\text{Cu}_2\text{ZnSn}(\text{S},\text{Se})_4$ Monograin Powders Synthesized in Molten KI. 2011.
104. **Kert Tamm.** Wave Propagation and Interaction in Mindlin-Type Microstructured Solids: Numerical Simulation. 2011.
105. **Adrian Popp.** Ordovician Proetid Trilobites in Baltoscandia and Germany. 2011.
106. **Ove Pärn.** Sea Ice Deformation Events in the Gulf of Finland and This Impact on Shipping. 2011.
107. **Germo Väli.** Numerical Experiments on Matter Transport in the Baltic Sea. 2011.
108. **Andrus Seiman.** Point-of-Care Analyser Based on Capillary Electrophoresis. 2011.
109. **Olga Katargina.** Tick-Borne Pathogens Circulating in Estonia (Tick-Borne Encephalitis Virus, *Anaplasma phagocytophilum*, *Babesia* Species): Their Prevalence and Genetic Characterization. 2011.
110. **Ingrid Sumeri.** The Study of Probiotic Bacteria in Human Gastrointestinal Tract Simulator. 2011.
111. **Kairit Zovo.** Functional Characterization of Cellular Copper Proteome. 2011.
112. **Natalja Makarytsheva.** Analysis of Organic Species in Sediments and Soil by High Performance Separation Methods. 2011.
113. **Monika Mortimer.** Evaluation of the Biological Effects of Engineered Nanoparticles on Unicellular Pro- and Eukaryotic Organisms. 2011.
114. **Kersti Tepp.** Molecular System Bioenergetics of Cardiac Cells: Quantitative Analysis of Structure-Function Relationship. 2011.
115. **Anna-Liisa Peikolainen.** Organic Aerogels Based on 5-Methylresorcinol. 2011.
116. **Leeli Amon.** Palaeoecological Reconstruction of Late-Glacial Vegetation Dynamics in Eastern Baltic Area: A View Based on Plant Macrofossil Analysis. 2011.
117. **Tanel Peets.** Dispersion Analysis of Wave Motion in Microstructured Solids. 2011.

118. **Liina Kaupmees**. Selenization of Molybdenum as Contact Material in Solar Cells. 2011.
119. **Allan Olsper**. Properties of VPg and Coat Protein of Sobemoviruses. 2011.
120. **Kadri Koppel**. Food Category Appraisal Using Sensory Methods. 2011.
121. **Jelena Gorbatšova**. Development of Methods for CE Analysis of Plant Phenolics and Vitamins. 2011.
122. **Karin Viipsi**. Impact of EDTA and Humic Substances on the Removal of Cd and Zn from Aqueous Solutions by Apatite. 2012.
123. **David Schryer**. Metabolic Flux Analysis of Compartmentalized Systems Using Dynamic Isotopologue Modeling. 2012.
124. **Ardo Illaste**. Analysis of Molecular Movements in Cardiac Myocytes. 2012.
125. **Indrek Reile**. 3-Alkylcyclopentane-1,2-Diones in Asymmetric Oxidation and Alkylation Reactions. 2012.
126. **Tatjana Tamberg**. Some Classes of Finite 2-Groups and Their Endomorphism Semigroups. 2012.
127. **Taavi Liblik**. Variability of Thermohaline Structure in the Gulf of Finland in Summer. 2012.
128. **Priidik Lagemaa**. Operational Forecasting in Estonian Marine Waters. 2012.
129. **Andrei Errapart**. Photoelastic Tomography in Linear and Non-linear Approximation. 2012.
130. **Külliki Krabbi**. Biochemical Diagnosis of Classical Galactosemia and Mucopolysaccharidoses in Estonia. 2012.
131. **Kristel Kaseleht**. Identification of Aroma Compounds in Food using SPME-GC/MS and GC-Olfactometry. 2012.
132. **Kristel Kodar**. Immunoglobulin G Glycosylation Profiling in Patients with Gastric Cancer. 2012.
133. **Kai Rosin**. Solar Radiation and Wind as Agents of the Formation of the Radiation Regime in Water Bodies. 2012.
134. **Ann Tiiman**. Interactions of Alzheimer's Amyloid-Beta Peptides with Zn(II) and Cu(II) Ions. 2012.
135. **Olga Gavrilova**. Application and Elaboration of Accounting Approaches for Sustainable Development. 2012.
136. **Olesja Bondarenko**. Development of Bacterial Biosensors and Human Stem Cell-Based *In Vitro* Assays for the Toxicological Profiling of Synthetic Nanoparticles. 2012.
137. **Katri Muska**. Study of Composition and Thermal Treatments of Quaternary Compounds for Monograin Layer Solar Cells. 2012.
138. **Ranno Nahku**. Validation of Critical Factors for the Quantitative Characterization of Bacterial Physiology in Accelerostat Cultures. 2012.
139. **Petri-Jaan Lahtvee**. Quantitative Omics-level Analysis of Growth Rate Dependent Energy Metabolism in *Lactococcus lactis*. 2012.
140. **Kerti Orumets**. Molecular Mechanisms Controlling Intracellular Glutathione Levels in Baker's Yeast *Saccharomyces cerevisiae* and its Random Mutagenized Glutathione Over-Accumulating Isolate. 2012.
141. **Loreida Timberg**. Spice-Cured Sprats Ripening, Sensory Parameters Development, and Quality Indicators. 2012.

142. **Anna Mihhalevski.** Rye Sourdough Fermentation and Bread Stability. 2012.
143. **Liisa Arike.** Quantitative Proteomics of *Escherichia coli*: From Relative to Absolute Scale. 2012.
144. **Kairi Otto.** Deposition of In₂S₃ Thin Films by Chemical Spray Pyrolysis. 2012.
145. **Mari Sepp.** Functions of the Basic Helix-Loop-Helix Transcription Factor TCF4 in Health and Disease. 2012.
146. **Anna Suhhova.** Detection of the Effect of Weak Stressors on Human Resting Electroencephalographic Signal. 2012.
147. **Aram Kazarjan.** Development and Production of Extruded Food and Feed Products Containing Probiotic Microorganisms. 2012.
148. **Rivo Uiboupin.** Application of Remote Sensing Methods for the Investigation of Spatio-Temporal Variability of Sea Surface Temperature and Chlorophyll Fields in the Gulf of Finland. 2013.
149. **Tiina Kriščiunaite.** A Study of Milk Coagulability. 2013.
150. **Tuuli Levandi.** Comparative Study of Cereal Varieties by Analytical Separation Methods and Chemometrics. 2013.
151. **Natalja Kabanova.** Development of a Microcalorimetric Method for the Study of Fermentation Processes. 2013.
152. **Himani Khanduri.** Magnetic Properties of Functional Oxides. 2013.
153. **Julia Smirnova.** Investigation of Properties and Reaction Mechanisms of Redox-Active Proteins by ESI MS. 2013.
154. **Mervi Sepp.** Estimation of Diffusion Restrictions in Cardiomyocytes Using Kinetic Measurements. 2013.
155. **Kersti Jääger.** Differentiation and Heterogeneity of Mesenchymal Stem Cells. 2013.
156. **Victor Alari.** Multi-Scale Wind Wave Modeling in the Baltic Sea. 2013.
157. **Taavi Päll.** Studies of CD44 Hyaluronan Binding Domain as Novel Angiogenesis Inhibitor. 2013.
158. **Allan Niidu.** Synthesis of Cyclopentane and Tetrahydrofuran Derivatives. 2013.
159. **Julia Geller.** Detection and Genetic Characterization of *Borrelia* Species Circulating in Tick Population in Estonia. 2013.
160. **Irina Stulova.** The Effects of Milk Composition and Treatment on the Growth of Lactic Acid Bacteria. 2013.
161. **Jana Holmar.** Optical Method for Uric Acid Removal Assessment During Dialysis. 2013.
162. **Kerti Ausmees.** Synthesis of Heterobicyclo[3.2.0]heptane Derivatives via Multicomponent Cascade Reaction. 2013.
163. **Minna Varikmaa.** Structural and Functional Studies of Mitochondrial Respiration Regulation in Muscle Cells. 2013.
164. **Indrek Koppel.** Transcriptional Mechanisms of BDNF Gene Regulation. 2014.
165. **Kristjan Pilt.** Optical Pulse Wave Signal Analysis for Determination of Early Arterial Ageing in Diabetic Patients. 2014.

166. **Andres Anier**. Estimation of the Complexity of the Electroencephalogram for Brain Monitoring in Intensive Care. 2014.
167. **Toivo Kallaste**. Pyroclastic Sanidine in the Lower Palaeozoic Bentonites – A Tool for Regional Geological Correlations. 2014.
168. **Erki Kärber**. Properties of ZnO-nanorod/In₂S₃/CuInS₂ Solar Cell and the Constituent Layers Deposited by Chemical Spray Method. 2014.
169. **Julia Lehner**. Formation of Cu₂ZnSnS₄ and Cu₂ZnSnSe₄ by Chalcogenisation of Electrochemically Deposited Precursor Layers. 2014.
170. **Peep Pitk**. Protein- and Lipid-rich Solid Slaughterhouse Waste Anaerobic Co-digestion: Resource Analysis and Process Optimization. 2014.
171. **Kaspar Valgepea**. Absolute Quantitative Multi-omics Characterization of Specific Growth Rate-dependent Metabolism of *Escherichia coli*. 2014.
172. **Artur Noole**. Asymmetric Organocatalytic Synthesis of 3,3'-Disubstituted Oxindoles. 2014.
173. **Robert Tsanev**. Identification and Structure-Functional Characterisation of the Gene Transcriptional Repressor Domain of Human Gli Proteins. 2014.
174. **Dmitri Kartofelev**. Nonlinear Sound Generation Mechanisms in Musical Acoustic. 2014.
175. **Sigrid Hade**. GIS Applications in the Studies of the Palaeozoic Graptolite Argillite and Landscape Change. 2014.
176. **Agne Velthut-Meikas**. Ovarian Follicle as the Environment of Oocyte Maturation: The Role of Granulosa Cells and Follicular Fluid at Pre-Ovulatory Development. 2014.
177. **Kristel Hälvin**. Determination of B-group Vitamins in Food Using an LC-MS Stable Isotope Dilution Assay. 2014.
178. **Mailis Pääri**. Characterization of the Oligoadenylate Synthetase Subgroup from Phylum Porifera. 2014.
179. **Jekaterina Kazantseva**. Alternative Splicing of *TAF4*: A Dynamic Switch between Distinct Cell Functions. 2014.
180. **Jaanus Suurväli**. Regulator of G Protein Signalling 16 (RGS16): Functions in Immunity and Genomic Location in an Ancient MHC-Related Evolutionarily Conserved Synteny Group. 2014.
181. **Ene Viiard**. Diversity and Stability of Lactic Acid Bacteria During Rye Sourdough Propagation. 2014.
182. **Kristella Hansen**. Prostaglandin Synthesis in Marine Arthropods and Red Algae. 2014.
183. **Helike Lõhelaid**. Allene Oxide Synthase-lipoxygenase Pathway in Coral Stress Response. 2015.
184. **Normunds Stivrīnš**. Postglacial Environmental Conditions, Vegetation Succession and Human Impact in Latvia. 2015.
185. **Mary-Liis Kütt**. Identification and Characterization of Bioactive Peptides with Antimicrobial and Immunoregulating Properties Derived from Bovine Colostrum and Milk. 2015.
186. **Kazbulat Šogenov**. Petrophysical Models of the CO₂ Plume at Prospective Storage Sites in the Baltic Basin. 2015.

187. **Taavi Raadik**. Application of Modulation Spectroscopy Methods in Photovoltaic Materials Research. 2015.
188. **Reio Põder**. Study of Oxygen Vacancy Dynamics in Sc-doped Ceria with NMR Techniques. 2015.
189. **Sven Siir**. Internal Geochemical Stratification of Bentonites (Altered Volcanic Ash Beds) and its Interpretation. 2015.
190. **Kaur Jaanson**. Novel Transgenic Models Based on Bacterial Artificial Chromosomes for Studying BDNF Gene Regulation. 2015.
191. **Niina Karro**. Analysis of ADP Compartmentation in Cardiomyocytes and Its Role in Protection Against Mitochondrial Permeability Transition Pore Opening. 2015.
192. **Piret Laht**. B-plexins Regulate the Maturation of Neurons Through Microtubule Dynamics. 2015.
193. **Sergei Žari**. Organocatalytic Asymmetric Addition to Unsaturated 1,4-Dicarbonyl Compounds. 2015.
194. **Natalja Buhhalko**. Processes Influencing the Spatio-temporal Dynamics of Nutrients and Phytoplankton in Summer in the Gulf of Finland, Baltic Sea. 2015.
195. **Natalia Maticiu**. Mechanism of Changes in the Properties of Chemically Deposited CdS Thin Films Induced by Thermal Annealing. 2015.
196. **Mario Öeren**. Computational Study of Cyclohexylhemicucurbiturils. 2015.
197. **Mari Kalda**. Mechanoenergetics of a Single Cardiomyocyte. 2015.
198. **Ieva Grudzinska**. Diatom Stratigraphy and Relative Sea Level Changes of the Eastern Baltic Sea over the Holocene. 2015.
199. **Anna Kazantseva**. Alternative Splicing in Health and Disease. 2015.
200. **Jana Kazarjan**. Investigation of Endogenous Antioxidants and Their Synthetic Analogues by Capillary Electrophoresis. 2016.
201. **Maria Safonova**. SnS Thin Films Deposition by Chemical Solution Method and Characterization. 2016.
202. **Jekaterina Mazina**. Detection of Psycho- and Bioactive Drugs in Different Sample Matrices by Fluorescence Spectroscopy and Capillary Electrophoresis. 2016.
203. **Karin Rosenstein**. Genes Regulated by Estrogen and Progesterone in Human Endometrium. 2016.
204. **Aleksei Tretjakov**. A Macromolecular Imprinting Approach to Design Synthetic Receptors for Label-Free Biosensing Applications. 2016.
205. **Mati Danilson**. Temperature Dependent Electrical Properties of Kesterite Monograin Layer Solar Cells. 2016.
206. **Kaspar Kevvai**. Applications of ¹⁵N-labeled Yeast Hydrolysates in Metabolic Studies of *Lactococcus lactis* and *Saccharomyces Cerevisiae*. 2016.
207. **Kadri Aller**. Development and Applications of Chemically Defined Media for Lactic Acid Bacteria. 2016.
208. **Gert Preegel**. Cyclopentane-1,2-dione and Cyclopent-2-en-1-one in Asymmetric Organocatalytic Reactions. 2016.
209. **Jekaterina Služenikina**. Applications of Marine Scatterometer Winds and Quality Aspects of their Assimilation into Numerical Weather Prediction Model HIRLAM. 2016.

210. **Erkki Kask.** Study of Kesterite Solar Cell Absorbers by Capacitance Spectroscopy Methods. 2016.
211. **Jürgen Arund.** Major Chromophores and Fluorophores in the Spent Dialysate as Cornerstones for Optical Monitoring of Kidney Replacement Therapy. 2016.
212. **Andrei Šamarin.** Hybrid PET/MR Imaging of Bone Metabolism and Morphology. 2016.
213. **Kairi Kasemets.** Inverse Problems for Parabolic Integro-Differential Equations with Instant and Integral Conditions. 2016.
214. **Edith Soosaar.** An Evolution of Freshwater Bulge in Laboratory Scale Experiments and Natural Conditions. 2016.
215. **Peeter Laas.** Spatiotemporal Niche-Partitioning of Bacterioplankton Community across Environmental Gradients in the Baltic Sea. 2016.
216. **Margus Voolma.** Geochemistry of Organic-Rich Metalliferous Oil Shale/Black Shale of Jordan and Estonia. 2016.
217. **Karin Ojamäe.** The Ecology and Photobiology of Mixotrophic Alveolates in the Baltic Sea. 2016.
218. **Anne Pink.** The Role of CD44 in the Control of Endothelial Cell Proliferation and Angiogenesis. 2016.
219. **Kristiina Kreek.** Metal-Doped Aerogels Based on Resorcinol Derivatives. 2016.